ALMA MATER STUDIORUM
UNIVERSITÀ DI BOLOGNA

DOTTORATO DI RICERCA IN
ASTROFISICA

Ciclo XXXV

Dynamical modelling of early-type galaxies: analytical multi-component systems, and application to spherical gas accretion

Presentata da:
Antonio Mancino

Supervisore:
Chiar.mo Prof.
Luca Ciotti

Coordinatore Dottorato:
Chiar.mo Prof.
Andrea Miglio

Co-supervisore:
Chiar.ma Prof.ssa
Silvia Pellegrini

Esame finale anno 2024

Settore Concorsuale: 02/C1 – Astronomia, Astrofisica, Fisica della Terra e dei Pianeti
Settore Scientifico Disciplinare: FIS/05 – Astronomia e Astrofisica

« “Radagast the Brown!” laughed Saruman, and he no longer concealed his scorn.
“Radagast the Bird-tamer! Radagast the Simple! Radagast the Fool!
Yet he had just the wit to play the part that I set him.
For you have come, and that was all the purpose of my message.
And here you will stay, Gandalf the Grey, and rest from journeys.
For I am Saruman the Wise, Saruman Ring-maker, Saruman of Many Colours!”.
« I looked then and saw that his robes, which had seemed white,
were not so, but were woven of all colours,
and if he moved they shimmered and changed hue so that the eye was bewildered.
« “I liked white better”, I said.
« “White!” he sneered. “It serves as a beginning. White cloth may be dyed.
The white page can be overwritten; and the white light can be broken”.
« “In which case it is no longer white”, said I.
“And he that breaks a thing to find out what it is has left the path of wisdom” ».

J.R.R. Tolkien, *The Lord of the Rings*, Book II, Chapter II

Abstract

Dynamical models, even when simplified, are of great importance, because they can be used, for example, to understand the dynamics of more complicated (i.e., realistic) models, as well as to obtain first indications about sensible choices of parameters to be subsequently refined with more time-consuming numerical methods. In this Thesis we present the construction of galaxy models simple enough to provide some insight into the main structural and dynamical properties of real galaxies. The work focuses on axisymmetric Jeans modelling for galaxies, assumed to be stationary collisionless stellar systems.

In particular, we consider ellipsoidal galaxies characterized by weakly flattened shape: this allows for the application of a technique, known as homoeoidal expansion, representing the theoretical framework underlying the entire modelling procedure. We apply this technique to two families of two-component (stars plus dark matter) galaxy models, solving the two-integral Jeans equations also in presence of a central black hole: most of the results are completely analytical; when this is not possible, an asymptotic analysis is discussed or a numerical inspection is presented. The expansion method is then reviewed, analyzing and applying its two different interpretations to the case of simple one-component models: here the effectiveness of the homoeoidal approximation is examined using both analytical and numerical techniques; this method is finally adopted for the phenomenological interpretation of a real globular cluster.

A part of the Thesis is devoted to the study of the polytropic accretion of gas onto the black hole at the centre of spherical galaxies, modelled as the spherical limit of one of the two families of axisymmetric models previously discussed. In order to study the motion of gas flows we generalize the classical Bondi problem by taking into account the effects of the gravitational field of the host galaxy, and the radiation pressure due to electron scattering. The isothermal and monoatomic adiabatic cases are discussed in fully analytical way, while for generic values of the polytropic index a numerical investigation is performed. We also elucidate some important thermodynamical properties of accretion, determining the underlying cooling/heating function leading to the phenomenological value of the polytropic index.

Contents

CHAPTER 1

INTRODUCTION

Galaxies are the building blocks of the Universe. Some of them have a simple structure, others are complex systems composed of many separate components (e.g., stars, gas, dust, or magnetic fields). One of the most evident property of galaxies related with their morphology is the fact that, at least from a qualitative point of view, they can be classified into few distinct types. In a commonly adopted classification, the first to be proposed, the so-called *Hubble classification* (e.g Hubble 1926; 1936), galaxies are classified as follows.

- ELLIPTICAL GALAXIES
  These are ellipsoidal stellar systems containing very little cold gas and dust. The galaxy NGC 4150, shown in Fig. 1.2, is a classic example of this type. In most galaxies belonging to this category, the stars are very old, with an age comparable to that of the Universe. The *isophotes*, i.e. the contours of constant surface brightness, are approximately concentric ellipses, with a minor-to-major axis ratio b/a ranging from 1 to around 0.3 (e.g. Cappellari 2016). Introducing the symbol En, where $n = 10 \times (1 - b/a)$, the most flattened elliptical galaxies are of type E7; flatter galaxies are not observed because dynamically unstable. The Hubble classification is based on the ellipticity of the isophotes near the so-called "effective radius", defined as the radius of the isophote containing half of the total luminosity, an important physical parameter used as a measure of the size of the galaxy.

- DISC GALAXIES
  These are galaxies, such as the Milky Way and M101 (see Fig. 1.1), containing an evident disc composed of stars, gas and dust. The disc, in turn, contains spiral arms (different in shape and length for each galaxy), huge filaments where stars are continuously forming; the dynamical reasons underlying the formation and maintenance of such structures (on timescales of the order of tens of galactic disc rotations) are quite complex, and have been investigated in extensive theoretical studies (e.g. Lin & Shu 1964; Bertin & Lin 1996; see also Bertin 2014, Part III). In the central regions there is a "swelling" in the disc, called *bulge*, a concentrated stellar system: some bulges resemble small elliptical galaxies and presumably followed the same formation process, while others (resembling thickened discs) might have formed as a result of complex dynamic processes (e.g. Kormendy & Kennicutt 2004).

- LENTICULAR GALAXIES
  They are transitional objects between elliptical and spiral galaxies: like ellipticals, they have very small amounts of cold gas and no recent star formation; like spirals, they contain a rotating disc, a bulge, and sometimes a bar; in contrast to spiral galaxies, they have no spiral

structure. They can be generally found in regions of high density, and constitute almost half of the galaxies in the central regions of galaxy clusters; for this reason, it is possible that such galaxies were spirals in the past, which over time have lost their interstellar gas through interactions with the hot intracluster gas (e.g. van Gorkom 2004). In the Hubble classification, lenticulars are denoted as S0, or SB0 if barred.

- Irregular Galaxies
  They do not present a well-defined morphology. Some distinctive features of these galaxies are the presence of a large amount of gas, a considerable number of young blue stars, and large HII regions. Furthermore, this type of galaxy is extremely common: for example, more than a third of the galaxies in the vicinity of the Milky Way are irregulars.

This is clearly only a qualitative and not exhaustive description: each class of galaxies can in turn be organized into subclasses according to specific criteria, and other morphological classifications have been proposed over time as alternatives to Hubble's (see e.g. de Vaucouleurs 1959; van den Bergh 1976; Kormendy & Bender 1996; Kormendy et al. 2009 and references therein; see also Delgado Serrano 2010 for a review). However, just a morphological classification certainly cannot be sufficient for a clear physical understanding of the galaxy properties; the major challenges are to understand how these particular structures form and maintain their shape, what processes allow the formation of an elliptical galaxy instead of a spiral one, or whether a galaxy of one type can transform into another. In the next Sections some concepts concerning the dynamics of galaxies will be clarified, especially regarding the global behavior of a very large number of gravitationally interacting stars.

1.1 Introduction to Stellar Dynamics

Stellar Dynamics is a large branch of Astrophysics (e.g. Chandrasekhar 1942; Binney & Tremaine 1987, hereafter BT87; Bertin 2014; Ciotti 2021, hereafter C21), and it is therefore not easy to give a simple definition. Its major aim is to achieve a qualitative understanding of the structure and evolution of stellar systems (e.g., open and globular clusters, galaxies, or galaxy clusters) and to develop mathematical methods (both analytical and numerical) capable of making quantitative predictions. In general, we may say that Stellar Dynamics focuses on studying the behaviour of gravitational systems composed of an extremely large number of "particles" (the so-called "N-body systems", say $N \gg 10$). Of course, the connections with Celestial Mechanics (i.e. that discipline which studies the behaviour of systems with a much smaller number of bodies, say $N < 10$) are very strong; in addition, Stellar Dynamics makes an extensive use of techniques and results also belonging to Analytical Mechanics, Statistical Mechanics, Hydrodynamics and Plasma Physics. One of the aspects that must never be underestimated is that of observations, which are the true point of contact between theory and the physical world: on the one hand, theory provides a source of interesting targets for observational astronomers, challenging their practical skills and instruments; on the other hand, observations of increasing accuracy can confirm or falsify results obtained by theoretical methods.

One of the most important problems in Stellar Dynamics concerns the formal treatment of the fundamental elements of each stellar system, i.e. the stars. For this purpose, let us consider as a simple model of stellar system a sphere of radius R containing a number N_* of homogeneously distributed objects (i.e. stars). We then define:

- R_*, the average radius of the stars;
- $\sigma_{\rm g} \equiv 4\pi R_*^2$, the geometrical cross section for the collision between two stars;
- $V_{\rm eff} \equiv \lambda \sigma_{\rm g}$, the "effective volume" of each star.

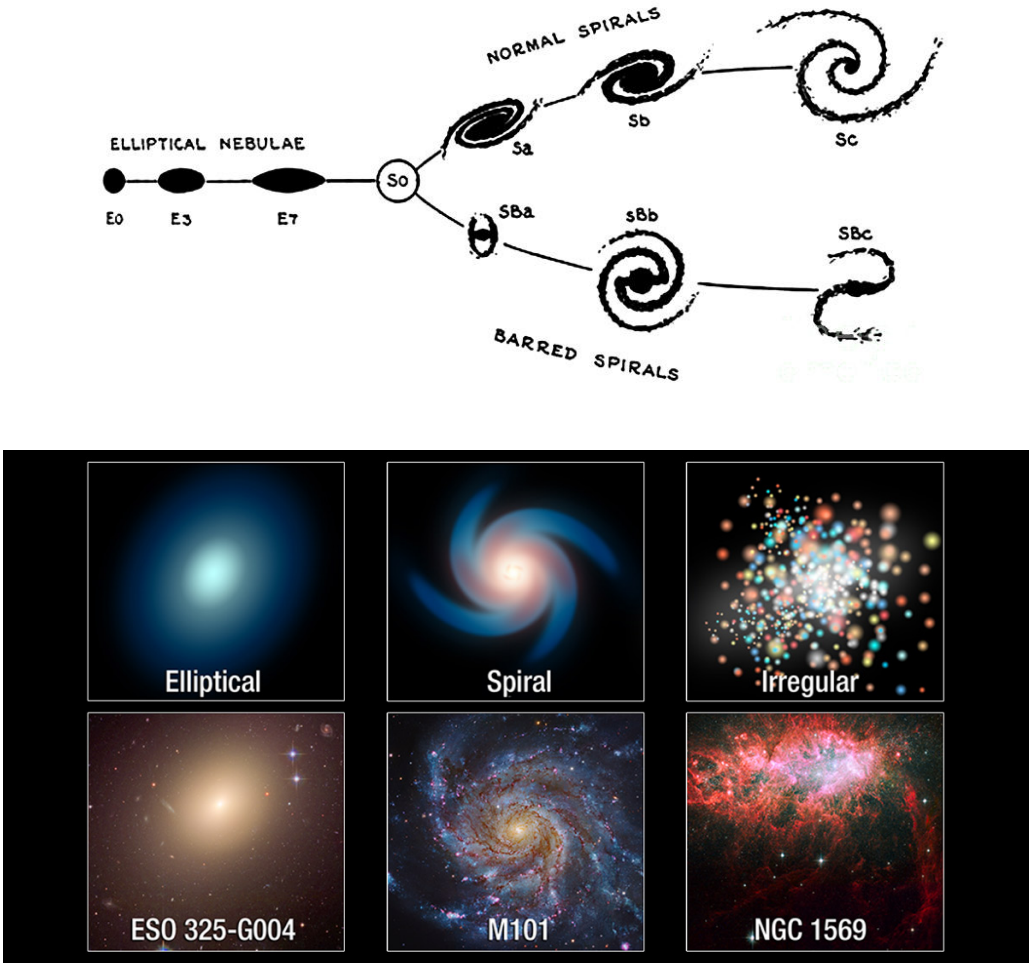

Figure 1.1. Top: the Hubble sequence, known as the "Hubble tuning-fork diagram"; credit E. Hubble (1936). Bottom: illustrations of the three types of galaxies (top), compared with actual photos of galaxies (bottom) that fit the categories; credit: A. Feild (Space Telescope Science Institute).

In particular, λ provides an estimate of the path that a star can travel on average without having a geometric collision (in practice, an impact) with any other star of the system. From the definition of effective volume given above, it follows that the product $N_* V_{\rm eff}$ must necessarily return the total volume of the system, i.e. $4\pi R_*^3/3$; as a consequence, simple algebra shows that

$$\frac{\lambda}{2R} = \frac{1}{6N_*}\left(\frac{R}{R_*}\right)^2 . \tag{1.1}$$

For a quantitative estimate, let us consider two examples of star systems: an early-type galaxy (ETG) and a Globular Cluster (GC). In the first case we can reasonably assume $N_* \approx 10^{11}$ and $R \approx 10\,\mathrm{kpc}$, while for GC we have $N_* \approx 10^6$ and $R \approx 10\,\mathrm{pc}$. Further assuming that in both cases all stars have a Sun-like size ($R_* \simeq 6.96 \times 10^5\,\mathrm{km}$) we obtain[1]

$$\frac{\lambda}{2R} \approx \begin{cases} 10^{11} & \text{(ETG)}, \\ 10^{10} & \text{(GC)}. \end{cases} \tag{1.2}$$

[1]Here and hereafter, "$\simeq$" indicates approximate numerical equivalence, while the symbol "$\approx$" is used to indicate an order-of-magnitude approximation.

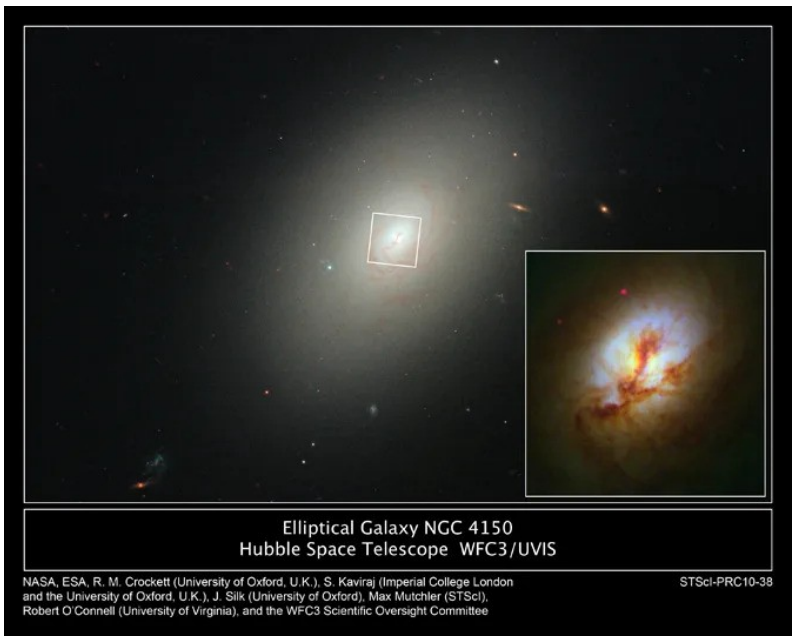

Figure 1.2. Top: the elliptical galaxy NGC4150 and its core taken in near-ultraviolet light; credit: NASA, ESA, R.M. Crockett (University of Oxford, U.K.), S. Kaviraj (Imperial College London and University of Oxford, U.K.), J. Silk (University of Oxford), M. Mutchler (Space Telescope Science Institute, Baltimore), R. O'Connell (University of Virginia, Charlottesville), and the WFC3 Scientific Oversight Committee. Bottom: image of M5, one of the oldest globular cluster of our Galaxy; credit: ESA/Hubble & NASA.

In addition, we know that the characteristic velocities of stars (v_*) are of the order of a few 10^2 km/sec in ETGs and of a few 10 km/sec in GCs. Therefore, even under the extreme hypothesis that elliptical galaxies and globular clusters have the same age as the Universe $t_{\rm H}$, we obtain $\lambda \gg v_* t_{\rm H}$ for both cases, being $t_{\rm H} \simeq 13.8\,{\rm Gyr}$. We therefore conclude that in stellar systems such as ETGs or GCs the possibility of geometric collisions between stars can be reasonably excluded even on time scales much longer than the age of the Universe itself.

In practice, *geometric collisions between individual stars can be totally ignored*. Each star can then be idealized as a material particle, so that the starting point of Stellar Dynamics is provided by the differential equations describing the well-known *N-body problem*. In the Newtonian formulation this problem is described (under the assumption of an inertial frame of reference) by the following $2N$ equations:

$$\frac{d\boldsymbol{x}_i}{dt} = \boldsymbol{v}_i, \qquad \frac{d\boldsymbol{v}_i}{dt} = -\frac{1}{m_i}\frac{\partial U}{\partial \boldsymbol{x}_i}, \qquad (i = 1, \ldots, N), \tag{1.3}$$

where m_i, $\boldsymbol{x}_i$ and $\boldsymbol{v}_i$ are respectively the mass, the position and the velocity of the i-th star, and U is the potential energy[2]. Unfortunately, the properties of the general solution of the N-body problem are currently unknown, making it a matter of great mathematical interest. Nevertheless, a number of mathematical techniques have been developed to "extract" information from the differential equations in (1.3), techniques which have played an essential role in achieving many fundamental results not only in Pure Mathematics but also in Numerical Analysis. In any case, it is sufficient to analyze the simplest results of a direct approach to the previous differential equations to understand the real need for an alternative approach to solve the problems addressed by Stellar Dynamics.

1.2 The construction of a galaxy model

One of the most powerful theoretical tools of investigation, replacing a direct attack on the differential equations defining the N-body problem, consists in switching from a "discrete" to a "continuous" formulation. Such a reduction may be performed by replacing the discrete N-body system with a smoothed-out three-dimensional density distribution $\rho(\boldsymbol{x}, t)$, which generally can be explicitly time-dependent; to this distribution is then associated a smoothed-out potential $\psi(\boldsymbol{x}, t)$ through *Poisson's equation* (e.g. Chandrasekhar 1942, Chapter II; C21, Chapter 7). In other words, we *substitute the study of the (ordinary) differential equations of motion of N bodies in the potential generated by themselves, with the study of the motion of a single test particle in the potential generated by a material "fluid" representing the continuous approximation of the N-body system itself*. In practice, this substitution can be made for systems characterized by a very large value of t_{2b}, a fundamental physical quantity called *two-body relaxation time*, defined as the time required in order for the cumulative effect of all the (hyperbolic) stellar encounters to deviate the orbit of an individual star significantly from the one it would have if the gravitational field were truly smooth. An asymptotic estimate for t_{2b} is given by

$$t_{2b} \sim \frac{N}{10 \ln N}\, t_{\rm cross}, \tag{1.4}$$

where $t_{\rm cross}$ is the so-called *crossing time*, defined as the time required to cross the entire system;

[2]The problem can of course be formulated using more sophisticated techniques, such as the *Lagrangian* and *Hamiltonian* approach; anyway, it must be formulated with the assignment of appropriate initial conditions (e.g. Arnold 1978).

notice that *the cumulative effect of stellar encounters becomes less important as the number of stars increases*. For a typical galaxy, $N \approx 10^{11}$, and $t_{\rm cross} \approx 10^2\,{\rm Myr}$; on the other hand, in case of a GC we have $N \approx 10^6$, and $t_{\rm cross} \approx 1\,{\rm Myr}$. Therefore, the previous equation yields

$$t_{2b} \approx \begin{cases} 10^6\,{\rm Gyr} \gg t_{\rm H} & \text{(galaxy)}, \\ 1\,{\rm Gyr} \quad < t_{\rm H} & \text{(GC)}. \end{cases} \tag{1.5}$$

Consequently, while the cumulative effects due to two-body interactions are important for the evolution of GCs (as confirmed by both numerical simulations and observations), *for all practical purposes galaxies are perfect examples of collisionless systems on time scales of the order of the life of the Universe*.

1.2.1 Collisionless stellar systems

The structure and dynamics of a collisionless system is completely determined by the *phase-space distribution function* $f(\boldsymbol{x}, \boldsymbol{v}, t)$, a fundamental concept in Statistical Mechanics which gives the distribution of the stars over position $\boldsymbol{x}$ and velocity $\boldsymbol{v}$ as a function of time. The distribution function satisfies the "Collisionless Boltzmann equation" (CBE), i.e.

$$\frac{\partial f}{\partial t} + \boldsymbol{v} \cdot \frac{\partial f}{\partial \boldsymbol{x}} + \frac{\partial \Psi}{\partial \boldsymbol{x}} \cdot \frac{\partial f}{\partial \boldsymbol{v}} = 0, \tag{1.6}$$

where $\Psi(\boldsymbol{x}, t) = \psi(\boldsymbol{x}, t) + \psi_{\rm ext}(\boldsymbol{x}, t)$ is the total gravitational potential under whose influence the stars move, which takes into account the effect of an additional potential generated by the eventual presence of a density different from that of the examined system (e.g. a density distribution of gas or dark matter); of course, $\psi_{\rm ext} = 0$ in the self-gravitating case. In addition, if the system is in a steady state, there is no an explicit time-dependence, so that $\partial f/\partial t = 0$. The density ρ is obtained from f via integration over the velocity space, i.e.

$$\int_{\Re^3} f(\boldsymbol{x}, \boldsymbol{v}, t) d^3\boldsymbol{v} = \rho(\boldsymbol{x}, t). \tag{1.7}$$

Finally, as mentioned at the beginning of the Section, the connection between the density ρ and the associated ψ is provided by Poisson's equation

$$\nabla^2 \psi = -4\pi G \rho. \tag{1.8}$$

In order to obtain a *dynamical model* for a stellar system, equations (1.6), (1.7) and (1.8) must be solved simultaneously; a solution f corresponds to a physically acceptable dynamical model only if $f \geq 0$. The problem of finding the distribution function for a stellar system is the fundamental problem of Stellar Dynamics. Unfortunately, current mathematical knowledge is not yet sufficient to have a complete understanding of the orbital structure in the three-dimensional space, so that the general problem is still unknown (e.g. Whittaker 1917; Chandrasekhar 1942; BT87; Bertin 2014; C21; see also Appendix A for more details); of course, even when simplified, dynamical models are of great importance, because they may be used, for example, to *understand the dynamics of more complicated (i.e., realistic) models*, as well as to obtain first indications about sensible choices of parameters to be subsequently refined with more time-consuming numerical methods. In general two main approaches can be identified:

- Method I ("direct problem" of Stellar Dynamics): from f-to-ρ.
  This approach is suitable for those systems where physical arguments can lead to a plausible

ansatz for the shape of the distribution function. This method is usually referred to as a "direct problem" since, once the distribution function f is assigned, the associated density ρ is just obtained from (1.7) by direct integration of f.

- METHOD II ("inverse problem" of Stellar Dynamics): from ρ-to-f.
  In this approach *a density profile is assumed*, together with a plausible guess about the model internal dynamics. This method is usually referred to as an "inverse problem" since the distribution function f must be recovered by *inverting* the integral expression (1.7); unsurprisingly, the problem of recovering f is in general a very difficult problem from a technical point of view; moreover, in the rare cases in which this is feasible, its uniqueness is not guaranteed, so a simple consistency analysis is still quite problematic.

Also, some methods have been developed over time to "extract" information from the CBE; one of these is known as the *method of moments*. The idea behind this third approach is to reduce equation (1.6) to a set of simpler differential equations; these "new" equations describe the relationships occuring between certain functions called "moments" of the distribution function over velocity space, and are historically known as *Jeans's equations* (see Appendix A): these are very important for a physically intuitive modelling of stellar systems, and represent some of the most useful tools in Stellar Dynamics, where are widely used for the phenomenological interpretation of observations of stellar systems such as galaxies and GCs. The latter method, whose general framework is described in detail in Appendix A, plays a major role in the following Chapters, being the one chosen in this Thesis to study the dynamical structure of axisymmetric galaxy models.

1.3 Outline of the Thesis

The present Thesis is mainly aimed at an analytical and numerical modelling of the structural and dynamical properties of multi-component systems. The purpose is the *construction of galaxy models sufficiently simple to provide some insight into the main dynamical properties of real galaxies*: e.g., to predict the qualitative trend of a quantity as a function of the model parameters, or to give a first approximate estimate.

The starting point are the JJ models (Ciotti & Ziaee Lorzad 2018), a family of two-component models where the stellar density profile, described by a Jaffe (1983) law, is immersed in another Jaffe model of different scale length. These models allow for an almost complete semi-analytical treatment of different quantities of interest in observational and theoretical work. In Ciotti et al. (2019) we improved the JJ models trying to keep the same analytical simplicity: the new models have been named J3, and they are two-component galaxy models with a stellar density profile again described by a Jaffe law, but with the additional property that the resulting DM halo is asymptotically similar to a Navarro-Frenk-White (Navarro et al. 1997) profile over the whole radial range.

Based on these two families of spherical models, the discussion has been divided into two main parts: one concerning the construction of axisymmetric galaxy models (Part I), and one involving the study of gas accretion in spherical galaxy models (Part II).

Part I focuses on the *homoeoidal expansion method*, a powerful technique which makes it possible to study in detail ellipsoidal models characterized by low values of the density flattening. Its content is detailed as follows.

- In Chapter 2 a summary of the main properties of ellipsoidal galaxy models is presented.
- In Chapter 3 the homoeoidal expansion method is described in detail, with a special emphasis on the axisymmetric case, for which the general expressions for the solution of Jeans's equations is presented.

- In Chapter 4 the homoeoidal expansion technique is exploited to generalize the JJ and J3 models to axisymmetric shape, thus constructing the corresponding JJe and J3e models. Thanks to the results described in the previous Chapter, the structural and intrinsic dynamical properties are discussed in fully analytical way; for the analysis of the projected dynamics, a numerical approach is instead adopted.

- In Chapter 5 two possible interpretations for a generic expanded model are discussed: the "η-linear" interpretation, in which the solutions of Jeans's equations contain only linear terms in the flattening, and the "η-quadratic" interpretation, where all terms are retained. To study the difference between the two views, two simple one-component galaxy models are considered: the ellipsoidal Plummer model and the Perfect Ellipsoid. The η-linear Plummer model is finally adopted for the phenomenological interpretation of the dynamics of the weakly flattened and rotating globular cluster NGC 4372.

Part II is devoted to the study of the polytropic Bondi accretion of gas onto the BH at the centre of spherically symmetric galaxies.

- In Chapter 6 the general considerations for studying the accretion of polytropic gas on the black hole at the centre of spherical galaxy models are discussed, also taking into account the additional effect of electron scattering. Some important thermodynamical aspects, implicitly described by the polytropic index, are also discussed.

- In Chapter 7 the results described in the previous Chapter are applied to the specific case of J3 models, linking hydrodynamical quantities with stellar ones. In the isothermal and monoatomic adiabatic cases the whole problem is carried out in a fully analytical manner; for generic values of the polytropic index, a numerical investigation is instead performed. The underlying cooling/heating function leading to the phenomenological value of the polytropic index is finally determined as a function of the model parameters.

Part I

Weakly flattened galaxy models

CHAPTER 2

Ellipsoidal Models

In this preliminary Chapter we summarize the main features of galaxy models defined by a density distribution stratified over ellipsoidal shapes. After a brief overview of the generic triaxial case, we shall proceed to analyze in detail the special family of axially symmetrical models, showing the formal solutions of Jeans's equations and summarizing the general expressions for the main projected dynamical fields.

2.1 The general case

Among all possible mass density distributions ρ, let us consider those stratified over ellipsoidal surfaces labelled by m:

$$\rho = \rho(m), \qquad m^2 \equiv \frac{x^2}{a^2} + \frac{y^2}{b^2} + \frac{z^2}{c^2}, \tag{2.1}$$

with (x, y, z) the usual Cartesian coordinates, and $a \geq b \geq c > 0$, so that the long axis of the model is in the x-direction and the short axis is in the z-direction. According to the foregoing equation, the density depends on the coordinates only through m, thus it takes the same value on all points which belong to the same ellipsoidal surface. In practice, the surfaces of constant density form a system of *similar ellipsoids* with common centres: we shall call "ellipsoidal" a density function of the form (2.1). It is evident from (2.1) that a model with mass density profile $\rho(m)$ has reflection symmetry in the three orthogonal principal planes. In particular, we may distinguish four main configurations:

- the general *triaxial* case, when $a > b > c$;
- the spheroidal *oblate* case, when $a = b > c$ (the z-axis being the symmetry axis);
- the spheroidal *prolate* case, when $a > b = c$ (the x-axis being the symmetry axis);
- the *spherical* case, when $a = b = c$.

In the Literature, such an object is usually referred to as a *heterogeneous ellipsoid*; in the particular case of a constant mass density, the ellipsoid is said to be *homogeneous* (see e.g. Chandrasekhar 1969, Chapter 3).

As a direct consequence of equation (2.1), the mass distribution is stratified over ellipsoidal surfaces. The expression for the cumulative mass contained within an ellipsoid of "radius" m is indeed given by

$$M(m) = 4\pi abc \int_0^m \rho(t) t^2 dt, \tag{2.2}$$

which is in complete accordance with the familiar expression for spherical symmetry, where $m = r/a$, being $r = \sqrt{x^2 + y^2 + z^2}$ the spherical radius (i.e. the distance from the centre of the system).

The associated (relative) potential[1] Ψ at a point $\boldsymbol{x} = (x, y, z)$, due to the distribution of matter with density $\rho(m)$, can be calculated by considering the density profile as a combination of infinitesimally thin ellipsoidal shells. By simple geometrical arguments it can be shown that the forces at the internal points of a shell cancel each other such that the associated internal potential is constant. The equipotential surfaces at the outer points of the shell are the ellipsoidal surfaces that are confocal with the shell. The summation of all contributions gives

$$\Psi(\boldsymbol{x}) = \pi G abc \int_0^\infty \frac{F[m(\boldsymbol{x}, \tau)]}{\Delta(\tau)} d\tau, \qquad F(x) \equiv 2 \int_x^\infty \rho(t) t \, dt, \tag{2.3}$$

(e.g. Kellogg 1967; Chandrasekhar 1969; BT87; C21), where G is the constant of gravitation, and

[1] We choose here to measure the gravitational potential by following the "positive-sign convention", in which the potential is usually indicated by Ψ, and the gravitational field $\boldsymbol{g}$ at a point $\boldsymbol{x}$ is given by the gradient of the potential with respect to $\boldsymbol{x}$, i.e. $\boldsymbol{g}(\boldsymbol{x}) = \boldsymbol{\nabla}\Psi$, being $\boldsymbol{\nabla} = \partial/\partial\boldsymbol{x}$ the gradient operator. On the contrary, following the "negative-sign convention", the potential is generally denoted by Φ, and the gravitational field equals the *negative* of the gradient of the potential, i.e. $\boldsymbol{g}(\boldsymbol{x}) = -\boldsymbol{\nabla}\Phi$. The two conventions, apart from an additive constant, are linked by the relation $\Psi = -\Phi$.

$$\Delta^2(\tau) \equiv (a^2+\tau)(b^2+\tau)(c^2+\tau), \qquad m^2(\boldsymbol{x},\tau) \equiv \frac{x^2}{a^2+\tau} + \frac{y^2}{b^2+\tau} + \frac{z^2}{c^2+\tau}. \tag{2.4}$$

Consequently, the explicit form of the potential function generated by a generic ellipsoidal density distribution usually cannot be expressed in closed form[2]. One exception is given by an interesting family of triaxial ellipsoidal models represented by the so-called *Ferrers ellipsoids* (see Ferrers 1877; BT87), for which many other additional physical properties, such as the mass within m or the projected density profile, can be evaluated via analytical methods (e.g. de Zeeuw and Pfenniger 1988; Lanzoni and Ciotti 2003). Another exception concerns galaxy models obtained by starting from a potential function expressed in *ellipsoidal coordinates* (see Lamé 1837; Jacobi 1839; Whittaker & Watson 1902; Lyttleton 1953), and among these the particular family of *Stäckel models*, studied in details by de Zeeuw and Lynden-Bell (see e.g. de Zeeuw 1985a; de Zeeuw and Lynden-Bell 1985; see also de Zeeuw 1984 and references therein). Of course, special values for the axis ratios lead to simpler expressions for the gravitational potential, and then to a simpler orbital structure (see e.g. de Zeeuw & Lynden-Bell 1985; de Zeeuw 1985a,b; de Zeeuw et al. 1987; Evans & de Zeeuw 1992), as for example in the case of oblate, prolate, and spherical models. Notice that, while the mass distribution is ellipsoidal in shape (see equation 2.2), a generic ellipsoidal density $\rho(m)$ does *not* produce in general an ellipsoidal potential[3].

Sometimes it may be convenient to rewrite equation (2.3) as

$$\Psi(\boldsymbol{x}) = \pi G a b c \int_0^\infty \frac{H(\infty) - H\left[m(\boldsymbol{x},\tau)\right]}{\Delta(\tau)}\, d\tau, \qquad H(x) \equiv 2\int_0^x \rho(t) t\, dt, \tag{2.5}$$

which, *when* $H(\infty)$ *converges to a finite value*, reduces to

$$\Psi(\boldsymbol{x}) = \Psi_0 - \pi G a b c \int_0^\infty \frac{H\left[m(\boldsymbol{x},\tau)\right]}{\Delta(\tau)}\, d\tau, \tag{2.6}$$

where $\Psi_0 \equiv 2\pi G a b c H(\infty) R_F(a^2, b^2, c^2)$ is the central potential, with R_F indicating one of the symmetric forms of elliptic integrals introduced by Carlson (1979). It is important to stress that the expressions (2.3) and (2.5), equivalent to each other, are equivalent to (2.6) *only* when the integral $H(\infty)$ converges and the potential has a finite value everywhere. Nevertheless, we have to consider two main cases for which this integral can diverge. It can diverge only at the lower limit ($t = 0$) due to a strong central cusp in the density; in this situation, the potential can be calculated by using equation (2.3): it is positive infinite at the centre, and vanishes at large distances. In an alternative way, the integral can diverge only at its upper limit ($t = \infty$); in this case the potential can be evaluated via equation (2.6), where Ψ_0 now represents just an additive constant: Ψ has a finite value Ψ_0 at the centre, and becomes negative at large distances. Finally, when the integral $H(\infty)$ diverges at both the lower and upper limits, none of the two expressions giving the potential can be applied, since both inner integrals now diverge. In practical terms, for example, for density profiles $\rho(m)$ that decrease faster than m^{-2} at large m, equations (2.3) and (2.5) place the zero of the potential at infinity. Shallower density distribution, instead, produce gravitational potentials that diverge at large distances; for, equation (2.6) may be used, and a further constant can be added to place the zero of Ψ at the centre or at a convenient (finite) value for m.

[2] For a wonderful historical summary on the problem of the determination of the gravitational potential of homogeneous and heterogeneous ellipsoids, see Chandrasekhar (1969, Chapter 1).

[3] For example, it is easy to show that the Laplacian of a generic ellipsoidal potential $\Psi(m)$, and so the associated mass density, is ellipsoidal only if the potential is a quadratic function of m (see C21, exercise 2.78).

An interesting question associated with a system described by a *generic* mass density ρ (not necessarily stratified on ellipsoidal surfaces) is the computation of the gravitational energy. For, one of the most important quantities describing the energetics of a system is given by the *self-interaction energy* W, a physical quantity representing the interaction energy of the density ρ with the gravitational field of the system itself; if ρ is distribuited in a generic volume V (which may have to be extended to the whole of space), W is defined as

$$W = \int_V \rho \boldsymbol{x} \cdot \boldsymbol{\nabla}\Psi \, d^3\boldsymbol{x}. \tag{2.7}$$

An insightful discussion, starting from the tensorial generalization of the fundamental energy quantities entering the so-called Tensor Virial Theorem (e.g., Section 10.5 in C21; see also Section 4.3 in BT87), can be found in Roberts (1962), where the following quite remarkable formula is obtained:

$$W = -\pi^2 G a b c (a^2 w_1 + b^2 w_2 + c^2 w_3) \int_0^\infty F^2(m) dm, \tag{2.8}$$

being the quantities w_i $(i = 1, 2, 3)$ defined as

$$w_1 \equiv abc \int_0^\infty \frac{d\tau}{(a^2+\tau)\Delta(\tau)}, \qquad w_2 \equiv abc \int_0^\infty \frac{d\tau}{(b^2+\tau)\Delta(\tau)}, \qquad w_3 \equiv abc \int_0^\infty \frac{d\tau}{(c^2+\tau)\Delta(\tau)}. \tag{2.9}$$

Note that the specific form for the density distribution does not appear in the previous definitions; moreover, with the adopted convention of $a \geq b \geq c$, one obtains $w_1 \leq w_2 \leq w_3$. It is usual in the Literature to write the results of the previous integrals as combinations of *elliptic integrals* of the first and second kind (see e.g. C21, equation 3.12); we prefer here to make use of Carlson's (1977; 1979) symmetric forms, with which we can rewrite the previous three coefficients w_i as

$$w_1 = \frac{2abc}{3} R_D(b^2, c^2, a^2), \qquad w_2 = \frac{2abc}{3} R_D(c^2, a^2, b^2), \qquad w_3 = \frac{2abc}{3} R_D(a^2, b^2, c^2), \tag{2.10}$$

where the function of three variables R_D is defined in Olver et al. (2010, § 19.16). Combining equations (2.8) and (2.10) we obtain

$$W = -\frac{2\pi^2 G a^2 b^2 c^2}{3} \left[a^2 R_D(b^2, c^2, a^2) + b^2 R_D(c^2, a^2, b^2) + c^2 R_D(a^2, b^2, c^2) \right] \int_0^\infty F^2(m) dm, \tag{2.11}$$

which, by using identity 19.21.9 in Olver et al. (2010), reduces to

$$W = -2\pi^2 G a^2 b^2 c^2 R_F(a^2, b^2, c^2) \int_0^\infty F^2(m) dm. \tag{2.12}$$

In particular, the ellipsoidal shape of the model affects only the factor preceding the integral, while the integral is exactly the same as for the corresponding spherical model (i.e. $a = b = c$), for which the function R_F takes the value $1/a$.

2.2 The axisymmetric case

A case of great astrophysical interest is that of a potential characterized by both an axis and a plane of symmetry. In this situation the natural coordinates are the cylindrical ones (R, φ, z), with all of the model properties independent of the azimuthal angle φ. As a consequence, the potential function can be expressed analytically as

$$\Psi = \Psi(R, z) = \Psi(R, -z), \tag{2.13}$$

where $R = \sqrt{x^2 + y^2}$ is the cylindrical radius (i.e. the distance from the centre of the system, in the plane $z = 0$); further, we choose the system such that the (x, y)-plane and the z-axis are the plane and the axis of symmetry, respectively. These kind of systems are called *axisymmetric systems* (e.g. BT87; C21), and they are the systems we shall be dealing with in this Part of the Thesis. We also assume that the density is stratified on *oblate* spheroidal surfaces ($a = b$), i.e.

$$\rho = \rho(m), \qquad\qquad m^2 \equiv \frac{R^2}{a^2} + \frac{z^2}{c^2}. \tag{2.14}$$

Accordingly, the potential (2.3) is replaced by

$$\Psi(R, z) = \pi G a^2 c \int_0^\infty \frac{F(m_\tau) d\tau}{(a^2 + \tau)\sqrt{c^2 + \tau}}, \qquad m_\tau^2 \equiv \frac{R^2}{a^2 + \tau} + \frac{z^2}{c^2 + \tau}. \tag{2.15}$$

Unsurprisingly, even though the hypothesis of perfect axisymmetry for the potential lead to great simplifications with respect to the general triaxial case, the double integral (2.15) yields non-elementary expressions for a number of models available in the Literature (e.g. Kuzmin 1956; Toomre 1963; Miyamoto and Nagai 1975; Nagai and Miyamoto 1976; Satoh 1980; Binney 1981; Evans 1994; Evans and de Zeeuw 1994). A peculiarity of axisymmetric systems is to allow orbits lying entirely in the (x, y)-plane; in other words, circular orbits represent possible solutions of the equations of motion for such systems[4]. This allows us to introduce a useful physical quantity known as *circular velocity* (see e.g. Chapter 5 in C21), defined as the speed, as a function of R, of a point mass in a circular orbit in the equatorial plane $z = 0$; we shall denote this quantity by v_c. In practice, for a generic potential of the kind in equation (2.13), the circular velocity is given by

$$v_c^2(R) = -R \left(\frac{\partial \Psi}{\partial R} \right)_{z=0}. \tag{2.16}$$

The quantity in brackets on the right-hand side is nothing more than the radial component of the gravitational field. As a consequence, a direct differentiation of equation (2.15) yields

[4] A fundamental property of a circular motion is its dynamical stability: any star whose orbit, at a certain initial instant, differs slightly from a circle, will continue for all time to have an orbit that differs only slightly from this circle. The stability of circular motions signifies that, if the changes in the coordinates are sufficiently small initially, they continue to be uniformly limited throughout time. In particular, the discussion of the stability of *nearly circular orbits* shows that such orbits are stable solutions of the equations of motion only if

$$\frac{\partial}{\partial R} \left(R^3 \frac{\partial \Psi}{\partial R} \right) < 0;$$

in practice, a circular orbit of radius R in the plane $z = 0$ is stable provided that the gravitational field at R decreases more slowly than an inverse cube law of force (see e.g. Ogorodnikov 1965; see also § 4.3 in Chandrasekhar 1942 for the proof of a more general theorem).

$$\frac{\partial\Psi}{\partial R} = -2\pi G a^2 c R \int_0^\infty \frac{\rho(m_\tau)d\tau}{(a^2+\tau)^2\sqrt{c^2+\tau}}, \tag{2.17}$$

whence it is easy to obtain, without any mathematical difficulty,

$$v_{\rm c}^2(R) = 2\pi G a^2 c R^2 \int_0^\infty \rho\left(\frac{R}{\sqrt{a^2+\tau}}\right)\frac{d\tau}{(a^2+\tau)^2\sqrt{c^2+\tau}}. \tag{2.18}$$

Later in this Thesis we shall introduce two families of ellipsoidal models for which $v_{\rm c}$ can be written in a fully analytical form. Of course, for a stellar system made of different mass components (e.g., a central supermassive black hole, a bulge, a stellar disc, a gaseous disc, and a dark matter halo), the squared of the total circular velocity equals the sum of the squared circular velocities of the single components (e.g. Ciotti & Ziaee Lorzad 2018, hereafter CZ18; Ciotti et al. 2019, hereafter CMP19; see also Mancino 2019 and references therein).

2.2.1 Intrinsic dynamics

As explained in detail in Appendix A, the evolution of a stellar system is completely described by the *Collisionless Boltzmann Equation* (CBE). By manipulating the CBE following a mathematical procedure known as *method of moments*, it is possible to obtain a number of certain general relations which are of great practical importance: these are the equations of "stellar hydrodynamics", also known as *Jeans's equations*. We assume that the axisymmetric stellar density $\rho(R,z)$ is supported by a two-integral phase-space distribution function $f(\mathcal{E},J_z)$, where $\mathcal{E}$ and J_z are the energy and orbital angular momentum z-component of stars (per unit mass), respectively. Also we indicate with v_R, v_φ and v_z the components of the velocity $\boldsymbol{v}$, and with a bar over a quantity its average value over the velocity space. As is well known (e.g. BT87; C21), for such a system:

1. the phase-space average of the mixed products of the velocity components vanishes, i.e., $\overline{v_R v_z} = \overline{v_R v_\varphi} = \overline{v_\varphi v_z} = 0$;
2. the only possible non-zero streaming motion is in the azimuthal direction, i.e. $\overline{v_\varphi}$;
3. at each point in the system, the radial and vertical velocity dispersions are equal, i.e., $\sigma_R^2 = \sigma_z^2 \equiv \sigma^2$.

With these assumptions, if the system is axisymmetric and in a steady state, Jeans's equations are given by equation (A28), i.e.

$$\begin{cases} \dfrac{\partial\rho\sigma^2}{\partial R} - \dfrac{\rho\Delta}{R} = \rho\dfrac{\partial\Psi}{\partial R}, \\ \dfrac{\partial\rho\sigma^2}{\partial z} = \rho\dfrac{\partial\Psi}{\partial z}, \end{cases} \qquad \Delta \equiv \overline{v_\varphi^2} - \sigma^2, \tag{2.19}$$

where σ is the *velocity dispersion* due to the potential Ψ (for more details, see § A.1). In the following, we shall call the first equation of the system (2.19) the *radial* Jeans equation, while we shall refer to the second one as the *vertical* Jeans equation. In order to split $\overline{v_\varphi^2}$ into ordered ($\overline{v_\varphi}$) and random (σ_φ) motions along the azimuthal direction, we adopt the phenomenological Satoh (1980) k-decomposition:

$$\overline{v_\varphi} = k\sqrt{\Delta}\,, \tag{2.20}$$

where k is a free parameter. However, the possibility of using Satoh's decomposition depends on the positivity of Δ. For $k = 0$, the system is azimuthally supported only by velocity dispersion, and no net rotation is present; when $k = 1$, the isotropic rotator is obtained, i.e. equation (2.20) gives the mean rotation such that the velocity dispersions around the mean rotation $\overline{v_\varphi}$ are isotropic everywhere in space[5]. Of course, the assumption (2.20) with constant k is not required by theoretical considerations, it is just the simplest starting point when trying to describe observations. Indeed, according to equation (2.20), the random component of the azimuthal velocity field can be written as

$$\sigma_\varphi^2 \equiv \overline{v_\varphi^2} - \overline{v_\varphi}^2 = \sigma^2 + (1 - k^2)\Delta; \tag{2.21}$$

now, imposing $\sigma_\varphi^2 \geq 0$, the restriction $\Delta \geq 0$ leads to the following inequality:

$$k^2 \leq 1 + \frac{\sigma^2}{\Delta}. \tag{2.22}$$

In other words, while in Satoh's decomposition k is independent of position, in principle it might be a function of R and z, bounded above by the function $k_{\max}(R, z) \equiv \sqrt{1 + \sigma^2/\Delta}$, defined by the condition[6] $\sigma_\varphi = 0$.

The solution of the vertical equation is easy to find. Indeed, after integrating at fixed R with the natural boundary condition of a vanishing "pressure" $\rho\sigma^2$ for $z \to \infty$, we readily obtain

$$\rho\sigma^2 = -\int_z^\infty \rho \frac{\partial \Psi}{\partial z'} dz', \tag{2.23}$$

which represents the *formal (integral) solution of the vertical Jeans equation for a generic axisymmetric density* $\rho(R, z)$.

Concerning the radial equation, in principle, once the vertical Jeans equation is solved, no further integration would be required because the quantity Δ can be obtained by differentiation. Indeed, rearranging the terms in the radial equation, we immediately obtain

$$\rho\Delta = R\left(\frac{\partial \rho\sigma^2}{\partial R} - \rho\frac{\partial \Psi}{\partial R}\right). \tag{2.24}$$

As a consequence, only one integration would be required to solve the system (2.19). However, this straightforward approach may produce formulae containing non-trivial simplifications, and hiding important properties of the solution. These problems can be avoided by a very elegant commutator-like formula for Δ, obtained by taking into account both equations of the system (2.19). By differentiating the radial equation with respect to z and the vertical equation with respect to R, and comparing the two expressions, we readily find

$$\frac{\partial}{\partial z}\left(\frac{\rho\Delta}{R}\right) + \frac{\partial}{\partial z}\left(\rho\frac{\partial \Psi}{\partial R}\right) = \frac{\partial}{\partial R}\left(\rho\frac{\partial \Psi}{\partial z}\right), \tag{2.25}$$

i.e., after some elementary reductions,

[5] Actually, the requirement $\Delta \geq 0$ may not be fulfilled in some special configurations: see Section 13.3.2 in C21, and exercises 13.28 and 13.29 therein.

[6] Fore a more detailed analysis, see e.g. Ciotti & Pellegrini 1996; the $k(R, z)$ formulation can also be used to add counterrotation in a controlled way (see e.g. Negri et al. 2014; see also Caravita et al. 2021).

$$\frac{\partial}{\partial z}\left(\frac{\rho\Delta}{R}\right) = \frac{\partial\rho}{\partial R}\frac{\partial\Psi}{\partial z} - \frac{\partial\rho}{\partial z}\frac{\partial\Psi}{\partial R}. \tag{2.26}$$

Hence, for untruncated distributions with vanishing "pressure" at infinity, equation (2.24) can be recast as the following commutator-like integral:

$$\rho\Delta = -R\int_z^\infty \left(\frac{\partial\rho}{\partial R}\frac{\partial\Psi}{\partial z'} - \frac{\partial\rho}{\partial z'}\frac{\partial\Psi}{\partial R}\right)dz'; \tag{2.27}$$

in analogy with equation (2.23), this is the *formal (integral) solution of the radial Jeans equation for a generic axisymmetric density* $\rho(R,z)$. Due to the strict relation of the isotropic Jeans equations and the hydrodynamic equations, it is not surprising that this relation appears both in Fluid Dynamics (see e.g. Rosseland 1926; Waxman 1978; Barnabè et al. 2006; Ciotti et al. 2021, hereafter CMPZ21; see also Tassoul 1978, C21, and references therein) and in Stellar Dynamics (see Hunter 1977; see also Smet 2015). Notice that the negativity of the integrand in equation (2.27) is a sufficient (but not necessary) condition to obtain $\Delta \geq 0$ everywhere[7]. Therefore, nowhere negative values for Δ are obtained if one assumes a potential Ψ for which $\partial\Psi/\partial R \leq 0$ and $\partial\Psi/\partial z \leq 0$ (the usual situation), and a density distribution ρ so that $\partial\rho/\partial z \leq 0$ and $\partial\rho/\partial R \geq 0$.

We shall now proceed to derive the solutions of Jeans's equations (2.19) for axisymmetric systems with a density of the form (2.14). For, it is sufficient to work with the integral expression defining the potential Ψ. By differentiating equation (2.15) with respect to z, in analogy with equation (2.17), it is easy to show that

$$\frac{\partial\Psi}{\partial z} = -2\pi G a^3 q z\int_0^\infty \frac{\rho(m_\tau)d\tau}{(a^2+\tau)(q^2a^2+\tau)^{3/2}}, \tag{2.28}$$

where $q \equiv c/a$ is the axial ratio. Now, by inserting this expression in equation (2.23) one has

$$\rho\sigma^2 = 2\pi G a^3 q\int_z^\infty dz'\rho(m')z'\int_0^\infty \frac{\rho(m'_\tau)d\tau}{(a^2+\tau)(q^2a^2+\tau)^{3/2}}, \tag{2.29}$$

where $m' = \sqrt{R^2/a^2 + z'^2/(q^2a^2)}$, and $m'_\tau = \sqrt{R^2/(a^2+\tau) + z'^2/(q^2a^2+\tau)}$. This represents the *formal solution of the vertical Jeans equation for an axisymmetric density distribution stratified over spheroidal surfaces.* Now we seek the solution of the radial equation (2.27). Firstly, we differentiate the density with respect to the coordinates:

$$\frac{\partial\rho}{\partial R} = \frac{1}{ma^2}\frac{d\rho}{dm}R, \qquad \frac{\partial\rho}{\partial z} = \frac{1}{ma^2}\frac{d\rho}{dm}\frac{z}{q^2}. \tag{2.30}$$

Secondly, using equations (2.17) and (2.28), the integrand on the right-hand side of equation (2.27) reduces to

$$\frac{\partial\rho}{\partial R}\frac{\partial\Psi}{\partial z} - \frac{\partial\rho}{\partial z}\frac{\partial\Psi}{\partial R} = 2\pi G a\frac{1-q^2}{q}\frac{Rz}{m}\frac{d\rho}{dm}\int_0^\infty \frac{\rho(m_\tau)\tau d\tau}{(a^2+\tau)^2(q^2a^2+\tau)^{3/2}}. \tag{2.31}$$

Now, inserting this expression in equation (2.27), we find

[7] For some general results regarding the positivity of Δ based on the use of the commutator, see e.g. Barnabè et al. (2006).

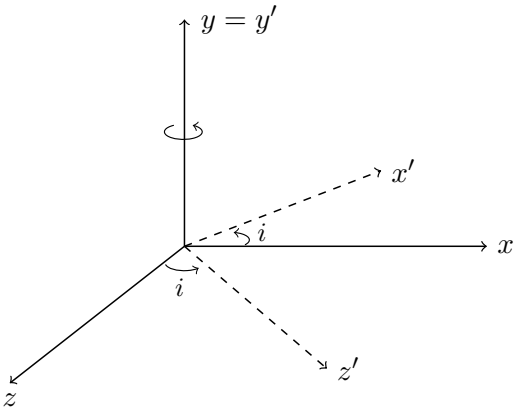

Figure 2.1. The rotation of angle i around y needed to define the total rotation matrix $\mathscr{R}$ between S_0 and the observer's system S'.

$$\rho\Delta = 2\pi G a \frac{1-q^2}{q} R^2 \int_z^\infty dz' \left|\frac{d\rho(m')}{dm'}\right| \frac{z'}{m'} \int_0^\infty \frac{\rho(m_\tau)\tau d\tau}{(a^2+\tau)^2(q^2a^2+\tau)^{3/2}}, \tag{2.32}$$

where we have reasonably assumed that the condition $d\rho/dm \leq 0$ is always satisfied. This equation gives the *formal solution of the radial Jeans equation for an axisymmetric density distribution stratified over spheroidal surfaces*. Notice that the right-hand side of equation (2.32) is nowhere negative, and so Satoh's decomposition can always be applied for an oblate density distribution of the form $\rho(m)$. From the previous results it is clear that, while in the spherical case Jeans's equations may be solved analytically (see e.g. Hernquist 1990; Ciotti 1999; Ciotti et al. 2009; CZ18; CMP21), for ellipsoidal systems this cannot be expected to be true in general, and *in a number of situations it is almost inevitable to resort to numerical methods to obtain the solutions. However, for weakly flattened systems, the corresponding density and potential can be approximated by using the so-called "homoeoidal expansion method"; later in this Thesis we shall show that, exploiting this technique, Jeans's equations can be reduced to a set of quite manageable integrals, usually elementary for arbitrary galaxy models* (see §§ 3.3.2 and 4.6).

2.2.2 Projected dynamics

Real stellar systems, when observed as astronomical objects, appear projected on the plane of the sky. Thus, it is necessary to set the framework for a clear understanding of the relationship between intrinsic dynamics and projected properties. Unfortunately, while in principle it is always possible to project a model and then compare the results with observational data, recovering three-dimensional information from projected properties is generally almost impossible because of geometric degeneracies. For, let us now review some of the general concepts of projected dynamics, defining the basic tools needed to project the most important properties of stellar systems on the projection plane.

As we are considering axisymmetric models, we need to specify just a single angle i which gives the direction of the *line of sight* (hereafter, los) to the observer[8]. Let our models be described in a Cartesian inertial frame of reference $(S_0; x, y, z)$; in addition, consider a second orthogonal

[8]For generic systems, i.e. not necessarily axisymmetric, to specify the orientation of S' with respect to S_0 it can be applied a so-called 3-2-3 rotation; an alternative way is to use the standard Eulerian angles (e.g. Whittaker 1917; Landau & Lifshitz 1960; Gantmacher 1975; Arnold 1978), defined by a 3-1-3 rotation. For an exhaustive discussion of projected dynamics in Stellar Dynamics, see e.g. Chapter 11 in C21.

reference system $(S';x',y',z')$ with same origin as S_0 (see Fig. 2.1). Due to axisymmetry, and without loss of generality, the relation between the two sets of coordinates is

$$\boldsymbol{x} = \mathscr{R}\boldsymbol{x}', \qquad \mathscr{R} \equiv \begin{pmatrix} \cos i & 0 & \sin i \\ 0 & 1 & 0 \\ -\sin i & 0 & \cos i \end{pmatrix}, \tag{2.33}$$

with $\boldsymbol{x} = (x,y,z)$ and $\boldsymbol{x}' = (x',y',z')$ are respectively the generic position vectors[9] in S_0 and S'. With this choice, the los is directed along z', and the unit vector $\boldsymbol{n}$, from S_0 to the observer, is $\boldsymbol{n} = (\sin i, 0, \cos i)$; notice that, for a given position $\boldsymbol{x}$, the corresponding coordinate z' is given by the scalar product $z' = \boldsymbol{x}\cdot\boldsymbol{n}$. We shall call the *projection plane* the plane perpendicular to $\boldsymbol{n}$ and containing the origin; this is given algebraically by $z' = 0$, and can be identified with the set of two-dimensional vectors $\boldsymbol{\ell} = (x',y')$.

Moreover, we consider a counter clockwise rotation of an angle i around the y-axis, coincident with the y'-axis of the observer. In particular:

1. for $i = 0$ (*face-on* projection), the los coincides with the z-axis, and $(x',y') = (x,y)$;
2. for $i = \pi/2$ (*edge-on* projection), the los coincides with the x-axis, and $(x',y') = (-z,y)$.

In any case, y' is aligned with the major axis of the projection.

Every so-called "observable" quantity, such as the rotational velocity along the line of sight or the projection in the plane of the sky of the velocity dispersion, can be interpreted from a statistical point of view as a "macroscopic" quantity. With this term we indicate a function $\overline{Q}(\boldsymbol{x})$ defined by integration on the velocity space of its "microscopic" counterpart $Q(\boldsymbol{x},\boldsymbol{v})$, using the phase-space distribution function[10] $f(\boldsymbol{x},\boldsymbol{v})$ as a weight function (see Appendix A and references therein). In the frame of reference S_0, $f(\boldsymbol{x},\boldsymbol{v})$ obeys the CBE (A4), and from it all of the moments can be obtained. In the frame of reference S', the distribution function is naturally given by

$$[f(\boldsymbol{x},\boldsymbol{v})]' \equiv f'(\boldsymbol{x}',\boldsymbol{v}') = f(\mathscr{R}\boldsymbol{x}',\mathscr{R}\boldsymbol{v}'). \tag{2.34}$$

The projection of a given macroscopic property $\overline{Q} = \overline{Q}(\boldsymbol{x})$ onto the projection plane is defined as

$$\Sigma(\boldsymbol{\ell})\overline{Q}_{\rm los}(\boldsymbol{\ell}) = \int_{-\infty}^{\infty} [\rho(\boldsymbol{x})\overline{Q}(\boldsymbol{x})]'\,dz', \tag{2.35}$$

where $\Sigma(x',y')$ is the projection of the density profile, given explicitly by

$$\Sigma(\boldsymbol{\ell}) = \int_{-\infty}^{\infty} [\rho(\boldsymbol{x})]'\,dz' = \int_{-\infty}^{\infty} \rho(x'\cos i + z'\sin i,\, y',\, -x'\sin i + z'\cos i)\,dz'. \tag{2.36}$$

Notice that this definition of projection assumes implicitly that the observer is at an infinite distance from the system, and that all of the information along $\boldsymbol{n}$ is summed in the projection plane with no superposition of two stars along the los.

We now report the projection formulae for the basic dynamical quantities; in writing the various expressions we shall use the notation of Cartesian tensors with the usual summation convention (e.g. Jeffreys 1931; see also Chapter 3 in Jeffreys & Jeffreys 1956).

[9] For typographic reasons, in the following vectors will be written as *row* vectors, even though they should be intended as column vectors for consistency with the rules of matrix multiplication.

[10] For simplicity, any time dependency will be omitted in the following discussion.

(a) *The los projected streaming velocity field*, $v_{\rm los}$

A microscopic property of great importance in both observational and theoretical works is the component of $\boldsymbol{v}$ along the direction $\boldsymbol{n}$, i.e. $Q(\boldsymbol{v}) = \boldsymbol{v}\cdot\boldsymbol{n} = v_i n_i$. By projecting the corresponding macroscopic function $\overline{Q}(\boldsymbol{x}) = \overline{v_i}\, n_i$ along the los according to equation (2.35), we find

$$\Sigma(\boldsymbol{\ell}) v_{\rm los}(\boldsymbol{\ell}) = \int_{-\infty}^{\infty} (\rho\, \overline{v_i}\, n_i)'\, dz', \tag{2.37}$$

where $v_{\rm los}$ is the so-called *los projected streaming velocity field*. Notice that if the system does not have intrinsic streaming motions (i.e., $\overline{v_i} = 0$ for $i = 1, 2, 3$), then both $\overline{v_i}\, n_i$ and $v_{\rm los}$ vanish. The converse is not true in general: the system can possess streaming motions even if both $\overline{v_i}\, n_i$ and $v_{\rm los}$ are zero for a given orientation of the los; trivially, when streaming motions are perpendicular to the direction $\boldsymbol{n}$.

(b) *The los projected squared velocity*, $v_{\rm p}$

A second important microscopic property is $Q(\boldsymbol{v}) = (\boldsymbol{v}\cdot\boldsymbol{n})^2 = v_i v_j n_i n_j$, whose macroscopic counterpart is given by $\overline{Q}(\boldsymbol{x}) = \overline{v_i v_j}\, n_i n_j$. According to equation (2.35), an integration along the los yields

$$\Sigma(\boldsymbol{\ell}) v_{\rm p}^2(\boldsymbol{\ell}) = \int_{-\infty}^{\infty} (\rho\, \overline{v_i v_j}\, n_i n_j)'\, dz', \tag{2.38}$$

where $v_{\rm p}$ is the *los projected squared velocity*; sometimes (e.g., Cappellari 2008) this quantity is indicated in the Literature as $V_{\rm rms}$. Now, by introducing the velocity dispersion tensor $\sigma_{ij}^2 = \overline{v_i v_j} - \overline{v_i}\,\overline{v_j}$, it follows that $v_{\rm p}^2$ can be rewritten as

$$v_{\rm p}^2 = \sigma_{\rm p}^2 + V_{\rm p}^2, \tag{2.39}$$

where the two contributions at the right-hand side are defined as

$$\Sigma(\boldsymbol{\ell}) \sigma_{\rm p}^2(\boldsymbol{\ell}) \equiv \int_{-\infty}^{\infty} (\rho \sigma_{ij}^2 n_i n_j)'\, dz', \qquad \Sigma(\boldsymbol{\ell}) V_{\rm p}^2(\boldsymbol{\ell}) \equiv \int_{-\infty}^{\infty} (\rho\, \overline{v_i}\,\overline{v_j}\, n_i n_j)'\, dz', \tag{2.40}$$

where $\sigma_{\rm p}$ is the so-called *los projected velocity dispersion*. According to equation (2.35), $\sigma_{\rm p}^2$ denotes the los projection of $\overline{Q}(\boldsymbol{x}) = \sigma_{ij}^2 n_i n_j$, which represents, from the definition of σ_{ij}^2 in equation (A13), the macroscopic counterpart of $Q(\boldsymbol{x}, \boldsymbol{v}) = (v_i n_i - \overline{v_i}\, n_i)^2$. This latter quantity, in practice, is a measure of the dispersion of stellar motions at point $\boldsymbol{x}$ in the direction $\boldsymbol{n}$ with respect to the local average value of $\overline{v_i}\, n_i$ along the same direction, while $\sigma_{\rm p}$ "measures" the (mass-weighted) integral of these dispersions along the los.

(c) *The observed los velocity dispersion field*, $\sigma_{\rm los}$

In general, $\sigma_{\rm p}$ does not coincide with the velocity dispersion measured in observations. In fact, the observations give the los velocity dispersion centered on the los streaming velocity field $v_{\rm los}$, and not on the local $\overline{v_i}\, n_i$ as in the case of $\sigma_{\rm p}$. As a consequence, in presence of a non-zero projected velocity field $v_{\rm p}$, the correct definition for the *observed los velocity dispersion* $\sigma_{\rm los}$, strictly related to the broadening of the spectral lines, is given by

$$\Sigma(\boldsymbol{\ell}) \sigma_{\rm los}^2(\boldsymbol{\ell}) = \int_{-\infty}^{\infty} \left[\rho\, \overline{(v_i n_i - v_{\rm los})^2}\,\right]' dz'. \tag{2.41}$$

It is easy to link $\sigma_{\rm los}$ to the fields $\sigma_{\rm p}$ and $v_{\rm los}$ just by working on the integrand. Indeed, since $v_{\rm los}$ does not depend explicitly on $\boldsymbol{v}$,

$$\overline{(v_i n_i - v_{\rm los})^2} = \overline{v_i v_j}\, n_i n_j + v_{\rm los}^2 - 2 v_{\rm los}\, \overline{v_i}\, n_i, \tag{2.42}$$

so that, by integrating along the los, after some elementary reductions we find that

$$\sigma_{\rm los}^2 = v_{\rm p}^2 - v_{\rm los}^2 = \sigma_{\rm p}^2 + V_{\rm p}^2 - v_{\rm los}^2. \tag{2.43}$$

Notice that $\sigma_{\rm los}$ can be positive even in an idealized stellar system with no intrinsic velocity dispersion (and thus $\sigma_{\rm p} = 0$), such as in the edge-on view of a "cool" stellar disc in which all stars circulate around the centre of the disc in the same direction. Another important conclusion, relevant for observational purposes, is that in stellar systems fully supported by pressure (i.e., $\overline{\boldsymbol{v}} = 0$ everywhere), $\sigma_{\rm los} = v_{\rm p} = \sigma_{\rm p}$. In Chapters 4 and 5 we shall consider in detail the construction of the projected velocity fields for some families of axisymmetric galaxy models.

The explicit expressions for $v_{\rm los}$ and $v_{\rm p}$

We now proceed to write down the explicit (integral) expressions for the two main projected dynamical quantities defining $\sigma_{\rm los}$.

Let us start with $v_{\rm los}$. Our fundamental assumption is that the streaming motion of stars occurs *only* in the azimuthal direction; in practice, the streaming velocity field is given by

$$\overline{\boldsymbol{v}} = \overline{v_\varphi}\, \boldsymbol{e}_\varphi, \qquad\qquad \boldsymbol{e}_\varphi = (-\sin\varphi, \cos\varphi, 0), \tag{2.44}$$

where φ is the usual azimuthal angle, and $\boldsymbol{e}_\varphi$ is the corresponding unit vector in cylindrical (or spherical) coordinates. Therefore, remembering the definition of the unit vector $\boldsymbol{n}$,

$$\overline{v_i}\, n_i = -\,\overline{v_\varphi} \sin\varphi \sin i, \tag{2.45}$$

from which it follows that $\overline{v_\varphi} > 0$ when the galaxy rotates in an anti-clockwise sense. Now, by inserting the foregoing expression in equation (2.37), and considering that i is fixed along the los, we readily obtain

$$\Sigma v_{\rm los} = -\sin i \int_{-\infty}^{\infty} (\rho\, \overline{v_\varphi} \sin\varphi)'\, dz'. \tag{2.46}$$

Clearly, since $\overline{v_\varphi}$ appears explicitly, $v_{\rm los}$ *depends on the specific velocity decomposition adopted*; in particular, in Satoh's k-decomposition (2.20) we have

$$\Sigma v_{\rm los} = -\,k \sin i \int_{-\infty}^{\infty} (\rho \sqrt{\Delta} \sin\varphi)'\, dz'. \tag{2.47}$$

Notice that $v_{\rm los}$ *vanishes in the limiting case of a face-on projection* ($i = 0$), even if streaming motions are present.

Let us now move to $v_{\rm p}$, i.e. to the determination of its contributions $\sigma_{\rm p}$ and $V_{\rm p}$. In order to obtain a more manageable expression for the integrand defining $\sigma_{\rm p}$, it is convenient to use Cartesian coordinates; from matrix algebra (where now we represent correctly $\boldsymbol{n}$ as a column vector), we find

$$\sigma_{ij}^2 n_i n_j = \begin{pmatrix} \sigma_{xx}^2 & \sigma_{xy}^2 & \sigma_{xz}^2 \\ \sigma_{yx}^2 & \sigma_{yy}^2 & \sigma_{yz}^2 \\ \sigma_{zx}^2 & \sigma_{zy}^2 & \sigma_{zz}^2 \end{pmatrix} \begin{pmatrix} \sin i \\ 0 \\ \cos i \end{pmatrix} \cdot \begin{pmatrix} \sin i \\ 0 \\ \cos i \end{pmatrix} \tag{2.48}$$

$$= \sigma_{xx}^2 \sin^2 i + \sigma_{xz}^2 \sin 2i + \sigma_{zz}^2 \cos^2 i.$$

The three velocity dispersions σ_{xx}^2, σ_{xz}^2, and σ_{zz}^2, by virtue of equation (A13), are given by

$$\sigma_{xx}^2 = \overline{(v_x - \overline{v_x})^2}, \qquad \sigma_{xz}^2 = \overline{(v_x - \overline{v_x})(v_z - \overline{v_z})}, \qquad \sigma_{zz}^2 = \overline{(v_z - \overline{v_z})^2}, \tag{2.49}$$

where the Cartesian components of $\boldsymbol{v}$ and $\overline{\boldsymbol{v}}$ are linked to the corresponding cylindrical components through the following transformations:

$$\begin{cases} v_x = v_R \cos\varphi - v_\varphi \sin\varphi, \\ v_y = v_R \sin\varphi + v_\varphi \cos\varphi, \\ v_z = v_z, \end{cases} \qquad \begin{cases} \overline{v_x} = -\overline{v_\varphi} \sin\varphi, \\ \overline{v_y} = \overline{v_\varphi} \cos\varphi, \\ \overline{v_z} = 0. \end{cases} \tag{2.50}$$

By inserting these expressions in (2.49) we obtain

$$\sigma_{xx}^2 = \sigma^2 \cos^2\varphi + \sigma_\varphi^2 \sin^2\varphi, \qquad \sigma_{xz}^2 = 0, \qquad \sigma_{zz}^2 = \sigma^2, \tag{2.51}$$

so that, after further simplifications,

$$\begin{aligned} \sigma_{ij}^2 n_i n_j &= \sigma^2 + (\sigma_\varphi^2 - \sigma^2) \sin^2\varphi \sin^2 i, \\ &= \sigma^2 + (\Delta - \overline{v_\varphi}^2) \sin^2\varphi \sin^2 i. \end{aligned} \tag{2.52}$$

For what concerns V_p, it is sufficient to realize that $\overline{v_i}\,\overline{v_j}\,n_i n_j$ is simply the square of $\overline{v_i}\,n_i$, i.e.

$$\overline{v_i}\,\overline{v_j}\,n_i n_j = \overline{v_\varphi}^2 \sin^2\varphi \sin^2 i. \tag{2.53}$$

Also in this case, the streaming velocity $\overline{v_\varphi}$ appears explicitly in both $\sigma_{ij}^2 n_i n_j$ and $\overline{v_i}\,\overline{v_j}\,n_i n_j$, and so even σ_p and V_p depend on the adopted velocity decomposition. Nevertheless, when computing the quantity via equation (2.39), the dependence on $\overline{v_\varphi}$ disappears, and we finally obtain

$$\Sigma v_\mathrm{p}^2 = \int_{-\infty}^{\infty} (\rho\sigma^2 + \rho\Delta \sin^2\varphi \sin^2 i)' dz'. \tag{2.54}$$

According to equation (2.39), the observed velocity dispersion can be then derived as

$$\Sigma \sigma_\mathrm{los}^2 = \Sigma v_\mathrm{p}^2 - \frac{(\Sigma v_\mathrm{los})^2}{\Sigma}, \tag{2.55}$$

with Σv_p^2 and Σv_los given respectively by equations (2.54) and (2.46).

CHAPTER 3

The Homoeoidal Expansion Method

For the discussion of several astrophysical problems, a major difficulty is set by the treatment of the potential. In general, to calculate the gravitational potential corresponding to a given density distribution, it is necessary to evaluate a three-dimensional integral. Except for special circumstances, in which a solution can be derived via elementary functions, one has to resort to numerical techniques and sophisticated mathematical methods, such as integral transforms or expansions in orthogonal functions. However, even when available, very complicated expressions rarely lead to a deep understanding of the physics behind the problem itself. At the same time, the work required to understand a physical problem which cannot be solved mathematically in a completely analytical form is often more useful than the knowledge of the formal solution itself. This is precisely the situation we address in this Chapter, aimed at presenting the basic properties of the so-called *homoeoidal expansion method*, a flexible mathematical tool allowing the construction of models of stellar systems that depart from spherical symmetry. In this technique, the initial ellipsoidally stratified density, and the associated potential, are expanded at the linear order in terms of the density flattening η. As a consequence, the use of numerical integration for the determination of the potential, usually a very time-consuming step in the numerical studies, may be avoided, and the formulas obtained are a very good approximation of the exact potential associated with the starting mass density profile. This method can then be seen as one of the simplest ways to take into account the effects on the internal dynamics of the flattening of the initial density profile: in fact, on the one hand it allows for an analytically simple treatment, and on the other hand to study important physical properties which could not be studied when considering spherically symmetrical systems.

3.1 The general theory

As mentioned in the previous Section, the gravitational potential associated with a generic ellipsoidal mass density distribution, obtained in general as a solution of a three-dimensional integral, usually cannot be expressed in explicit form[1]. One possible way to overcome this difficulty is to consider, among all possible ellipsoidal models, only the *weakly flattened* ones; hence, in the following we focus on the limit for "small flattenings" of equation (2.3). We shall refer to this framework as the *homoeoidal expansion method* (see e.g. Ciotti & Bertin 2005; see also Muccione & Ciotti 2004). As we shall see in this Section and in later Chapters, this expansion produces quite remarkable formulae, sufficiently flexible to allow for the construction of galaxy models which deviate from spherical symmetry. Moreover, the homoeoidal expansion can be used as guidelines for more detailed studies: for example, in orbit computations in ellipsoidal stellar systems, in the construction of hydrostatic equilibria for the hot gaseous atmospheres of triaxial galaxies (see e.g. Barnabè et. al 2006), or in hydrodynamical simulations of gas flows in galaxies, where the stellar velocity fields are major ingredients in the description of the energy and momentum source terms due to the evolving stellar populations (see e.g. Posacki et al. 2013; Negri et. al 2014).

We start by introducing the two axial ratios of the ellipsoidal equidensity surfaces: $q_y \equiv b/a$ and $q_z \equiv c/a$. For, equation (2.1) can be rewritten as

$$m^2 = \frac{x^2}{a^2} + \frac{y^2}{a^2 q_y^2} + \frac{z^2}{a^2 q_z^2} = \tilde{x}^2 + \frac{\tilde{y}^2}{q_y^2} + \frac{\tilde{z}^2}{q_z^2}, \tag{3.1}$$

with the natural normalizations $\tilde{x} \equiv x/a$, $\tilde{y} \equiv y/a$, and $\tilde{z} \equiv z/a$. In words, we can *identify an ellipsoid by a scale length and by two dimensionless form factors which define its shape*. From the definitions previously adopted, it follows that in the general triaxial case one has $0 < q_z < q_y < 1$, the oblate case correspods to $q_y = 1$ and $0 < q_z < 1$, and the prolate case to $0 < q_z = q_y < 1$; when $q_y = q_z = 1$, the distribution is spherically symmetric. Under these assumptions, we choose to write the density distribution at a point $\boldsymbol{x}$ as

$$\rho(\boldsymbol{x}) = \rho_{\rm n} \frac{\tilde{\rho}(m)}{q_y q_z}, \qquad\qquad \rho_{\rm n} \equiv \frac{M_{\rm n}}{4\pi a^3}, \tag{3.2}$$

where $M_{\rm n}$ is the finite total mass; with this choice, $M_{\rm n}$ is *independent* of the adopted flattenings (the so-called "constrained case"). In this case, the normalization assures that the cumulative mass is conserved independently of the value of the flattenings, and, in particular,

$$\int_0^\infty \tilde{\rho}(m) m^2 dm = 1. \tag{3.3}$$

Notice that $M_{\rm n}$, instead of being the total mass, could be the mass contained in some prescribed ellipsoid of ellipsoidal radius m_0: in this case, the previous normalization integral extends up to m_0. In case of an *infinite* total mass, instead, the condition (3.3) assures that the mass contained inside any m is conserved.

For simplicity we define $\epsilon \equiv 1 - q_y$ and $\eta \equiv 1 - q_z$, and in the following we shall refer to them as the *flattenings*; as a consequence, the spherical case is obtained when $\epsilon = 0$ and $\eta = 0$. By expanding equation (3.2) for $\epsilon \to 0$ and $\eta \to 0$, one has

[1] When considering spherical symmetry, the relation between the potential and the density profile can be reduced to a one-dimensional integral, while in case of axisymmetric systems one is left in general with a two-dimensional integral. Consequently, the majority of explicit density-potential pairs refers to spherical symmetry, while only a few of axially symmetric pairs are known (see e.g. Bertin 2014; C21). In the particular case in which a density-potential pair is available in an appropriate parametric form, there exist systematic procedures to generate new non-trivial density-potential pairs (see Miyamoto & Nagai 1975; see also Evans & de Zeeuw 1992).

$$\frac{\rho(\boldsymbol{x})}{\rho_{\rm n}} = \tilde{\varrho}_0(s) + (\epsilon+\eta)\tilde{\varrho}_1(s) + \big(\epsilon\tilde{y}^2 + \eta\tilde{z}^2\big)\tilde{\varrho}_2(s) + \mathcal{O}\big(\epsilon^2+\eta^2\big), \tag{3.4}$$

where $s \equiv r/a$ is the spherical radius r in units of a, and

$$\tilde{\varrho}_0(s) = \tilde{\varrho}_1(s) = \tilde{\rho}(s), \qquad\qquad \tilde{\varrho}_2(s) = \frac{1}{s}\frac{d\tilde{\rho}(s)}{ds}, \tag{3.5}$$

in which $d\tilde{\rho}(s)/ds$ denotes $d\tilde{\rho}(m)/dm$ evaluated in $\epsilon = \eta = 0$. In particular, the functions $\tilde{\varrho}_0$ and $\tilde{\varrho}_1$ are nowhere negative, while $\tilde{\varrho}_2$ can always be reasonably regarded as a nowhere posivite function of s. Clearly, *even though the starting density* (3.2) *is nowhere negative by construction, the homoeidally expanded density* (3.4) *might be negative somewhere*; as we shall see in § 3.2, the non-negativity requirement limits the domain of occupancy of the expanded models in the (ϵ, η)-plane.

The mass distribution associated to the density profile $\rho(\boldsymbol{x})$ is

$$M(\boldsymbol{x}) = M_{\rm n}\tilde{M}(m), \qquad\qquad \tilde{M}(m) \equiv \int_0^m \tilde{\rho}(t)t^2dt. \tag{3.6}$$

Of course, according to equation (3.3), M converges to the total mass $M_{\rm n}$ for $m \to \infty$. Following the same procedure adopted to derive the expansion (3.4), in the limit of small flattenings the profile $M(\boldsymbol{x})$ can be written as

$$\frac{M(\boldsymbol{x})}{M_{\rm n}} = \tilde{M}_0(s) + \big(\epsilon\tilde{y}^2 + \eta\tilde{z}^2\big)\tilde{M}_1(s) + \mathcal{O}\big(\epsilon^2+\eta^2\big), \tag{3.7}$$

where the dimensionless functions are given by

$$\tilde{M}_0(s) = \tilde{M}(s), \qquad\qquad \tilde{M}_1(s) = s\tilde{\rho}(s). \tag{3.8}$$

Notice that, in the spherical limit $\epsilon = \eta = 0$, as expected, $M_{\rm n}\tilde{M}_0(s)$ is nothing else than the radial mass profile corresponding to the density $\rho_{\rm n}\tilde{\rho}(s)$.

With a mass density profile $\rho(\boldsymbol{x})$ given by equation (3.2), in place of equation (2.3) we have

$$\Psi(\boldsymbol{x}) = \frac{\Psi_{\rm n}}{4}\int_0^\infty \frac{\tilde{F}[\tilde{m}(\boldsymbol{x},u)]}{\tilde{\Delta}(u)}\,du, \qquad\qquad \tilde{F}(x) \equiv 2\int_x^\infty \tilde{\rho}(t)t\,dt, \tag{3.9}$$

where $\Psi_{\rm n} \equiv GM_{\rm n}/a$ is a potential scale, and

$$\tilde{\Delta}^2(u) \equiv (1+u)(q_y^2+u)(q_z^2+u), \qquad\qquad \tilde{m}^2(\boldsymbol{x},u) \equiv \frac{\tilde{x}^2}{1+u} + \frac{\tilde{y}^2}{q_y^2+u} + \frac{\tilde{z}^2}{q_z^2+u}. \tag{3.10}$$

A direct expansion in terms of the flattenings ϵ and η shows that

$$\frac{\tilde{F}[\tilde{m}(\boldsymbol{x},u)]}{\tilde{\Delta}(u)} = \frac{\tilde{F}\big(s/\sqrt{1+u}\big)}{(1+u)^{3/2}} + (\epsilon+\eta)\frac{\tilde{F}\big(s/\sqrt{1+u}\big)}{(1+u)^{5/2}} - \big(\epsilon\tilde{y}^2+\eta\tilde{z}^2\big)\frac{2\tilde{\rho}\big(s/\sqrt{1+u}\big)}{(1+u)^{7/2}} + \mathcal{O}\big(\epsilon^2+\eta^2\big), \tag{3.11}$$

where, again, $s = r/a$. The integration of the right-hand side of equation (3.11) presents no formal

difficulties. First, by integrating the spherical term over the range of u, changing the order of integration, and defining $A \equiv (s^2 - t^2)/t^2$, we obtain

$$\begin{aligned}\int_0^\infty \frac{\tilde{F}\big(s/\sqrt{1+u}\big)}{(1+u)^{3/2}}\,du &= 2\int_0^s dt\,\tilde{\rho}(t)\,t\int_A^\infty \frac{du}{(1+u)^{3/2}} + 2\int_s^\infty dt\,\tilde{\rho}(t)\,t\int_0^\infty \frac{du}{(1+u)^{3/2}} \\ &= \frac{4}{s}\int_0^s \tilde{\rho}(t)t^2dt + 4\int_s^\infty \tilde{\rho}(t)t\,dt.\end{aligned} \tag{3.12}$$

Next, with analogous calculations one readily has

$$\int_0^\infty \frac{\tilde{F}\big(s/\sqrt{1+u}\big)}{(1+u)^{5/2}}\,du = \frac{4}{3s^3}\int_0^s \tilde{\rho}(t)t^4dt + \frac{4}{3}\int_s^\infty \tilde{\rho}(t)t\,dt. \tag{3.13}$$

Finally, for what concerns the third term at the right-hand side of equation (3.11), the substitution $t \equiv s/\sqrt{1+u}$ yields

$$\int_0^\infty \frac{2\tilde{\rho}\big(s/\sqrt{1+u}\big)}{(1+u)^{7/2}}\,du = \frac{4}{s^5}\int_0^s \tilde{\rho}(t)t^4dt. \tag{3.14}$$

Summarising, by combining equations (3.12), (3.13), and (3.14), in view of equation (3.9) we obtain the asymptotic expansion for small flattenings of the homoeoidal potential quadrature formula:

$$\frac{\Psi(\boldsymbol{x})}{\Psi_\mathrm{n}} = \tilde{\psi}_0(s) + (\epsilon+\eta)\tilde{\psi}_1(s) + \big(\epsilon\tilde{y}^2 + \eta\tilde{z}^2\big)\tilde{\psi}_2(s) + \mathcal{O}\big(\epsilon^2+\eta^2\big), \tag{3.15}$$

where

$$\tilde{\psi}_i(s) = \begin{cases} \dfrac{1}{s}\displaystyle\int_0^s \tilde{\rho}(t)t^2dt + \int_s^\infty \tilde{\rho}(t)t\,dt, & (i=0), \\[2ex] \dfrac{1}{3s^3}\displaystyle\int_0^s \tilde{\rho}(t)t^4dt + \frac{1}{3}\int_s^\infty \tilde{\rho}(t)t\,dt, & (i=1), \\[2ex] -\dfrac{1}{s^5}\displaystyle\int_0^s \tilde{\rho}(t)t^4dt, & (i=2); \end{cases} \tag{3.16}$$

note that $\tilde{\psi}_0$ is the potential associated with $\tilde{\varrho}_0$. Evidently, at variance with the general case, in the limit of small flattenings the expression for Ψ is quite simple. In accordance with the foregoing equation, since $\tilde{\rho}(m) \geq 0$ everywhere, the radial functions $\tilde{\psi}_0$ and $\tilde{\psi}_1$ are nowhere negative, whereas $\tilde{\psi}_2$ is a nowhere positive function of s. Further, as expected, in the spherical case (for which $m = s$) the function Ψ reduces to the gravitational potential generated by the spherically symmetric density distribution $\rho(r) = \rho_\mathrm{n}\tilde{\rho}(s)$.

Since the potential $\Psi(\boldsymbol{x})$, in general, is associated with the density $\rho(m)$ through Poisson's equation, a relationship between the radial functions $\tilde{\psi}_i$ and the corresponding $\tilde{\varrho}_i$ (for $i = 0, 1, 2$) must exist. When considering the dimensionless density-potential pair, Poisson's equation becomes

$$\tilde{\nabla}^2\,\frac{\Psi(\boldsymbol{x})}{\Psi_\mathrm{n}} = -\,\frac{\rho(\boldsymbol{x})}{\rho_\mathrm{n}}, \qquad\qquad \tilde{\nabla}^2 \equiv a^2\nabla^2. \tag{3.17}$$

First, taking the laplacian of equation (3.15) we have

$$\tilde{\nabla}^2 \frac{\Psi(\boldsymbol{x})}{\Psi_{\rm n}} = \tilde{\nabla}^2\tilde{\psi}_0 + (\epsilon+\eta)\tilde{\nabla}^2\tilde{\psi}_1 + \epsilon\tilde{\nabla}^2\big(\tilde{y}^2\tilde{\psi}_2\big) + \eta\tilde{\nabla}^2\big(\tilde{z}^2\tilde{\psi}_2\big) + \mathcal{O}\big(\epsilon^2+\eta^2\big). \tag{3.18}$$

The third and the fourth terms on the right-hand side of equation (3.18) can be easily evaluated; indeed, simple algebra[2] shows that

$$\tilde{\nabla}^2\big(\tilde{y}^2\tilde{\psi}_2\big) = \tilde{y}^2\left(\tilde{\nabla}^2\tilde{\psi}_2 + \frac{4}{s}\frac{d\tilde{\psi}_2}{ds}\right) + 2\tilde{\psi}_2, \qquad \tilde{\nabla}^2\big(\tilde{z}^2\tilde{\psi}_2\big) = \tilde{z}^2\left(\tilde{\nabla}^2\tilde{\psi}_2 + \frac{4}{s}\frac{d\tilde{\psi}_2}{ds}\right) + 2\tilde{\psi}_2. \tag{3.19}$$

Next, by inserting the foregoing expressions in equation (3.18) we obtain

$$\tilde{\nabla}^2 \frac{\Psi(\boldsymbol{x})}{\Psi_{\rm n}} = \tilde{\nabla}^2\tilde{\psi}_0 + (\epsilon+\eta)\Big(\tilde{\nabla}^2\tilde{\psi}_1 + 2\tilde{\psi}_2\Big) + \big(\epsilon\tilde{y}^2 + \eta\tilde{z}^2\big)\left(\tilde{\nabla}^2\tilde{\psi}_2 + \frac{4}{s}\frac{d\tilde{\psi}_2}{ds}\right) + \mathcal{O}\big(\epsilon^2+\eta^2\big). \tag{3.20}$$

Finally, comparing equations (3.4), (3.17), and (3.20), we conclude that

$$\tilde{\nabla}^2\tilde{\psi}_i + \tilde{\varrho}_i = \begin{cases} 0, & (i=0), \\ -2\tilde{\psi}_2, & (i=1), \\ -\dfrac{4}{s}\dfrac{d\tilde{\psi}_2}{ds}, & (i=2), \end{cases} \qquad \tilde{\nabla}^2 = \frac{d^2}{ds^2} + \frac{2}{s}\frac{d}{ds}, \tag{3.21}$$

which represents the "expanded" Poisson equation.

We now move to the expression for the self-interaction energy of weakly flattened ellipsoidal systems. Actually, there is no difficult in writing down the limit for small flattenings of equation (2.12). Indeed, inserting the expression for the density given in equation (3.2), and remembering that $b = aq_y$ and $c = aq_z$, the energy W reduces to

$$W = -\frac{U_{\rm n}}{8} R_F(1, q_y^2, q_z^2) \int_0^\infty \tilde{F}^2(m)dm, \qquad U_{\rm n} \equiv \frac{GM_{\rm n}^2}{a}. \tag{3.22}$$

The information about the flattening of the density distribution is contained in the function R_F, whose expansion when $\epsilon \to 0$ and $\eta \to 0$ reads

$$R_F\big[1, (1-\epsilon)^2, (1-\eta)^2\big] = 1 + \frac{\epsilon+\eta}{3} + \mathcal{O}\big(\epsilon^2+\eta^2\big). \tag{3.23}$$

Notice that the function R_F takes the value unity in the spherical case, so that the value of W when the density distribution is spherically symmetric may be simply written as

$$W_0 = U_{\rm n}\tilde{W}_0, \qquad \tilde{W}_0 \equiv -\frac{1}{8}\int_0^\infty \tilde{F}^2(m)dm. \tag{3.24}$$

[2] Quite generally, given two arbitrary functions $f(\boldsymbol{x})$ and $g(\boldsymbol{x})$, we have the identity

$$\nabla^2(fg) = \boldsymbol{\nabla}\cdot\boldsymbol{\nabla}(fg) = f\nabla^2 g + 2\boldsymbol{\nabla}f\cdot\boldsymbol{\nabla}g + g\nabla^2 f,$$

where $\boldsymbol{\nabla}$ is the gradient operator. To find the quantities $\tilde{\nabla}^2\big(\tilde{y}^2\tilde{\psi}_2\big)$ and $\tilde{\nabla}^2\big(\tilde{z}^2\tilde{\psi}_2\big)$ it is sufficient to make use of the previous identity just by setting $\tilde{\boldsymbol{\nabla}} = a\boldsymbol{\nabla}$.

Finally, by combining equations (3.22), (3.23), and (3.24), we find the following expansion for the self-interaction energy:

$$\frac{W}{U_{\mathrm{n}}} = \left(1 + \frac{\epsilon + \eta}{3}\right)\tilde{W}_0 + \mathcal{O}\big(\epsilon^2 + \eta^2\big). \tag{3.25}$$

3.2 Limits on the flattening

In order to be physically acceptable, we have to impose that the expanded density in equation (3.4) is nowhere negative: this lead us to set an upper limit on the possible values of ϵ and η as a function of the specific density profile adopted. By assuming that $d\tilde{\rho}(s)/ds$ is nowhere positive, the non-negativity condition for the expanded density reads

$$\left|\frac{d\tilde{\rho}(s)}{ds}\right| \frac{\epsilon\tilde{y}^2 + \eta\tilde{z}^2}{s} \leq (1 + \epsilon + \eta)\tilde{\rho}(s), \tag{3.26}$$

i.e., by changing variables to spherical coordinates (r, ϑ, φ),

$$\left|\frac{d\ln\tilde{\rho}(s)}{d\ln s}\right| f(\vartheta,\varphi) \leq 1, \qquad f(\vartheta,\varphi) \equiv \frac{\epsilon\sin^2\vartheta\sin^2\varphi + \eta\cos^2\vartheta}{1 + \epsilon + \eta}. \tag{3.27}$$

As the foregoing inequality must be verified for all values of $s \geq 0$, $0 \leq \vartheta \leq \pi$, and $0 \leq \varphi \leq 2\pi$, it follows that we must impose

$$\sup_{s\geq 0}\left|\frac{d\ln\tilde{\rho}(s)}{d\ln s}\right| \times \sup_{\mathcal{J}} f(\vartheta,\varphi) \leq 1, \tag{3.28}$$

where $\mathcal{J} \equiv \{(\vartheta,\varphi)\,|\,0 \leq \vartheta \leq \pi/2,\, 0 \leq \varphi \leq \pi/2\}$: note that we restrict to angular values between 0 and $\pi/2$ since $f(\pi - \vartheta, \pi - \varphi) = f(\vartheta,\varphi)$. It is not difficult to show that

$$\sup_{\mathcal{J}} f(\vartheta,\varphi) = \frac{\eta}{1 + \epsilon + \eta}. \tag{3.29}$$

As a consequence, from equation (3.28) one finally has

$$\epsilon \geq (A_M - 1)\eta - 1, \qquad A_M \equiv \sup_{s\geq 0}\left|\frac{d\ln\tilde{\rho}(s)}{d\ln s}\right|. \tag{3.30}$$

Thus, *once the density profile is chosen, in order to construct an acceptable homoeoidally expanded model the values of the flattenings must satisfy the inequality* $\epsilon \geq (A_M - 1)\eta - 1$. For example, let us consider a general normalized density profile of the form

$$\tilde{\rho}(m) = \frac{1}{m^a(1 + m^b)^c}, \tag{3.31}$$

with $a \geq 0$, $b \geq 0$, and $c \geq 0$, whence one easily finds $A_M = a + bc$. A particularly interesting case of expansion is represented by the γ-models (Dehnen 1993; Tremaine et al. 1994), in which $a = \gamma$, $b = 1$, and $c = 4 - \gamma$. Thus, by virtue of equation (3.30), to construct an acceptable homoeoidally expanded γ-model, the two flattenings must satisfy the condition $\epsilon \geq 3\eta - 1$. Figure 3.1 shows where in the (η,ϵ)-plane an expanded γ-model exists. Note how the additional relation provided by equation (3.30) modifies the general condition $0 \leq \epsilon \leq \eta < 1$: in particular, in the case of

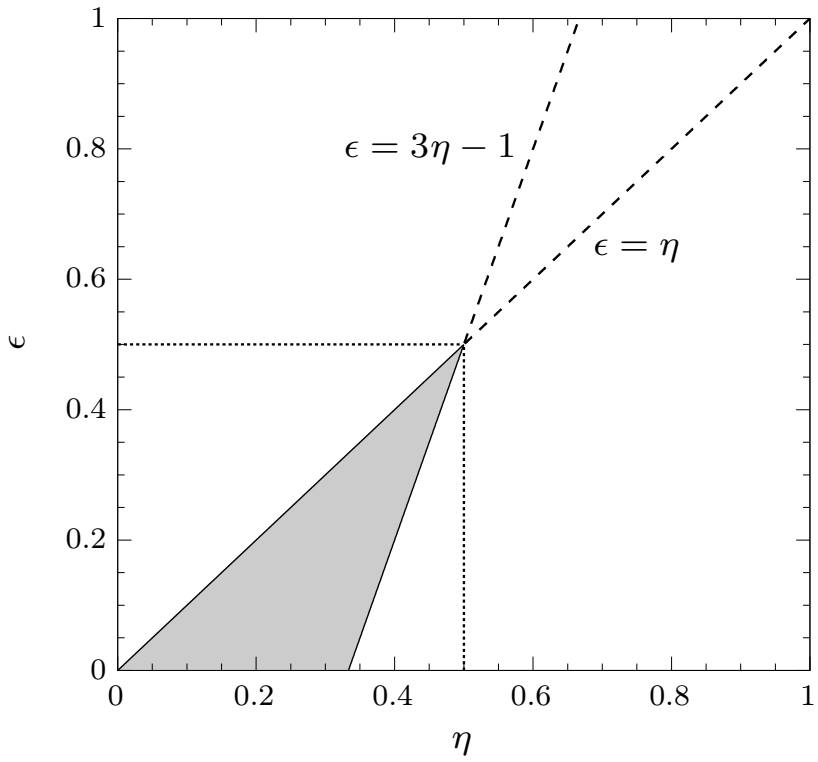

Figure 3.1. The filled region represents the locus of the points (η, ϵ) that allows a nowhere negative expanded density belonging to the family of the γ-models. For a fixed value of $\epsilon \leq 1/2$, the flattening η must satisfy the condition $\epsilon \leq \eta \leq (\epsilon + 1)/3$. For a fixed value of η, instead, ϵ cannot be greater than η if $\eta \leq 1/3$, while it must satisfy the condition $3\eta - 1 \leq \epsilon \leq \eta$ when $1/3 \leq \eta \leq 1/2$. In particular, oblate axisymmetric models are possible when $0 < \eta \leq 1/3$, whereas prolate models exist when $0 < \eta \leq 1/2$.

oblate axially symmetric models (i.e., $\epsilon = 0$) the value of η cannot exceed $1/3$, while in the prolate case (i.e., $\epsilon = \eta$) one has $\eta \leq 1/2$.

3.3 Axisymmetric models

Let us consider an axisymmetric system. In the oblate case, as we remarked earlier, the relationship between the semiaxes is $a = b > c > 0$, which implies $q_y = 1$; moreover, we define $q \equiv q_z$, suppressing the subscript since in this situation there is only one axial ratio greater than unity. Therefore, by introducing the cylindrical radius $R = \sqrt{x^2 + y^2}$, equation (3.2) reduces to

$$\rho(R, z) = \rho_{\mathrm{n}} \frac{\tilde{\rho}(m)}{q}, \qquad m^2 = \frac{R^2}{a^2} + \frac{z^2}{a^2 q^2} = \tilde{R}^2 + \frac{\tilde{z}^2}{q^2}, \tag{3.32}$$

where $\tilde{R} \equiv R/a$ is the normalized cylindrical radius. The gravitational potential (3.9), instead, can be rewritten in the form

$$\Psi(R, z) = \frac{\Psi_{\mathrm{n}}}{4} \int_0^\infty \frac{\tilde{F}(m_u) du}{(1 + u)\sqrt{q^2 + u}}, \qquad m_u^2 \equiv \frac{\tilde{R}^2}{1 + u} + \frac{\tilde{z}^2}{q^2 + u}. \tag{3.33}$$

Consequently, by setting $\epsilon = 0$ in equation (3.4), the (normalised) expanded density and potential reduce to the following expressions:

$$\frac{\rho(R,z)}{\rho_{\rm n}} = \tilde{\varrho}_0(s) + \eta\tilde{\varrho}_1(s) + \eta\tilde{z}^2\tilde{\varrho}_2(s) + \mathcal{O}\big(\eta^2\big), \qquad \frac{\Psi(R,z)}{\Psi_{\rm n}} = \tilde{\psi}_0(s) + \eta\tilde{\psi}_1(s) + \eta\tilde{z}^2\tilde{\psi}_2(s) + \mathcal{O}\big(\eta^2\big), \tag{3.34}$$

where $\eta = 1 - q$ is the flattening; note that, as in the general triaxial case, the radial functions $\tilde{\varrho}_i$ and $\tilde{\psi}_i$ (for $i = 0, 1, 2$) are defined in equations (3.5) and (3.16), respectively. When the vertical coordinate z is explicit in the expressions for ρ and Ψ, as in the case of the previous equation, we say that we are using the "explicit-z" formulation. However, when studying the dynamics of oblate galaxy models, it can be convenient to express the expanded density-potential pair having the cylindrical radius R explicit instead of the vertical coordinate z. The resulting "explicit-R" formulation is obtained simply by making use of the identity $R^2 = r^2 - z^2$ in the previous expressions:

$$\frac{\rho(R,z)}{\rho_{\rm n}} = \tilde{\rho}_0(s) + \eta\tilde{\rho}_1(s) + \eta\tilde{R}^2\tilde{\rho}_2(s) + \mathcal{O}\big(\eta^2\big), \qquad \frac{\Psi(R,z)}{\Psi_{\rm n}} = \tilde{\Psi}_0(s) + \eta\tilde{\Psi}_1(s) + \eta\tilde{R}^2\tilde{\Psi}_2(s) + \mathcal{O}\big(\eta^2\big); \tag{3.35}$$

the relationships between the corresponding normalized quantities are given by

$$\begin{cases} \tilde{\rho}_0 = \tilde{\varrho}_0, \\ \tilde{\rho}_1 = \tilde{\varrho}_1 + s^2\tilde{\varrho}_2, \\ \tilde{\rho}_2 = -\,\tilde{\varrho}_2, \end{cases} \qquad \begin{cases} \tilde{\Psi}_0 = \tilde{\psi}_0, \\ \tilde{\Psi}_1 = \tilde{\psi}_1 + s^2\tilde{\psi}_2, \\ \tilde{\Psi}_2 = -\,\tilde{\psi}_2. \end{cases} \tag{3.36}$$

By following the same procedure described after equation (3.17), or directly applying the transformations (3.36) to equation (3.21), it can be shown that the "expanded" Poisson equation for the dimensionless density-potential pair in the explicit-R formulation is given by

$$\tilde{\nabla}^2\tilde{\Psi}_i + \tilde{\rho}_i = \begin{cases} 0\,, & (i=0), \\ -\,4\tilde{\Psi}_2\,, & (i=1), \\ -\,\dfrac{4}{s}\dfrac{d\tilde{\Psi}_2}{ds}, & (i=2), \end{cases} \qquad \tilde{\nabla}^2 = \frac{d^2}{ds^2} + \frac{2}{s}\frac{d}{ds}. \tag{3.37}$$

The similarity of this equation with equation (3.21) is to be noted.

We shall now clarify the advantage of considering an expanded density-potential pair having R explicit rather than z explicit. For, let us consider an arbitrary axisymmetric function $\mathcal{F}(R,z)$ defined as

$$\mathcal{F}(R,z) = \begin{cases} f_0(r) + \eta f_1(r) + \eta z^2 f_2(r) + \mathcal{O}\big(\eta^2\big), & (\text{explicit-}z\text{ formulation}), \\ F_0(r) + \eta F_1(r) + \eta R^2 F_2(r) + \mathcal{O}\big(\eta^2\big), & (\text{explicit-}R\text{ formulation}), \end{cases} \tag{3.38}$$

where, in analogy with equation (3.36), the transformations relating the radial functions f_i and F_i are

$$f_0 = F_0\,, \qquad f_1 = F_1 + r^2F_2, \qquad f_2 = -\,F_2. \tag{3.39}$$

Now suppose we need to compute the derivative of $\mathcal{F}(R,z)$ with respect to R. Since R and z are independent variables, it follows that the explicit-z formulation is certainly the most convenient one; indeed, from equation (3.38),

$$\frac{\partial\mathcal{F}}{\partial R} = \frac{R}{r}\left(\frac{df_0}{dr} + \eta\frac{df_1}{dr} + \eta z^2\frac{df_2}{dr}\right) + \mathcal{O}(\eta^2). \tag{3.40}$$

A further differentiation gives

$$\frac{\partial^2\mathcal{F}}{\partial R^2} = \frac{z^2}{r^2 R}\frac{\partial\mathcal{F}}{\partial R} + \frac{R^2}{r^2}\left(\frac{d^2f_0}{dr^2} + \eta\frac{d^2f_1}{dr^2} + \eta z^2\frac{d^2f_2}{dr^2}\right) + \mathcal{O}(\eta^2). \tag{3.41}$$

On the contrary, the explicit-R formulation becomes useful to express the z-derivatives. Without any difficulty, we find

$$\frac{\partial\mathcal{F}}{\partial z} = \frac{z}{r}\left(\frac{dF_0}{dr} + \eta\frac{dF_1}{dr} + \eta R^2\frac{dF_2}{dr}\right) + \mathcal{O}(\eta^2), \tag{3.42}$$

and

$$\frac{\partial^2\mathcal{F}}{\partial z^2} = \frac{R^2}{r^2 z}\frac{\partial\mathcal{F}}{\partial z} + \frac{z^2}{r^2}\left(\frac{d^2F_0}{dr^2} + \eta\frac{d^2F_1}{dr^2} + \eta R^2\frac{d^2F_2}{dr^2}\right) + \mathcal{O}(\eta^2). \tag{3.43}$$

Note the complete similarity of equations (3.40)-(3.41) with equations (3.42)-(3.43).

As a consequence, for example, when computing properties on the equatorial plane (i.e., $z = 0$), as in the derivation of the *circular velocity* $v_\mathrm{c}(R)$, it is useful to work with the explicit-z formulation. From the standard definition of the circular velocity given in Chapter 2, we have

$$v_\mathrm{c}^2(R) = -R\left(\frac{\partial\Psi}{\partial R}\right)_0, \tag{3.44}$$

where the subscript "0" indicates that the quantity in the parenthesis has to be evaluated at $z = 0$. Measuring v_c^2 in units of Ψ_n, and using equation (3.40), at the linear order in the flattening we have

$$\frac{v_\mathrm{c}^2(R)}{\Psi_\mathrm{n}} = \tilde{v}_{\mathrm{c}0}^2(\tilde{R}) + \eta\,\tilde{v}_{\mathrm{c}1}^2(\tilde{R}) + \mathcal{O}(\eta^2), \qquad \tilde{v}_{\mathrm{c}i}^2(\tilde{R}) \equiv -\tilde{R}\,\frac{d\tilde{\psi}_i(\tilde{R})}{d\tilde{R}}, \tag{3.45}$$

for $i = 0, 1$. Further, once we have $v_\mathrm{c}(R)$, the corresponding *angular momentum* (per unit mass) can be defined as $J_\mathrm{c}(R) \equiv R v_\mathrm{c}(R)$. Then, with $J_\mathrm{n} \equiv a\sqrt{\Psi_\mathrm{n}} = \sqrt{GM_\mathrm{n}a}$, from equation (3.45) we have, limiting to the linear term in the flattening,

$$\frac{J_\mathrm{c}^2(R)}{J_\mathrm{n}^2} = \tilde{J}_{\mathrm{c}0}^2(\tilde{R}) + \eta\tilde{J}_{\mathrm{c}1}^2(\tilde{R}) + \mathcal{O}(\eta^2), \qquad \tilde{J}_{\mathrm{c}i}(\tilde{R}) \equiv \tilde{R}\,\tilde{v}_{\mathrm{c}i}(\tilde{R}), \tag{3.46}$$

for $i = 0, 1$. Closely related to $J_\mathrm{c}(R)$ is the *radial epicyclic frequency* $\kappa_R(R)$, defined by

$$\kappa_R^2(R) = \frac{1}{R^3}\frac{dJ_\mathrm{c}^2(R)}{dR}, \tag{3.47}$$

which is sometimes referred to as the *Rayleigh discriminant*[3]. Now, by inserting equation (3.46) in equation (3.47), and defining $\kappa_{\rm n} \equiv J_{\rm n}/a^2$, a simple computation yields

$$\frac{\kappa_R^2(R)}{\kappa_{\rm n}^2} = \tilde{\kappa}_{R0}^2(\tilde{R}) + \eta\tilde{\kappa}_{R1}^2(\tilde{R}) + \mathcal{O}(\eta^2), \qquad \tilde{\kappa}_{Ri}^2(\tilde{R}) \equiv \frac{1}{\tilde{R}^3}\frac{d\tilde{J}_{ci}^2(\tilde{R})}{d\tilde{R}}, \tag{3.48}$$

for $i = 0, 1$. Of course, by virtue of equation (3.45) the quantity $J_{\rm c}(R)$, and therefore $\kappa_R(R)$, may be expressed in terms of the functions $\tilde{\psi}_i$.

On the other hand, the explicit-R formulation is convenient when differentiating with respect to z. In this case, in analogy with the previous discussion, an interesting quantity is the *vertical epicyclic frequency* $\kappa_z(R)$, defined by

$$\kappa_z^2(R) \equiv -\left(\frac{\partial^2\Psi}{\partial z^2}\right)_0. \tag{3.49}$$

Then, from equation (3.43) it follows that

$$\frac{\kappa_z^2(R)}{\kappa_{\rm n}^2} = \tilde{\kappa}_{z0}^2(\tilde{R}) + \eta\tilde{\kappa}_{z1}^2(\tilde{R}) + \eta\tilde{R}^2\tilde{\kappa}_{z2}^2(\tilde{R}) + \mathcal{O}(\eta^2), \qquad \tilde{\kappa}_{zi}^2(\tilde{R}) \equiv -\frac{1}{\tilde{R}}\frac{d\tilde{\Psi}_i(\tilde{R})}{d\tilde{R}}, \tag{3.50}$$

for $i = 0, 1, 2$. Finally, we may notice that another example where it is useful to have R explicit occurs when integrating Jeans's equations (see § 2.2.1 and the references therein).

3.3.1 The gravitational energy

We dedicate a separate Section to the calculation of the self-interaction energy W. It is in fact clear that, to find the expansion of W for small flattenings in the axisymmetric case, it is sufficient to set $\epsilon = 0$ in equation (3.25). However, the same result can also be obtained by acting directly on the starting definition (2.7). In this alternative approach, we insert the expanded exressions for the density ρ and for the potential Ψ in the integral definition of W, and *discard all the quadratic terms in the flattening*. In other words, *we are assuming that the operations of expansion and integration are interchangeable, i.e. that the expansion of an integral coincides with the integral of the expansion of the integrand function*; we shall again make a major use of this procedure in the next Section, when we shall address the fundamental problem of Jeans's equations.

We start by writing $\boldsymbol{x} = R\boldsymbol{e}_R + z\boldsymbol{e}_z$, being $\boldsymbol{e}_R$ and $\boldsymbol{e}_z$ the radial and vertical unit vectors in cylindrical coordinates, respectively. As a consequence, the integrand in equation (2.7) reduces to

$$\boldsymbol{x}\cdot\frac{\partial\Psi}{\partial\boldsymbol{x}} = R\frac{\partial\Psi}{\partial R} + z\frac{\partial\Psi}{\partial z}. \tag{3.51}$$

[3] In general, if a particle travelling in a circular orbit at speed $v_{\rm c}(R)$ is kicked, in the plane of the orbit, slightly away from this path, it will gyrate (in an *elliptical* epicycle) about the radius of its original circle with a frequency equal to κ_R, assuming κ_R is real. Then, when $\kappa_R^2 > 0$ the amplitude of the disturbance oscillates about a fixed mean position, and the circular orbit is stable to small perturbations; on the contrary, if $\kappa_R^2 < 0$ the resulting trajectory will begin to depart exponentially from the original path, and the circular orbit is unstable (see C21 for an exhaustive discussion of the Classical Epicyclic Theory; see also Chandrasekhar 1961 for a detailed treatment of the so-called *Rayleigh criterion*). Also, it is interesting to note that there exist a straightforward relativistic generalization of this result; in particular, it can be shown that orbits around a black hole become unstable outside the event horizon bacause the angular momentum required for smaller circular orbits increases, rather than decreases, as the particle approaches the event horizon (see e.g. Misner et al. 1973; Chandrasekhar 1983).

Now, by inserting the expansion of Ψ in its explicit-R formulation, and making use of equations (3.40)-(3.42), we can rewrite the previous expression as

$$\boldsymbol{x}\cdot\boldsymbol{\nabla}\Psi=\Psi_{\rm n}\left[\left(\frac{d\tilde{\Psi}_0}{ds}+\eta\frac{d\tilde{\Psi}_1}{ds}\right)s+\eta\tilde{R}^2\left(s\frac{d\tilde{\Psi}_2}{ds}+2\tilde{\Psi}_2\right)\right]. \tag{3.52}$$

Therefore, from the explicit-R formulation of the expanded density, and removing all the η^2 terms, after some minor reductions we obtain

$$\frac{\rho\boldsymbol{x}\cdot\boldsymbol{\nabla}\Psi}{\rho_{\rm n}\Psi_{\rm n}}=\mathcal{E}_0(s)+\eta\mathcal{E}_1(s)+\eta\tilde{R}^2\mathcal{E}_2(s), \tag{3.53}$$

where for simplicity we have defined

$$\mathcal{E}_0(s)\equiv\tilde{\rho}_0\frac{d\tilde{\Psi}_0}{ds}s,\qquad \mathcal{E}_1(s)\equiv\left(\tilde{\rho}_0\frac{d\tilde{\Psi}_1}{ds}+\tilde{\rho}_1\frac{d\tilde{\Psi}_0}{ds}\right)s,\qquad \mathcal{E}_2(s)\equiv\left(\tilde{\rho}_2\frac{d\tilde{\Psi}_0}{ds}+\tilde{\rho}_0\frac{d\tilde{\Psi}_2}{ds}\right)s+2\tilde{\rho}_0\tilde{\Psi}_2. \tag{3.54}$$

By inserting equations (3.53)-(3.54) in (2.7), with $d^3\boldsymbol{x}=r^2\sin\vartheta dr d\vartheta d\varphi$, we obtain

$$\begin{aligned}\frac{W}{U_{\rm n}}&=\frac{1}{2}\int_0^\infty\int_0^\pi[\mathcal{E}_0(s)+\eta\mathcal{E}_1(s)+\eta s^2\sin^2\vartheta\,\mathcal{E}_2(s)]s^2\sin\vartheta ds d\vartheta,\\&=\int_0^\infty\left[\mathcal{E}_0(s)+\eta\frac{3\mathcal{E}_1(s)+2s^2\mathcal{E}_2(s)}{3}\right]s^2ds.\end{aligned} \tag{3.55}$$

Finally, on simplification and rearrangement, the expanded self-interaction energy reduces to

$$\frac{W}{U_{\rm n}}=\mathcal{U}_0+\eta(\mathcal{U}_1+\mathcal{U}_2), \tag{3.56}$$

where the dimensionless quantities on the right-hand side are defined by the following definitions:

$$\begin{cases}\mathcal{U}_0\equiv\displaystyle\int_0^\infty\tilde{\rho}_0(s)\frac{d\tilde{\Psi}_0(s)}{ds}s^3ds,\\[2ex]\mathcal{U}_1\equiv\displaystyle\int_0^\infty\left[\tilde{\rho}_1(s)+\frac{2}{3}s^2\tilde{\rho}_2(s)\right]\frac{d\tilde{\Psi}_0(s)}{ds}s^3ds,\\[2ex]\mathcal{U}_2\equiv\displaystyle\int_0^\infty\tilde{\rho}_0(s)\frac{d}{ds}\left[\tilde{\Psi}_1(s)+\frac{2}{3}s^2\tilde{\Psi}_2(s)\right]s^3ds.\end{cases} \tag{3.57}$$

With some lengthy but straightforward reductions it is possible to show that equation (3.56) coincides with equation (3.25) for $\epsilon=0$.

3.3.2 The solutions of Jeans's equations

We now discuss a fundamental topic in this First Part of the Thesis, i.e., how to solve Jeans's equations in homoeoidal expansion. In Section § 2.2.1 we have already shown what are the formal expressions, in integral form, of the velocity dispersion σ and of the quantity Δ: these are given by equations (2.29) and (2.32), respectively.

Let us first focus on σ, and consider an axisymmetric density of the form (3.32). After changing variable from τ to $u \equiv \tau/a^2$ in the inner integral of equation (2.29), the quantity $\rho\sigma^2$ expressed in units of $\rho_{\rm n}\Psi_{\rm n}$ reads

$$\frac{\rho\sigma^2}{\rho_{\rm n}\Psi_{\rm n}} = \frac{1}{2q}\int_{\tilde{z}}^{\infty} d\tilde{z}'\,\tilde{\rho}(m')\,\tilde{z}' \int_0^{\infty} \frac{\tilde{\rho}(m'_u)\,du}{(1+u)(q^2+u)^{3/2}}, \tag{3.58}$$

where $m'^2 = \tilde{R}^2 + \tilde{z}'^2/q^2$, and $m'^2_u = \tilde{R}^2/(1+u) + \tilde{z}'^2/(q^2+u)$. With similar reductions, it is easy to show that equation (2.32) can be recast as

$$\frac{\rho\Delta}{\rho_{\rm n}\Psi_{\rm n}} = \frac{1-q^2}{2q^3}R^2 \int_{\tilde{z}}^{\infty} d\tilde{z}' \left|\frac{d\tilde{\rho}(m')}{dm'}\right| \frac{\tilde{z}'}{m'} \int_0^{\infty} \frac{\tilde{\rho}(m'_u)\,u\,du}{(1+u)^2(q^2+u)^{3/2}}. \tag{3.59}$$

Equations (3.58)-(3.59) are the normalized version of equations (2.29)-(2.32).

In the same way as we obtained the expansion of the potential from its integral expression (3.9), to derive the expanded expressions for $\rho\sigma^2$ and $\rho\Delta$, we could directly expand the equations (3.58)-(3.59) for $\eta \to 0$ (i.e. $q \to 1$). Since this approach would produce a number of non-trivial calculations, we prefer to proceed as in Section 3.3.1, i.e. by assuming that the operations of expansion and integration are interchangeable. For, we just insert the expanded exressions for the density ρ and potential Ψ in the integral form solutions (2.23) and (2.27), and neglect all the quadratic terms in the flattening.

The solution of the vertical equation

We start from the vertical Jeans equation. With the density-potential pair given by equation (3.35), at the linear order in η we have

$$\rho\frac{\partial\Psi}{\partial z} = \frac{\rho_{\rm n}\Psi_{\rm n}}{a}\frac{z}{r}\left[\tilde{\rho}_0\frac{d\tilde{\Psi}_0}{ds} + \eta\left(\tilde{\rho}_0\frac{d\tilde{\Psi}_1}{ds} + \tilde{\rho}_1\frac{d\tilde{\Psi}_0}{ds}\right) + \eta\tilde{R}^2\left(\tilde{\rho}_0\frac{d\tilde{\Psi}_2}{ds} + \tilde{\rho}_2\frac{d\tilde{\Psi}_0}{ds}\right)\right]. \tag{3.60}$$

Now we insert this expression in equation (2.23), and change the integration variable, at fixed R, from z' to r'; in this way, the integration acts only on spherical function. As a result, the solution of the vertical Jeans equation in the homoeoidal expansion framework can be written as

$$\frac{\rho\sigma^2}{\rho_{\rm n}\Psi_{\rm n}} = I_0(s) + \eta I_1(s) + \eta\tilde{R}^2 I_2(s), \tag{3.61}$$

where the three radial functions are given by

$$\begin{cases} I_0(s) \equiv -\displaystyle\int_s^\infty \tilde{\rho}_0(s') \frac{d\tilde{\Psi}_0(s')}{ds'} ds', \\ I_1(s) \equiv -\displaystyle\int_s^\infty \left[\tilde{\rho}_0(s') \frac{d\tilde{\Psi}_1(s')}{ds'} + \tilde{\rho}_1(s') \frac{d\tilde{\Psi}_0(s')}{ds'} \right] ds', \\ I_2(s) \equiv -\displaystyle\int_s^\infty \left[\tilde{\rho}_0(s') \frac{d\tilde{\Psi}_2(s')}{ds'} + \tilde{\rho}_2(s') \frac{d\tilde{\Psi}_0(s')}{ds'} \right] ds'. \end{cases} \tag{3.62}$$

In the limiting case $\eta = 0$, i.e. for spherically symmetric models, only $I_0(s)$ occurs in the determination of the velocity dispersion; from equations (3.16)-(3.36), it is quite easy to show that I_0 can be rewritten in the following form:

$$I_0(s) = \int_s^\infty \tilde{\rho}(s') \frac{\tilde{M}(s')}{s'^2} ds', \tag{3.63}$$

where $\tilde{M}$ is defined in equation (3.6); of course, this expression coincides with the isotropic solution of Jeans's equation for spherical systems, and is evidently nowhere negative.

The solution of the radial equation

We now return to the solution of the radial Jeans equation. It is interesting to note that the right-hand side of equation (2.27) can be rewritten as the following commutator-like integral:

$$\frac{\rho\Delta}{R} = -[\rho, \Psi], \tag{3.64}$$

where, being $f(R, z)$ and $g(R, z)$ two generic axisymmetric functions, we define

$$[f, g] \equiv \int_z^\infty \left(\frac{\partial f}{\partial R} \frac{\partial g}{\partial z'} - \frac{\partial f}{\partial z'} \frac{\partial g}{\partial R} \right) dz'. \tag{3.65}$$

It is useful to report some revelant properties of the commutator just defined. For example it is clear that, for any pair of purely radial functions, the commutator vanishes; thus, for fully spherical models one has $\Delta = 0$, so that, *in Satoh's decomposition, spherical models cannot rotate, and are necessarily isotropic, independently of the value of k.* Moreover, it is easy to prove that, given three generic functions $F(R, z)$, $G(R, z)$, and $H(R, z)$, and two constants α and β, the commutator (3.65) obeys the rules of the Lie Algebra (e.g. Artin 1991; see also Arnold 1978), i.e.

1. $[F, G] = -[G, F]$; (anticommutativity);
2. $[\alpha F + \beta G, H] = \alpha[F, H] + \beta[G, H]$, (bilinearity);
3. $[F, [G, H]] + [G, [H, F]] + [H, [F, G]] = 0$, (Jacobi identity).

From the bilinearity property, and from the fact that the commutator vanishes for generic pairs of spherical functions, it follows that

$$\frac{[\rho, \Psi]}{\rho_{\rm n}\Psi_{\rm n}} = \eta[\tilde{\rho}_0(s), \tilde{R}^2\tilde{\Psi}_2(s)] + \eta[\tilde{R}^2\tilde{\rho}_2(s), \tilde{\Psi}_0(s)], \tag{3.66}$$

and so Δ can be produced only by the effect of the Ψ_2 term on ρ_0, and by the Ψ_0 term on ρ_2. Also, notice that, as a result of the homoeoidal expansion method, $\rho\Delta$ *is proportional to* η; as a consequence, in the limit for small flattenings, $\overline{v_\varphi} \propto \sqrt{\eta}$.

We shall now derive some general properties of the commutator useful to simplify equation (3.66); for, we consider two generic functions ϕ and ψ of the cylindrical radius, and two spherically simmetric functions u and v, i.e.

$$\phi = \phi(R), \qquad \psi = \psi(R), \qquad u = u(r), \qquad v = v(r), \tag{3.67}$$

and evaluate the following commutator:

$$[\phi u, \psi v] = \int_z^\infty A(R, z')dz', \qquad A(R, z) \equiv \frac{\partial \phi u}{\partial R}\frac{\partial \psi v}{\partial z} - \frac{\partial \phi u}{\partial z}\frac{\partial \psi v}{\partial R}. \tag{3.68}$$

By elementary calculations we find

$$A(R, z) = \left(\frac{d\phi}{dR}u + \phi\frac{\partial u}{\partial R}\right)\psi\frac{\partial v}{\partial z} - \phi\frac{\partial u}{\partial z}\left(\frac{d\psi}{dR}v + \psi\frac{\partial v}{\partial R}\right), \tag{3.69}$$

from which, simplifying, we readily obtain

$$A(R, z) = \frac{z}{r}\left(\frac{d\phi}{dR}\psi u\frac{dv}{dr} - \phi\frac{d\psi}{dR}\frac{du}{dr}v\right). \tag{3.70}$$

Now, inserting this expression in equation (3.68), and changing the integration variable (at fixed R) from z' to r', we find the following remarkable formula:

$$[\phi(R)u(r), \psi(R)v(r)] = \frac{d\phi(R)}{dR}\psi(R)\int_r^\infty u(t)\frac{dv(t)}{dt}dt - \phi(R)\frac{d\psi(R)}{dR}\int_r^\infty \frac{du(t)}{dt}v(t)dt. \tag{3.71}$$

In particular, when dealing with homoeoidally expanded functions in the explicit-R formulation, we may be faced with four special cases:

1. $[u(r), v(r)] = 0$;
2. $[R^2u(r), v(r)] = 2R\int_r^\infty u(t)\frac{dv(t)}{dt}dt$;
3. $[u(r), R^2v(r)] = -2R\int_r^\infty \frac{du(t)}{dt}v(t)dt$;
4. $[R^2u(r), R^2v(r)] = 2R^3\int_r^\infty \left[u(t)\frac{dv(t)}{dt} - \frac{du(t)}{dt}v(t)\right]dt$.

Note that the latter case corresponds to a quadratic order term in the flattening, which in principle ought to be discarded; we have included it in the list of notable cases since an in-depth study of the different "interpretations" of the density-potential pair, based precisely on the effect of the η^2 terms, will be addressed in the next Chapter.

Thanks to these formulae, we are now in a position to calculate the right-hand side of equation (3.66). By applying the third of the previous identities, one finds

$$[\tilde{\rho}_0(s), \tilde{R}^2\tilde{\Psi}_2(s)] = -\frac{2\tilde{R}}{a}\int_s^\infty \frac{d\tilde{\rho}_0(s')}{ds'}\,\tilde{\Psi}_2(s')\,ds',$$

$$= -\frac{2\tilde{R}}{a}\left[\ell - \tilde{\rho}_0(s)\tilde{\Psi}_2(s) - \int_s^\infty \tilde{\rho}_0(s')\frac{d\tilde{\Psi}_2(s')}{ds'}\,ds'\right], \qquad \ell \equiv \lim_{t\to\infty}\tilde{\rho}_0(t)\tilde{\Psi}_2(t), \tag{3.72}$$

where the second line results from an integration by parts. Since the limit vanishes for any reasonable density profile[4], we conclude that

$$[\tilde{\rho}_0(s), \tilde{R}^2\tilde{\Psi}_2(s)] = \frac{2\tilde{R}}{a}\left[\tilde{\rho}_0(s)\tilde{\Psi}_2(s) + \int_s^\infty \tilde{\rho}_0(s')\frac{d\tilde{\Psi}_2(s')}{ds'}\,ds'\right]. \tag{3.73}$$

For what concerns the second term at the right-hand side of equation (3.66),

$$[\tilde{R}^2\tilde{\rho}_2(s), \tilde{\Psi}_0(s)] = \frac{2\tilde{R}}{a}\int_s^\infty \tilde{\rho}_2(s')\frac{d\tilde{\Psi}_0(s')}{ds'}\,ds'. \tag{3.74}$$

Therefore, by inserting the two previous expressions in equation (3.64) we obtain for the solution of the radial Jeans equation in homoeoidal expansion the following remarkable formula:

$$\frac{\rho\Delta}{\rho_{\rm n}\Psi_{\rm n}} = 2\eta\tilde{R}^2[I_2(s) - \tilde{\rho}_0(s)\tilde{\Psi}_2(s)]; \tag{3.75}$$

note how $\rho\Delta$ vanishes in case of a spherical model, as is expected for two-integral systems.

[4]From equations (3.36) and (3.16), the limit ℓ is given explicitly by

$$\ell = \lim_{t\to\infty}\tilde{\rho}(t)\frac{I(t)}{t^5}, \qquad I(t) \equiv \int_0^t \tilde{\rho}(m)m^4 dm.$$

Since the density vanishes at large radii, the value of ℓ depends on the convergence of the integral $I(t)$. However, it is trivial to prove that $\ell = 0$ always: indeed, if $I(t)$ converges for $t \to \infty$, ℓ is evidently zero; if $I(t)$ diverges, the vanishing of ℓ is assured by de l'Hôpital's (1696) theorem on indeterminate forms.

CHAPTER 4

Two-component Homoeoidally Expanded Models

Two-component (stars plus dark matter) spherical galaxy models with an analytical solution for Jeans's equations have been presented in CZ18 and CMP19. In a first family (JJ models), the stellar profile is described by a Jaffe law, while the total is another Jaffe model of larger total mass and different scale length. In a second family (J3 models), the stellar density follows again a Jaffe profile, while the total follows a r^{-3} law at large radii. Both JJ and J3 models allow for a complete analytical treatment with quite simple expressions of several quantities of interest in observational and theoretical works. In this Chapter we present the generalization of these spherical models to axisymmetrical shapes, and study their structural and dynamical properties by applying the homoeoidal expansion method. By adopting Satoh's decomposition to split the azimuthal velocity field in its ordered and random components, we solve analytically the two-integral Jeans equations, and the global quantities entering the Virial theorem are explicitly calculated. The projection of the kinematic fields are finally obtained by means of numerical methods.

4.1 Spherical models as a starting point

Spherically symmetric galaxy models, thanks to their simplicity, can be useful in exploratory works in Stellar Dynamics (e.g. BT87; Bertin 2014; C21; see also Bertin & Stiavelli 1993). A successful spherical model compensates its geometric limitations with other features, such as the possibilities to:

1. derive manageable analytical expressions for the most important dynamical quantities;

2. easily include a dark matter (DM) halo with an adjustable density profile (or, alternatively, to specify the total density profile);

3. model the dynamical effects of a central black hole (BH);

4. control orbital anisotropy.

For example, the density profile of the stellar distribution of the model, once projected, should be similar to that of early-type galaxies, i.e. to the de Vaucouleurs (1948) $R^{1/4}$ law, or better, to its generalization, the so-called $R^{1/m}$ law (Sersic 1963); unfortunately, the $R^{1/m}$ law does not allow for an explicit deprojection in terms of elementary functions (e.g. Ciotti 1991). The so-called γ models (Dehnen 1993; Tremaine et al. 1994), in projection, are well fitted by the $R^{1/m}$ law with sufficient accuracy (for most applications) over a large radial range: this is especially true for the Jaffe (1983) and Hernquist (1990) models, often natural choices to describe the stellar distribution of early-type galaxies in the spherical approximation.

Once the stellar profile of the model is considered acceptable, a second request of a useful spherical model is the possibility to reproduce, with a minor effort, the large-scale observational properties of the total density profile (e.g. Bertin et al. 1994; Rix et al. 1997; Gerhard et al. 2001; Treu & Koopmans 2002, 2004; Rusin et al. 2003; Rusin & Kochanek 2005; Koopmans et al. 2006; Gavazzi et al. 2007; Czoske et al. 2008; Dye et al. 2008; Nipoti et al. 2008, see also Shankar et al. 2017). For example, simple models with flat circular velocity have been constructed (e.g. Kochanek 1994; Naab & Ostriker 2007); in particular, we recall the family of two-component galaxy models whose total mass density is proportional to r^{-2}, while the visible (stellar) mass is described by the γ models (Ciotti et al. 2009; see also the double power-law models of Hiotelis 1994). Also, it is well-known that supermassive BHs with a mass of the order of $M_{\rm BH} \simeq 10^{-3} M_*$ are routinely found at the centre of the stellar spheroids of total mass M_* (e.g. see Magorrian et al. 1998; Kormendy & Ho 2013), so that another important feature is the possibility to easily compute the dynamical properties of the stellar component even in presence of a central BH.

4.1.1 The case of JJ and J3 models

Following the arguments previously described, two families of two-component (stars plus DM) spherical galaxy models have been recently presented. These are the JJ and J3 models, fully discussed in CZ18 and CMP19, respectively. Now we shall briefly recall how these spherical models are defined.

In the first family of spherical models (JJ models), the stellar density distribution ρ_* is described by a Jaffe (1983) law, while the galaxy profile $\rho_{\rm g}$ is another spherical Jaffe model of larger total mass and different scale length. In the second family (J3 models) the stellar density follows again a Jaffe model, while the total is a spherical density profile with a logarithmic slope equal to -3 at large radii. Denoting by r_* the stellar scale length, $r_{\rm g}$ the galaxy scale length, and M_* the (finite) total stellar mass, the two density profiles describing the JJ and J3 models read

$$\text{JJ:}\begin{cases}\rho_*(r) = \dfrac{\rho_\mathrm{n}}{s^2(1+s)^2},\\[2ex] \rho_\mathrm{g}(r) = \dfrac{\mathcal{R}\xi\rho_\mathrm{n}}{s^2(\xi+s)^2},\end{cases}\qquad\qquad \text{J3:}\begin{cases}\rho_*(r) = \dfrac{\rho_\mathrm{n}}{s^2(1+s)^2},\\[2ex] \rho_\mathrm{g}(r) = \dfrac{\mathcal{R}\rho_\mathrm{n}}{s^2(\xi+s)},\end{cases} \tag{4.1}$$

where the following definitions apply:

$$\rho_\mathrm{n} \equiv \frac{M_*}{4\pi r_*^3}, \qquad\qquad s \equiv \frac{r}{r_*}, \qquad\qquad \xi \equiv \frac{r_\mathrm{g}}{r_*}. \tag{4.2}$$

It is quite evident that, at variance with the case of JJ models, the total mass of the galaxy is infinite in the J3 models. For this reason, the parameter $\mathcal{R}$ assumes a different meaning for the two families: for JJ models, $\mathcal{R} = M_\mathrm{g}/M_*$, being M_g the total galaxy mass; for J3 models, $\mathcal{R}$ is the limiting value of $\xi\rho_\mathrm{g}(r)/\rho_*(r)$ when $r \to 0$, so that $\mathcal{R}/\xi$ can be formally interpreted as a density ratio[1].

In both models, the DM profile is then recovered by *difference*, subtracting the stellar profile from the total: $\rho_\mathrm{DM}(r) = \rho_\mathrm{g}(r) - \rho_*(r)$; we remark that the approach used to build these models is different from the standard one, where a DM halo is *added* to the stellar distribution (e.g. Ciotti, Lanzoni & Renzini 1996; Ciotti 1996, 1999; section 4.4 in Ciotti et al. 2009). Finally, a BH is added at the centre of the galaxy in both models.

In CZ18, it was shown that it is always possible to choose a total mass so that the DM halo resulting from the difference between the total and the stellar density distributions reproduces remarkably well the Navarro–Frenk–White profile (Navarro, Frenk & White 1997, hereafter NFW) in the inner region. This interesting possibility was further improved in CMP19, where it was proved that the DM halo in the so-called minimum halo model (e.g. Mancino 2019, § 2.3.1) can be tuned to reproduce very well the NFW profile over the whole radial range. Summarising, *JJ and J3 models present several interesting features, such as analytical simplicity, flexibility in the choice of the structural parameters, realistic stellar and DM density profiles, and fully analytical solutions for Jeans's equations even in presence of a central BH.* For both models, indeed, Jeans's equations with Osipkov-Merritt radial anisotropy (see Osipkov 1979, Merritt 1985) can be solved analytically; further, the projected velocity dispersion can be expressed by means of simple formulae both at small and large radii for generic values of the model parameters. Moreover, also the positivity of the phase-space distribution function may be easily studied, together with the maximum amount of radial anisotropy allowable for consistency.

In the JJ models, in the special *minumum halo* case, the DM profile behaves like r^{-1} close to the centre, similarly to the NFW profile; at large radii, instead, the DM profile decreases as r^{-4}, at variance with the NFW profile that goes as r^{-3}. In CMP19 it is shown that, indeed, it is possible to construct models with similar analytical properties of JJ models, but with the additional property that the DM follows the NFW shape over the *whole* radial range; we called the resulting models "J3" to stress that the stellar density is again a Jaffe model, while the DM decreases as r^{-3} at large radii (see Mancino 2019 for more details).

4.2 From spherical to ellipsoidal models: the JJe and J3e models

Once the model properties are controlled in the spherical limit, then more sophisticated investigations, based on axisymmetric (or even triaxial) galaxy models, can be undertaken avoiding a

[1] The expression for the cumulative mass profile $M_\mathrm{g}(r)$ provides an alternative method to define the dimensionless factor $\mathcal{R}$: indeed, evaluating $M_\mathrm{g}(r)$ for $r = r_\mathrm{g}$, one readily finds $M_\mathrm{g}(r_\mathrm{g})/M_* = \mathcal{R}\ln 2$, which lead us to express $\mathcal{R}$ also as a mass ratio.

large exploration of the parameter space (e.g. Cappellari et al. 2007; van den Bosch et al. 2008). As a consequence, it is then natural to explore the possibility of a *generalization of the JJ and J3 models to ellipsoidal axisymmetrical shapes*: we shall call the new models JJe and J3e, respectively. One of the main ideas behind the construction of such models is to combine the modelling based on the assignment of the total and stellar profiles with the homoeoidal expansion technique.

4.2.1 The stellar and galaxy density profiles

The stellar component of JJe and J3e models is given by the mass-conserving ellipsoidal generalization of ρ_* in equation (4.1):

$$\rho_*(R,z) = \frac{\rho_{\rm n}}{q_* m_*^2 (1+m_*)^2}, \qquad 0 < q_* \leq 1, \qquad m_*^2 = \tilde{R}^2 + \frac{\tilde{z}^2}{q_*^2}, \tag{4.3}$$

where q_* measures the flattening of the density distribution, and $\tilde{R} \equiv R/r_*$ and $\tilde{z} \equiv z/r_*$ are the cylindrical coordinates in units of the stellar scale lenght. From volume integration of equation (4.3), the independence of the total mass M_* on q_* can be immediately verified (see Chapter 3). As shown in Fig. 4.1 (top panel), the contour lines of the stellar density in the meridional plane (R,z) are elongated along the major axis. The bottom panel of Fig. 4.1 shows the radial profile of ρ_* on the plane $z=0$, for three values of the axial ratio: the highly flattened case $q_*=0.1$ (solid), the case $q_*=0.4$ (dotted), and the spherical limiting case $q_*=1$ (dashed): according to equation (4.3) for R fixed, ρ_* increases as q_* decreases.

In analogy with equation (4.3), for the total galaxy density profile we shall assume

$$\rho_{\rm g}(R,z) = \rho_{\rm n} \times \begin{cases} \dfrac{\mathcal{R}\xi}{q_{\rm g} m_{\rm g}^2 (\xi + m_{\rm g})^2}, & \text{(JJe)}, \\ \dfrac{\mathcal{R}}{q_{\rm g} m_{\rm g}^2 (\xi + m_{\rm g})}, & \text{(J3e)}, \end{cases} \qquad 0 < q_{\rm g} \leq 1, \qquad m_{\rm g}^2 = \tilde{R}^2 + \frac{\tilde{z}^2}{q_{\rm g}^2}, \tag{4.4}$$

where $q_{\rm g}$, in analogy with q_*, is the axial ratio of the total density profile. Notice that, even for the galaxy profile, we continue to measure the coordinates R and z in units of r_*. Of course, when $q_* = q_{\rm g} = 1$, JJe and J3e models reduce respectively to JJ and J3 models. Of course, any expression (if not differently stated) applies to positive values of ξ, even if *realistic* cases are obtained for $\xi \geq 1$.

The associated stellar and galaxy mass distribution can be obtained by making use of the general expression (2.2). By elementary calculations we find

$$M_*(R,z) = \frac{M_* m_*}{1+m_*}, \qquad M_{\rm g}(R,z) = M_* \times \begin{cases} \dfrac{\mathcal{R} m_{\rm g}}{\xi + m_{\rm g}}, & \text{(JJe)}, \\ \mathcal{R} \ln \dfrac{\xi + m_{\rm g}}{\xi}, & \text{(J3e)}; \end{cases} \tag{4.5}$$

as expected, the total mass $M_{\rm g}(R,z)$ converges to a finite $\mathcal{R} M_* = M_{\rm g}$ in JJe models, and diverges in the J3e case. As a natural generalization of the spherical case, the "unit ellipsoid" $m_* = 1$ represents the half stellar mass ellipsoid for both models; analogously, for JJe models the mass of the galaxy is one-half of $M_{\rm g}$ at the points (R,z) on the surface of the ellipsoid $m_{\rm g} = \xi$.

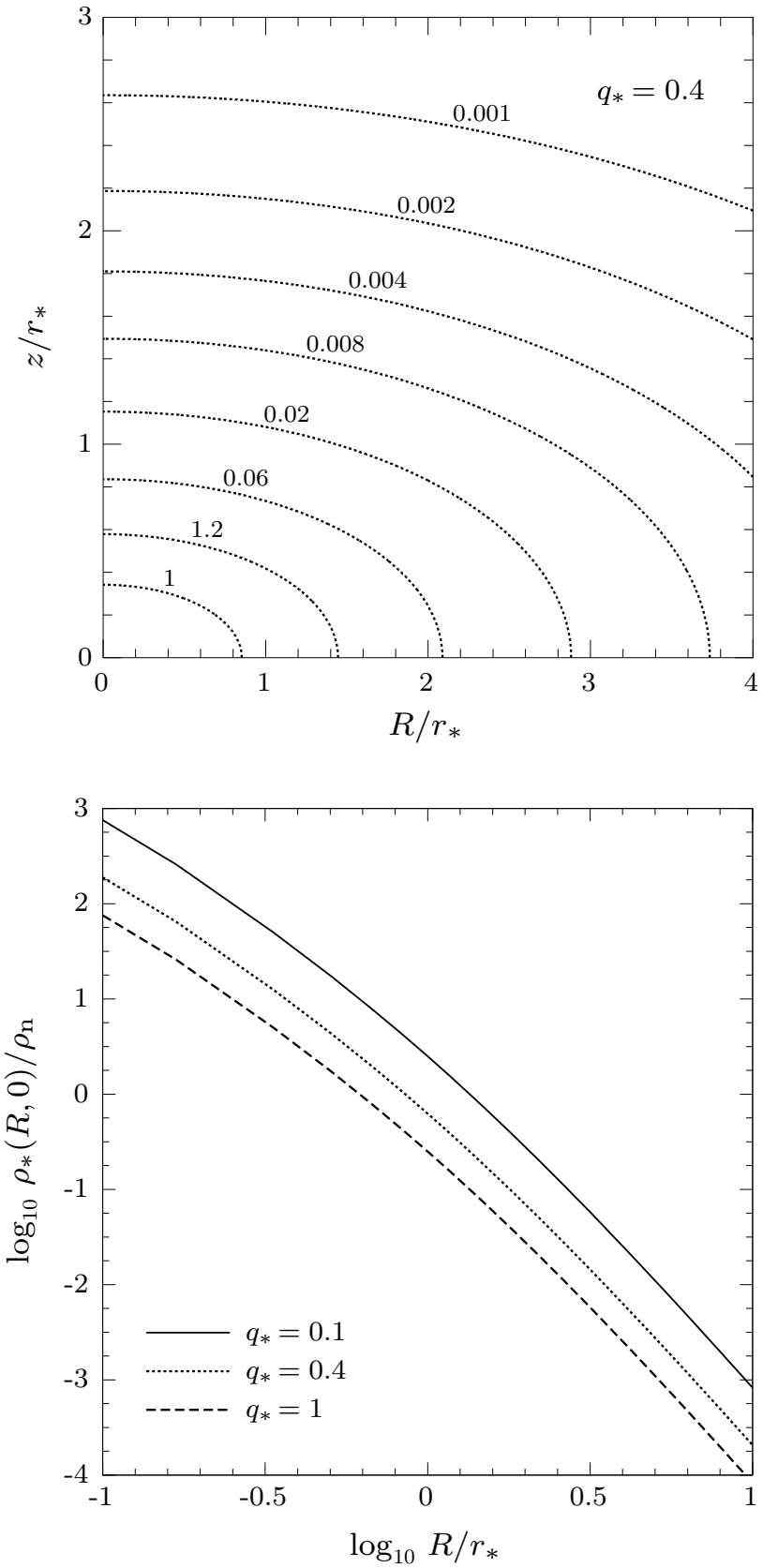

Figure 4.1. Top panel: stellar isodensity contours for $q_* = 0.4$, according to equation (4.3); the density is normalized to $\rho_{\rm n}$, and the contour values are labelled on the corresponding curves. Bottom panel: radial profile on the equatorial plane ($z = 0$) of the stellar density (4.3), for $q_* = 0.1$ (solid), $q_* = 0.4$ (dotted), and $q_* = 1$ (dashed).

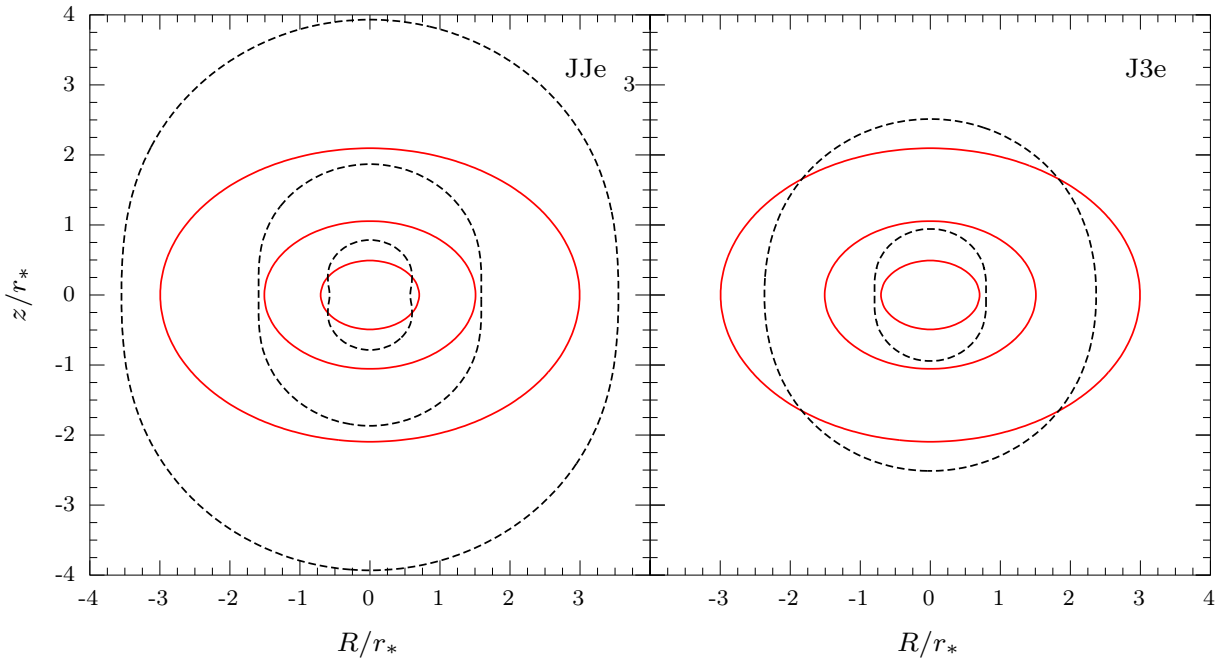

Figure 4.2. Isodensity contours of the stellar (solid) and DM (dotted) density distributions, for JJe (left) and J3e (right) models. The densities are normalized to $\rho_{\rm n}$, and the lengths to r_*. The contours correspond to values of 10, 1, and 10^{-1}, from inside to outside. The stellar distribution is flatter than the total, with $q_* = 0.7$, while the galaxy is spherical, i.e. $q_{\rm g} = 1$. For both panels, $\xi = 2$ and $\mathcal{R} = 3$. Note how at any fixed distance from the galactic centre (especially outside r_*) the DM density is larger for J3e than for JJe models.

4.2.2 The DM profile

The DM component for these models is defined as the difference between the galaxy and stellar distributions, i.e.

$$\rho_{\rm DM}(R,z) = \rho_{\rm n} \times \begin{cases} \dfrac{\mathcal{R}\xi}{q_{\rm g} m_{\rm g}^2 (\xi + m_{\rm g})^2} - \dfrac{1}{q_* m_*^2 (1+m_*)^2}, & \text{(JJe)}, \\ \dfrac{\mathcal{R}}{q_{\rm g} m_{\rm g}^2 (\xi + m_{\rm g})} - \dfrac{1}{q_* m_*^2 (1+m_*)^2}, & \text{(J3e)}. \end{cases} \tag{4.6}$$

It is important to note that for $q_{\rm g} \neq q_*$, i.e. in the case of different flattenings for the galaxy and stellar densities, $\rho_{\rm DM}$ is *not* stratified on ellipsoidal surfaces. For illustrative purposes, in Fig. 4.2 we compare the sodensity contours in the meridional plane of the stellar distribution (red solid) with those of the DM density distributions (black dotted): JJe models are shown in the left panel, J3e models in the right one. We choose a spherical galaxy (i.e. $q_{\rm g} = 1$), with $\xi = 2$ and $\mathcal{R} = 3$, while for the stellar component we adopt $q_* = 0.7$. It is evident that the DM distribution is elongated along the z-axis, with a prolate-like shape; also, we find that at any fixed distance from the galactic centre (but especially outside r_*) the DM density is larger for J3e than for JJe models: in the right panel, indeed, the contour line connecting all points with a density of $10^{-1}\rho_{\rm n}$ does not appear since it refers to points lying outside the range of the plot.

One of the peculiarities of these models is that the DM profile, instead of being added to a stellar component to form a total density distribution, is obtained from the difference of the two starting density distributions, $\rho_{\rm g}$ and ρ_*. This means that its positivity is not necessarily guaranteed, but depends strongly on the parameters defining the model. Accordingly, a preliminary study of its non-negativity as a function of the model parameters must be considered. For, we

shall now follow a similar approach already developed for spherical models in CZ18 and CMP19; of course, the situation is now more complicated, due to the possible different shape of the two starting distributions. Quite surprisingly, we find that the discussion can be carried out analytically, and the constraints on the model parameters in order to have a positive DM can be expressed via extremely simple algebraic relations. As a consequence, *the non-negativity problem in JJe and J3e models does not require numerical investigations.*

The non-negativity condition: a general result

It is convenient to set up the problem in the more general case of two arbitrary ellipsoidal distributions, and then to specialized the results to the specific cases. For, let

$$\rho_* = E_*(m_*), \qquad \rho_{\rm g} = \mathcal{R}\, E_{\rm g}(m_{\rm g}), \tag{4.7}$$

be the stellar and galaxy density ellipsoidal distributions. By virtue of equation (4.7), the non-negativity condition for the DM component reduces a condition on the parameter $\mathcal{R}$:

$$\rho_{\rm DM}(R,z) \geq 0 \qquad \Leftrightarrow \qquad \mathcal{R} \geq \frac{E_*(m_*)}{E_{\rm g}(m_{\rm g})}, \tag{4.8}$$

where the foregoing inequality must hold at all points of the space, i.e. for $R \geq 0$ and every value of the vertical coordinate z. To better address the problem, we now change variables from (R,z) to $(r\sin\theta, r\cos\theta)$, r being the spherical radius, and ϑ the polar angle, so that

$$m_* = s\,\Omega_*(\vartheta), \qquad m_{\rm g} = s\,\Omega_{\rm g}(\vartheta), \tag{4.9}$$

where s is given in equation (4.2), and the two strictly positive angular functions are defined as

$$\Omega_*^2 \equiv \sin^2\vartheta + \frac{\cos^2\vartheta}{q_*^2}, \qquad \Omega_{\rm g}^2 \equiv \sin^2\vartheta + \frac{\cos^2\vartheta}{q_{\rm g}^2}; \tag{4.10}$$

more precisely, both Ω_*^2 and $\Omega_{\rm g}^2$ are always ≥ 1 for arbitrary values of the axial ratios, and equals unity only in the spherical case $q_* = q_{\rm g} = 1$ (see Fig.).

Thanks to this change of variables, the condition (4.8) becomes

$$\mathcal{R} \geq \mathcal{R}_{\rm m} = \sup_{\mathcal{I}} \mathcal{F}(s,\vartheta), \qquad \mathcal{F}(s,\vartheta) \equiv \frac{E_*(m_*)}{E_{\rm g}(m_{\rm g})}, \tag{4.11}$$

where $\mathcal{I} \equiv \{(s,\vartheta)\,|\,s \geq 0,\ 0 \leq \vartheta \leq \pi/2\}$; notice that we restrict to values of ϑ between 0 and $\pi/2$ since $\mathcal{F}(s,\pi-\vartheta) = \mathcal{F}(s,\vartheta)$. For given values of the model parameters defining the explicit form E_* and $E_{\rm g}$, the dimensionless quantity $\mathcal{R}_{\rm m}$ is the *minimum* value of $\mathcal{R}$ in order to have a nowhere negative DM halo; for this reason, we call *minimum halo* a DM halo of a model with $\mathcal{R} = \mathcal{R}_{\rm m}$. Clearly, if $\mathcal{R}$ decreases slightly below $\mathcal{R}_{\rm m}$, the DM density becomes first negative at the position where $\mathcal{F}(s,\theta) = \mathcal{R}_{\rm m}$.

Fig. 4.4 shows a graphic representation of the set $\mathcal{I}$. Geometrically, the supremum of the two-variable function $\mathcal{F}(s,\theta)$ can be located only:

- at the center, $\mathcal{I}_{\rm c} \equiv \{(s,\vartheta)\,|\,s = 0,\ 0 \leq \vartheta \leq \pi/2\}$;
- at infinity, $\mathcal{I}_\infty \equiv \{(s,\vartheta)\,|\,s = \infty,\ 0 \leq \vartheta \leq \pi/2\}$;
- along the symmetry axis, $\mathcal{I}_0 \equiv \{(s,\vartheta)\,|\,s \geq 0,\ \vartheta = 0\}$;

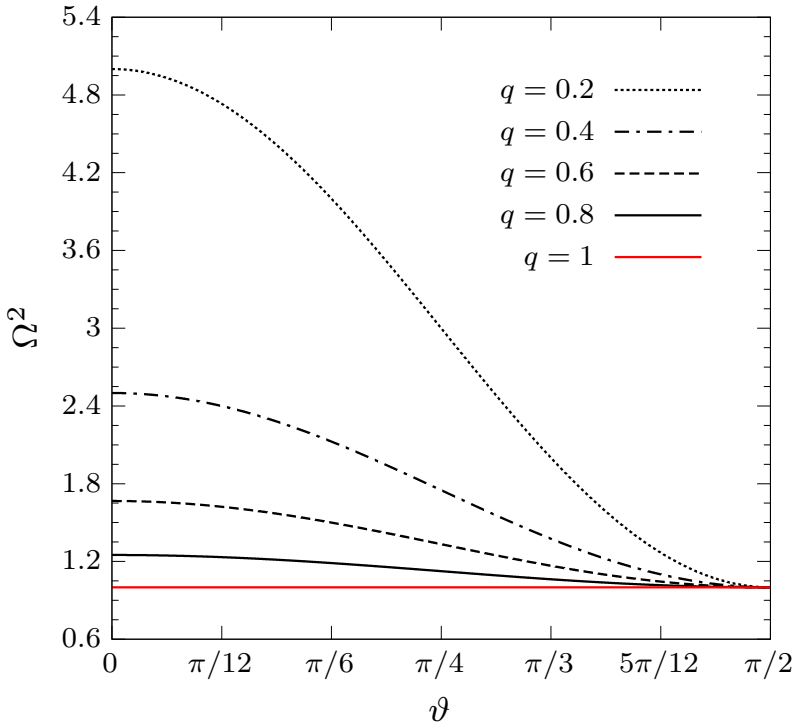

Figure 4.3. Angular profile of $\Omega^2(\vartheta) = \sin^2\vartheta + (\cos^2\vartheta)/q^2$, for different values of the axial ratio q. In the purely spherical case ($q = 1$, red line), $\Omega = 1$; for arbitrary values of $0 < q < 1$ (black lines), the function Ω^2 is always greater than unity. For fixed ϑ, Ω^2 increases for decreasing q.

- on the equatorial plane, $\mathcal{I}_{\frac{\pi}{2}} \equiv \{(s,\vartheta)\,|\,s \geq 0,\ \vartheta = \pi/2\}$;
- in the interior, $\mathrm{int}(\mathcal{I}) \equiv \{(s,\vartheta)\,|\,0 < s < \infty,\ 0 < \vartheta < \pi/2\}$.

By defining

$$\mathcal{R}_{\mathrm{c}} \equiv \sup_{\mathcal{I}_{\mathrm{c}}} \mathcal{F}, \qquad \mathcal{R}_{\infty} \equiv \sup_{\mathcal{I}_{\infty}} \mathcal{F}, \qquad \mathcal{R}_{0} \equiv \sup_{\mathcal{I}_{0}} \mathcal{F}, \qquad \mathcal{R}_{\frac{\pi}{2}} \equiv \sup_{\mathcal{I}_{\frac{\pi}{2}}} \mathcal{F}, \qquad \mathcal{R}_{\mathrm{int}} \equiv \sup_{\mathrm{int}(\mathcal{I})} \mathcal{F}, \tag{4.12}$$

the value of $\mathcal{R}_{\mathrm{m}}$ can be in practice determined as

$$\mathcal{R}_{\mathrm{m}} = \max(\mathcal{R}_{\mathrm{c}}, \mathcal{R}_{\infty}, \mathcal{R}_{0}, \mathcal{R}_{\frac{\pi}{2}}, \mathcal{R}_{\mathrm{int}}); \tag{4.13}$$

of course, $\mathcal{R}_{\mathrm{m}}$ depends strongly not only on the axial ratios q_* and q_{g}, but also on all the other structural parameters of the considered model.

An interesting analytical discussion on the value $\mathcal{R}_{\mathrm{int}}$ can be performed. The possible maximum points on the interior of $\mathcal{I}$ are to be found among the *stationary points* of $\mathcal{F}$, i.e. the points where the two derivatives $\partial\mathcal{F}/\partial s$ and $\partial\mathcal{F}/\partial\vartheta$ vanish simultaneously. According to equations (4.11) and (4.9), we have

$$\frac{\partial\mathcal{F}}{\partial s} = \frac{1}{E_{\mathrm{g}}^2}\left(\Omega_* \frac{dE_*}{dm_*} E_{\mathrm{g}} - \Omega_{\mathrm{g}} \frac{dE_{\mathrm{g}}}{dm_{\mathrm{g}}} E_*\right), \qquad \frac{\partial\mathcal{F}}{\partial\vartheta} = \frac{s}{E_{\mathrm{g}}^2}\left(\frac{d\Omega_*}{d\theta}\frac{dE_*}{dm_*} E_{\mathrm{g}} - \frac{d\Omega_{\mathrm{g}}}{d\theta}\frac{dE_{\mathrm{g}}}{dm_{\mathrm{g}}} E_*\right), \tag{4.14}$$

so that we have to focus on the solutions (s,ϑ), with $s > 0$ and $0 < \vartheta < \pi/2$, of the following system:

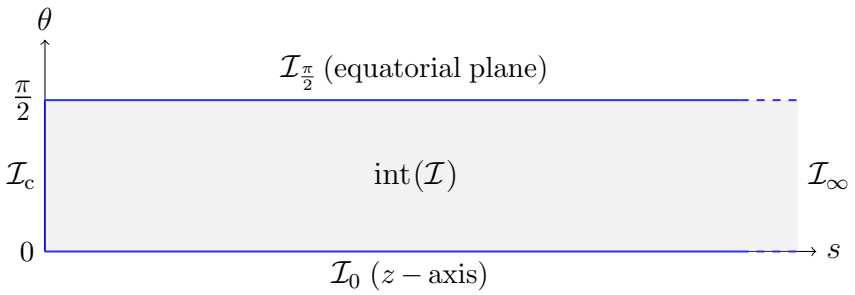

Figure 4.4. Illustration of the region $\mathcal{I}$ over which the function $\mathcal{F}(s,\vartheta)$ must be maximized in order to guarantee non-negativity of the DM density distribution $\rho_{\rm DM} = \mathcal{R}E_{\rm g}(m_{\rm g}) - E_*(m_*)$. The range of the polar angle ϑ is restricted to $[0,\pi/2]$ since $\mathcal{F}(s,\vartheta) = \mathcal{F}(s,\pi-\vartheta)$.

$$\begin{cases} \Omega_* \dfrac{dE_*}{dm_*} E_{\rm g} = \Omega_{\rm g} \dfrac{dE_{\rm g}}{dm_{\rm g}} E_*, \\ \dfrac{d\Omega_*}{d\theta} \dfrac{dE_*}{dm_*} E_{\rm g} = \dfrac{d\Omega_{\rm g}}{d\theta} \dfrac{dE_{\rm g}}{dm_{\rm g}} E_*. \end{cases} \tag{4.15}$$

If the first equation, corresponding to $\partial\mathcal{F}/\partial s = 0$, is not satisfied in the interior of $\mathcal{I}$, there is nothing to prove. So, let us assume that the first identity is satisfied somewhere in $\mathrm{int}(\mathcal{I})$. Then, for non-negative and monotonically decreasing density distributions, it is easy to show that the second equation reduces to

$$\Omega_* \frac{d\Omega_{\rm g}}{d\vartheta} = \Omega_{\rm g} \frac{d\Omega_*}{d\vartheta}, \tag{4.16}$$

i.e., according to equation (4.10),

$$\left(\sin^2\vartheta + \frac{\cos^2\vartheta}{q_*^2}\right)\left(1 - \frac{1}{q_{\rm g}^2}\right) = \left(\sin^2\vartheta + \frac{\cos^2\vartheta}{q_{\rm g}^2}\right)\left(1 - \frac{1}{q_*^2}\right). \tag{4.17}$$

It is evident that, for $q_* \neq q_{\rm g}$, there are no solutions for $0 < \vartheta < \pi/2$. We are then left with the case $q_* = q_{\rm g}$; in this circumstance, the two equations of the system (4.15) become of course coincident. Therefore, $\mathcal{R}_{\rm int}$ must be determined by imposing the condition $q_* = q_{\rm g}$. Notice that, since $m_* = m_{\rm g}$ when $q_* = q_{\rm g}$, the problem *formally* reduces to the the study of the non-negativity in the spherically symmetric case.

The case of JJe models

We shall now apply the previous considerations to the case of the JJe models. Since Jaffe's model belongs to the family of γ models (Dehnen 1993; Tremaine et al. 1994), it can be useful to extend our discussion to the ellipsoidal generalization of the spherical two-component γ models (see CZ18), for which the stellar and galaxy distributions are defined in our notation as

$$E_*(m_*) = \frac{\rho_{\rm n}}{q_* m_*^\gamma (1+m_*)^{4-\gamma}} \qquad E_{\rm g}(m_{\rm g}) = \frac{\rho_{\rm n}\,\xi}{q_{\rm g} m_{\rm g}^\gamma (\xi+m_{\rm g})^{4-\gamma}} \tag{4.18}$$

with $0 \leq \gamma < 3$; clearly, the JJe models are obtained just by setting $\gamma = 2$. As a consequence, the function $\mathcal{F}$ appearing in equation (4.11) reads

$$\mathcal{F}(s,\vartheta) = \frac{q_{\rm g}}{q_*\xi}\left(\frac{\Omega_{\rm g}}{\Omega_*}\right)^{\gamma}\left(\frac{\xi + s\,\Omega_{\rm g}}{1 + s\,\Omega_*}\right)^{4-\gamma}, \tag{4.19}$$

where the relations (4.9) have been used.

We start with the discussion of the non-negativity condition on the boundary of $\mathcal{I}$ (see Fig. 4.4). Along $\mathcal{I}_{\rm c}$, $\mathcal{R}_{\rm c}$ corresponds to the supremum of the function

$$\mathcal{F}(0,\vartheta) = \xi^{3-\gamma}\,\frac{q_{\rm g}}{q_*}\left(\frac{\Omega_{\rm g}}{\Omega_*}\right)^{\gamma}, \qquad \left(0 \le \vartheta \le \frac{\pi}{2}\right). \tag{4.20}$$

The first derivative of $\mathcal{F}(0,\vartheta)$ with respect to ϑ reads

$$\frac{d\mathcal{F}(0,\vartheta)}{d\vartheta} = \frac{\gamma\xi^{3-\gamma}}{2q_*q_{\rm g}}\frac{\Omega_{\rm g}^{\gamma-2}}{\Omega_*^{\gamma+2}}\left(\frac{q_{\rm g}^2}{q_*^2} - 1\right)\sin 2\vartheta = f(\vartheta)(q_{\rm g}^2 - q_*^2), \tag{4.21}$$

where evidently $f(\vartheta) \ge 0$ for each value of ϑ in the considered interval. As a consequence: for $q_* < q_{\rm g}$, the maximum is reached at $\vartheta = \pi/2$, where the ratio $\Omega_{\rm g}/\Omega_*$ equals unity; for $q_* = q_{\rm g}$, $\Omega_* = \Omega_{\rm g}$, so that $\mathcal{F}$ assumes the constant value $\xi^{3-\gamma}$; for $q_* > q_{\rm g}$, the maximum is reached at $\vartheta = 0$, where $\Omega_{\rm g}/\Omega_*$ equals $q_*/q_{\rm g}$. Therefore, combining all these results we find

$$\mathcal{R}_{\rm c} = \xi^{3-\gamma}\,\frac{q_{\rm g}}{q_*}\max\left(1, \frac{q_*^{\gamma}}{q_{\rm g}^{\gamma}}\right). \tag{4.22}$$

On the sets $\mathcal{I}_{\infty}$, $\mathcal{I}_0$, and $\mathcal{I}_{\frac{\pi}{2}}$, the function $\mathcal{F}$ reduces instead respectively to

$$\mathcal{F}(\infty,\vartheta) = \frac{q_{\rm g}}{q_*\xi}\left(\frac{\Omega_{\rm g}}{\Omega_*}\right)^{4}, \qquad \mathcal{F}(s,0) = \frac{q_*^3}{q_{\rm g}^3\xi}\left(\frac{\xi q_{\rm g} + s}{q_* + s}\right)^{4-\gamma}, \qquad \mathcal{F}\left(s,\frac{\pi}{2}\right) = \frac{q_{\rm g}}{q_*\xi}\left(\frac{\xi + s}{1 + s}\right)^{4-\gamma}, \tag{4.23}$$

where $\mathcal{F}(\infty,\vartheta)$ is defined for $0 \le \vartheta \le \pi/2$, while $\mathcal{F}(s,0)$ and $\mathcal{F}(s,\pi/2)$ are defined for $s \ge 0$. By perform an analysis similar to that used to obtain $\mathcal{R}_{\rm c}$, one finds

$$\mathcal{R}_{\infty} = \frac{q_{\rm g}}{q_*\xi}\max\left(1, \frac{q_*^4}{q_{\rm g}^4}\right), \qquad \mathcal{R}_0 = \frac{q_*^3}{q_{\rm g}^3\xi}\max\left(1, \frac{q_{\rm g}^{4-\gamma}\xi^{4-\gamma}}{q_*^{4-\gamma}}\right), \qquad \mathcal{R}_{\frac{\pi}{2}} = \frac{q_{\rm g}}{q_*\xi}\max\left(1, \xi^{4-\gamma}\right). \tag{4.24}$$

The discussion of the non-negativity condition on the boundary of $\mathcal{I}$ is then completed.

Finally, we consider $\mathrm{int}(\mathcal{I})$, and, according to equation (4.15), only for $q_* = q_{\rm g}$. Under this condition, the study of equation (4.19) is trivial, and it shows that no critical ponits (s,ϑ), with $s > 0$ and $0 < \vartheta < \pi/2$, are found, unless for the special case $\xi = 1$, for which $\mathcal{F}$ equals unity.

Summarising, by combining all the previous results, the condition for having a nowhere negative DM profile can be written for the JJe models ($\gamma = 2$) as

$$\mathcal{R}_{\rm m} = \begin{cases} \dfrac{q_{\rm g}}{q_*}\max\left(\dfrac{1}{\xi}, \xi\right), & q_* \le q_{\rm g}, \\[2ex] \dfrac{q_*}{q_{\rm g}}\max\left(\dfrac{q_*^2}{q_{\rm g}^2\xi}, \xi\right), & q_* \ge q_{\rm g}. \end{cases} \tag{4.25}$$

For example, for a JJe model with $q_* = 0.7$, $q_{\rm g} = 1$, and $\xi = 2$, it is found that $\mathcal{R}_{\rm m} = 20/7$, so that the DM distribution in Fig. (4.2), for which $\mathcal{R} = 3$, does not take negative values anywhere.

The case of J3e models

For J3e models, the functions E_* and E_g defining the stellar and galaxy profiles are given by

$$E_*(m_*) = \frac{\rho_\mathrm{n}}{q_* m_*^2 (1+m_*)^2} \qquad E_\mathrm{g}(m_\mathrm{g}) = \frac{\rho_\mathrm{n}}{q_\mathrm{g} m_\mathrm{g}^2 (\xi + m_\mathrm{g})}, \tag{4.26}$$

so that equation (4.19) is now replaced by

$$\mathcal{F}(s,\theta) = \frac{q_\mathrm{g}}{q_*}\left(\frac{\Omega_\mathrm{g}}{\Omega_*}\right)^2 \frac{\xi + s\,\Omega_\mathrm{g}}{(1+s\,\Omega_*)^2}. \tag{4.27}$$

On the set $\mathcal{I}_\mathrm{c}$, $\mathcal{R}_\mathrm{c}$ corresponds to the supremum of the function

$$\mathcal{F}(0,\vartheta) = \frac{q_\mathrm{g}\xi}{q_*}\left(\frac{\Omega_\mathrm{g}}{\Omega_*}\right)^2, \qquad \left(0 \le \vartheta \le \frac{\pi}{2}\right), \tag{4.28}$$

which is identical to $\mathcal{F}(0,\vartheta)$ in equation (4.20) for $\gamma = 2$, so that, in analogy with equation (4.22),

$$\mathcal{R}_\mathrm{c} = \frac{q_\mathrm{g}\xi}{q_*}\max\left(1, \frac{q_*^2}{q_\mathrm{g}^2}\right). \tag{4.29}$$

For what concerns $\mathcal{I}_\infty$, as in J3e models the total density profile decreases more slowly than the stellar density for $s \to \infty$, positivity at large radii is assured independently of the value of $\mathcal{R}$, so that formally $\mathcal{R}_\infty = 0$. On the sets $\mathcal{I}_0$ and $\mathcal{I}_{\frac{\pi}{2}}$, the function $\mathcal{F}$ reduces instead respectively to

$$\mathcal{F}(s,0) = \frac{q_*^3}{q_\mathrm{g}^2}\frac{q_\mathrm{g}\xi + s}{(q_* + s)^2}, \qquad \mathcal{F}\left(s,\frac{\pi}{2}\right) = \frac{q_\mathrm{g}}{q_*}\frac{\xi + s}{(1+s)^2}, \tag{4.30}$$

where both functions are defined for $s \ge 0$. A simple study of these radial function yields

$$\mathcal{R}_0 = \frac{q_*^3}{q_\mathrm{g}^2} \times \begin{cases} \dfrac{1}{4(q_* - q_\mathrm{g}\xi)}, & \xi \le \dfrac{q_*}{2q_\mathrm{g}}, \\[2ex] \dfrac{q_\mathrm{g}\xi}{q_*^2}, & \xi \ge \dfrac{q_*}{2q_\mathrm{g}}, \end{cases} \qquad \mathcal{R}_{\frac{\pi}{2}} = \frac{q_\mathrm{g}}{q_*} \times \begin{cases} \dfrac{1}{4(1-\xi)}, & \xi \le \dfrac{1}{2}, \\[2ex] \xi, & \xi \ge \dfrac{1}{2}; \end{cases} \tag{4.31}$$

Notice that, in the special case $q_* = q_\mathrm{g}$, the two values above coincide.

For what concerns the positivity in the interior of $\mathcal{I}$, the only case to be considered is $q_* = q_\mathrm{g}$. It is easy to show that $\mathcal{F}$ has no critical points in $\mathrm{int}(\mathcal{I})$ when $\xi \ge 1/2$; for $\xi < 1/2$, instead, $\mathcal{R}_\mathrm{int} = 1/[4(1-\xi)]$.

Summarising, in the case of the J3e models we can combine the previous results as follows:

- $q_* \neq q_\mathrm{g}$: $\mathcal{R}_\mathrm{m} = \max(\mathcal{R}_\mathrm{c}, \mathcal{R}_0, \mathcal{R}_{\frac{\pi}{2}})$;
- $q_* = q_\mathrm{g}$: $\mathcal{R}_\mathrm{m} = \begin{cases} \dfrac{1}{4(1-\xi)}, & \xi \le \dfrac{1}{2}, \\[2ex] \xi, & \xi \ge \dfrac{1}{2}. \end{cases}$

As expected, the non-negativity condition in the case $q_* = q_\mathrm{g}$ coincides with that obtained for spherical J3 models in CMP19. For a J3e model with $q_* = 0.7$, $q_\mathrm{g} = 1$, and $\xi = 2$, it is found that $\mathcal{R}_\mathrm{m} = 20/7$, equal to the value of $\mathcal{R}_\mathrm{m}$ for a JJe model with the same parameters; therefore, even in this case the non-negativity of the DM distribution shown in Fig. (4.2) is assured.

4.3 Expansion for small flattenings

Before proceeding with the explicit calculation of the expansion of the density distributions and gravitational potential for "small" values of the flattenings $\eta_* \equiv 1 - q_*$ and $\eta_{\rm g} \equiv 1 - q_{\rm g}$, we must remember that *the expansion of a generic nowhere negative function, such as a typical density profile of a stellar system, does not produce necessarily a nowhere negative expanded function.* As we have seen in the previous Chapter, the non-negativity condition (3.30) provides in fact an upper limit to the possible values of the expansion parameter, i.e. the flattening. Thus, let us see for which values of η_* and $\eta_{\rm g}$ we can be sure to obtain physically acceptable densities.

As a starting point, we write the stellar density (4.3) as it appears in equation (3.2), putting in evidence the density scale $\rho_{\rm n}$ and the axial ratio q_*:

$$\rho_*(R,z) = \rho_{\rm n}\frac{\tilde{\rho}_*(m_*)}{q_*}, \qquad \tilde{\rho}_*(m_*) \equiv \frac{1}{m_*^2(1+m_*)^2}. \tag{4.32}$$

Since the Jaffe model belongs to the family of γ-model (obtained for $\gamma = 2$), according to the discussion at the end of § 3.2, $A_M = 4$. Therefore, to have a nowhere negative expanded stellar density, the flattening η_* has to satisfy the following inequality: $3\eta_* - 1 \leq 0$.

In analogy with the foregoing equation, the galaxy density (4.4) can be rewritten as

$$\rho_{\rm g}(R,z) = \rho_{\rm n}\mathcal{R}\,\frac{\tilde{\rho}_{\rm g}(m_{\rm g})}{q_{\rm g}}, \qquad \tilde{\rho}_{\rm g}(m_{\rm g}) \equiv \begin{cases} \dfrac{\xi}{m_{\rm g}^2(\xi+m_{\rm g})^2}, & \text{(JJe)}, \\ \\ \dfrac{1}{m_{\rm g}^2(\xi+m_{\rm g})}, & \text{(J3e)}, \end{cases} \tag{4.33}$$

where it must be remembered that the factor $\mathcal{R}$ has a different meaning for the two models. The expression for ρ_* in equation (4.32) can be obtained by setting $\mathcal{R} = \xi = 1$, and $q_{\rm g} = q_*$, in the JJe case of equation (4.33). As a consequence, the following fact will recur frequently in the next Sections, and will serve as a useful check for all the future expanded formulae: *for $\mathcal{R} = \xi = 1$, and $\eta_{\rm g} = \eta_*$, the expression for an arbitrary stellar quantity coincides (for both models) with the corresponding galaxy quantity for JJe models.* Since for JJe models the galaxy density profile is described again by a Jaffe law (with different scale lenght), the condition on $\eta_{\rm g}$ is identical to that on η_*, so that $3\eta_{\rm g} - 1 \leq 0$. Regarding the case of J3e models, according to equation (3.30), simple algebra shows that $A_M = 3$, and so the condition on $\eta_{\rm g}$ reduces to $2\eta_{\rm g} - 1 \leq 0$. Summarising, *in order to have physically acceptable stellar and galaxy densities*, the following restrictions hold:

- JJe: $\eta_* \leq 1/3$ (i.e. $q_* \geq 2/3$), $\eta_{\rm g} \leq 1/3$ (i.e. $q_{\rm g} \geq 2/3$);
- J3e: $\eta_* \leq 1/3$ (i.e. $q_* \geq 2/3$), $\eta_{\rm g} \leq 1/2$ (i.e. $q_{\rm g} \geq 1/2$).

If a galaxy model (JJe or J3e) is characterized by flattenings that do not obey the inequalities above, it means that there may be regions of space in which the corresponding stellar or galaxy density is less than zero: such a model is necessarily to be excluded being physically unacceptable.

4.3.1 The expansion of the density-potential pair

Following Chapter 3, we now set up the construction the JJe and J3e models. For, we start by expanding the stellar and galaxy density-potential pairs (ρ_*, Ψ_*) and $(\rho_{\rm g}, \Psi_{\rm g})$ for both models.

The expansion of the stellar density (4.32), truncated up to the linear order[2] in η_*, can be written in two different formulations: by putting in evidence the vertical coordinate (explicit-

[2] In this first part of the Chapter, any direct expansion or combination of homoeoidally expanded quantities will be always truncated to *linear order* in the flattening.

z formulation), or by making emphasis on the radial coordinate (explicit-R formulation). In practice we have

$$\begin{aligned}\frac{\rho_*(R,z)}{\rho_{\rm n}} &= \tilde{\varrho}_{*0}(s)+\eta_*\tilde{\varrho}_{*1}(s)+\eta_*\tilde{z}^2\tilde{\varrho}_{*2}(s),\\ &= \tilde{\rho}_{*0}(s)+\eta_*\tilde{\rho}_{*1}(s)+\eta_*\tilde{R}^2\tilde{\rho}_{*2}(s),\end{aligned} \tag{4.34}$$

The dimensionless functions $\tilde{\varrho}_{*0}$, $\tilde{\varrho}_{*1}$, and $\tilde{\varrho}_{*2}$, defining the stellar density in the explicit-z formulation and obtained via equations (3.5), are given by

$$\tilde{\varrho}_{*0}(s)=\tilde{\varrho}_{*1}(s)=\frac{1}{s^2(1+s)^2},\qquad \tilde{\varrho}_{*2}(s)=-\frac{2(1+2s)}{s^4(1+s)^3}, \tag{4.35}$$

while the analogous functions $\tilde{\rho}_{*0}$, $\tilde{\rho}_{*1}$, and $\tilde{\rho}_{*2}$, appearing in the explicit-R formulation and obtained through equation (3.36), read

$$\tilde{\rho}_{*0}(s)=\frac{1}{s^2(1+s)^2},\qquad \tilde{\rho}_{*1}(s)=-\frac{1+3s}{s^2(1+s)^3},\qquad \tilde{\rho}_{*2}(s)=\frac{2(1+2s)}{s^4(1+s)^3}. \tag{4.36}$$

Equation (4.34), in its analytical simplicity, provides then an approximation of the ellipsoidal stellar density distribution when considering small values of η_*, i.e. significantly smaller than the limiting value $\eta_*=1/3$. Fig. 4.5 shows the isodensity contours of the stellar density profile for two different value of the flattening: $\eta_*=0.2$ (left), and $\eta_*=0.3$ (right). Black dashed lines correspond to the ellipsoidal Jaffe model, described by equation (4.32), while red solid lines refer to the homoeoidally expanded Jaffe model, provided by equation (4.34): notice how the outermost expanded contours differ from the elliptical shape as η_* approaches the value 1/3.

In analogy with equation (4.34), the expansion of the galaxy density (4.33) for $\eta_{\rm g}\to 0$ is

$$\begin{aligned}\frac{\rho_{\rm g}(R,z)}{\rho_{\rm n}} &= \mathcal{R}\left[\tilde{\varrho}_{\rm g0}(s)+\eta_{\rm g}\tilde{\varrho}_{\rm g1}(s)+\eta_{\rm g}\tilde{z}^2\tilde{\varrho}_{\rm g2}(s)\right],\\ &= \mathcal{R}\left[\tilde{\rho}_{\rm g0}(s)+\eta_{\rm g}\tilde{\rho}_{\rm g1}(s)+\eta_{\rm g}\tilde{R}^2\tilde{\rho}_{\rm g2}(s)\right],\end{aligned} \tag{4.37}$$

and for simplicity we give only the expressions for the functions appearing in the explicit-R formulation:

$$\tilde{\rho}_{{\rm g}i}({\rm JJe})=\begin{cases}\dfrac{\xi}{s^2(\xi+s)^2}, & (i=0),\\[2ex] -\dfrac{\xi(\xi+3s)}{s^2(\xi+s)^3}, & (i=1),\\[2ex] \dfrac{2\xi(\xi+2s)}{s^4(\xi+s)^3}, & (i=2),\end{cases}\qquad \tilde{\rho}_{{\rm g}i}({\rm J3e})=\begin{cases}\dfrac{1}{s^2(\xi+s)}, & (i=0),\\[2ex] -\dfrac{\xi+2s}{s^2(\xi+s)^2}, & (i=1),\\[2ex] \dfrac{2\xi+3s}{s^4(\xi+s)^2}, & (i=2);\end{cases} \tag{4.38}$$

of course, to find the corresponding functions $\tilde{\varrho}_{{\rm g}i}$ $(i=0,1,2)$, the trasformations in equation (3.36) must be used. As anticipated in the previous Section, the three functions in the JJe case of equation (4.38) coincide with those defining the stellar density given in equation (4.36) when setting $\xi=1$.

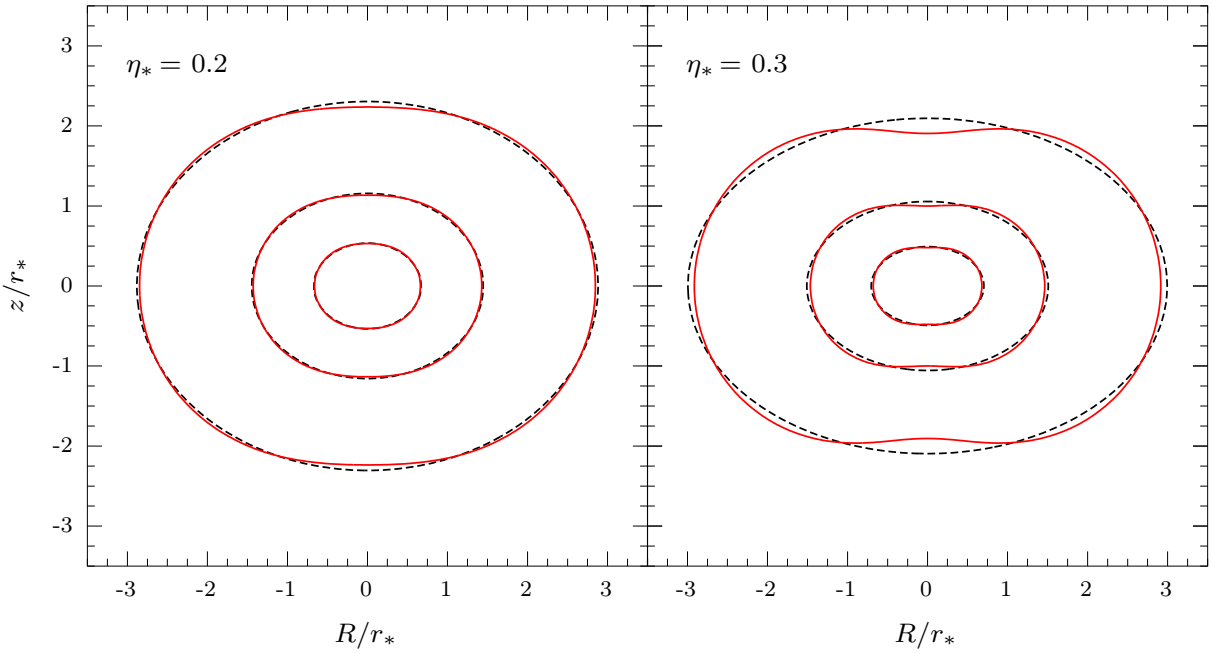

Figure 4.5. Stellar isodensity contours for two values of η_*. Both panels show the comparison between the homeoidally expanded density (red solid line, see equation 4.34) and the true ellipsoidal density (black dashed, see equation 4.3). The densities are normalized to $\rho_{\rm n}$, the lengths to r_*; the contours correspond to values of 1, 10^{-1}, 10^{-2}, from inside to outside.

For what concerns the stellar gravitational potential Ψ_*, as for the associated density distributions, it also can be written in two different formulations when performing the expansion for small stellar flattenings (i.e. $\eta_* \to 0$):

$$\begin{aligned} \frac{\Psi_*(R,z)}{\Psi_{\rm n}} &= \tilde{\psi}_{*0}(s) + \eta_* \tilde{\psi}_{*1}(s) + \eta_* \tilde{z}^2 \tilde{\psi}_{*2}(s), \\ &= \tilde{\Psi}_{*0}(s) + \eta_* \tilde{\Psi}_{*1}(s) + \eta_* \tilde{R}^2 \tilde{\Psi}_{*2}(s). \end{aligned} \tag{4.39}$$

For the stellar component of the JJe and J3e models, by virtue of equation (3.16), elementary integrations show that

$$\tilde{\psi}_{*i}(s) = \begin{cases} \ln \dfrac{1+s}{s}, & (i=0), \\ -\dfrac{s-2}{3s^2} + \dfrac{1}{3} \ln \dfrac{1+s}{s} - \dfrac{2}{3s^3} \ln(1+s), & (i=1), \\ -\dfrac{s+2}{s^4(1+s)} + \dfrac{2}{s^5} \ln(1+s), & (i=2), \end{cases} \tag{4.40}$$

and, thanks again to the transformations (3.36),

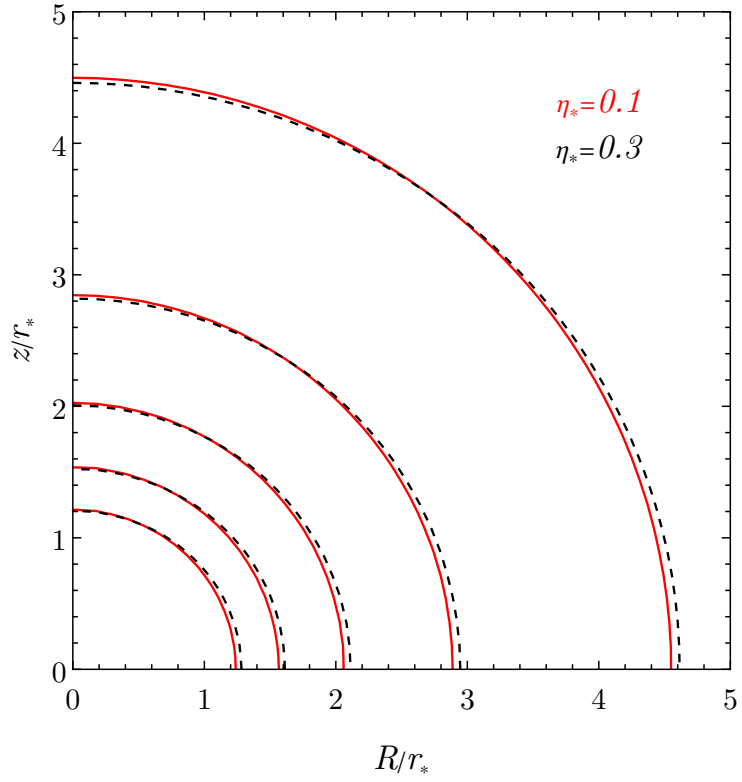

Figure 4.6. Isopotential contours of an *homoeoidally expanded* Jaffe density distribution, defined by equation (4.39), for $\eta_* = 0.1$ (red solid), and $\eta_* = 0.3$ (black dashed). The potentials are normalized to $\Psi_{\rm n}$, the lengths to r_*; the contours correspond to values of 0.2, 0.3, 0.4, 0.5, 0.6, from outside to inside. Note how the increase of η_* inverts the elongation of the contour lines, while still keeping them quite round, even when considering a flattening close to the value 1/3.

$$\tilde{\Psi}_{*i}(s) = \begin{cases} \ln\dfrac{1+s}{s}, & (i=0), \\ -\dfrac{s^2+2s+4}{3s^2(1+s)} + \dfrac{1}{3}\ln\dfrac{1+s}{s} + \dfrac{4}{3s^3}\ln(1+s), & (i=1), \\ \dfrac{s+2}{s^4(1+s)} - \dfrac{2}{s^5}\ln(1+s), & (i=2). \end{cases} \tag{4.41}$$

Further calculations show that the formulae (4.35)-(4.40) and (4.36)-(4.41) obey respectively the linearizations (3.21) and (3.37) of Poisson's equation for the dimensionless stellar density-potential pair. Notice that the homoeoidally expanded stellar potential, as the associated expansion of the density, is written in terms of elementary functions; in analogy with equation (4.34), equation (4.39) represents an approximation of the ellipsoidal stellar potential for small values of the flattening. It is useful to compare the expanded stellar potential with the "true" potential produced by the ellipsoidal distribution (4.32). For, equation (3.33) must be used: the function $\tilde{F}$, defined in equation (3.9), is easy to compute for a Jaffe distribution, so that Ψ_* is given by

$$\frac{\Psi_*(R,z)}{\Psi_{\rm n}} = \frac{1}{2}\int_0^\infty \left(\ln\frac{1+m_u}{m_u} - \frac{1}{1+m_u}\right)\frac{du}{(1+u)\sqrt{q_*^2+u}}, \qquad m_u^2 = \frac{\tilde{R}^2}{1+u} + \frac{\tilde{z}^2}{q_*^2+u}. \tag{4.42}$$

The foregoing equation gives an idea of how mathematically difficult the determination of the

potential for an ellipsoidal distribution can be, even for a "simple" case such as that of a Jaffe profile; in this view, it is quite clear that the homoeoidal expansion offers the advantage of working with a potential having a much simpler and more tractable mathematical structure. In Fig. 4.6 we show the contour lines of the expanded potential Ψ_*, given by equation (4.39), in the meridional plane, for two values of the flattening: $\eta_* = 0.1$ (red solid) and $\eta_* = 0.3$ (black dashed). It is then evident that the two families of isopotential curves (red and black) are quite similar; however, note how a higher value of the flattening reverses the elongation of the contours, while keeping them sufficiently round.

In analogy with equation (4.41), the expansion of the galaxy potential Ψ_g for $\eta_\mathrm{g} \to 0$ reads

$$\begin{aligned} \frac{\Psi_\mathrm{g}(R,z)}{\Psi_\mathrm{n}} &= \mathcal{R}\left[\tilde{\psi}_{\mathrm{g}0}(s) + \eta_\mathrm{g}\tilde{\psi}_{\mathrm{g}1}(s) + \eta_\mathrm{g}\tilde{z}^2\tilde{\psi}_{\mathrm{g}2}(s)\right], \\ &= \mathcal{R}\left[\tilde{\Psi}_{\mathrm{g}0}(s) + \eta_\mathrm{g}\tilde{\Psi}_{\mathrm{g}1}(s) + \eta_\mathrm{g}\tilde{R}^2\tilde{\Psi}_{\mathrm{g}2}(s)\right]. \end{aligned} \tag{4.43}$$

Also for the galaxy component, all the dimensionless functions $\tilde{\psi}_{\mathrm{g}i}$ and $\tilde{\Psi}_{\mathrm{g}i}$ $(i = 0, 1, 2)$ are elementary, for both JJe and J3e models; in particular, in the explicit-R formulation we find

$$\tilde{\Psi}_{\mathrm{g}i}(\mathrm{JJe}) = \begin{cases} \dfrac{1}{\xi}\ln\dfrac{\xi+s}{s}, & (i=0), \\ -\dfrac{s^2+2\xi s+4\xi^2}{3s^2(\xi+s)} + \dfrac{1}{3\xi}\ln\dfrac{\xi+s}{s} + \dfrac{4\xi^2}{3s^3}\ln\dfrac{\xi+s}{\xi}, & (i=1), \\ \dfrac{\xi(s+2\xi)}{s^4(\xi+s)} - \dfrac{2\xi^2}{s^5}\ln\dfrac{\xi+s}{\xi}, & (i=2), \end{cases} \tag{4.44}$$

and

$$\tilde{\Psi}_{\mathrm{g}i}(\mathrm{J3e}) = \begin{cases} \dfrac{1}{\xi}\ln\dfrac{\xi+s}{s} + \dfrac{1}{s}\ln\dfrac{\xi+s}{\xi}, & (i=0), \\ -\dfrac{s-2\xi}{3s^2} + \dfrac{1}{3\xi}\ln\dfrac{\xi+s}{s} - \dfrac{2\xi^2}{3s^3}\ln\dfrac{\xi+s}{\xi}, & (i=1), \\ \dfrac{s-2\xi}{2s^4} + \dfrac{\xi^2}{s^5}\ln\dfrac{\xi+s}{\xi}, & (i=2); \end{cases} \tag{4.45}$$

as usual, the corresponding $\tilde{\psi}_{\mathrm{g}i}$ $(i = 0, 1, 2)$ ca be obtained from (4.44) and (4.45) just by applying the trasformations (3.36). Also in this case, equations (4.38)-(4.44) and (4.38)-(4.45) have been verified to satisfy the linearized Poisson equation (3.37). Again, notice that equations (4.44) and (4.41) coincide for $\xi = 1$.

4.4 The circular velocity of JJe and J3e models

A useful quantity to characterize the total potential is the circular velocity $v_\mathrm{c}(R)$ in the equatorial plane $z = 0$. By definition (see § 2.2), the contribution of the galaxy to v_c is given by

$$v_\mathrm{g}^2(R) = -R\left(\frac{\partial\Psi_\mathrm{g}}{\partial R}\right)_{z=0}. \tag{4.46}$$

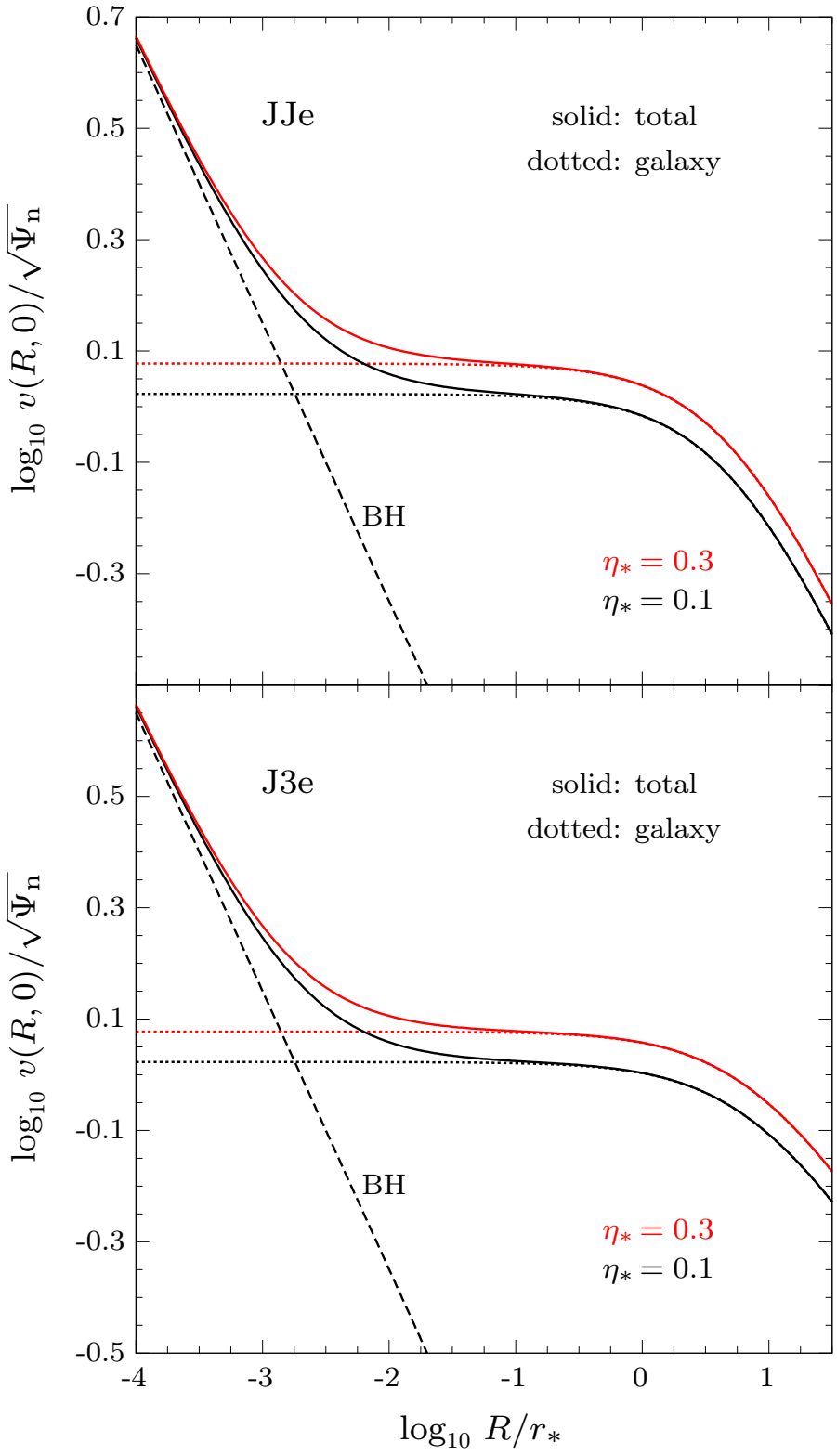

Figure 4.7. Trend of $v_c(R)$ for two minimum halo models with $\xi = 5$, $\eta_g = 0$, and $\mu = 2 \times 10^{-3}$, for JJe (top) and J3e (bottom) models. Black solid line shows the quite flat case with $\eta_* = 0.1$, red solid line refer to the $\eta_* = 0.3$ case; the corresponding dotted lines show the contribution of the galaxy, while black dashed line (independently of the stellar and galaxy flattenings) refers to the BH contribution. Over the whole radial range, v_c increases for increasing η_* at fixed R; for $R \lesssim 0.1\, r_*$, and in absence of the central BH, v_c reduces to a constant value strongly dependent on η_*. Notice that, inside a radius $R \simeq r_*$, the behaviour of v_c is almost identical for both models, while for fixed $R \gtrsim r_*$ the J3e models lead to higher circular velocities than those corresponding to the JJe models.

Now, following Chapter (3), the foregoing equation can be rewritten as

$$\frac{v_{\rm g}^2(R)}{\Psi_{\rm n}} = \mathcal{R}\left[\tilde{v}_{\rm g0}^2(\tilde{R}) + \eta_{\rm g}\tilde{v}_{\rm g1}^2(\tilde{R})\right], \qquad \tilde{v}_{{\rm g}i}^2(\tilde{R}) \equiv -\tilde{R}\,\frac{d\tilde{\psi}_{{\rm g}i}(\tilde{R})}{d\tilde{R}}, \tag{4.47}$$

and, for our models, we find

$$\text{JJe:}\quad \tilde{v}_{\rm g0}^2(\tilde{R}) = \frac{1}{\xi+\tilde{R}}, \qquad \tilde{v}_{\rm g1}^2(\tilde{R}) = \frac{\xi(\tilde{R}+2\xi)}{\tilde{R}^2(\xi+\tilde{R})} - \frac{2\xi^2}{\tilde{R}^3}\ln\frac{\xi+\tilde{R}}{\xi}, \tag{4.48}$$

and

$$\text{J3e:}\quad \tilde{v}_{\rm g0}^2(\tilde{R}) = \frac{1}{\tilde{R}}\ln\frac{\xi+\tilde{R}}{\xi}, \qquad \tilde{v}_{\rm g1}^2(\tilde{R}) = \frac{\tilde{R}-2\xi}{2\tilde{R}^2} + \frac{\xi^2}{\tilde{R}^3}\ln\frac{\xi+\tilde{R}}{\xi}. \tag{4.49}$$

Of course, to obtain the component of $v_{\rm c}$ due only to the stars, it is sufficient to replace $\Psi_{\rm g}$ with Ψ_* in equation (4.46); as a consequence, in analogy with equation (4.47), we have

$$\frac{v_*^2(R)}{\Psi_{\rm n}} = \tilde{v}_{*0}^2(\tilde{R}) + \eta_*\tilde{v}_{*1}^2(\tilde{R}), \qquad \tilde{v}_{*i}^2(\tilde{R}) \equiv -\tilde{R}\,\frac{d\tilde{\psi}_{*i}(\tilde{R})}{d\tilde{R}}, \tag{4.50}$$

where

$$\tilde{v}_{*0}^2(\tilde{R}) = \frac{1}{1+\tilde{R}}, \qquad \tilde{v}_{*1}^2(\tilde{R}) = \frac{\tilde{R}+2}{\tilde{R}^2(1+\tilde{R})} - \frac{2}{\tilde{R}^3}\ln(1+\tilde{R}), \tag{4.51}$$

which can also be obtained by setting $\xi = 1$ in equation (4.48).

Finally, as anticipated at the beginning of the Chapter, a BH of mass $M_{\rm BH}$ is added at the centre of both models. As a result, the total gravitational potential $\Psi_{\rm T}$ is obtained just by adding to $\Psi_{\rm g}$ the contribution of a point mass:

$$\Psi_{\rm T}(R,z) = \Psi_{\rm g}(R,z) + \Psi_{\rm BH}(r), \tag{4.52}$$

where $\Psi_{\rm BH}(r) = GM_{\rm BH}/r$. Therefore, the circular velocity $v_{\rm c}$ in presence of the BH becomes

$$v_{\rm c}^2(R) = v_{\rm g}^2(R) + v_{\rm BH}^2(R), \tag{4.53}$$

where $v_{\rm BH}^2(R) = GM_{\rm BH}/R$. The trend of $v_{\rm c}(R)$ is shown in Fig. 4.7 (solid lines) for two minimum halo models with $\xi = 5$, $\eta_{\rm g} = 0$, and with $\mu \equiv M_{\rm BH}/M_* = 0.002$ (see Kormendy & Ho 2013 for this choice of μ); black lines show the case $\eta_* = 0.10$, red lines refer to the $\eta_* = 0.30$ case. Over the whole radial range, $v_{\rm c}$ increases for increasing η_* at fixed R; in the inner regions (in practice, for $R \lesssim 0.1\,r_*$), and in absence of the central BH, $v_{\rm c}$ reduces instead to a constant value strongly dependent on η_*. This might seem inconsistent the expression for $\Psi_{\rm g}$ in (4.47), which in principle is independent on η_*. Moreover, the model we show in Fig. 4.7 is a minimum halo model, so that in this case $v_{\rm c}$ depends on η_* via $\mathcal{R} = \mathcal{R}_{\rm m}$. Furthermore, notice that, inside a radius $R \simeq r_*$, the behaviour of $v_{\rm c}$ is almost identical for both models, while for $R \gtrsim r_*$ the rotation curve at large radii is higher in the J3e models than for the JJe models; this is not surprising, considering the different asymptotic trends of the density profile for large distances from the centre of the system. We shall return on this point in the next Section.

4.5 The asymptotic behaviours of the structural properties

Let us now analyze the asymptotic behaviour of the main structural properties of the JJe and J3e models for small and large distances from the centre; these are the stellar and galaxy density, the stellar and galaxy potential, and the circular velocity.

A preliminary consideration can be done without going into mathematical details. The stellar component is the same for both models; consequently, of course, the stellar density and potential have the same asymptotic trend both at small and large radii, independently of the considered model. For what concernes the galaxy component, instead, $\rho_{\rm g} \propto 1/m_{\rm g}^2$ at the centre of both JJe and J3e models. In other words, in the inner regions of both models, the stars follows the same identical distribution, while the galaxy distribution decreases with the same ellipsoidal behaviour; thus, we should expect for the two models *a very similar behaviour in the central regions, and major differences only in the outer regions.*

4.5.1 The inner regions

To find the central behaviour of the stellar density and potential, we expand equations (4.34) and (4.39) for $R \to 0$ and $z \to 0$. At the leading order, such expansions are

$$\frac{\rho_*}{\rho_{\rm n}} \sim \frac{1}{s^2}\left(1+\eta_* - \frac{2\eta_*\tilde{z}^2}{s^2}\right), \qquad \frac{\Psi_*}{\Psi_{\rm n}} \sim -\frac{3+\eta_*}{3}\ln s, \tag{4.54}$$

of course identical for JJe and J3e models[3]. The potential Ψ_* is basically spherically symmetric in the central regions, and this explains the contour lines in Fig. 4.6, which are quite round even for distances from the centre larger than the stellar scale length.

The corresponding expansions for the galaxy density and potential are given by

$$\frac{\rho_{\rm g}}{\rho_{\rm n}} \sim \frac{\mathcal{R}}{\xi s^2}\left(1+\eta_{\rm g} - \frac{2\eta_{\rm g}\tilde{z}^2}{s^2}\right), \qquad \frac{\Psi_{\rm g}}{\Psi_{\rm n}} \sim -\mathcal{R}\frac{3+\eta_{\rm g}}{3\xi}\ln s, \tag{4.55}$$

again for both models, which as expected reduce to (4.54) when fixing $\mathcal{R} = \xi = 1$ and $\eta_{\rm g} = \eta_*$. Finally, the asymptotic behaviour of the circular velocity, given in equation (4.47), reads

$$\frac{v_{\rm g}^2}{\Psi_{\rm n}} \sim \mathcal{R}\frac{3+\eta_{\rm g}}{3\xi}; \tag{4.56}$$

notice that this expression can be verified by inserting the expansion of $\Psi_{\rm g}$ in the general definition for $v_{\rm g}$, and considering only the leading order term. In practice, for distances from the centre sufficiently small, $v_{\rm c}$ reduces to a constant depending on the model parameters. This fact explains the trend of the dotted lines in Fig. 4.7 for small values of R. In both panels we plot minimum halo models, i.e. $\mathcal{R} = \mathcal{R}_{\rm m}$; in particular, for both models, $\mathcal{R}_{\rm m} = 50/9$ for $\eta_* = 0.1$ (black), whereas $\mathcal{R}_{\rm m} = 50/7$ when $\eta_* = 0.3$ (red). As $\eta_{\rm g} = 0$, the circular velocity at the centre is given by

$$\frac{v_{\rm g}(0)}{\sqrt{\Psi_{\rm n}}} = \sqrt{\frac{\mathcal{R}_{\rm m}}{\xi}} \simeq \begin{cases} 1.05, & (\eta_* = 0.1), \\ 1.19, & (\eta_* = 0.3). \end{cases} \tag{4.57}$$

[3]Note that the expressions (4.54), as well as all those we shall denote as asymptotic expansions, are in practice the result of a "double expansion": indeed, we expand at small and large radii functions that are themselves expansions for small flattenings of ellipsoidal quantities.

4.5.2 The external regions

At large radii, i.e. for $R \to \infty$ and $z \to \infty$, the expansion of the stellar density and potential is the same for the two models. At the leading order, we have

$$\frac{\rho_*}{\rho_\mathrm{n}} \sim \frac{1}{s^4}\left(1+\eta_* - \frac{4\eta_*\tilde{z}^2}{s^2}\right), \qquad \frac{\Psi_*}{\Psi_\mathrm{n}} \sim \frac{1}{s}. \tag{4.58}$$

For what concerns the galaxy component, the behaviour of the two models is different. Indeed, by expanding equations (4.37) and (4.43) we have

$$\frac{\rho_\mathrm{g}}{\rho_\mathrm{n}} \sim \begin{cases} \dfrac{\mathcal{R}\xi}{s^4}\left(1+\eta_\mathrm{g} - \dfrac{4\eta_\mathrm{g}\tilde{z}^2}{s^2}\right), & \text{(JJe)}, \\[2ex] \dfrac{\mathcal{R}}{s^3}\left(1+\eta_\mathrm{g} - \dfrac{3\eta_\mathrm{g}\tilde{z}^2}{s^2}\right), & \text{(J3e)}, \end{cases} \qquad \frac{\Psi_\mathrm{g}}{\Psi_\mathrm{n}} \sim \begin{cases} \dfrac{\mathcal{R}}{s}, & \text{(JJe)}, \\[2ex] \mathcal{R}\,\dfrac{\ln s}{s}, & \text{(J3e)}; \end{cases} \tag{4.59}$$

note that at variance with the density, the galaxy potential Ψ_g at large radii is spherical, also for the J3e models with their divergent total mass.

In analogy with equation (4.56), the asymptotic behaviour in the external regions of the circular velocity is

$$\frac{v_\mathrm{g}^2}{\Psi_\mathrm{n}} \sim \begin{cases} \dfrac{\mathcal{R}}{\tilde{R}}, & \text{(JJe)}, \\[2ex] \mathcal{R}\,\dfrac{\ln\tilde{R}}{\tilde{R}}, & \text{(J3e)}, \end{cases} \tag{4.60}$$

From Fig. 4.7 it is evident that the radial trend of the circular velocity has a strong dependence on η_*, which in principle is absent in the foregoing equation; however, having plotted minimum halo models, the dependence on the stellar flattening is actually present, and it is contained in the parameter $\mathcal{R} = \mathcal{R}_\mathrm{m}$. For the particular choice of parameters in Fig. 4.7, the circular velocity increases as η_* increases for fixed R, for both JJe and J3e models.

4.6 Internal dynamics of JJe and J3e models

Having analyzed in detail the kinematic structure of the JJe and J3e models, we now proceed to study quantitatively their internal dynamics. Following § 4.6, the fundamental equations with which we are dealing are Jeans's equations, namely,

$$\text{Vertical equation:} \quad \frac{\partial\rho_*\sigma^2}{\partial z} = \rho_*\frac{\partial\Psi_\mathrm{T}}{\partial z}, \tag{4.61}$$

$$\text{Radial equation:} \quad \frac{\partial\rho_*\sigma^2}{\partial R} - \frac{\rho_*\Delta}{R} = \rho_*\frac{\partial\Psi_\mathrm{T}}{\partial R}, \qquad \Delta \equiv \overline{v_\varphi^2} - \sigma^2, \tag{4.62}$$

where Ψ_T is given by equation (4.52), and represents the total potential. The corresponding solutions are given in their integral form just by setting $\rho = \rho_*$ and $\Psi = \Psi_\mathrm{T}$ in equations (2.23) and (2.27), i.e.,

$$\rho_*\sigma^2 = -\int_z^\infty \rho_* \frac{\partial \Psi_\mathrm{T}}{\partial z'}\, dz', \qquad \rho_*\Delta = -R\int_z^\infty \left(\frac{\partial \rho_*}{\partial R}\frac{\partial \Psi_\mathrm{T}}{\partial z'} - \frac{\partial \rho_*}{\partial z'}\frac{\partial \Psi_\mathrm{T}}{\partial R}\right) dz'. \tag{4.63}$$

Since the total potential is now given by the sum of that of the galaxy and that of the central BH, the formulae presented in § 3.3.2 must be slightly generalised.

We begin with the vertical equation. The splitting of the total potential $\Psi_\mathrm{T} = \Psi_\mathrm{g} + \Psi_\mathrm{BH}$ produces an analogous splitting in σ; in practice, the "total" stellar velocity dispersion is given by the following quadrature sum:

$$\sigma^2 = \sigma_\mathrm{g}^2 + \sigma_\mathrm{BH}^2, \qquad \begin{cases} \rho_*\sigma_\mathrm{g}^2 = -\displaystyle\int_z^\infty \rho_* \frac{\partial \Psi_\mathrm{g}}{\partial z'}\, dz', \\ \\ \rho_*\sigma_\mathrm{BH}^2 = -\displaystyle\int_z^\infty \rho_* \frac{\partial \Psi_\mathrm{BH}}{\partial z'}\, dz', \end{cases} \tag{4.64}$$

where σ_g indicates the contribution of the galaxy, and σ_BH that of the central BH. With the density-potential pair given by equations (4.34)-(4.43), by discarding all the quadratic terms in the flattenings (i.e., the mixed terms $\eta_*\eta_\mathrm{g}$) we have

$$\rho_*\frac{\partial \Psi_\mathrm{g}}{\partial z} = \frac{\rho_\mathrm{n}\Psi_\mathrm{n}\mathcal{R}}{a}\frac{z}{r}\left(\tilde{\rho}_{*0}\frac{d\tilde{\Psi}_{\mathrm{g}0}}{ds} + \eta_*\tilde{\rho}_{*1}\frac{d\tilde{\Psi}_{\mathrm{g}0}}{ds} + \eta_*\tilde{R}^2\tilde{\rho}_{*2}\frac{d\tilde{\Psi}_{\mathrm{g}0}}{ds} + \eta_\mathrm{g}\tilde{\rho}_{*0}\frac{d\tilde{\Psi}_{\mathrm{g}1}}{ds} + \eta_\mathrm{g}\tilde{R}^2\tilde{\rho}_{*0}\frac{d\tilde{\Psi}_{\mathrm{g}2}}{ds}\right). \tag{4.65}$$

After performing the integration, we are left with

$$\frac{\rho_*\sigma_\mathrm{g}^2}{\rho_\mathrm{n}\Psi_\mathrm{n}} = \mathcal{R}\left[A(s) + \eta_* B(s) + \eta_*\tilde{R}^2 C(s) + \eta_\mathrm{g} D(s) + \eta_\mathrm{g}\tilde{R}^2 E(s)\right], \tag{4.66}$$

where the dimensionless functions from $A(s)$ to $E(s)$ are defined as

$$A(s) \equiv -\int_s^\infty \tilde{\rho}_{*0}\frac{d\tilde{\Psi}_{\mathrm{g}0}}{ds'}\, ds', \qquad B(s) \equiv -\int_s^\infty \tilde{\rho}_{*1}\frac{d\tilde{\Psi}_{\mathrm{g}0}}{ds'}\, ds', \qquad C(s) \equiv -\int_s^\infty \tilde{\rho}_{*2}\frac{d\tilde{\Psi}_{\mathrm{g}0}}{ds'}\, ds', \tag{4.67}$$

and

$$D(s) \equiv -\int_s^\infty \tilde{\rho}_{*0}\frac{d\tilde{\Psi}_{\mathrm{g}1}}{ds'}\, ds', \qquad E(s) \equiv -\int_s^\infty \tilde{\rho}_{*0}\frac{d\tilde{\Psi}_{\mathrm{g}2}}{ds'}\, ds'. \tag{4.68}$$

Notice that, in presence of a *spherical* galaxy component (i.e., $\eta_\mathrm{g} = 0$), only the functions $A(s)$, $B(s)$ and $C(s)$ occur in the determination of σ_g; if the stellar component is also spherical ($\eta_* = 0$), then the only contribution is given by $A(s)$. *All the previous functions can be expressed in analytical form*, and the corresponding excplicit formulae are given in Appendix B.

By following a similar procedure, the BH contribution to σ can be written, in analogy with equation (4.66), as

$$\frac{\rho_*\sigma_\mathrm{BH}^2}{\rho_\mathrm{n}\Psi_\mathrm{n}} = \mu\left[F(s) + \eta_* G(s) + \eta_*\tilde{R}^2 H(s)\right], \tag{4.69}$$

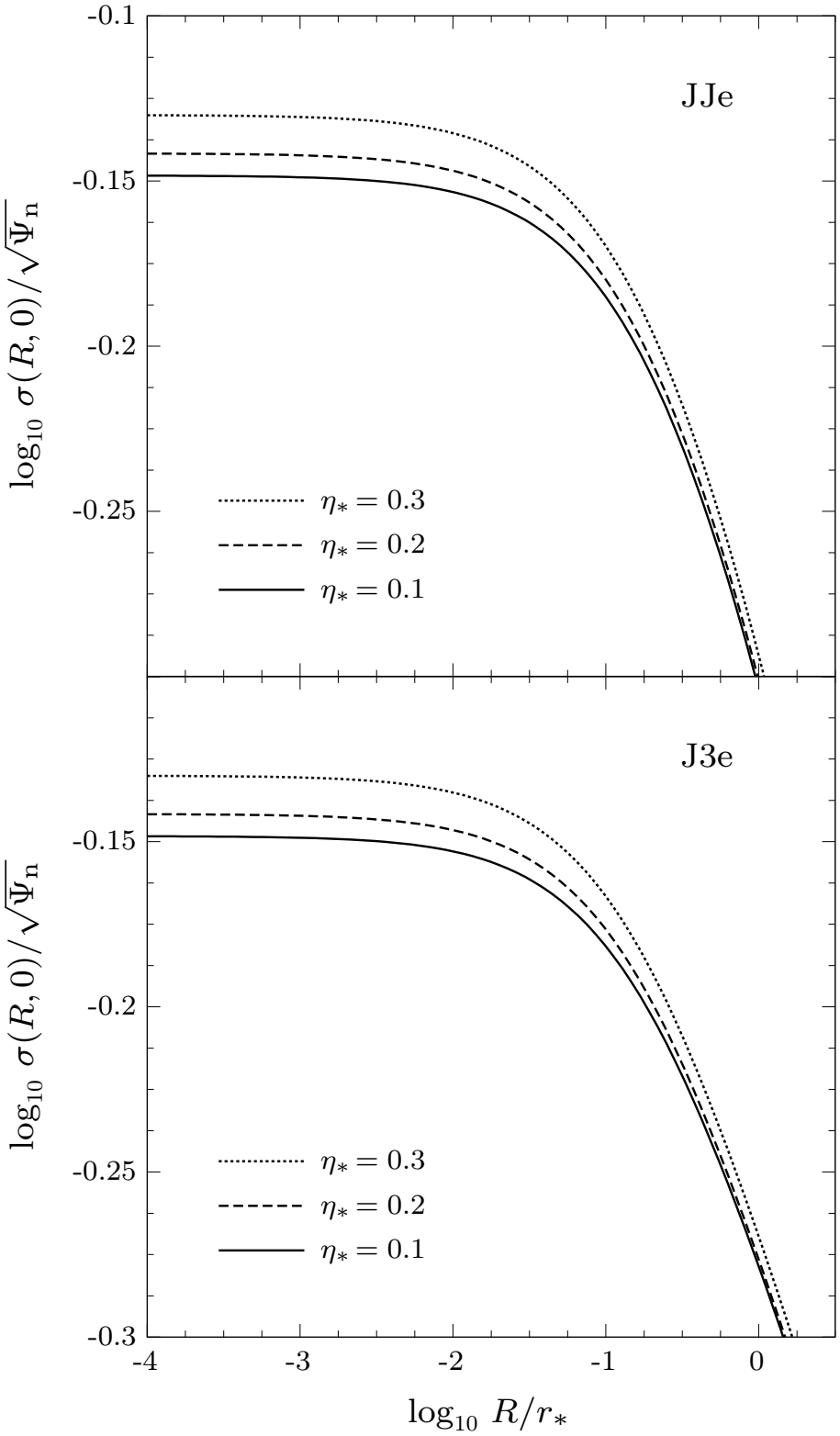

Figure 4.8. Trend of $\sigma(R,0)$ for three minimum halo models with $\xi = 5$, $\eta_g = 0$, and in absence of a central BH, for JJe (top) and J3e (bottom) models. Solid line shows the case $\eta_* = 0.1$ ($\mathcal{R}_m = 50/9$), dashed line the case $\eta_* = 0.2$ ($\mathcal{R}_m = 25/4$), and dotted line the case $\eta_* = 0.3$ ($\mathcal{R}_m = 50/7$). For $R \lesssim 10^{-3}\, r_*$ the velocity dispersion is quite flat, and at the centre it reduces to a η_*-dependent constant value; The global trend is extremely similar for both models in the central regions, and it starts to significantly differ only for $R \gtrsim 0.5\, r_*$: here, for a given distance from the centre, σ_g associated with the J3e models significantly exceeds that corresponding to the JJe models.

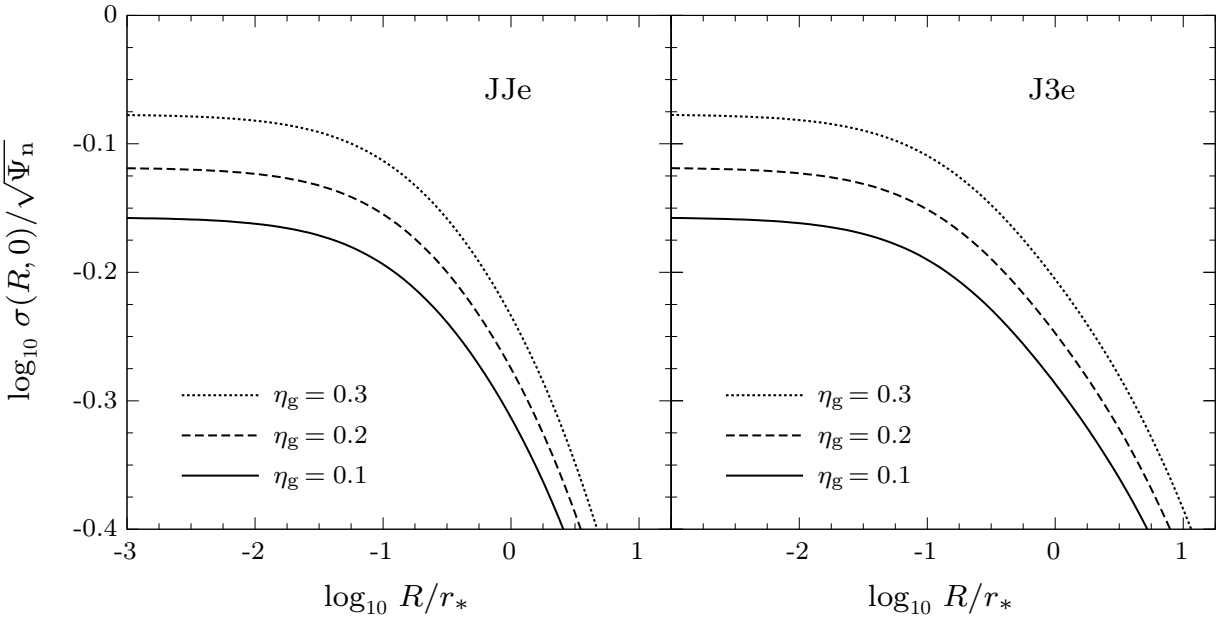

Figure 4.9. Trend of $\sigma(R,0)$ for three minimum halo models with $\xi = 5$, $\eta_* = 0.1$, and in absence of a central BH, for JJe (top) and J3e (bottom) models. Solid line shows the case $\eta_g = 0.1$ ($\mathcal{R}_m = 5$), dashed line the case $\eta_g = 0.2$ ($\mathcal{R}_m = 45/8$), and dotted line the case $\eta_g = 0.3$ ($\mathcal{R}_m = 45/7$); in practice, with respect to the previous figure, the roles of η_* and η_g are now interchanged. It is evident how, for fixed R, a flatter galactic component produces higher velocity dispersion values. Of course, for both models the global trend is identical near the centre, and it starts to differ only for $R \gtrsim 0.1\, r_*$: here, for a given distance from the centre, σ_g associated with the J3e models is greater than that corresponding to the JJe models.

where we have defined

$$F(s) \equiv \int_s^\infty \frac{\tilde{\rho}_{*0}(s')}{s'^2}\, ds', \qquad G(s) \equiv \int_s^\infty \frac{\tilde{\rho}_{*1}(s')}{s'^2}\, ds', \qquad H(s) \equiv \int_s^\infty \frac{\tilde{\rho}_{*2}(s')}{s'^2}\, ds'. \tag{4.70}$$

Clearly, *as the gravitational potential of the BH is a spherically symmetric function, no term must now be discarded.* From equation (4.36), it is easy to recognize that $F(s) \geq 0$, $G(s) \leq 0$, and $H(s) \geq 0$, for all $s \geq 0$: this is not a peculiarity of the JJe and J3e models, but a sort of general behaviour associated to the definitions (4.70). From equations (4.35)-(3.36) it follows indeed that

$$\tilde{\rho}_{*0}(s) = \tilde{\rho}(s), \qquad \tilde{\rho}_{*1}(s) = \tilde{\rho}(s) + s\,\frac{d\tilde{\rho}(s)}{ds}, \qquad \tilde{\rho}_{*2}(s) = -\frac{1}{s}\,\frac{d\tilde{\rho}(s)}{ds}; \tag{4.71}$$

therefore, by assuming a non-negative and monotonically decreasing stellar density, it is readily evident that $F(s) \geq 0$, and $H(s) \geq 0$. Regarding $G(s)$, it would appear that its positivity or negativity depends on the model parameters; an elementary calculation shows in fact that $\tilde{\rho}_{*1}$ is a nowhere negative function if and only if

$$\frac{d\ln\tilde{\rho}(s)}{d\ln s} \geq -1 \qquad (\text{for all } s \geq 0). \tag{4.72}$$

This condition is generally not satisfied by realistic density profiles, so that we can reasonably

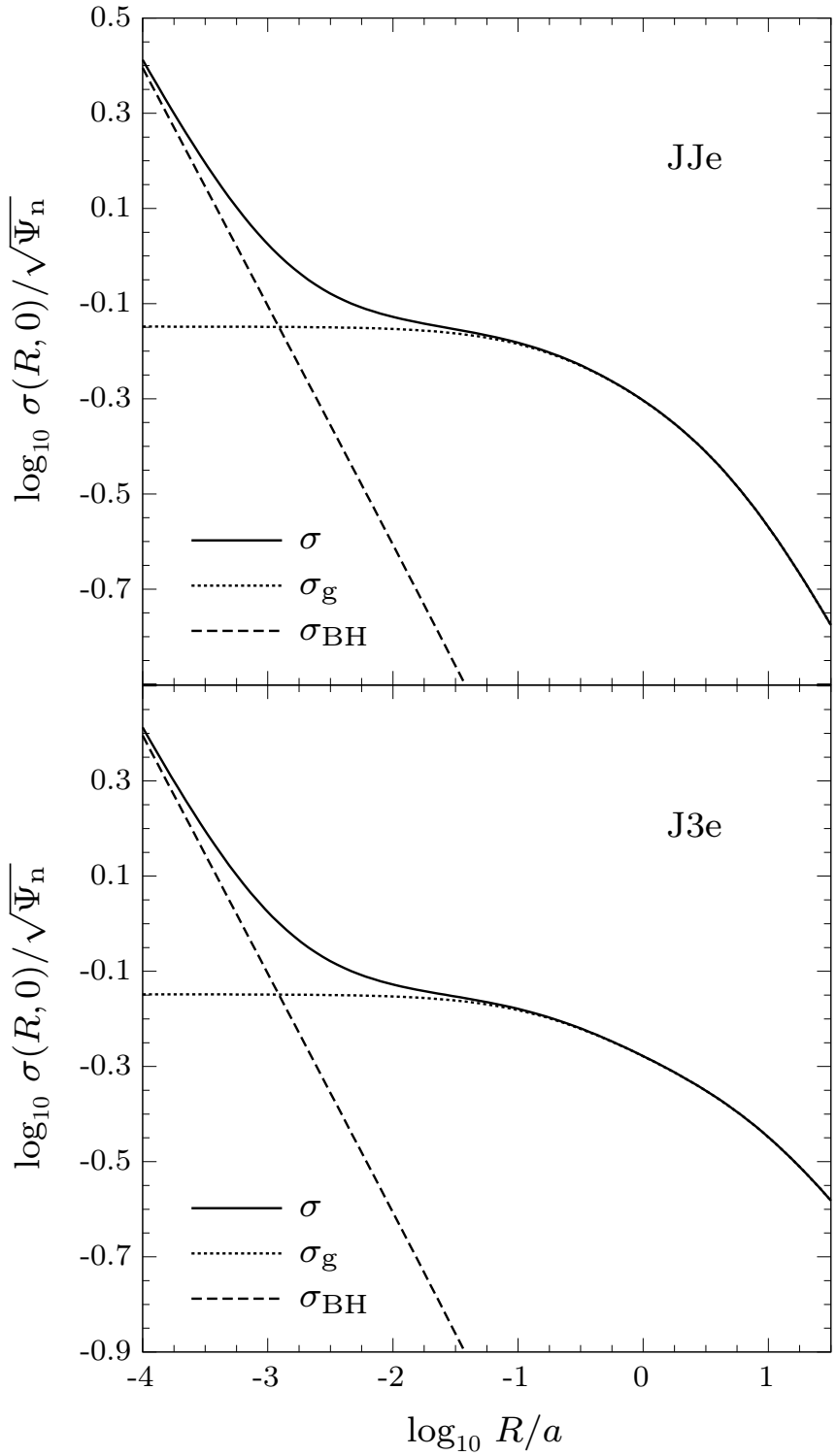

Figure 4.10. Radial trend of σ, on the equatorial plane $z = 0$, for the minimum halo model with $\xi = 5$, $\eta_* = 0.1$ and $\eta_{\rm g} = 0$, in presence of a central BH with $\mu = 2\times10^{-3}$, for JJe (top) and J3e (bottom) models; for both models, $\mathcal{R} = \mathcal{R}_{\rm m} = 50/9$. Dashed lines correspond to the contribution of the BH only, proportional to $R^{-1/2}$ over the whole radial range; dotted lines refer to the galaxy component.

assume $G(s)$ to be a negative function for generic density profiles. However, we note that even $\rho_*\sigma^2_{\rm BH}$ *can be expressed in fully analytical form*, and the explicit formulae for $F(s)$, $G(s)$ and $H(s)$ are given in Appendix B.

Now, before proceeding, it is important to clarify an aspect that might seem obvious but actually hides a number of delicate points we shall address in detail in the next Chapter. The aspect concerns the "practical" way in which the velocity dispersion σ is obtained. In fact, as clear from equation (4.63), the vertical Jeans equation returns $\rho_*\sigma^2$, and not σ directly! In order to obtain σ it is necessary, as a first step, to divide $\rho_*\sigma^2$ by the stellar density: for, we *choose* to divide by the *linear expansion* of ρ_*. In practice, we *define*

$$\sigma \equiv \sqrt{\frac{\text{expansion of } \rho_*\sigma^2 \text{ for } \eta_* \to 0 \text{ and } \eta_{\rm g} \to 0}{\text{expansion of } \rho_* \text{ for } \eta_* \to 0}}\,. \tag{4.73}$$

In other words, *the quantity we call σ is the square root of the ratio of two homoeoidally expanded functions, and not the correct linear expansion of the velocity dispersion*: to obtain such an expression, indeed, formally one should firstly divide by ρ_* the right-hand side of the integral expression for $\rho_*\sigma^2$ (see equation 4.63), extract the root, and then perform a direct expansion in terms of the flattenings. From the foregoing equation it follows that, since $\sigma^2 = \sigma^2_{\rm g} + \sigma^2_{\rm BH}$, the contributions of the galaxy and of the central BH to the velocity dispersion can be consequently defined as

$$\sigma_{\rm g} \equiv \sqrt{\frac{\rho_*\sigma^2_{\rm g}}{\rho_*}}, \qquad\qquad \sigma_{\rm BH} \equiv \sqrt{\frac{\rho_*\sigma^2_{\rm BH}}{\rho_*}}, \tag{4.74}$$

where $\rho_*\sigma^2_{\rm g}$ and $\rho_*\sigma^2_{\rm BH}$ are given respectively by equations (4.66) and (4.69), and the density in the two denominators is given by the linear expansion (4.34).

We are now in a position to show and discuss some concrete results concerning the velocity dispersion profiles. Figure 4.8 shows the trend of $\sigma_{\rm g}$ in the equatorial plane for three JJe (top) and J3e (bottom) minimum halo models with $\xi = 5$ and $\eta_{\rm g} = 0$, in absence a central BH for simplicity (i.e., $\mu = 0$); solid lines refers to $\eta_* = 0.1$, dashed lines to $\eta_* = 0.2$, and dotted lines to $\eta_* = 0.3$. The associated values of $\mathcal{R}_{\rm m}$, given in the caption, are identical for both models. The trend is quite flat in the central regions (in practice, for $R \lesssim 10^{-3}\, r_*$), meaning that *the velocity dispersion at the centre reduces to a constant value*, dependent (for this particular choice of parameters) only on the stellar flattening; this behaviour will be clarified in the next Section, where we shall analyze the asymptotic trend of the velocity fields. Clearly, as expected, the central trend is extremely similar for the two models, and it starts to significantly differ only for $R \gtrsim 0.5\, r_*$: here, for a given distance from the centre, $\sigma_{\rm g}$ associated with the J3e models significantly exceeds that corresponding to the JJe models. Note that only the effect of the stellar component appears explicitly in this example; in order to illustrate the effect of a positive galaxy flattening, we show in Fig. 4.9 the velocity dispersion behaviour, again in the $z = 0$ plane, for three minimum halo models which differ only in the value of $\eta_{\rm g}$. We fix $\xi = 5$, $\eta_* = 0.1$, and $\mu = 0$, and we vary the value of $\eta_{\rm g}$: 0.1 (solid), 0.2 (dashed), and 0.3 (dotted); an evident conclusion arises for fixed R: a flatter galactic component produces higher velocity dispersion values. Finally, the effect of a central BH of mass $M_{\rm BH} \simeq 10^{-3}\, M_*$ is shown for the JJe and J3e models in Fig. 4.10. In each plot, the solid line is the total, the dashed line is the BH contribution, and the dotted line is the galaxy component; the radial range is now extended down to $R = 10^{-4}\, r_*$ to better appreciate the dynamical effects of the BH. Notice that for $R \approx 10^{-1}\, r_*$, the lines corresponding to the total σ start to deviate from the galaxy contributions: this distance could be adopted, for example, as a measure for the radius of the the so-called *sphere of influence* of the BH.

We now move to discuss the solution of the radial equation. First, in analogy with equation (4.64), we write

$$\Delta = \Delta_{\rm g} + \Delta_{\rm BH}, \qquad \begin{cases} \rho_* \Delta_{\rm g} = -\,[\rho_*, \Psi_{\rm g}], \\ \\ \rho_* \Delta_{\rm BH} = -\,[\rho_*, \Psi_{\rm BH}], \end{cases} \tag{4.75}$$

where $\Delta_{\rm g}$ and $\Delta_{\rm BH}$ indicate the contribution to Δ of the galaxy potential and of the central BH. Then, remembering that the commutator between two spherical functions vanishes (see § 3.3.2), at the linear order in the flattening we have

$$[\rho_*, \Psi_{\rm g}] = \rho_{\rm n} \Psi_{\rm n} \mathcal{R} \{\eta_* [\tilde{R}^2 \tilde{\rho}_{*2}(s), \tilde{\Psi}_{\rm g0}(s)] + \eta_{\rm g} [\tilde{\rho}_{*0}(s), \tilde{R}^2 \tilde{\Psi}_{\rm g2}(s)]\}. \tag{4.76}$$

Now, following a procedure identical to that described for the derivation of equation (3.75), we find that the galaxy contribution to Δ is given by

$$\frac{\rho_* \Delta_{\rm g}}{\rho_{\rm n} \Psi_{\rm n}} = 2 \mathcal{R} \tilde{R}^2 \big[\eta_* C(s) + \eta_{\rm g} E(s) - \eta_{\rm g} \tilde{\rho}_{*0}(s) \tilde{\Psi}_{\rm g2}(s)\big]; \tag{4.77}$$

notice that, as expected, $\rho_* \Delta_{\rm g}$ vanishes in the fully spherical case. For what concerns the BH contribution it is clear that, since $\Psi_{\rm BH}$ is spherically symmetric, $\Delta_{\rm BH}$ can be produced *only* by the effect of $\Psi_{\rm BH}$ itself on $\tilde{\rho}_{*2}$; in practice, we have:

$$\frac{\rho_* \Delta_{\rm BH}}{\rho_{\rm n} \Psi_{\rm n}} = 2 \mu \eta_* \tilde{R}^2 H(s) = 2 \mu \eta_* \tilde{R}^2 \int_0^\infty \left| \frac{d \tilde{\rho}_*(s')}{d s'} \right| \frac{d s'}{s'^3}, \tag{4.78}$$

where in the last expression we have rewritten the function $H(s)$ in terms of the stellar density ρ_* by making use of the relations (3.5)-(3.36). The solution of the radial equation is finally obtained by simply combining equations (4.77) and (5.17). Notice that no additional functions beyond those defining σ are needed to express Δ. As a result, since all these functions, from $A(s)$ to $H(s)$, can be expressed completely in terms of elementary functions for both the JJe and J3e models, we can conclude that *it is possible to study the whole internal dynamics of these models in a completely analytical way, without necessarily resorting to numerical methods.*

We now proceed to discuss some concrete results; for, as for the case of the velocity dispersion, we must choose a practical way to calculate $\overline{v_\varphi}$. In analogy with equation (4.73), and considering a Satoh decomposition, we define

$$\overline{v_\varphi} \equiv k \sqrt{\frac{\text{expansion of } \rho_* \Delta \text{ for } \eta_* \to 0 \text{ and } \eta_{\rm g} \to 0}{\text{expansion of } \rho_* \text{ for } \eta_* \to 0}}. \tag{4.79}$$

In other words, *the quantity we call $\overline{v_\varphi}$ is k times the square root of the ratio of two homoeoidally expanded functions, and not the correct linear expansion of the streaming velocity field*: to obtain such an expansion, indeed, formally one should firstly divide by ρ_* the right-hand side of the integral expression for $\rho_* \Delta$ (see equation 4.63), extract the root, multiply by k, and then perform a direct expansion in terms of the flattenings. Since $\Delta = \Delta_{\rm g} + \Delta_{\rm BH}$, from the foregoing equation it follows that the contributions of the galaxy and of the central BH to the streaming velocity can be consequently defined as

$$\overline{v_\varphi}_{\rm g} \equiv k \sqrt{\frac{\rho_* \Delta_{\rm g}}{\rho_*}}, \qquad \overline{v_\varphi}_{\rm BH} \equiv k \sqrt{\frac{\rho_* \Delta_{\rm BH}}{\rho_*}}, \tag{4.80}$$

being $\rho_* \Delta_{\rm g}$ and $\rho_* \Delta_{\rm BH}$ given respectively by equations (4.77) and (5.17), and the density in the two denominators given by the linear expansion (4.34).

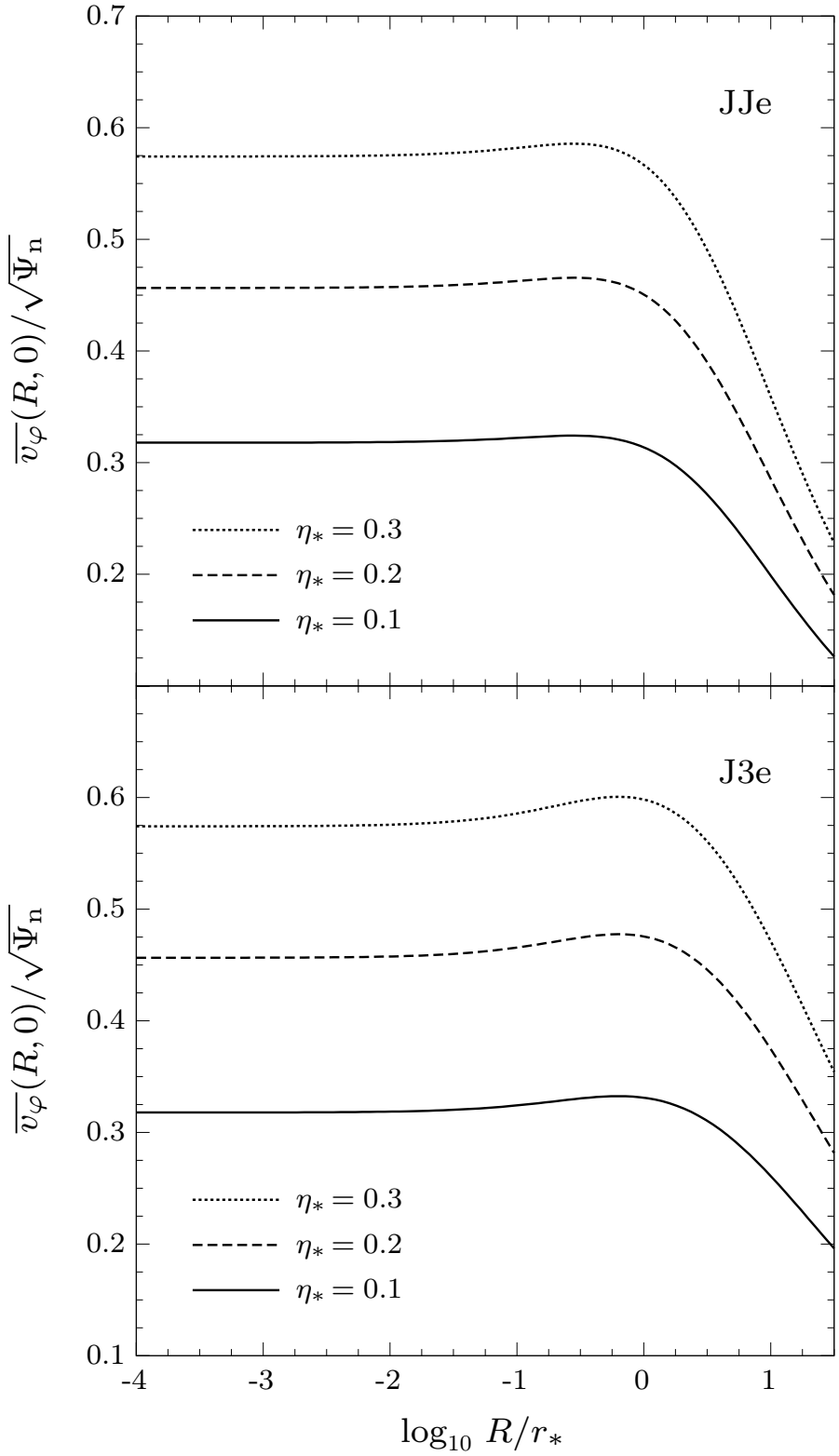

Figure 4.11. Radial trend of $\overline{v_\varphi}(R,0)$ for the same three minimum halo models showed in Fig. 4.8, in the isotropic case $k = 1$, for JJe (top) and J3e (bottom) models. The behaviour of $\overline{v_\varphi}$ is similar for both models: it is flat in the central regions, then it reaches a maximum value, and and finally it decreases outward; these features are quite on the adopted stellar flattening. Notice the bump after $R \simeq 0.1\, r_*$: for the J3e models it is reached at distances slightly greater and in a more pronounced manner, leading to significantly higher values of $\overline{v_\varphi}$ in the outer regions ($R \gtrsim r_*$, say) with respect to the JJe models.

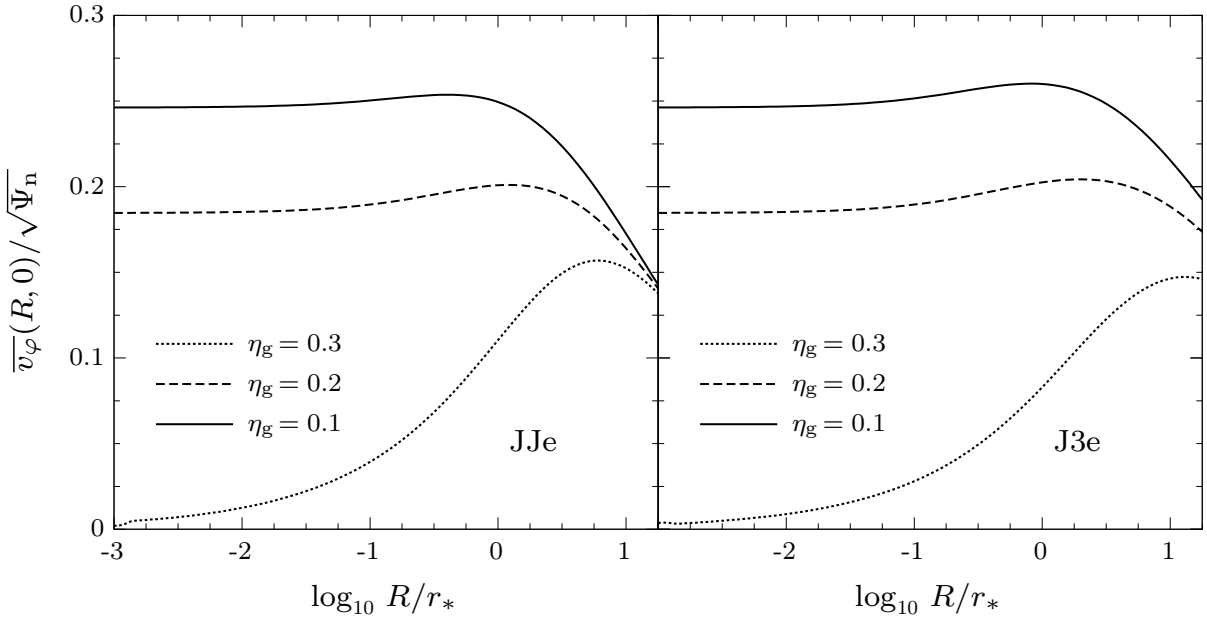

Figure 4.12. Radial trend of $\overline{v_\varphi}$ on the plane $z = 0$, for the same three minimum halo models showed in Fig. 4.9, in the isotropic case $k = 1$, for JJe (top) and J3e (bottom) models. It is evident how the values of $\overline{v_\varphi}$ increase for increasing η_g. Also, notice how in the particular case $\eta_g = 0.3$, in accordance with equation (4.88).

Let us now show and comment some result regarding the streaming velocity. We begin with the trend of $\overline{v_\varphi}$ in the plane $z = 0$, showed in Fig. 4.11 for the same JJe and J3e minimum halo models of Fig. 4.8 in the isotropic case $k = 1$. Qualitatively, the profile of $\overline{v_\varphi}$ is flat in the central regions, reaches a maximum value, and decreases outward; these features are quite independent on the family of models and on the adopted stellar flattening. A direct comparison of the two families of models confirms an identical behaviour in the central regions ($R \lesssim 10^{-2} r_*$, say), and highlights a particular feature: for the J3e models the bump in the intermediate region is reached at distances slightly greater and in a more pronounced manner, leading to significantly higher values of $\overline{v_\varphi}$ in the outer regions ($R \gtrsim r_*$, say) with respect to the JJe models. Also, η_* has a significant effect on the global trend of $\overline{v_\varphi}$: for fixed values of R over the whole radial range, flatter density distributions produce considerably larger values of $\overline{v_\varphi}$, a feature shared by both models. To better understand the effect of the galaxy flattening, Fig. 4.12 shows, for different values of η_g, the radial profile of $\overline{v_\varphi}$ in the equatorial plane for the same JJe and J3e minimum halo models of Fig. 4.11 in the case $k = 1$. Not surprisingly, the values of streaming velocity increase for increasing η_g. Another fact is also evident from the figure: in the particular case $\eta_g = 0.3$, $\overline{v_\varphi}$ vanishes at the centre; we postpone the discussion of this fact, which might seem quite strange at first sight, to the next Section, where we discuss the associated asymptotic forms. Finally, Fig. 4.13 shows the effect of a central BH. As in the case of the velocity dispersion (see Fig. 4.10), the total streaming velocity is influenced by the presence of the BH within a radius $R \approx 10^{-1} r_*$.

The results illustrated so far refer only to the equatorial plane. To have a better understanding of the internal dynamics for the two models, Fig. 4.14 shows the two-dimensional maps in the meridional plane for σ (top), σ_φ (middle), and $\overline{v_\varphi}$ (bottom), in units of $\sqrt{\Psi_n}$. As an illustrative example, we consider two JJe (left) and J3e (right) minimum halo models with $\xi = 5$, $\eta_* = 0.1$, $\eta_g = 0$, and $\mu = 0$; in words, a galaxy model without a central BH and with a slightly flattened stellar component embedded in a spherical total. The innermost contour corresponds to values of 0.5 for the normalized σ and σ_φ, and of 0.3 for $\overline{v_\varphi}$; the values for the other contour lines decrease outward with steps of 0.02. We present below a brief analysis of the figure.

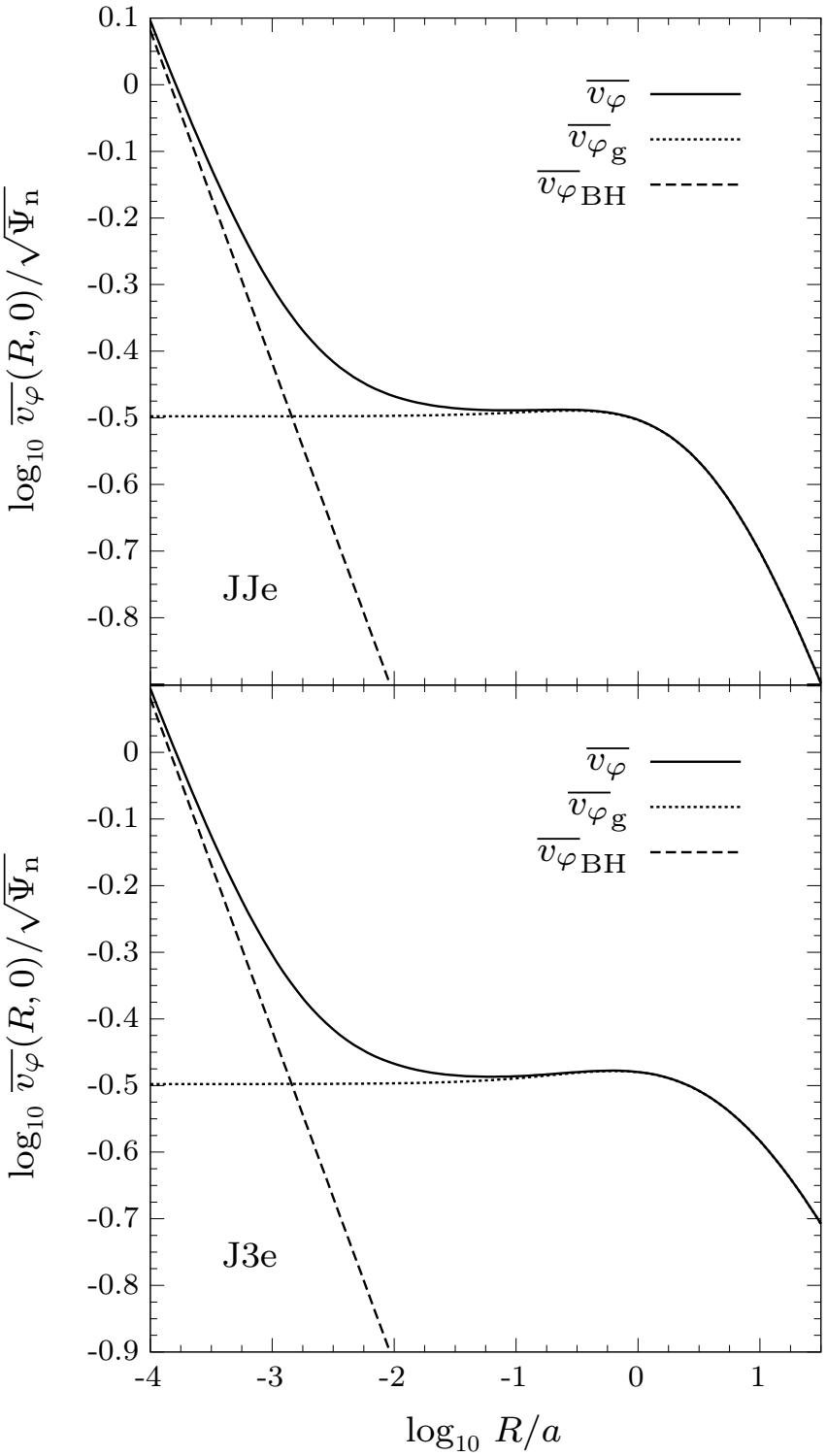

Figure 4.13. Radial trend of σ, on the equatorial plane $z = 0$, for the minimum halo model with $\xi = 5$, $\eta_* = 0.1$ and $\eta_{\rm g} = 0$, in presence of a central BH with $\mu = 2 \times 10^{-3}$, for JJe (top) and J3e (bottom) models; for both models, $\mathcal{R} = \mathcal{R}_{\rm m} = 50/9$. Dashed lines correspond to the contribution of the BH only, proportional to $R^{-1/2}$ (see equation 4.86) over the whole radial range; dotted lines refer to the galaxy component.

1. Top Panels – maps of constant $\sigma/\sqrt{\Psi_{\rm n}}$.
   The velocity dispersion is obtained from the first expression in equation (4.74) by setting $\eta_{\rm g} = 0$. The contours show a clear elongation along the z-axis. This elongation, for a given level, is more pronounced for the J3e models. Also, note how the distance between two consecutive contours in the J3e case is higher than that in the JJe case, an effect that tends to become more pronounced moving further away from the centre; in other words, for J3e models the velocity dispersion increases faster towards the centre.

2. Middle Panels: maps of constant $\sigma_\varphi/\sqrt{\Psi_{\rm n}}$, for $k = 0$ (no net rotation).
   From equation (2.21), $\sigma_\varphi^2 = \sigma^2 + \Delta$ in case of vanishing k. To obtain the map, we derive the expression for σ_φ in analogy with equations (4.73) and (4.79) by extracting the root of the quantity $(\rho_*\sigma^2 + \rho_*\Delta)/\rho_*$, discarding the BH contributions and setting $\eta_{\rm g} = 0$. A qualitative comparison with the two upper panels shows two features. The first is that on the symmetry axis $R = 0$ the values of σ_φ do not deviate too much from those of σ; the second is that, for a fixed distance from the centre on the equatorial plane, the value of σ_φ exceeds that of σ: in practice, $\sigma_\varphi(\alpha r_*, 0) > \sigma(\alpha r_*, 0)$ for arbitrary $\alpha > 0$.

3. Bottom Panels: maps of constant $\overline{v_\varphi}/\sqrt{\Psi_{\rm n}}$, for $k = 1$ (isotropic case).
   The streaming velocity here illustrated is obtained from the first expression in equation (4.80) with $k = 1$ and $\eta_{\rm g} = 0$; notice that $\overline{v_\varphi}$ has a very simple form since $\rho_*\Delta_{\rm g}$ reduces to $2\rho_{\rm n}\Psi_{\rm n}\mathcal{R}\tilde{R}^2\eta_* C(s)$. Again, notice how the values of $\overline{v_\varphi}$ keep larger for the J3e model than for the JJe one at the same distance from the centre.

We conclude this Section by stressing that the possibility to study and plot the (intrinsic) kinematical fields expressed in analytical form for realistic ellipsoidal two-component models, without the need for resorting to numerical time-expensive integrations, is a very useful property of JJe and J3e models.

4.6.1 The asymptotic behaviour of the dynamical properties

A more quantitative analysis of the effects of the model parameters on the dynamical properties of the stellar component is provided by the asymptotic expansion of the solutions near the centre and at large radii. Of course, as already stated several times, and graphically verified, we expect that the two models behave very similarly in the central regions, and in a significantly different way only in the outer regions.

The inner regions

The asymptotic behaviours for the galaxy and BH contributions of $\rho_*\sigma^2$ at small radii are obtained by expanding equations (4.66) and (4.69) for $s \to 0$. At the leading order, we find

$$\frac{\rho_*\sigma_{\rm g}^2}{\rho_{\rm n}\Psi_{\rm n}} \sim \mathcal{R}\,\frac{3(1-\eta_*\cos^2\vartheta)+\eta_{\rm g}(1+\sin^2\vartheta)}{6\xi s^2}, \qquad \frac{\rho_*\sigma_{\rm BH}^2}{\rho_{\rm n}\Psi_{\rm n}} \sim \mu\,\frac{5+\eta_*(1-6\cos^2\vartheta)}{15 s^3}, \tag{4.81}$$

identical for both models, where $\sin\vartheta = \tilde{R}/s$, and $\cos\vartheta = \tilde{z}/s$. By adding a higher-order term in the approximation for $\rho_*\sigma_{\rm g}^2$, the two foregoing contributions to the total pressure can be combined to give the following remarkable formula:

$$\frac{\rho_*\sigma^2}{\rho_{\rm n}\Psi_{\rm n}} \sim \mu\left[\frac{5+\eta_*(1-6\cos^2\vartheta)}{15 s^3} - \frac{2+\eta_*\sin^2\vartheta}{2s^2}\right] + \mathcal{R}\,\frac{3(1-\eta_*\cos^2\vartheta)+\eta_{\rm g}(1+\sin^2\vartheta)}{6\xi s^2}. \tag{4.82}$$

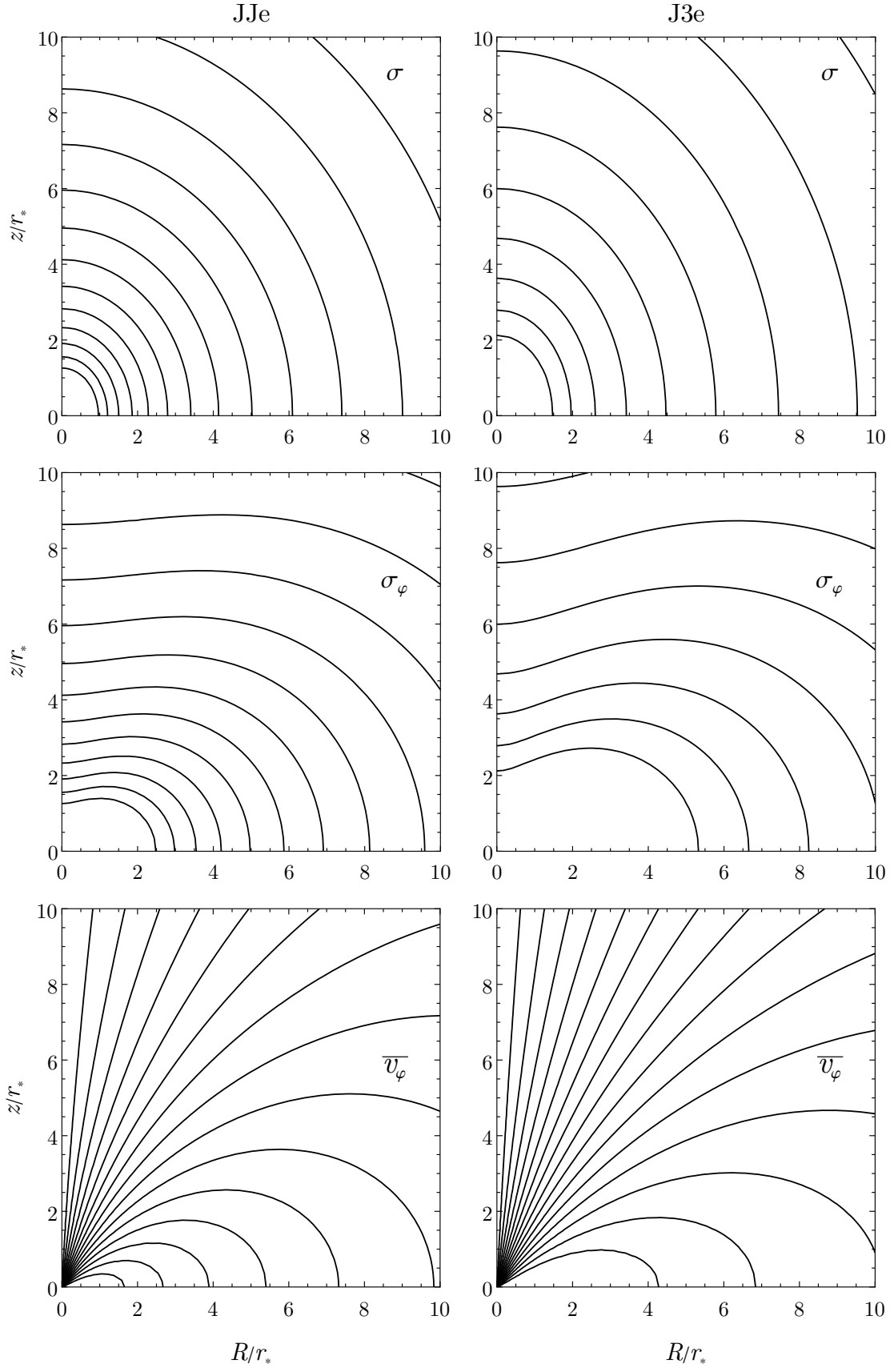

Figure 4.14. Two-dimensional maps of σ (top), $\overline{v_\varphi}$ (middle, $k = 0$), and $\overline{v_\varphi}$ (bottom, $k = 1$), normalized to $\sqrt{\Psi_n}$, for the minimum halo models with $\xi = 5$, $\eta_* = 0.1$, $\eta_g = 0$, and $\mu = 0$. Left panels refer to the JJe case, right panels to the J3e ones. The innermost contour corresponds to values of 0.5 for the normalized σ and σ_φ, and of 0.3 for $\overline{v_\varphi}$; the values for the other contour lines decrease outward with steps of 0.02.

From this asymptotic form it is clear that both families of models exhibit a peculiar behaviour near the centre of the system; in particular, the velocity dispersion in the non-spherical case for $\mu = 0$ is *finite but discontinuous*. Indeed, from the asymptotic trends (4.54) and (4.81), and neglecting the contribution of the BH, it follows that

$$\sigma^2(0,0) \equiv \frac{(\rho_*\sigma^2)_{\text{centre}}}{(\rho_*)_{\text{centre}}} \simeq \frac{\Psi_{\text{n}}\mathcal{R}}{6\xi} \times \frac{3(1-\eta_*\cos^2\vartheta)+\eta_{\text{g}}(1+\sin^2\vartheta)}{1+\eta_*(1-2\cos^2\vartheta)}, \tag{4.83}$$

an expression evidently depending on ϑ. In words: *approaching the centre along different ϑ directions, one determines different values of the velocity dispersion*; this results from the non-spherical shape of ρ_*, the central slope of ρ_*, and the gravitational potential entering Jeans's equations[4]. We have already seen that it is possible to study the internal dynamics in a fully analytical manner, however the functions defining $\rho_*\sigma^2$ may not be easy to manage; equation (4.83) shows that we can however provide a *qualitative estimate of the central dispersion, as a function of the model parameters*. Let us consider for example the direction $\vartheta = \pi/2$, corresponding to the plane $z = 0$; with this choice, the velocity dispersion at the centre is no longer discontinuous, but settles down to a precise value dependent on certain parameters. We are in the situation illustrated in Figs. 4.8 and 4.9, in which the central value of σ is a constant dependent on η_*. In particular, the model shown in Fig. 4.8 is a minimum halo model with $\eta_{\text{g}} = 0$ and $\xi = 5$; consequently, by virtue of equation (4.83),

$$\frac{\sigma(0,0)}{\sqrt{\Psi_{\text{n}}}} \simeq \sqrt{\frac{\mathcal{R}_{\text{m}}}{2\xi(1+\eta_*)}} \simeq \begin{cases} 0.711, & (\eta_* = 0.1), \\ 0.722, & (\eta_* = 0.2), \\ 0.741, & (\eta_* = 0.3), \end{cases} \tag{4.85}$$

in accordance with what is shown in the figure. On the other hand, by fixing $\eta_* = 0.1$ and varying η_{g} as in the case illustrated in Fig. 4.9, equation (4.83) leads to the following values for the normalized $\sigma(0,0)$: 0.696 for $\eta_{\text{g}} = 0.1$, 0.761 for $\eta_{\text{g}} = 0.2$, and 0.837 for $\eta_{\text{g}} = 0.3$; a direct comparison with the plot shows that the agreement is again satisfactory.

For what concerns the asymptotic behaviour of $\rho_*\sigma^2_{\text{BH}}$ in equation (4.81), it can be useful to explain the central trend in Fig. 4.9: in this region, in fact, as $\rho_* \propto r^{-2}$, it follows that σ_{BH} diverges as $r^{-1/2}$ (dashed line).

In analogy with equation (4.81), to find the asymptotic behaviours for the galaxy and BH contributions of $\rho_*\Delta$ at small radii we expand equations (4.77) and (5.17) for $s \to 0$. At the leading order we obtain

[4]For example, let us consider the case of a self-gravitating ellipsoidal system described by $\rho = \rho_0 m^{-\gamma}$, with $0 < \gamma < 3$. By applying the homoeoidal expansion method, the asymptotic behaviours at small radii of the density and of the pressure (i.e. the solution of the vertical Jeans equation) are given by $\rho \sim a(\vartheta)s^{-\gamma}$, and $\rho\sigma^2 \sim b(\vartheta)s^{-2(\gamma-2)}$. Therefore, the square of the central velocity dispersion, defined as the ratio of the previous asymptotic forms, reads

$$\sigma^2(0) \simeq \frac{c(\vartheta)}{s^{\gamma-2}} \to \begin{cases} 0, & 0 < \gamma < 2, \\ c(\vartheta), & \gamma = 2, \\ \infty, & 2 < \gamma < 3; \end{cases} \tag{4.84}$$

in other words, $\sigma(0)$ is zero for $0 < \gamma < 2$, finite discontinuous (as the models in this Chapter) for $\gamma = 2$, and infinite for $\gamma > 2$. Furthermore, for generic values of γ, σ diverges if a central BH is present, while it is finite discontinuous if the ellipsoid is embedded in the potential of the Singular Isothermal Sphere (e.g. C21).

$$\frac{\rho_*\Delta_{\rm g}}{\rho_{\rm n}\Psi_{\rm n}} \sim \mathcal{R}\,\frac{(3\eta_*-\eta_{\rm g})\sin^2\vartheta}{3\xi s^2}, \qquad \frac{\rho_*\Delta_{\rm BH}}{\rho_{\rm n}\Psi_{\rm n}} \sim \mu\,\frac{4\eta_*\sin^2\vartheta}{5s^3}. \tag{4.86}$$

Note that the non-negativity of $\rho_*\Delta_{\rm g}$ is not guaranteed for every choice of parameters: in particular, *in order to have a nowhere negative* $\rho_*\Delta_{\rm g}$, *the condition* $3\eta_*-\eta_{\rm g}\geq 0$ *must be satisfied*, a requirement which further restricts the space of parameters. By adding a higher-order term in the approximation for $\rho_*\Delta_{\rm g}$, and combine the two contributions, we find

$$\frac{\rho_*\Delta}{\rho_{\rm n}\Psi_{\rm n}} \sim \mu\left(\frac{4}{5s^3}-\frac{1}{s^2}\right)\eta_*\sin^2\vartheta + \mathcal{R}\,\frac{(3\eta_*-\eta_{\rm g})\sin^2\vartheta}{3\xi s^2}. \tag{4.87}$$

As a consequence, by excluding the contribution of the central BH, the central value of Δ reads

$$\Delta(0,0) \equiv \frac{(\rho_*\Delta)_{\rm centre}}{(\rho_*)_{\rm centre}} \simeq \frac{\Psi_{\rm n}\mathcal{R}}{3\xi} \times \frac{(3\eta_*-\eta_{\rm g})\sin^2\vartheta}{1+\eta_*(1-2\cos^2\vartheta)}, \tag{4.88}$$

where $(\rho_*)_{\rm centre}$ indicates the first expression in equation (4.54). Therefore, as for the velocity dispersion, *in the non-spherical case without the central BH, the value of* Δ *is finite but discontinuous*. In the equatorial plane (i.e. along the direction $\vartheta=\pi/2$), for an isotropic minimum halo model with $\xi=5$ and fixed $\eta_{\rm g}=0$ we find

$$\frac{\overline{v_\varphi}(0,0)}{\sqrt{\Psi_{\rm n}}} \simeq \sqrt{\frac{\mathcal{R}_{\rm m}\eta_*}{\xi(1+\eta_*)}} \simeq \begin{cases} 0.318, & (\eta_*=0.1),\\ 0.456, & (\eta_*=0.2),\\ 0.574, & (\eta_*=0.3), \end{cases} \tag{4.89}$$

in accordance with the central values of $\overline{v_\varphi}$ shown in Fig. 4.11 for both JJe and J3e models. Also, we are now in a position to explain the strange behaviour of $\overline{v_\varphi}$ illustrated in Fig. 4.12; here the flattening we keep fixed is that corresponding to the stellar distribution, while we vary that of the galaxy. Particularly curious is the behaviour of the dotted line, related to the case $\eta_*=0.1$ and $\eta_{\rm g}=0.3$, for which, the central value of $\overline{v_\varphi}$ vanishes in accordance with equation (4.88); for the other two lines, by virtue of (4.88), the central value of $\overline{v_\varphi}$ reduces to $0.185\sqrt{\Psi_{\rm n}}$ (dashed) and $0.246\sqrt{\Psi_{\rm n}}$ (solid).

Finally, concerning the behaviour of $\overline{v_\varphi}$ in presence of a BH, since $\rho_*\Delta_{\rm BH}\propto r^{-3}$ at the centre, $\overline{v_\varphi}\propto r^{-1/2}$, as illustrated by the dashed lines in Fig. 4.13.

The external regions

It remains to analyze the asymptotic trend of the velocity dispersion and of the streaming velocity at large distances from the centre, i.e. for $s\to\infty$. By following an approach similar to that we have used for the central region, it is not difficult to show that, far from the centre,

$$\frac{\rho_*\sigma^2}{\rho_{\rm n}\Psi_{\rm n}} \sim \frac{7-\eta_*(1+20\cos^2\vartheta)}{35s^5} \times \begin{cases} \mathcal{R}+\mu, & ({\rm JJe}),\\ \mathcal{R}\ln s, & ({\rm J3e}), \end{cases} \qquad \frac{\rho_*\Delta}{\rho_{\rm n}\Psi_{\rm n}} \sim \frac{8\eta_*\sin^2\vartheta}{7s^5} \times \begin{cases} \mathcal{R}+\mu, & ({\rm JJe}),\\ \mathcal{R}\ln s, & ({\rm J3e}). \end{cases} \tag{4.90}$$

Note how, due to the total finite mass, the mass of the BH appears in the JJe case, so that both σ^2 and Δ are dominated by the monopole term of $\Psi_{\rm g}$; of course, as $\mu\approx 10^{-3}$, the presence of μ is

totally irrelevant for any practical application. For the same reason, μ does not appear in the case of the J3e models, which have an infinite mass. As a direct consequence, already qualitatively intuited from by the previous one-dimensional plots, and now quantitatively confirmed by the two asymptotic expressions in the equation above, *in general σ and $\overline{v_\varphi}$ keep larger for the J3e model than for the JJe one when considering the external regions.*

4.7 Projected dynamics of JJe and J3e models

The projection of a galaxy model on the plane of the sky is an important step in the model construction, needed in order to determine the observational properties of the model itself. As discussed in § 2.2.2, for axisymmetric models we need to specify just a single angle i that gives the direction of the line of sight (los) to the observer. Anyway, even though the simple functional form of the density and of the intrinsic kinematical fields in the homoeoidal framework leads to significant simplifications with respect the general case, the study of the projected dynamics is sufficiently challenging (especially in the case of multi-component models) to preclude a fully analytical treatment.

For example, the projection of the stellar density $\rho_*(R,z)$ is obtained by inserting the expansion (4.34) in equation (2.36), i.e.

$$\frac{\Sigma_*(x',y')}{\Sigma_\mathrm{n}} = \int_{-\infty}^{\infty} [\tilde{\rho}_{*0}(s) + \eta_* \tilde{\rho}_{*1}(s) + \eta_* \tilde{R}^2 \tilde{\rho}_{*2}(s)]' \, d\tilde{z}', \qquad \Sigma_\mathrm{n} \equiv \frac{M_*}{4\pi r_*^2}, \tag{4.91}$$

where Σ_n is a projected density scale. Of course, the radial distance r' in the reference $(S';x',y',z')$ is identical to the corresponding radial distance r evaluated in the reference $(S_0;x,y,z)$; this can be easily verified from equations (2.33)-(2.34) as

$$(s^2)' = (\tilde{x}'\cos i + \tilde{z}'\sin i)^2 + \tilde{y}'^2 + (-\tilde{x}'\sin i + \tilde{z}'\cos i)^2 = s'^2. \tag{4.92}$$

Further, the (dimensionless) cylindrical radius $\tilde{R} = \sqrt{\tilde{x}^2 + \tilde{y}^2}$ is transformed in the system S' as

$$\begin{aligned} (\tilde{R}^2)' &= (\tilde{x}'\cos i + \tilde{z}'\sin i)^2 + \tilde{y}'^2 \\ &= \tilde{x}'^2\cos^2 i + \tilde{x}'\tilde{z}'\sin 2i + \tilde{z}'^2\sin^2 i + \tilde{y}'^2, \\ &= \tilde{\ell}^2 + (\tilde{z}'^2 - \tilde{y}'^2)\sin^2 i + \tilde{x}'\tilde{z}'\sin 2i, \end{aligned} \tag{4.93}$$

where $\tilde{\ell} = \sqrt{\tilde{x}'^2 + \tilde{y}'^2}$ is the distance from the centre in the projection plane. Therefore, after some minor reductions, the projected stellar density can be written as

$$\frac{\Sigma_*(x',y')}{\Sigma_\mathrm{n}} = \tilde{\Sigma}_{*0}(\tilde{x}',\tilde{y}') + \eta\tilde{\Sigma}_{*1}(\tilde{x}',\tilde{y}') + \eta\tilde{\Sigma}_{*2}(\tilde{x}',\tilde{y}'), \tag{4.94}$$

where

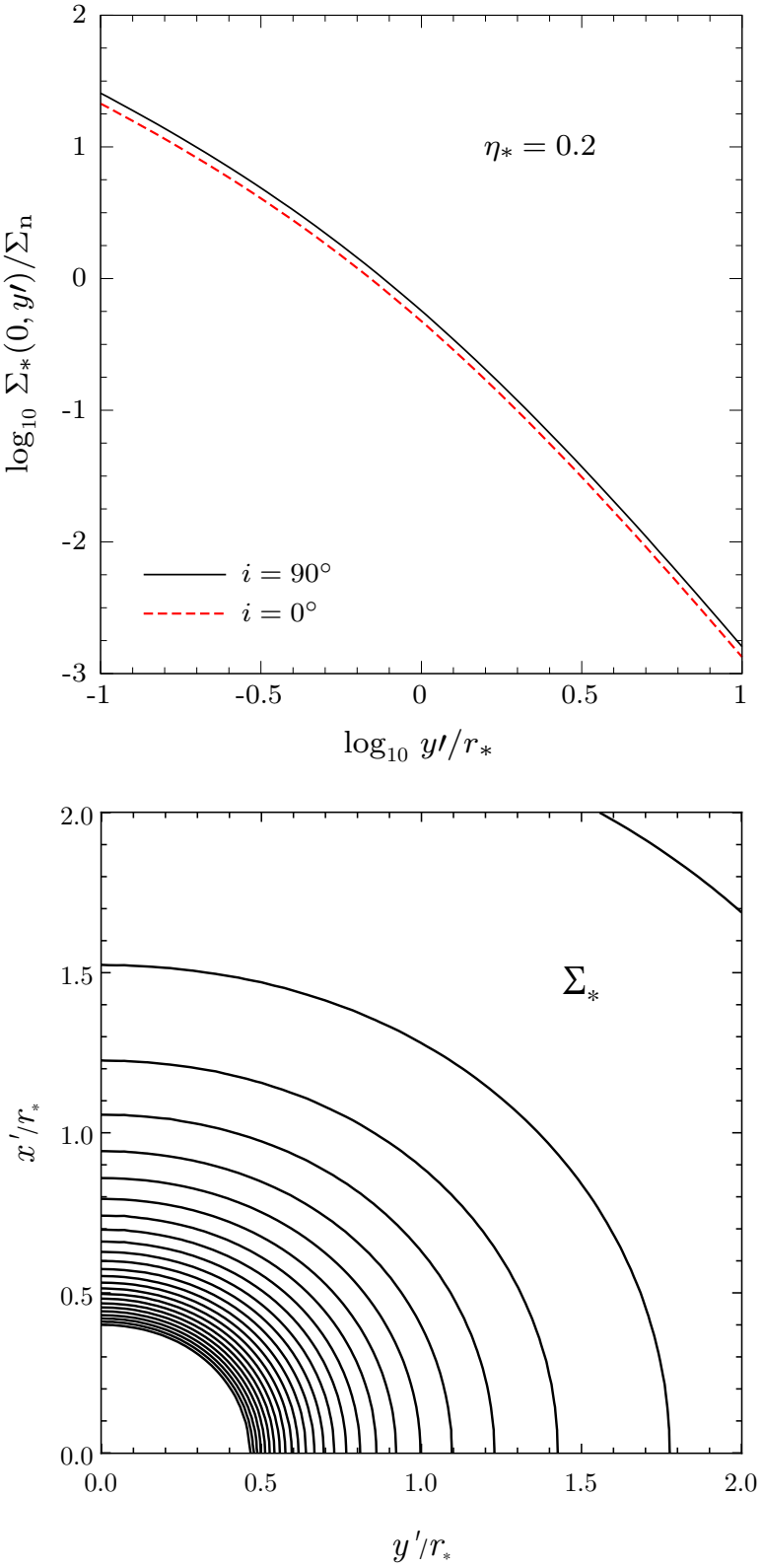

Figure 4.15. The stellar density (4.94) for the chosen flattening $\eta_* = 0.2$. Top panel shows the trend of Σ_* on the plane $x' = 0$, for the two limiting cases $i = 0°$ (face-on) and $i = 90°$ (edge-on); notice how in both cases a gradual decrease is seen over the entire displayed range of y', with a change of slope in the vicinity of $y' \simeq 0.5\, r_*$. Bottom panel shows the two-dimensional map of Σ_*/Σ_n on the projection plane (x', y'), for the the case $i = 90°$: the contour lines correspond to values that, starting from 0.05, increase with step 0.1 from outside to inside.

$$\begin{cases} \tilde{\Sigma}_{*0}(\tilde{x}', \tilde{y}') \equiv \displaystyle\int_{-\infty}^{\infty} \tilde{\rho}_{*0}(s')d\tilde{z}', \\ \\ \tilde{\Sigma}_{*1}(\tilde{x}', \tilde{y}') \equiv \displaystyle\int_{-\infty}^{\infty} \tilde{\rho}_{*1}(s')d\tilde{z}', \\ \\ \tilde{\Sigma}_{*2}(\tilde{x}', \tilde{y}') \equiv \displaystyle\int_{-\infty}^{\infty} [\tilde{\ell}^2 + (\tilde{z}'^2 - \tilde{y}'^2)\sin^2 i]\tilde{\rho}_{*2}(s')d\tilde{z}'; \end{cases} \tag{4.95}$$

notice that, as $\tilde{\ell}$ and $\tilde{y}'$ does not depend on the integration variable $\tilde{z}'$, only the integration of $\tilde{\rho}_{*2}(s')$ and $\tilde{z}'^2\tilde{\rho}_{*2}(s')$ is actually required to evaluate $\tilde{\Sigma}_{*2}(\tilde{x}', \tilde{y}')$. The three expressions in the equation above can be calculated in terms of analytical functions for both JJ e and J3e models (which are not shown in this Thesis), although even for a simple density profile such as that of Jaffe they are quite cumbersome. For this reason, we prefer here to provide a *numerical* analysis, showing and discussing some plots of the projected velocity fields obtained by solving numerically the projection integrals presented in § 2.2.2.

In Fig. 4.15 we show the stellar density (4.94) for the choice $\eta_* = 0.2$. Top panel shows the trend of Σ_* on the plane $x' = 0$, for the two limiting cases $i = 0°$ (face-on; red dotted) and $i = 90°$ (edge-on; solid). In both cases a gradual decrease is seen over the entire displayed range of y', with a change of slope in the vicinity of $y' \simeq 0.5\, r_*$. Moreover, although the difference is minimal in quantitative terms, in the edge-on case view the values of Σ_* are higher for arbitrary y'; clearly, the profile corresponding to an intermediate value for the inclination angle lies between the dotted and the solid curves. The situation in the case $i = 90°$ is better illustrated in the bottom panel, where we show the two-dimensional map of $\Sigma_*/\Sigma_\mathrm{n}$ on the projection plane (x', y'): here the contour lines correspond to values that, starting from 0.05, increase with step 0.1 from outside to inside.

Figure 4.16 shows the trend of $-v_\mathrm{los}$ on the plane $x' = 0$ for a selection of JJe (top) and J3e (bottom) minimum halo models with $\eta_* = 0.1$, $\eta_\mathrm{g} = 0$ and $\xi = 5$: different line styles corresponds to different values of i. The trend is flat in the central regions (in practice, for $R \lesssim 3 \times 10^{-3}\, r_*$), independently of the chosen inclination angle; of course, in the face-one view, no rotational motion is observed (red dotted line). As expected, the central behaviour is almost identical for the two models; in the intermediate region ($10^{-3} \lesssim R/r_* \lesssim 1$) the difference between the two models becomes progressively more appreciable as i increases from 0° to 90°; finally, at a large distance from the centre ($R \gtrsim 2\, r_*$) the rotational velocity (in absolute value) for fixed y' is significantly greater in the J3e case.

Again in the plane $x' = 0$, Fig. 4.17 shows the trend of the los velocity dispersion corresponding to the v_los profile just described. In contrast to the rotational velocity, the radial profile of σ_los does not change significantly when changing the angle of inclination; for this reason, only three curves are shown: the face-on case, the edge-one case, and the intermediate case $i = 45°$. Also, notice that now the highest values of σ_los are obtained in the face-on view, a behaviour directly derived from the definition (2.43).

Finally, it is of course important to consider also the behavior over the full projection plane. For, in Fig. 4.18 we show the two-dimensional maps of σ_los (top) and $-v_\mathrm{los}$ (bottom), measured in units of $\sqrt{\Psi_\mathrm{n}}$; the model parameters coincide with those used in the previous figures, while as an "average" angle of inclination we chose $i = 45°$. The innermost contours correspond to values of 0.5 for σ_los, and of 0.16 for v_los; in each map the other contour lines decrease outward with steps of 0.02. The qualitative features discussed about the intrinsic velocity fields (see Fig. 4.14) are also valid when projecting along the line of sight: for J3e models the los velocity dispersion increases faster towards the centre, while the values of v_los keep larger for the J3e model than for

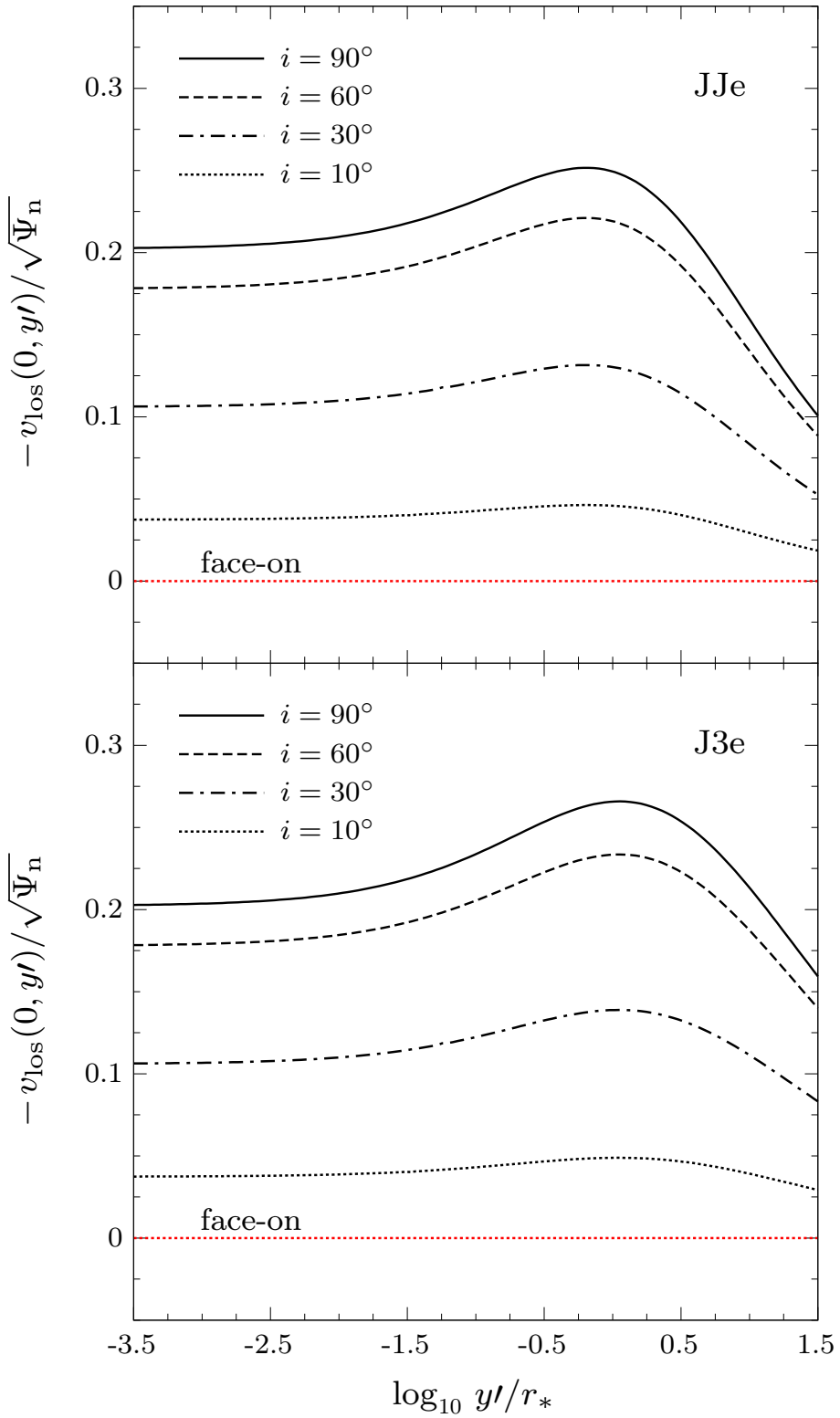

Figure 4.16. The trend of $-v_{\rm los}$ on the plane $x' = 0$ for a selection of JJe and J3e isotropic minimum halo models with $\eta_* = 0.1$, $\eta_{\rm g} = 0$, $\xi = 5$ and $\mu = 0$; different line styles corresponds to different values of i. Notice the flat behaviour in the central regions, independently of the chosen inclination angle. The central behaviour, as expected, is almost identical for the two models; while at a large distance from the centre ($R \gtrsim 2\,r_*$) the rotational velocity (in absolute value) for fixed y' is significantly greater in the J3e case.

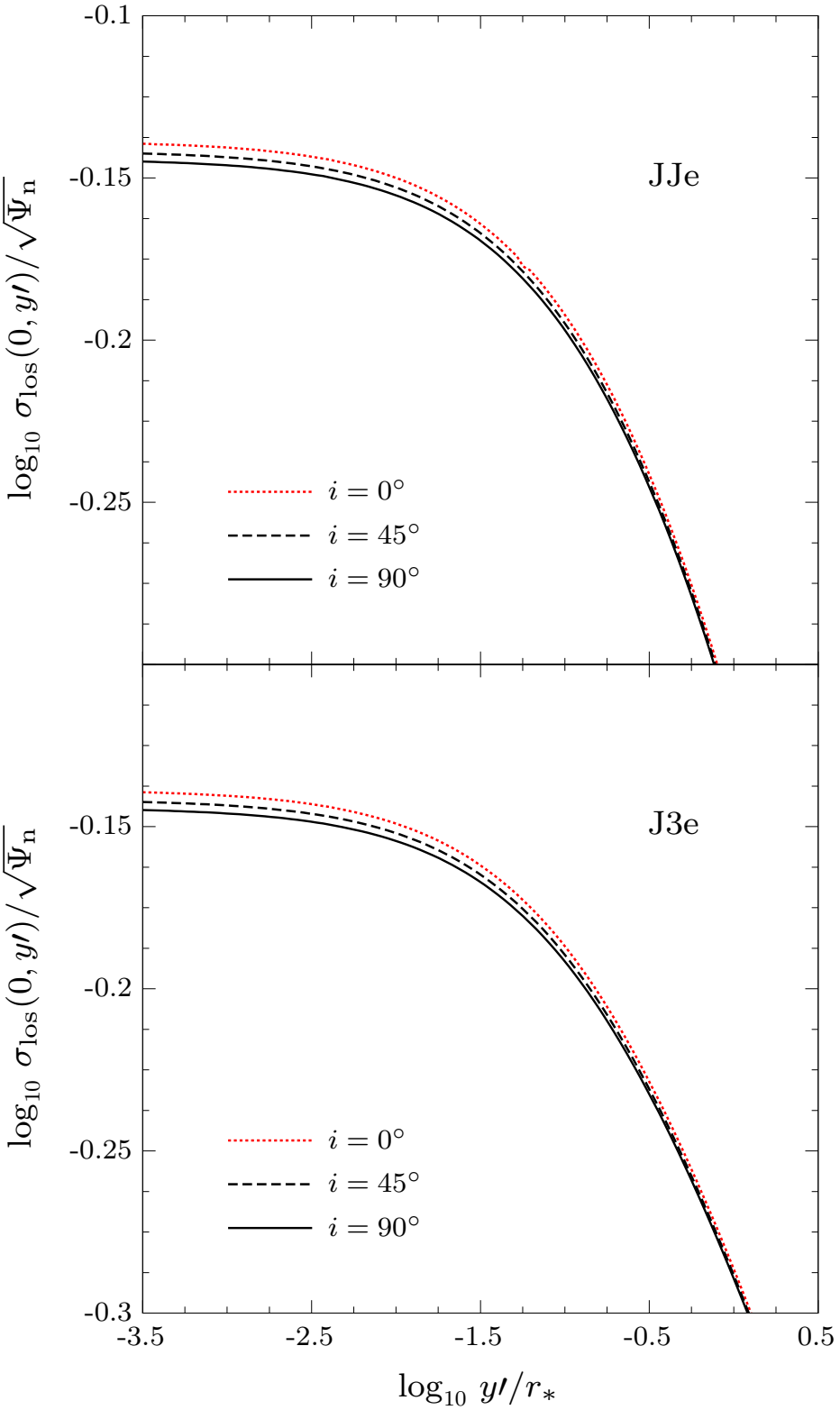

Figure 4.17. The trend of $\sigma_{\rm los}$, on the plane $x' = 0$, corresponding to the $v_{\rm los}$ profile shown in Fig. 4.16. Notice how the radial profile of $\sigma_{\rm los}$, in contrast with $v_{\rm los}$, does not change significantly when changing the angle of inclination. The highest values of $\sigma_{\rm los}$ are obtained in the face-on view (red dotted), a behaviour directly derived from the definition (2.43).

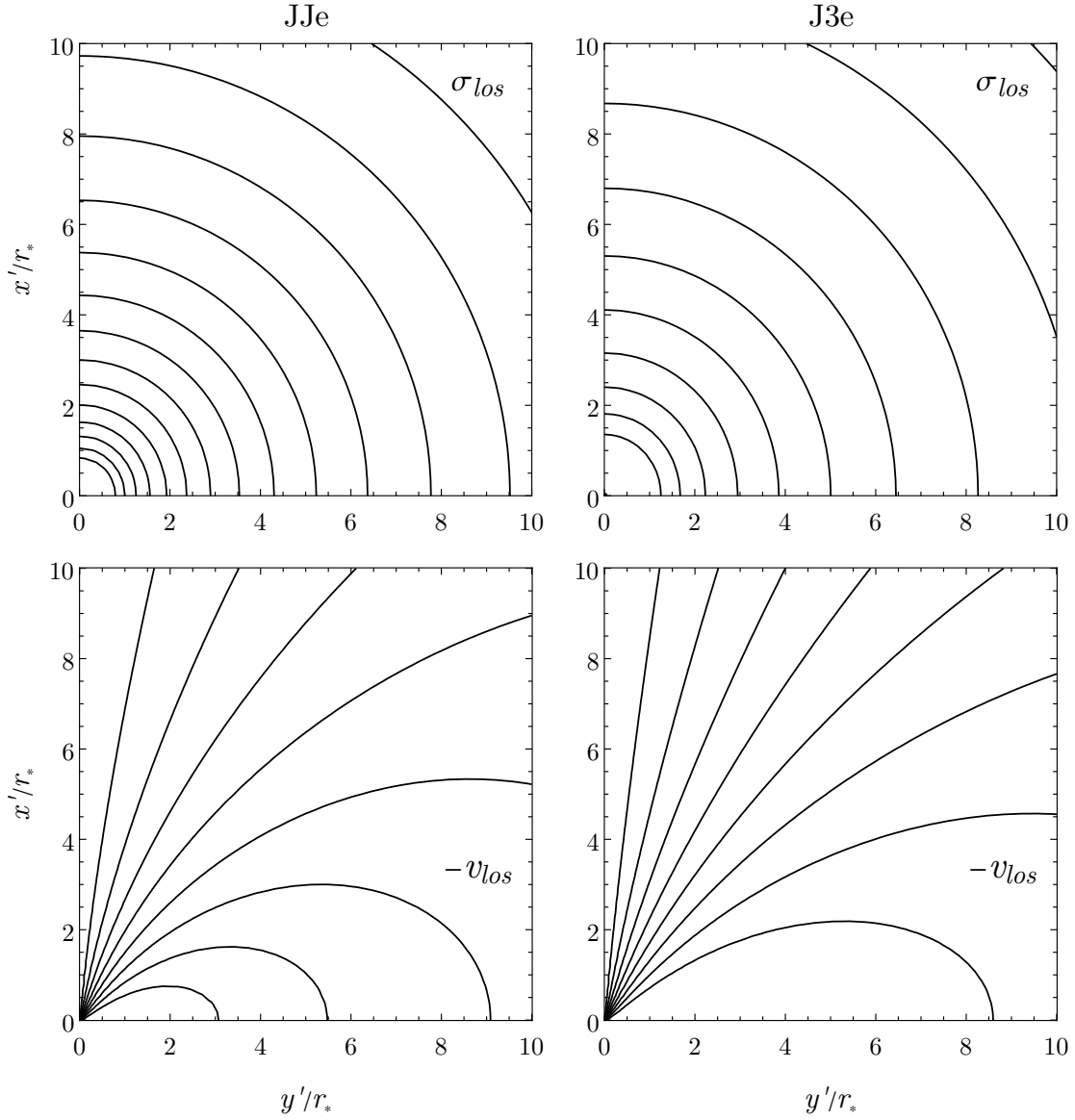

Figure 4.18. Two-dimensional maps of $\sigma_{\rm los}$ (top) and $v_{\rm los}$ (bottom), normalized to $\sqrt{\Psi_{\rm n}}$, for isotropic ($k = 1$) minimum halo models with $\xi = 5$, $\eta_* = 0.1$, $\eta_{\rm g} = 0$, and $\mu = 0$; the chosen inclination angle is $i = 45^\circ$. The innermost contours correspond to values of 0.5 for $\sigma_{\rm los}$, and of 0.16 for $v_{\rm los}$; in each map the other contour lines decrease outward with steps of 0.02.

the JJe one at the same distance from the origin.

CHAPTER 5

Homoeoidally Expanded Models: The Effect of The Quadratic Terms

In the homoeoidal expansion, a given ellipsoidally stratified density distribution, and its associated potential, are expanded in terms of the (small) density flattening parameter η, and usually truncated at the linear order. The truncated density-potential pair obeys exactly Poisson's equation, and it can be interpreted as the first-order expansion of the original ellipsoidal density-potential pair, or as a new autonomous system. In the first interpretation, in the solutions of Jeans's equations the quadratic terms in η must be discarded ("η-linear" solutions), while in the second ("η-quadratic") all terms are retained. Here we study the importance of the quadratic terms by using the ellipsoidal Plummer model and the Perfect Ellipsoid, which allow for fully analytical η-quadratic solutions. These solutions are then compared with those obtained numerically for the original ellipsoidal models, finding that the η-linear models already provide an excellent approximation of the numerical solutions. As an application, the η-linear Plummer model (with a central black hole) is used for the phenomenological interpretation of the dynamics of the weakly flattened and rotating globular cluster NGC 4372, confirming that this system cannot be interpreted as an isotropic rotator, a conclusion reached previously with more sophisticated studies.

5.1 Two interpretations for the Homoeoidal Expansion

In the previous Chapter we discussed the structural and dynamical properties of the JJe and J3e models, two families of galaxy models characterized by small deviations from spherical symmetry. To carry out our study we made use of the homoeoidal expansion method, thus we could investigate in a simple way some important physical phenomena, such as rotation. In this technique, a chosen ellipsoidally stratified density distribution, and the associated potential, are usually expanded and *truncated* at the linear order in terms of the density flattening η, therefore producing, thanks to the linearity of Poisson's equation, an exact density-potential pair. Both the density and the potential, as well as any axisymmetric quantity expanded to linear order in the flattening, take the following generic form:

$$F(R,z) = F_0(r) + \eta F_1(r) + \eta \tilde{R}^2 F_2(r); \tag{5.1}$$

in practice, they are written as a spherical part plus a non-spherical term proportional to η. This very specific structure allows for manageable solutions of Jeans's equations. Of course, *the truncation at the linear order in η of the original density-potential pair is only a matter of convenience, as the linearity of Poisson's equation implies that, at any truncation order in η, the resulting truncated functions are an exact density-potential pair.* However, if we analize the procedure by which the solutions of Jeans's equations are obtained, it is quite easy to realize that the truncated density-potential pair can be viewed in two different ways:

1. as the first-order expansion of the ellipsoidal parent galaxy model in the limit of *small* (i.e. vanishing) flattening;

2. as an independent non-spherical system with *small but finite* flattening.

In the first interpretation, which we call *"η-linear"*, only the linear terms in the flattening must be considered in the solutions of Jeans's equations; in the second interpretation, which we indicate as *"η-quadratic"*, Jeans's equations will contain all terms up to the quadratic ones in the flattening.

The difference in the two interpretations can be better understood if we take a look at the multiplication between two generic homoeidally expanded quantities. For, let us consider the asymptotic expansion for $\eta \to 0$, truncated at the linear order, of two arbitrary axisymmetric functions X and Y, i.e.

$$X(R,z) = X_0(s) + \eta X_1(s) + \eta \tilde{R}^2 X_2(s), \qquad Y(R,z) = Y_0(s) + \eta Y_1(s) + \eta \tilde{R}^2 Y_2(s). \tag{5.2}$$

In the η-linear approximation, consistent with the concept of first-order expansion itself, all the quadratic terms in the flattening must be neglected when performing the multiplication, yielding

$$(XY)_{\eta-\text{linear}} = X_0 Y_0 + \eta(X_0 Y_1 + X_1 Y_0) + \eta \tilde{R}^2 (X_0 Y_2 + X_2 Y_0). \tag{5.3}$$

In the η-quadratic approximation, instead, we interpret X and Y as two quantities formally introduced into the discussion through equation (5.2), "ignoring" how they were obtained, thus considering η a parameter not necessarily infinitesimal; according to this interpretation, no term should be discarded in evaluating their product, which now reads

$$(XY)_{\eta-\text{quadratic}} = (XY)_{\eta-\text{linear}} + \eta^2 X_1 Y_1 + \eta^2 \tilde{R}^2 (X_1 Y_2 + X_2 Y_1) + \eta^2 \tilde{R}^4 X_2 Y_2. \tag{5.4}$$

Right from the start it is useful to clarify an aspect which will guide us throughout the entire discussion, i.e. that *the expression above does not represent the correct expansion for* $\eta \to 0$*, truncated to the quadratic order, of the product of the two starting ellipsoidal quantities* $X(R,z)$ *and* $Y(R,z)$. In fact, to obtain such an expansion, one should start form the expansion of X and Y *truncated up to the quadratic* order in the flattening, and then keep only linear and quadratic terms (thus discarding η^3 and η^4 terms). In other words, *more than one term is missing in equation* (5.4) *in order for it to represent the true quadratic expansion of* XY *for vanishing* η; of course the discarded terms, proportional to η^2 and depending on coordinates, are not necessarily small, and in principle in some regions of space they could be even larger than lower order terms.

For the purposes intended by the present discussion, it is convenient to introduce the following terminology.

- η*-linear solution*: the solution of Jeans's equations in the η-linear interpretation;
- η*-quadratic solution*: the solution of Jeans's equations in the η-quadratic interpretation.

In the previous Chapter we made use of the the first interpretation to discuss in detail the structure and dynamics of two-component axisymmetrical models, showing that it is possible to exploit the homoeoidal expansion technique to conduct a fully analytical treatment (at least for the case of intrinsic dynamics). In light of this dual interpretation for the density-potential pair, one is faced with the interesting problem of investigating the effects of including higher order η-terms in the solutions of Jeans's equations: it is quite obvious that the discarded terms, proportional to η^2 and depending on coordinates, are not necessarily small, and, in principle, in some regions of space they could be even larger than lower order terms. Also, in order to study the difference between the two approaches, and thus analyze the importance of the quadratic terms, it is necessary to have a suitable reference model, which allows to obtain (for example) the exact velocity dispersion and streaming velocity profiles; of course, such a "reference model" is obtained by deriving the exact (analytical or numerical) solutions of Jeans's equations (2.19). Therefore, in this Chapter *we shall compared the* η*-linear and* η*-quadratic solutions with those corresponding to the original ellipsoidal model*, hereafter called *full solution*.

5.2 The η-quadratic solution of Jeans's equations

Let us now see how to write the solutions of Jeans's equations in the η-quadratic interpretation. Following the discussion presented in § 3.3.2, we focus for simplicity on self-gravitating stellar-dynamical model described by the following density-potential pair:

$$\frac{\rho_*(R,z)}{\rho_{\rm n}} = \tilde{\rho}_{*0}(s) + \eta\tilde{\rho}_{*1}(s) + \eta\tilde{R}^2\tilde{\rho}_{*2}(s), \qquad \frac{\Psi_*(R,z)}{\Psi_{\rm n}} = \tilde{\Psi}_{*0}(s) + \eta\tilde{\Psi}_{*1}(s) + \eta\tilde{R}^2\tilde{\Psi}_{*2}(s). \quad (5.5)$$

What is required is simply to *repeat* the same calculations performed to derive the η-linear solutions (3.61) and (3.75), but now *without discarding any terms* from the final result. We also add a BH of mass $M_{\rm BH} = \mu M_*$ at the centre of the system, so that the total gravitational potential reads $\Psi_{\rm T}(R,z) = \Psi_*(R,z) + \Psi_{\rm BH}(r)$, with $\Psi_{\rm BH}(r) = GM_{\rm BH}/r$.

5.2.1 The vertical Jeans equation

The vertical equation makes it possible to calculate the velocity dispersion σ, which we split as usual as $\sigma^2 = \sigma_*^2 + \sigma_{\rm BH}^2$, where σ_* is the contribution due Ψ_*, and $\sigma_{\rm BH}$ denotes the contribution due to the potential $\Psi_{\rm BH}$. These two contributions are formally given by

$$\rho_*\sigma_*^2 = -\int_z^\infty \rho_* \frac{\partial \Psi_*}{\partial z'}\, dz', \qquad \rho_*\sigma_{\rm BH}^2 = -\int_z^\infty \rho_* \frac{\partial \Psi_{\rm BH}}{\partial z'}\, dz'. \tag{5.6}$$

Let us start from σ_*. From equation (5.5) we obtain

$$\begin{aligned}\rho_* \frac{\partial \Psi_*}{\partial z} = \frac{\rho_{\rm n}\Psi_{\rm n}}{a}\frac{z}{r}\Bigg[&\tilde\rho_{*0}\frac{d\tilde\Psi_{*0}}{ds} + \eta\left(\tilde\rho_{*0}\frac{d\tilde\Psi_{*1}}{ds} + \tilde\rho_{*1}\frac{d\tilde\Psi_{*0}}{ds}\right) + \eta\tilde R^2\left(\tilde\rho_{*0}\frac{d\tilde\Psi_{*2}}{ds} + \tilde\rho_{*2}\frac{d\tilde\Psi_{*0}}{ds}\right)\\ &+ \eta^2\tilde\rho_{*1}\frac{d\tilde\Psi_{*1}}{ds} + \eta^2\tilde R^2\left(\tilde\rho_{*1}\frac{d\tilde\Psi_{*2}}{ds} + \tilde\rho_{*2}\frac{d\tilde\Psi_{*1}}{ds}\right) + \eta^2\tilde R^4\tilde\rho_{*2}\frac{d\tilde\Psi_{*2}}{ds}\Bigg];\end{aligned} \tag{5.7}$$

notice that now several additional terms appear with respect to (3.60). By inserting this expression in equation (2.23), and changing the integration variable from z' to r' at fixed R we find

$$\begin{aligned}\frac{\rho_*\sigma_*^2}{\rho_{\rm n}\Psi_{\rm n}} = {}& H_{00}(s) + \eta[H_{01}(s) + H_{10}(s)] + \eta\tilde R^2[H_{02}(s) + H_{20}(s)]\\ &+ \eta^2 H_{11}(s) + \eta^2\tilde R^2[H_{12}(s) + H_{21}(s)] + \eta^2\tilde R^4 H_{22}(s),\end{aligned} \tag{5.8}$$

where the two-index radial function H_{ij} is defined as

$$H_{ij}(s) \equiv -\int_s^\infty \tilde\rho_{*i}(s')\frac{d\tilde\Psi_{*j}(s')}{ds'}\, ds', \qquad (i,j = 0,1,2). \tag{5.9}$$

Therefore, if the the expanded density-potential pair is interpreted as the first-order expansion of the ellipsoidal parent model, *only zero and first-order terms in the flattening must be retained in equation* (5.8), obtaining the so-called η-linear case (3.61) with

$$I_0(s) = H_{00}(s), \qquad I_1(s) = H_{01}(s) + H_{10}(s), \qquad I_2(s) = H_{02}(s) + H_{20}(s); \tag{5.10}$$

in the second interpretation (the η-quadratic case), instead, Jeans's equations contain up to quadratic terms in the flattening.

For what concerns $\sigma_{\rm BH}$, notice that *no additional term with respect to the η-linear case can appear in the explicit expression of $\rho_*\sigma_{\rm BH}^2$ when changing the interpretation for the density-potential pair.* Therefore, $\rho_*\sigma_{\rm BH}^2$ is just given by equation (4.69), which now we rewrite as

$$\frac{\rho_*\sigma_{\rm BH}^2}{\rho_{\rm n}\Psi_{\rm n}} = \mu\big[H_0(s) + \eta H_1(s) + \eta\tilde R^2 H_2(s)\big], \qquad H_i(s) \equiv \int_s^\infty \frac{\tilde\rho_{*i}(t)}{t^2}\, dt. \tag{5.11}$$

5.2.2 The radial Jeans equation

As for the velocity dispersion, we split Δ in the two contributions as Δ_* and $\Delta_{\rm BH}$, which are formally obtained as

$$\rho_*\Delta_* = -R[\rho_*, \Psi_*], \qquad \text{where} \qquad [\rho_*, \Psi_*] = \int_z^\infty \left(\frac{\partial\rho_*}{\partial R}\frac{\partial\Psi_*}{\partial z'} - \frac{\partial\rho_*}{\partial z'}\frac{\partial\Psi_*}{\partial R}\right) dz', \tag{5.12}$$

and

$$\rho_*\Delta_{\rm BH} = -R[\rho_*, \Psi_{\rm BH}], \qquad \text{where} \qquad [\rho_*, \Psi_{\rm BH}] = \int_z^\infty \left(\frac{\partial \rho_*}{\partial R}\frac{\partial \Psi_{\rm BH}}{\partial z'} - \frac{\partial \rho_*}{\partial z'}\frac{\partial \Psi_{\rm BH}}{\partial R} \right) dz'. \quad (5.13)$$

Let us start with Δ_*. For the specific density-potential pair (5.5) we have

$$\begin{aligned} \frac{[\rho_*, \Psi_*]}{\rho_{\rm n}\Psi_{\rm n}} &= \eta[\tilde{\rho}_{*0}(s), \tilde{R}^2\tilde{\Psi}_{*2}(s)] + \eta[\tilde{R}^2\tilde{\rho}_{*2}(s), \tilde{\Psi}_{*0}(s)] \\ &+ \eta^2[\tilde{\rho}_{*1}(s), \tilde{R}^2\tilde{\Psi}_{*2}(s)] + \eta^2[\tilde{R}^2\tilde{\rho}_{*2}(s), \tilde{\Psi}_{*1}(s)] + \eta^2[\tilde{R}^2\tilde{\rho}_{*2}(s), \tilde{R}^2\tilde{\Psi}_{*2}(s)], \end{aligned} \quad (5.14)$$

where now three additional (quadratic) terms appear with respect the η-linear case (3.66). Following a procedure exaclty analogous to that used in reducing equation (3.66) to (3.75), it is straightforward to show that the η-quadratic solution of equation (5.12) can be written as

$$\frac{\rho_*\Delta_*}{\rho_{\rm n}\Psi_{\rm n}} = 2\eta\tilde{R}^2[K_{02}(s) + \eta K_{12}(s) + \eta\tilde{R}^2 K_{22}(s)], \quad (5.15)$$

where we have defined

$$K_{ij}(s) \equiv H_{ij}(s) - \tilde{\rho}_i(s)\tilde{\Psi}_j(s) + H_{ji}(s); \quad (5.16)$$

since the additional terms are all proportional to η^2, even in the η-quadratic case the quantity Δ_* vanishes for $\eta = 0$.

Also in the case of $\Delta_{\rm BH}$, no additional term appears with respect the corresponding η-linear case, which in this Section rewrite as

$$\frac{\rho_*\Delta_{\rm BH}}{\rho_{\rm n}\Psi_{\rm n}} = 2\mu\eta\tilde{R}^2 H_2(s). \quad (5.17)$$

5.3 The ellipsoidal Plummer model and the Perfect Ellipsoid

For a quantitative discussion of the effect of quadratic terms on the solutions of Jeans's equations, we consider two simple ellipsoidal models: the Perfect Ellipsoid (de Zeeuw & Lynden-Bell 1985, hereafter ZL85) and the ellipsoidal Plummer (1911, hereafter P11) models.

5.3.1 Structure of the models

The P11 and ZL85 models are axisymmetric models, with total mass M and scale length a, described by the following density distribution:

$$\rho_*(R,z) = \rho_{\rm n} \times \frac{\tilde{\rho}_*(m)}{q}, \qquad \tilde{\rho}_*(m) = \begin{cases} \dfrac{3}{(1+m^2)^{5/2}}, & \text{(P11)}, \\ \dfrac{4}{\pi(1+m^2)^2}, & \text{(ZL85)}. \end{cases} \quad (5.18)$$

In the previous equation, $\rho_{\rm n} \equiv M_*/(4\pi a^3)$ is the usual density scale, a is a scale lenght, and

$m^2 = R^2/a^2 + z^2/(q^2a^2)$ labels spheroidal surfaces of axial ratio $q \equiv 1 - \eta$. A special feature of these models is that they have a constant density in the central regions; at large distances from the centre, instead, $\tilde{\rho}_*$ fall of as $1/m^5$ for P11 models, while as $1/m^4$ for ZL85 ones. From equation (3.5)-(3.36), the dimensionless functions appearing in the explicit-R formulation (5.5) are

$$\tilde{\rho}_{*i}(\mathrm{P11}) = \begin{cases} \dfrac{3}{(1+s^2)^{5/2}}, & (i=0), \\ \dfrac{3(1-4s^2)}{(1+s^2)^{7/2}}, & (i=1), \\ \dfrac{15}{(1+s^2)^{7/2}}, & (i=2), \end{cases} \qquad \tilde{\rho}_{*i}(\mathrm{ZL85}) = \begin{cases} \dfrac{4}{\pi(1+s^2)^{2}}, & (i=0), \\ \dfrac{4(1-3s^2)}{\pi(1+s^2)^{3}}, & (i=1), \\ \dfrac{16}{\pi(1+s^2)^{3}}, & (i=2). \end{cases} \tag{5.19}$$

We know that in the homoeoidal expansion there is an upper limit on η (which depends on the truncation order); then, for η smaller than the critical value, the truncated density is nowhere negative: from equation (3.30), $\eta \leq 1/4$ for P11 models, and $\eta \leq 1/3$ for ZL85 models. Reassuringly, these critical values are quite large, allowing to deal with moderately flattened stellar systems such as those will be discussed in § 5.4. In general, as we have seen in the previous chapters, the density tends to become negative along the z-axis for η close to the limit, producing densities with a "torus-like" structure (similar to the Binney logarithmic halo for potential flattening near the critical value; see BT08), and to complex shifted models (e.g. Ciotti & Giampieri 2007). In Fig. 5.1 we show the isodensity contours of P11 and ZL85 models, for two different η values. Black dashed lines show the original ellipsoidal models in equation (5.18), while red solid lines show the homoeoidally expanded models in equation (5.19). The figure shows how well the truncated density reproduces the original model with $\eta = 0.15$, and how a toroidal shape in the outer parts of the systems appears for η approaching the critical value. Of course, truncating the density up to the quadratic order in η increases the upper limit on the flattening, and both black and red isodensities are almost indistinguishable (see Fig. 5.2).

For what concerns the gravitational potential Ψ_*, the three dimensional functions defining its homoeoidal expansion can be obtained by making use of equations (3.16)-(3.36); simple calculations yield

$$\tilde{\Psi}_{*i}(\mathrm{P11}) = \begin{cases} \dfrac{1}{(1+s^2)^{1/2}}, \\ \dfrac{3s^2+2}{s^2(1+s^2)^{3/2}} - \dfrac{2\,\mathrm{arcsinh}\,s}{s^3}, \\ -\dfrac{4s^2+3}{s^4(1+s^2)^{3/2}} + \dfrac{3\,\mathrm{arcsinh}\,s}{s^5}, \end{cases} \qquad \tilde{\Psi}_{*i}(\mathrm{ZL85}) = \begin{cases} \dfrac{2\arctan s}{\pi s}, \\ \dfrac{4\arctan s}{\pi s^3} - \dfrac{2(s^2+2)}{\pi s^2(1+s^2)}, \\ -\dfrac{6\arctan s}{\pi s^5} + \dfrac{2(2s^2+3)}{\pi s^4(1+s^2)}, \end{cases} \tag{5.20}$$

for $i = 0, 1, 2$, from top to bottom, respectively.

There are at least two quantities, describing the structure of the P11 and ZL85 models, which can be obtained analytically for the (non-expanded) ellipsoidal case: the distribution of mass $M_*(R, z)$ and the circular velocity $v_c(R)$. The mass profile associated to the previous density distributions is obtained from equation (3.6): simple algebra yields

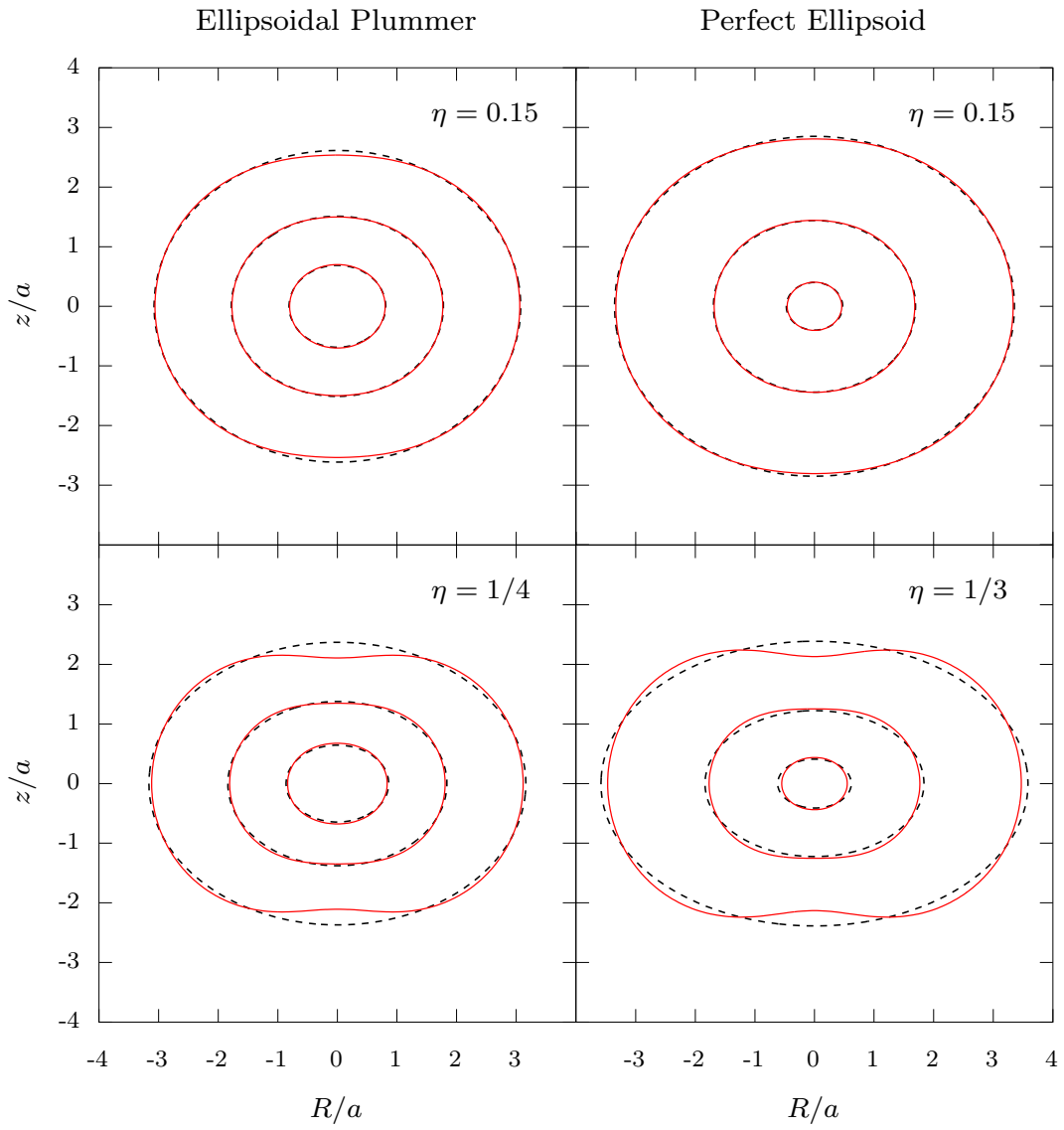

Figure 5.1. Isodensity contours, normalized to $\rho_{\rm n}$, for the P11 (left) and ZL85 (right) models. Dashed lines refer to the ellipsoidal (original) model, while solid red lines to the η-linear expansion of the density, as given in equation (5.19). Contours correspond to values of 1, 10^{-1}, and 10^{-2} from inside to outside. The bottom panels show the case of the critical flattenings $\eta = 1/4$ for P11 models, and $\eta = 1/3$ for ZL85 ones: for larger values of η the truncated density would be negative near the z-axis. The outermost expanded contours differ most from the elliptical shape as η increases.

$$M_*(R,z) = M_* \times \tilde{M}_*(m), \qquad \tilde{M}_*(m) = \begin{cases} \dfrac{m^3}{(1+m^2)^{3/2}}, & \text{(P11)}, \\ \dfrac{2}{\pi}\left(\arctan m - \dfrac{m}{1+m^2}\right), & \text{(ZL85)}. \end{cases} \tag{5.21}$$

As expected, the cumulative mass converges to M_* for $m \to \infty$, whereas the so called half-mass radius (i.e. the ellipsoidal radius m containing half the total mass) equals $\simeq 1.305$ for P11 models, and $\simeq 2.264$ for ZL85 ones. Regarding the circular velocity $v_{\rm c}$, it can be obtained via the equation (2.18), which can be rewritten in dimensionless form as

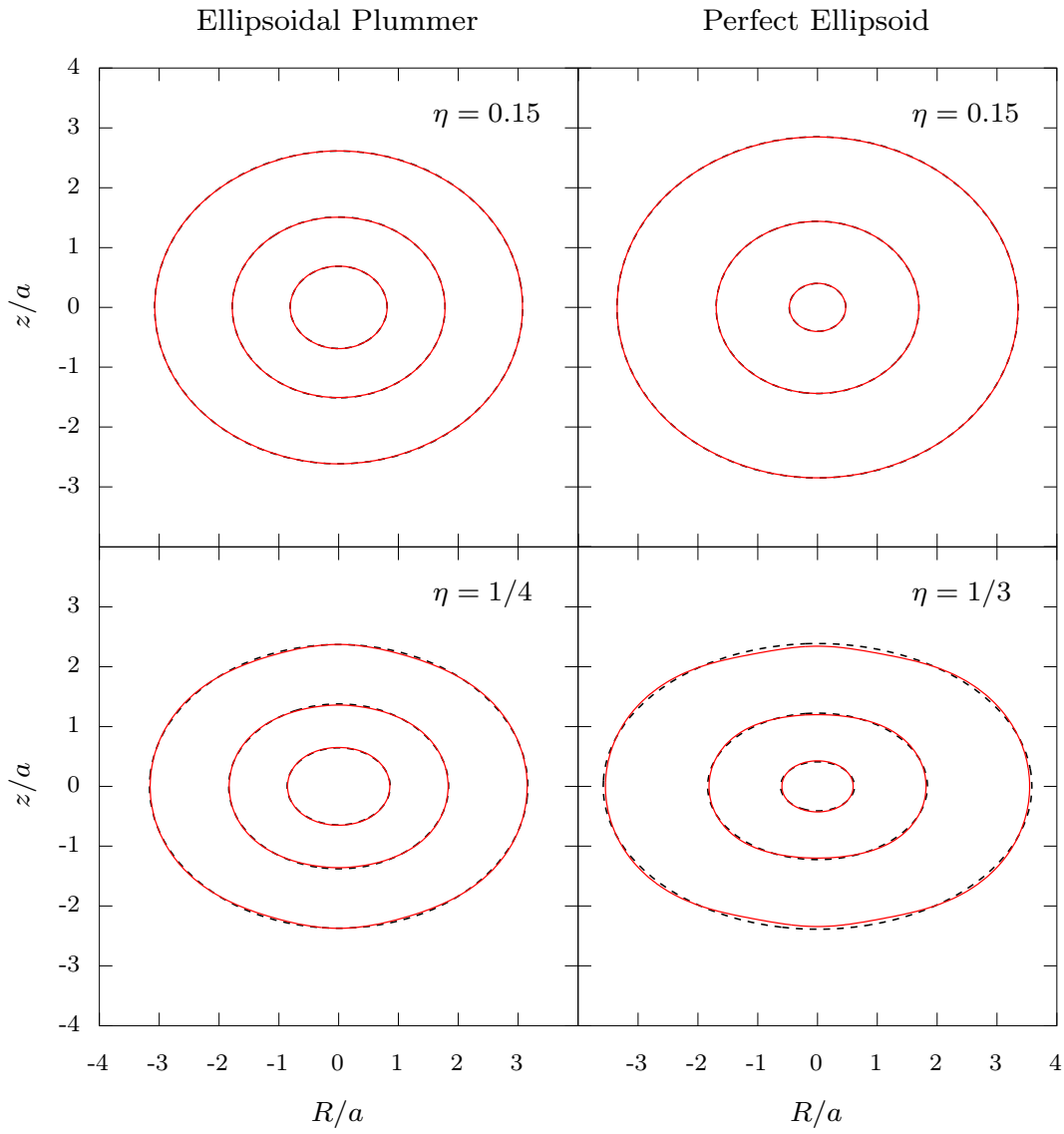

Figure 5.2. Same as Fig. 5.1, where now the density is expanded up to the quadratic order in η.

$$\frac{v_*^2(R)}{\Psi_{\rm n}} = \frac{\tilde{R}^2}{2}\int_0^\infty \frac{\tilde{\rho}_*\big(\tilde{R}/\sqrt{1+u}\big)}{(1+u)^2\sqrt{q^2+u}}\,du = \int_0^{\tilde{R}} \frac{\tilde{\rho}_*(t)t^2dt}{(\tilde{R}^2-p^2t^2)^{1/2}}, \tag{5.22}$$

where $p^2 \equiv 1-q^2$, and the latter identity follows from the first by making use of the substitution $t \equiv \tilde{R}/\sqrt{1+u}$. In the case of the models we are examining, v_* can be determined analytically. For what concerns the P11 models, by inserting equation (5.18) in (5.22) we obtain

$$\frac{v_*^2(R)}{\Psi_{\rm n}} = \int_0^{\tilde{R}} \frac{3t^2dt}{(1+t^2)^{5/2}(\tilde{R}^2-p^2t^2)^{1/2}}. \tag{5.23}$$

Now, defining $t \equiv \tilde{R}\sin\theta/(p^2+\tilde{R}^2\cos^2\theta)^{1/2}$, a substitution suggested in BT87 (equation 2-94) for ellipsoidal densities, after some lengthy but straightforward reductions we find

$$\frac{v_*^2(R)}{\Psi_\mathrm{n}} = \frac{3\tilde{R}^2}{(p^2+\tilde{R}^2)^{3/2}} \int_0^\phi \sin^2\theta \sqrt{1+n^2\cos^2\theta}\, d\theta, \tag{5.24}$$

where we have defined

$$\phi \equiv \arcsin\sqrt{\frac{p^2+\tilde{R}^2}{1+\tilde{R}^2}}, \qquad\qquad n^2 \equiv \frac{\tilde{R}^2}{p^2+\tilde{R}^2}. \tag{5.25}$$

The solution of the integral at the right-hand side of equation (5.24) requires the use of elliptic integrals; with some care one can explicitly obtain

$$\frac{v_*^2(R)}{\Psi_\mathrm{n}} = \frac{p^2\mathbb{F}(\phi,k)+(\tilde{R}^2-p^2)\mathbb{E}(\phi,k)}{(p^2+\tilde{R}^2)^{3/2}} - \frac{q\tilde{R}^2}{(p^2+\tilde{R}^2)(1+\tilde{R}^2)^{3/2}}, \qquad k \equiv \sqrt{n}. \tag{5.26}$$

where $\mathbb{F}(\phi,k)$ and $\mathbb{E}(\phi,k)$ are the Legendre elliptic integrals of first and second kind in trigonometric form (e.g. Byrd & Friedman 1971; Gradshteyn & Ryzhik 2007; se also C21, Appendix A.2.2). For ZL85, with the same substitution used to reduced the integral in (5.23) we find

$$\frac{v_*^2(R)}{\Psi_\mathrm{n}} = \frac{4\tilde{R}^2}{\pi(p^2+\tilde{R}^2)^{3/2}} \int_0^\phi \sin^2\theta\, d\theta, \tag{5.27}$$

whence we readily obtain

$$\frac{v_*^2(R)}{\Psi_\mathrm{n}} = \frac{2\tilde{R}^2}{\pi(p^2+\tilde{R}^2)}\left[\frac{\phi}{(p^2+\tilde{R}^2)^{1/2}} - \frac{q}{1+\tilde{R}^2}\right]. \tag{5.28}$$

Equations (5.21), (5.26) and (5.28) are *exact for any finite value of the flattening*; with some work, they can be expanded to any desired order in η, thus providing a check for the corresponding homoeoidally expressions. In particular, regarding the circular velocity, its homoeoidal expansion is given by equation (4.50): for the considered models, the dimensionless radial functions $\tilde{v}_{*0}$ and $\tilde{v}_{*1}$ are given by

$$\tilde{v}_{*i}^2(\mathrm{P11}) = \begin{cases} \dfrac{\tilde{R}^2}{(1+\tilde{R}^2)^{3/2}}, \\[2ex] \dfrac{3\,\mathrm{arcsinh}\,\tilde{R}}{\tilde{R}^3} - \dfrac{4\tilde{R}^2+3}{\tilde{R}^2(1+\tilde{R}^2)^{3/2}}, \end{cases} \qquad \tilde{v}_{*i}^2(\mathrm{ZL85}) = \begin{cases} \dfrac{2\arctan\tilde{R}}{\pi\tilde{R}} - \dfrac{2}{\pi(1+\tilde{R}^2)}, \\[2ex] \dfrac{2(2\tilde{R}^2+3)}{\pi\tilde{R}^2(1+\tilde{R}^2)} - \dfrac{6\arctan\tilde{R}}{\pi\tilde{R}^3}, \end{cases} \tag{5.29}$$

for $i = 0, 1$, from top to bottom, respectively. It is straightforward to prove that these expressions are in perfect agreement with a direct linear expansion of (5.26) and (5.28) for $\eta \to 0$.

5.3.2 Dynamics of the models

We can now address the first goal of this work, i.e., *to evaluate how η-linear and η-quadratic solutions compare between them and with respect to the full solutions for genuine ellipsoidal models.*

For now, let us concentrate on the stellar components. As a first step, we need a practical procedure to derive the profiles of σ_*^2 and Δ_*; such a procedure is analogous to that we discussed in § 4.6 for the case of the JJe and J3e models, and is shortly described as follows.

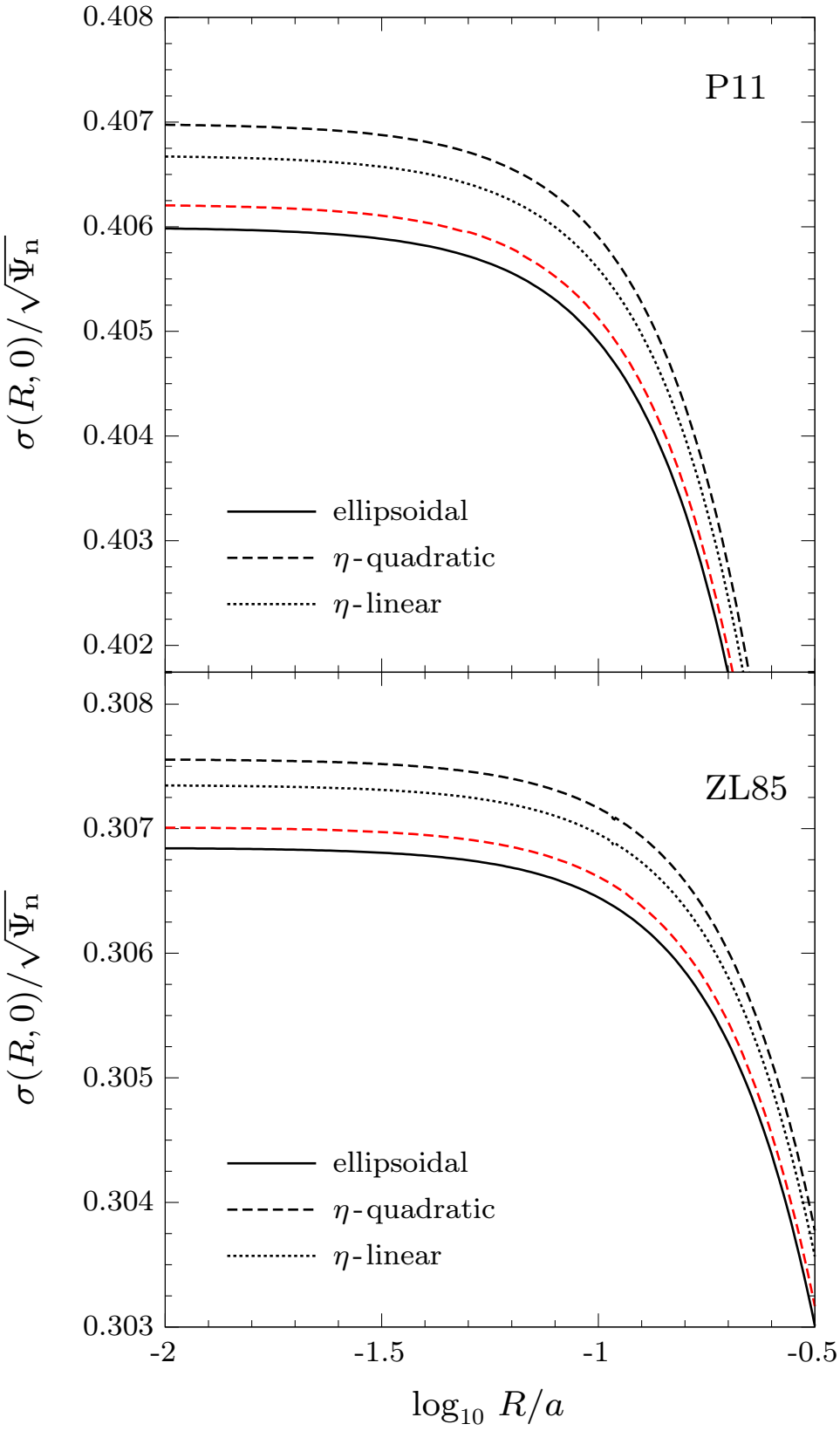

Figure 5.3. Radial profile of the velocity dispersion σ in the equatorial plane ($z = 0$), with $\eta = 0.1$, and without a central BH ($\mu = 0$). The homoeoidal approximation reproduces remarkably well the full solution (solid line), over the displayed radial range of $0.01 < R/a \lesssim 0.32$. The values of σ for the η-linear models overestimate the full solution, and retaining the quadratic terms in the flattening further increases this overestimate. The red dashed line shows the expansion up to the quadratic order in η of the full solution.

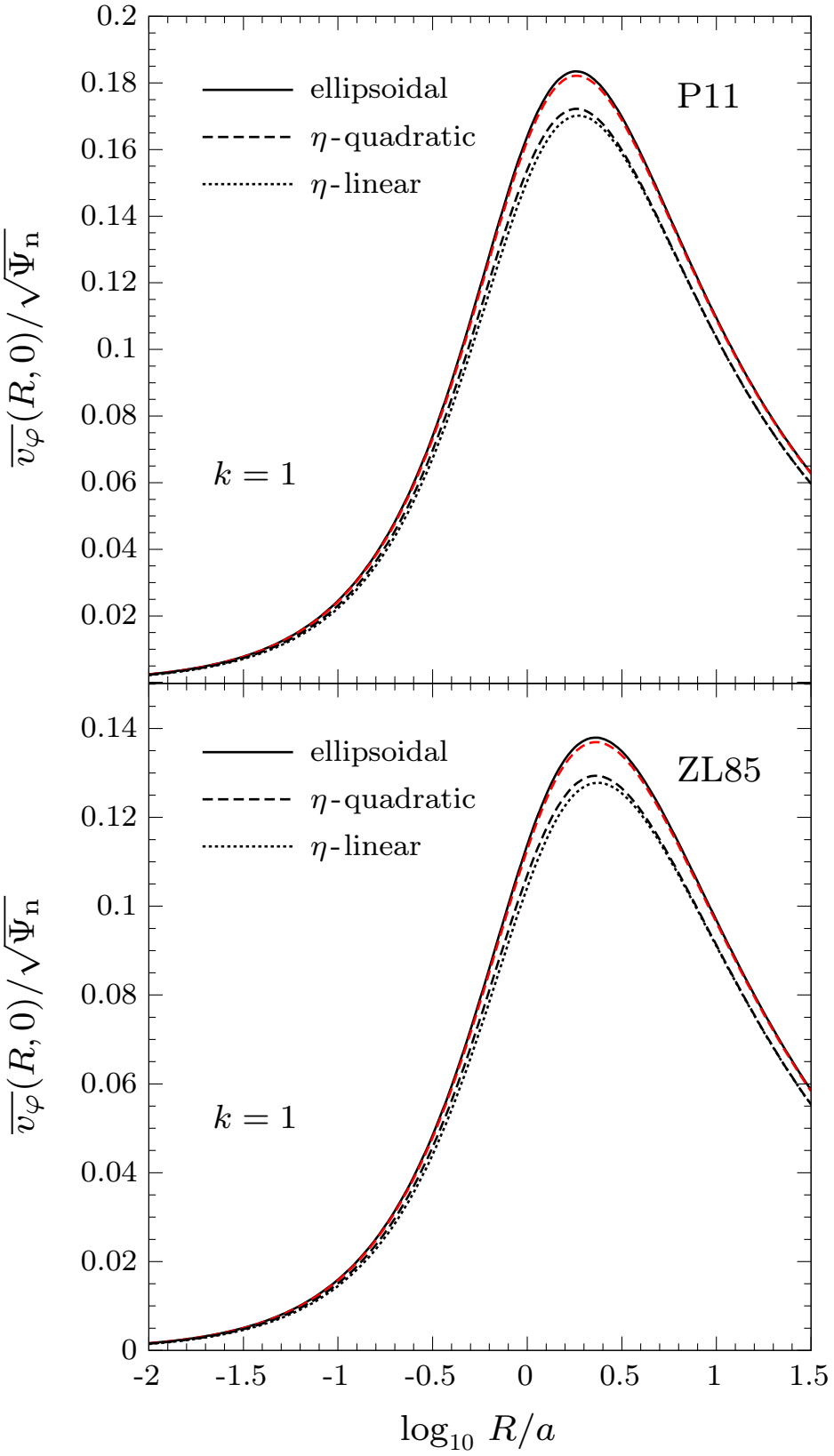

Figure 5.4. Radial trend of $\overline{v_\varphi}$ on the equatorial plane, for the same models on the left, and with the same meaning of the line-type; the case of the isotropic rotator is shown. The values of $\overline{v_\varphi}$ for the η-linear and η-quadratic models underestimate those of the full solution. The red dashed line shows the expansion up to the quadratic order in η of the full solution.

- The η-linear σ_*^2 (i.e. the square of the velocity dispersion in the η-linear interpretation) is obtained dividing the expression at the right-hand side of equation (5.8), *truncated at the linear order in the flattening*, by the *linear* homoeoidal expansion of the density.
- The η-quadratic σ_*^2 is obtained dividing the *full expression* at the right-hand side of equation (5.8) by the *linear* homoeoidal expansion of the density.
- The full σ_*^2 is recovered by solving *numerically* the integral at the right-hand side of equation (3.58), and dividing by the *ellipsoidal* density (5.18).

Once σ_*^2 is obtained, σ_* is derived just by extracting its square root. *A procedure totally analogous to the previous one, based however on the equations* (5.15) *and* (3.59)*, is used to derive the profile of* Δ_*, from which $\overline{v_{\varphi_*}}$ (i.e. the component of the straming velocity $\overline{v_\varphi}$ due the stars) is obtained as $k\sqrt{\Delta_*}$. It is important to note that the radial functions $H_{ij}(s)$ and $K_{ij}(s)$ are *analytical* for both P11 and ZL85 models, and are given explicitly in Appendix C: both the η-linear and η-quadratic solutions are thus analytical, so that *a fully analytical study can be carried out for the two models when considering small values of the density flattening.* In Figs. 5.3 and 5.4 we show respectively the velocity dispersion σ and the isotropic ($k = 1$) streaming velocity $\overline{v_\varphi}$, in the equatorial plane $z = 0$, for P11 and ZL85 models with a flattening $\eta = 0.1$; for simplicity we plot the situation in absence of the central BH (i.e. $\mu = 0$).

We first focus on σ. For each model, Fig. 5.3 show the full solution for the ellipsoidal model (black solid line), the η-linear solution (dotted line), and the η-quadratic solution (dashed line). Qualitatively, σ is flat in the central regions and, at a distance much smaller than a scale lenght, it gradually begins to decrease until vanishing; this particular radial trend will be analyzed in detail later, when we shall discuss quantitatively the asymptotic behaviour of the velocity fields. In general, notice how close the full solution and those in the homoeoidal approximation are, over the whole radial range: the percentual differences are so small (less than 0.3%; notice the limited range of values on the σ-axis) to be completely negligible in all practical applications. Therefore, we can conclude that *the effect of quadratic* η *terms is negligible, and that the* η*-linear approximation, with its simplifications, can be safely used to model systems with low flattening.* Moreover, an interesting result emerges from the figure. For both models, *the* η*-linear solution always overestimates the full solution* (with differences decreasing for increasing R), and so do the other approximations; however, the η-quadratic solutions differ from the full solution *more* than the η-linear solutions. This result might be unexpected, since a quadratic approximation should perform better than a linear one. But it should be recalled that the η-quadratic solution is *not* the quadratic approximation of the full solution; to better clarify this point (repeatedly mentioned only in words), also the *true* quadratic approximation $(\rho\sigma^2)_{\text{quadratic}}$ is shown in Fig. 5.3 (dashed red lines), confirming that $(\rho\sigma^2)_{\text{quadratic}}$ *performs better than the* η*-linear solution* $(\rho\sigma^2)_{\eta-\text{linear}}$. In principle, the quadratic expansion of the full solution could be computed formally starting from the homoeoidal truncation of the density-potential pair *up to the quadratic order in* η, solving Jeans's equations, and finally discarding all terms in flattening of order higher than quadratic; however, instead of performing such laborious mathematical calculations, *we prefer to compute numerically the true quadratic approximation for* $\rho\sigma^2$ as

$$(\rho\sigma^2)_{\text{quadratic}} \simeq (\rho\sigma^2)_{\eta-\text{linear}} + \eta^2 Q, \qquad Q \equiv \lim_{\eta\to 0} \frac{(\rho\sigma^2)_{\text{full}} - (\rho\sigma^2)_{\eta-\text{linear}}}{\eta^2}, \tag{5.30}$$

where $(\rho\sigma^2)_{\text{full}}$ denotes the full (numerical) solution. In the formula above, *the numerical values of* η *are reduced until convergence is reached (but maintained large enough to avoid numerical fluctuations).* The fact that the η-quadratic solution is *not* the quadratic truncation of the expansion of the full solution is made apparent by the fact that the black dashed lines (the η-quadratic

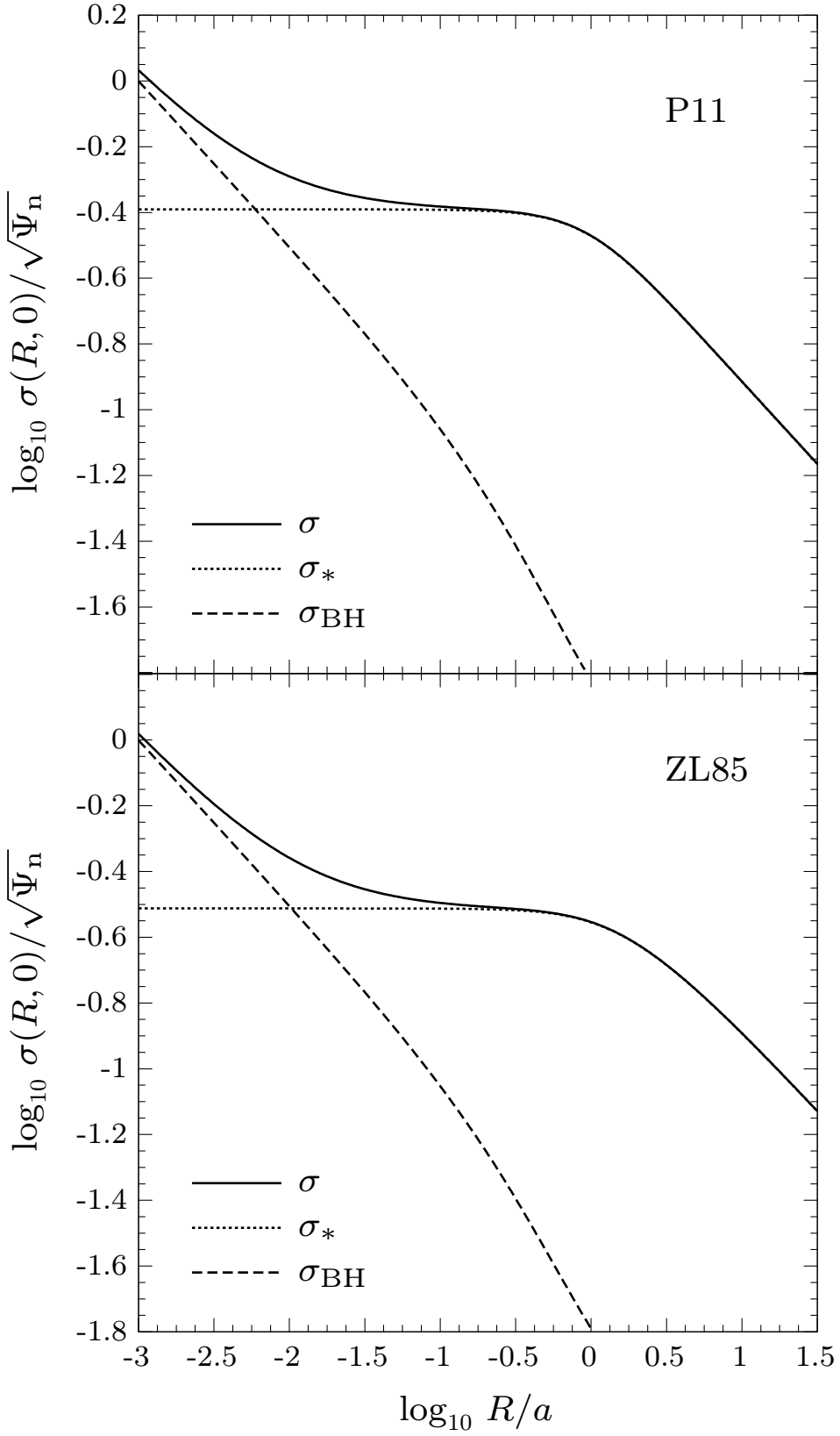

Figure 5.5. The η-linear modelling of an isotropic ($k = 1$) system with $\eta = 0.1$, and a central BH with $\mu = 0.001$. Solid lines show σ on the equatorial plane ($z = 0$). Dotted and dashed lines show respectively the contributions of the stellar-dynamical model and the BH. Due to the presence of the BH, the velocity dispersion diverges at small radii as $1/\sqrt{R}$.

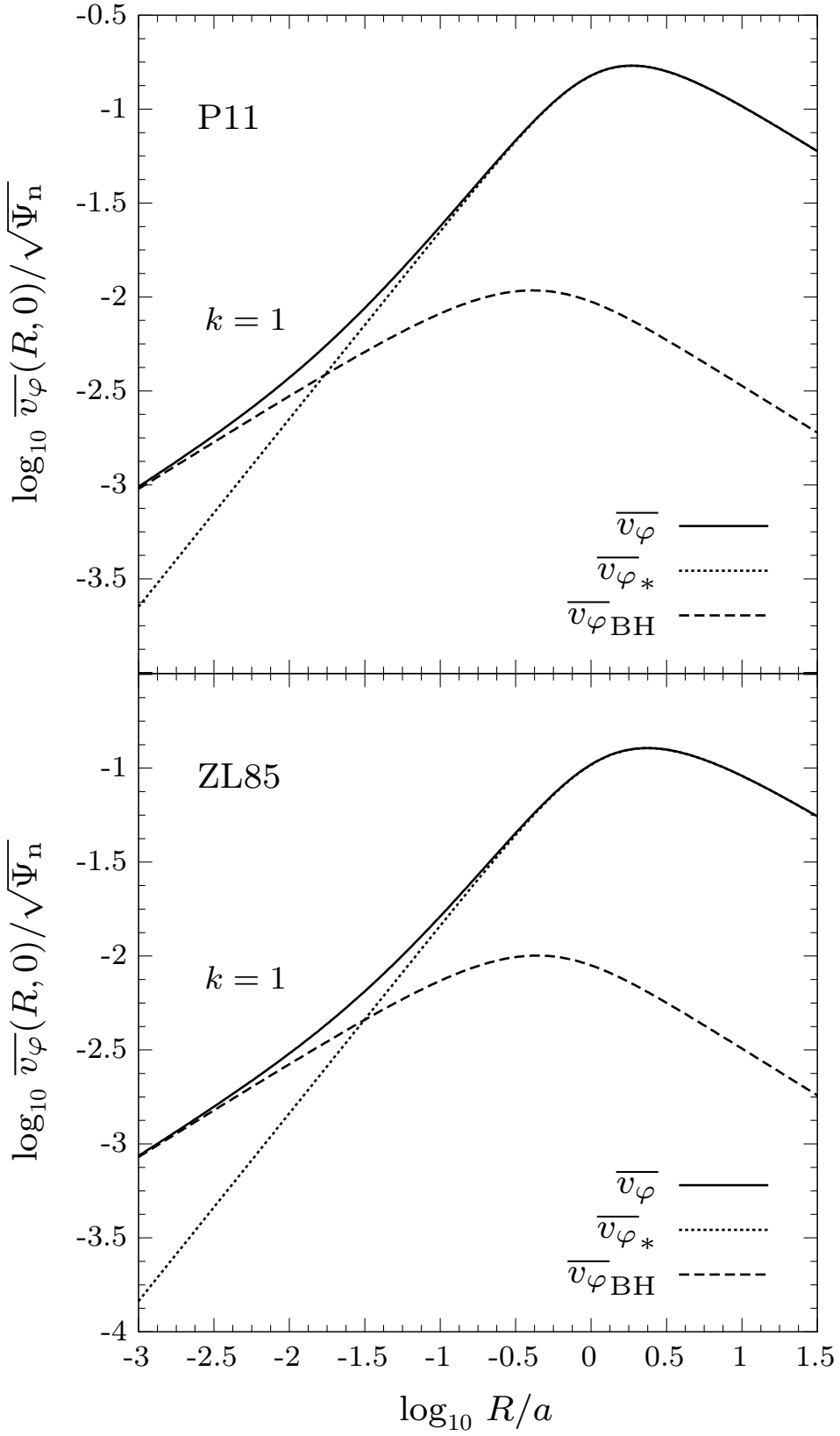

Figure 5.6. The η-linear modelling of an isotropic ($k = 1$) system with $\eta = 0.1$, and a central BH with $\mu = 0.001$. Solid lines show $\overline{v_\varphi}$ on the equatorial plane ($z = 0$). Dotted and dashed lines show respectively the contributions of the stellar-dynamical model and the BH. Due to the presence of the BH, the streaming velocity vanishes towards the centre as $\sqrt{R}$.

solutions) are more distant from the solid line than the η-linear solution (dotted lines); this is due to the missing quadratic terms, which can be shown to be collectively negative. The conclusion is that, when using the homoeoidal expansion to describe an ellipsoidal system, the η-linear interpretation is to be preferred to the η-quadratic solution, not only for its greater simplicity, but also for its better accuracy.

Figure 5.4 show the corresponding streaming velocity profile $\overline{v_\varphi}$ in the equatorial plane for the isotropic case ($k = 1$); the radial range has been extended to $R \simeq 32a$, in order to display the whole peak present at around $R \simeq 1.6a$. Satoh's decomposition can be adopted for these models given the positivity of Δ, which is to be expected since Δ is nowhere negative for an oblate self-gravitating ellipsoid (see § 2.2.1). Several of the comments concerning the solutions for the velocity dispersion apply also to $\overline{v_\varphi}$, in particular that on the almost perfect (for practical purposes) coincidence of the η-linear, η-quadratic, and full solutions. However, the η-linear solutions are now the most discrepant with respect to the full solutions, followed, in order, by the η-quadratic and the true quadratic expansion.

Let us now move to discuss the effects of a central BH. Since we have that the maintaining of the quadratic terms in the flattening does not appreciably affect the solutions of Jeans's equations, we shall focus on the η-lnear models. Figures 5.5 and 5.6 show the η-linear. solution for $\mu = 0.001$ (i.e. in presence of a central BH of mass $M_{\rm BH} = 10^{-3}M$). In both figures, the solid line is the total, the dashed line is the BH contribution, and the dotted line is the model for the stellar component already shown in Figs. 5.3 and 5.4; the radial range is now extended down to $R = 10^{-3}a$ to better appreciate the dynamical effects of the BH. From equation (5.21), the radius contaning the fraction $\mu = 10^{-3}$ of the total mass (of the spherical model), that is the commonly adopted estimate for the dynamical radius of the BH (see Chapter 4 in BT08), is $R_{\rm dyn} \approx 0.1a$. This value is nicely close to the position where the lines corresponding to the total σ and $\overline{v_\varphi}$ start to deviate from the stellar-dynamical model contributions[1]. In particular, the BH determines an increase of σ towards the centre that goes as $R^{-1/2}$; instead, $\overline{v_\varphi}$ still vanishes at the centre even in the presence of the BH. This property can be quantified with the asymptotic analysis of Δ_* and $\Delta_{\rm BH}$ near the center: without the BH, the isotropic $\overline{v_\varphi}$ decreases at small radii as R, whereas in presence of the BH it decreases as $R^{1/2}$; thus, $\overline{v_\varphi}$ does not diverge at the centre, as instead σ and $v_{\rm c}$ do. This is explained by noticing that, for a generic model density with a central profile $(1+m^2)^{-\alpha}$, $\Delta_{\rm BH} \propto R^2/r$ at small radii, and so in Satoh's decomposition $\overline{v_\varphi}$ vanishes towards the centre, while $\overline{v_\varphi^2}$ diverges as σ^2. Of course, when adopting a different decomposition of $\overline{v_\varphi^2}$ (such as that in equation 13.107 in C21; see also De Deo et al. 2024), a central cusp in $\overline{v_\varphi}$ would be obtained. We conclude that special care should be used when interpreting the results of models used to predict the effects of a central BH on the streaming velocity field of the stars.

The previous discussion focused on the different solutions on the equatorial plane. It is of course important to consider also their behavior over the full (R, z) plane, as 2D spectroscopy is nowadays routinely performed (e.g. Emsellem et al. 2007; Krajnović et al. 2008; Jeong et al. 2009). In Fig. 5.7 we show the two-dimensional maps of σ, σ_φ, and $\overline{v_\varphi}$ (for $k = 1$), for a P11 model with $\eta = 0.1$ and $\mu = 0$; contours are displayed for the full and the η-linear solutions. The comparison shows that the η-linear σ keeps extremely close to that of the full solution, even outside the equatorial plane; a similar agreement persists for σ_φ, while it becomes slightly worse for $\overline{v_\varphi}$. However, even if the shape of the isorotational surfaces in the η-linear approximation seems more discrepant from that of the true solution than for the σ and σ_φ cases, the $\overline{v_\varphi}$ values of the η-linear and full solutions along cuts at fixed z are still very similar, as we verified with plots of these cuts (where indeed the differences in velocity are of the same extent as in Fig. 5.3).

[1] Alternatively (e.g., see Binney & Tremaine 2008, § 4.8.1), the radius of the sphere of influence of the BH can be defined as the distance from the centre at which the circular velocity due to the BH equals the projected velocity dispersion, i.e. $R_{\rm infl} = GM_{\rm BH}/\sigma^2_{\rm los}(R_{\rm infl})$. For our models, in the limit of spherical symmetry, and under the assumption of isotropic velocity dispersion, $R_{\rm infl} \simeq 6\mu a$, almost 17 times smaller than $R_{\rm dyn}$.

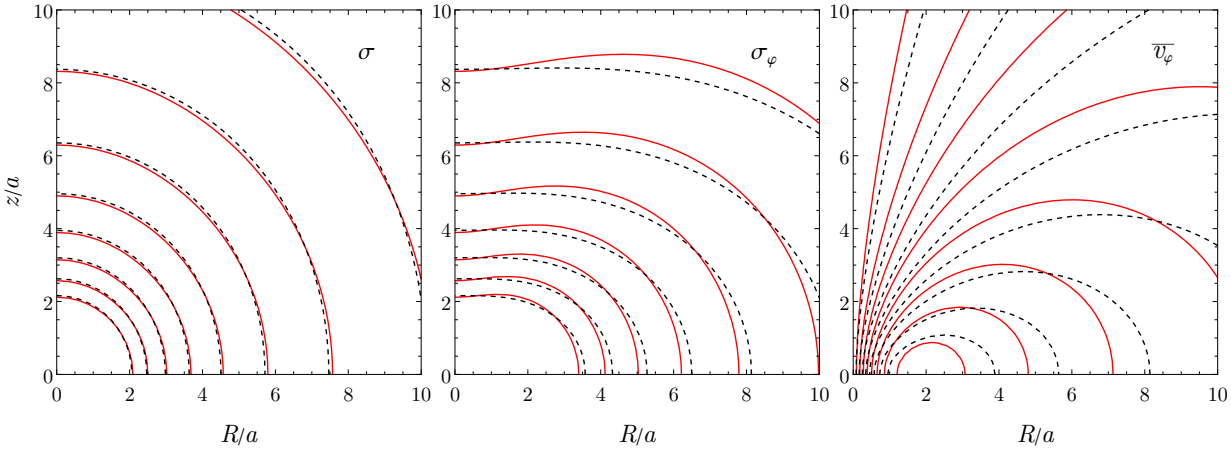

Figure 5.7. Maps of σ (left), σ_φ (middle, $k=0$), and $\overline{v_\varphi}$ (right, $k=1$), in units of $\sqrt{\Psi_\mathrm{n}}$, for P11 models with $\eta=0.1$ and $\mu=0$. Dashed lines show the full solution, solid red lines show the solution of the η-linear modelling. The innermost contour corresponds to values of 0.26 for the normalized σ and σ_φ, and of 0.16 for $\overline{v_\varphi}$. The values for the other contour lines decrease outward with steps of 0.02.

The asymptotic behaviour at small radii

An interesting feature of the two presented models is their constant velocity dispersion at the centre. This is quite evident from the inspection of Fig. 5.3, where the displayed radial range is $0.01a < R \lesssim 0.32a$. This is confirmed by the asymptotic behaviour of equation (5.8) at small radii (i.e. $s \to 0$). In fact, from Taylor expansion with $\tilde{R} = s\sin\vartheta$ we obtain

$$\frac{\rho_*\sigma_*^2}{\rho_\mathrm{n}\Psi_\mathrm{n}} \sim \begin{cases} \dfrac{2+4(67-96\ln 2)\eta+3(355-512\ln 2)\eta^2}{4}, & \text{(P11)},\\[2ex] \dfrac{3(32-3\pi^2)+8(9\pi^2-88)\eta+24(15\pi^2-148)\eta^2}{6\pi^2}, & \text{(ZL85)}, \end{cases} \tag{5.31}$$

where the η-linear case is obtained by neglecting the η^2 terms at the numerators. To find the central value of σ_*^2 it is then sufficient to divide by the central behaviour of stellar density, i.e. $3\rho_\mathrm{n}(1+\eta)$ for the P11 models, and $4\rho_\mathrm{n}(1+\eta)/\pi$ for the ZL85 ones; the result is

$$\frac{\sigma_*^2(0,0)}{\Psi_\mathrm{n}} = \begin{cases} \dfrac{2+4(67-96\ln 2)\eta+3(355-512\ln 2)\eta^2}{12(1+\eta)}, & \text{(P11)},\\[2ex] \dfrac{3(32-3\pi^2)+8(9\pi^2-88)\eta+24(15\pi^2-148)\eta^2}{24\pi(1+\eta)}, & \text{(ZL85)}. \end{cases} \tag{5.32}$$

By applying both interpretations, we are therefore in a position to predict the central value of the velocity dispersion as a function of flattening only. Regarding $\overline{v_\varphi}$, the asymptotic behaviour of equation (5.15) is

$$\frac{\rho_*\Delta_*}{\rho_\mathrm{n}\Psi_\mathrm{n}} \sim 2s^2\sin^2\vartheta \times \begin{cases} 3(89-128\ln 2)\eta+6(355-512\ln 2)\eta^2, & \text{(P11)},\\[2ex] \dfrac{(135\pi^2-1328)\eta+84(15\pi^2-148)\eta^2}{3\pi^2}, & \text{(ZL85)}. \end{cases} \tag{5.33}$$

In particular, by virtue of the central trend of ρ_* it follows that, on the equatorial plane (i.e.

$\vartheta = \pi/2$), $\overline{v_\varphi} \propto R$, i.e. *the streaming velocity increases linearly with radius* (see Fig. 5.4); as a consequence, $\overline{v_\varphi}$ vanishes at the centre.

The asymptotic behaviour at large radii

We conclude by showing the asymptotic behaviour in the outer regions, where $\rho_* \propto 1/r^5$ for P11 models, and $\rho_* \propto 1/r^4$ for ZL85 ones. Expanding equations (5.8) and (5.15) for $s \to \infty$ we obtain

$$\frac{\rho_* \sigma_*^2}{\rho_{\rm n} \Psi_{\rm n}} \sim \begin{cases} \dfrac{4 - (1 + 15\cos^2\vartheta)\eta}{8 s^6}, & \text{(P11)}, \\ \dfrac{28 - 4(1 + 20\cos^2\vartheta)\eta}{35\pi s^5}, & \text{(ZL85)}, \end{cases} \qquad \frac{\rho_* \Delta_*}{\rho_{\rm n} \Psi_{\rm n}} \sim \eta \sin^2\vartheta \times \begin{cases} \dfrac{15}{4 s^6}, & \text{(P11)}, \\ \dfrac{32}{7\pi s^5}, & \text{(ZL85)}, \end{cases} \tag{5.34}$$

from which it readily follows that, on the equatorial plane, the decline of *both* σ and $\overline{v_\varphi}$ in the two models goes as $1/\sqrt{R}$.

5.4 An application to Globular Clusters: the case of NGC 4372

Globular Clusters (GCs) have traditionally been regarded as simple spherical, non-rotating stellar systems; however, small ellipticities have been observed since a long ago, and rotation is being detected in a growing number of them (e.g., Bianchini et al. 2018, Kamann et al. 2018, Ferraro et al. 2018). The origin of the observed flattening has been attributed to the effects of internal rotation, velocity dispersion anisotropy, and external tides (for a more extended discussion, see e.g. van den Bergh 2008). In particular, dynamical phenomena such as violent relaxation and two-body relaxation tend to produce isotropic velocity distributions in the central regions of stellar systems, so that, if flattening is observed there, rotation should be considered a possible explanation. In addition to contributing to the shape of these systems, rotation is also expected to change their dynamical evolution (e.g., Fiestas et al. 2006), and to be linked to their "dynamical age" (e.g., Tiongco et al. 2017; Livernois et al. 2022, Leanza et al. 2022). Finally, rotation has been suggested to have a role in the formation of multiple stellar populations in them (Lacchin et al. 2022). Therefore, an assessment of the respective amounts of rotation and anisotropic pressure is particularly important. Indeed, in recent years much effort has been devoted to dynamical modelling of GCs, using different strategies, as for example N-body simulations (e.g., Hurley & Shara 2021), Monte Carlo models (e.g., Giersz et al. 2013; Kamlah et al. 2022), or self-consistent models specific for quasi-relaxed, rotating stellar systems (Varri & Bertin 2012, Bianchini et al. 2013, Jeffreson et al. 2017); see Spurzem & Kamlah (2023) for a recent review.

In general, these techniques are quite complex, and their application time-consuming: it would be desirable to have a simple but robust method to assess phenomenologically the importance of rotation, before applying more sophisticated tools, and we suggest that the homoeoidal expansion and the η-linear solutions of Jeans's equations could be one of such possibilities. Moreover, for the choice of Satoh's decomposition and for a density profile roughly constant in the central regions, the homoeoidal expansion predicts a sort of "universal profile" for the streaming velocity $\overline{v_\varphi}$, of shape given by the first of equation (2.20) with $k = 1$, coupled to equations (5.15) and (5.17). In particular, three main properties for $\overline{v_\varphi}$ are predicted:

1. it scales as the square root of flattening, and increases linearly with radius;

2. it reaches a maximum;

3. it decreases afterward.

Of course these properties transfer also to the projected streaming velocity field $v_{\rm los}$. Thus, a simple and direct relation between the shape of the system and its rotation profile is expected, and it is tempting here to test whether it is satisfied by well observed systems. At first sight, the three features of $\overline{v_\varphi}$ (and $v_{\rm los}$) agree with what observed, for a chosen test-case object (see below), and also for others (e.g., Leanza et al. 2022). Therefore, the method could provide a fast and flexible tool to address, in a preliminary way, the following questions: are observations consistent with velocity dispersion isotropy? if not, does a rescaling of $v_{\rm los}$ with a different costant k value make the model consistent with observations? or, is there the need for a change of k with radius?

As a test-case for the application of the homoeoidal method we chose NGC 4372, a GC for which a detailed photometric and spectroscopic study was conducted (Kacharov et al. 2014). NGC 4372 has an observed low ellipticity of $\eta = 0.08$; and, thanks to a large number of precise radial velocity measurements, it has a $v_{\rm los}$ profile extending at least out to its half-light radius[2], and a velocity dispersion profile extending even further out. Kacharov et al. (2014) adopted a Plummer model, one of the two illustrating cases above, as an optimal representation of the observed properties; they estimated $a = 5.1\,{\rm pc}$, and $M_* = 1.7 \times 10^5\,M_\odot$. All this makes NGC 4372 an obvious candidate for our test. We modelled then NGC 4372 with the P11 profile, of parameters as in Kacharov et al., and, based on the results of the previous Section, with the η-linear solution of Jeans's equations. For the model, and for $k = 1$:

- Fig. 5.8 shows the intrinsic streaming velocity $\overline{v_\varphi}$ (blue solid curves) and the line-of-sight velocity $v_{\rm los}$ (blue dashed curves);
- Fig. 5.9 shows the line-of-sight velocity dispersion $\sigma_{\rm los}$, obtained as described in § 2.2.2.

For comparison, the corresponding observed data points (red dots) are also shown, together with the their error bars. Note that $\overline{v_\varphi}$ and $\sigma_{\rm los}$ are measured in this Thesis in units of $\sqrt{\Psi_{\rm n}}$, which can be converted into practical units as

$$\sqrt{\Psi_{\rm n}} \simeq 20.8 \left(\frac{M_*}{10^5\,M_\odot}\right)^{\frac{1}{2}} \left(\frac{a}{1\,{\rm pc}}\right)^{-\frac{1}{2}}\ {\rm km/sec}. \tag{5.35}$$

When projecting, we adopted two inclination angles: $i = 90°$ (upper panels) and $i = 45°$ (lower panels). In the first case, NGC 4372 is supposed to be viewed edge-on, and the model was built with an intrinsic flattening coincident with the observed one ($\eta = 0.08$); in the second case, the intrinsic flattening increases[3] to $\eta = 0.17$. Overall, for both inclinations, $\sigma_{\rm los}$ of the model accounts quite well for the observed profile, while the isotropic $v_{\rm los}$ does not: its innermost rising part does not reproduce well the observed curve, and, more important, at distances larger than $\simeq a$ it remains too high. *We are then forced to exclude the possibility that NGC 4372 is an isotropic rotator, and also that it is a rotator with a different but constant k, that would have a $v_{\rm los}$ profile with the same shape*, just rescaled. Notice that decreasing further the inclination angle would not change significantly this conclusion: it would produce an increased intrinsic flattening, and then an increase of the isotropic $\overline{v_\varphi}$, that would be almost perfectly compensated by the decrease of the projection angle.

Having discarded the possibility of an isotropic rotator, we attempted then to reproduce the observed profile with a *radially dependent* Satoh decomposition. Since the blue solid curves in Fig. 5.8 give the $\overline{v_\varphi}$ field with $k = 1$ in equation (2.20), in practice they also show $\sqrt{\Delta}$ and its projection; the modifications needed on k can be then easily deduced from these curves. Quite

[2] For a Plummer model, the characteristic radius a corresponds to the half-mass radius.

[3] When the line-of-sight is inclined by an angle i with respect to the z-axis, the relation between the intrinsic flattening q and the observed flattening $q_{\rm obs}$ is $q^2_{\rm obs} = \cos^2 i + q^2 \sin^2 i$ (e.g., see C21).

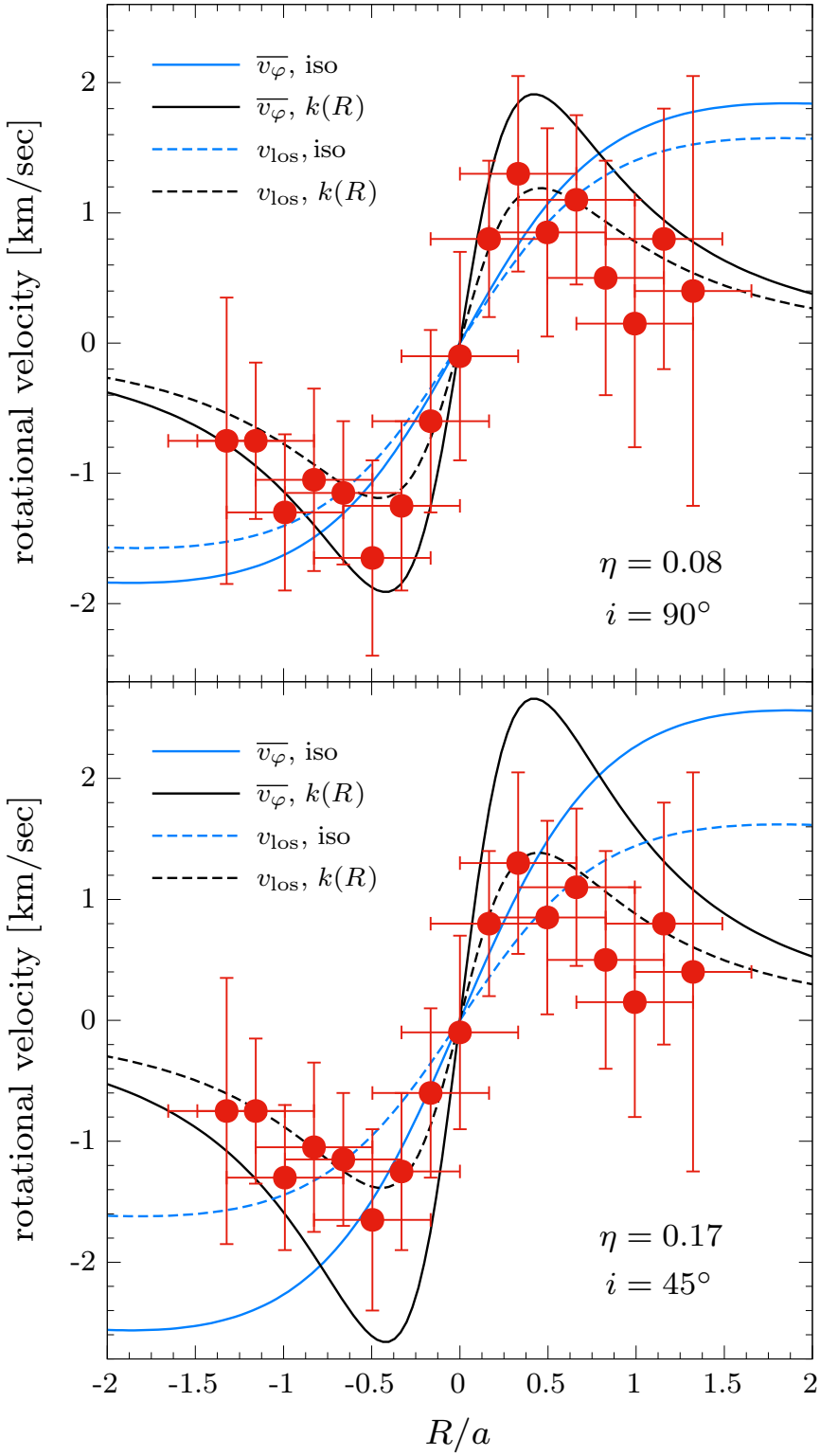

Figure 5.8. The η-linear modelling of the Globular Cluster NGC 4372, whose observed (projected along the line-of-sight) kinematics is shown by red points (from Kacharov et al. 2014). Solid lines show the intrinsic velocity $\overline{v_\varphi}$, while dashed lines show the projected velocity $v_{\rm los}$. Blue lines show the isotropic case ($k = 1$), black lines the spatially-dependent $k(R)$ in equation (5.36). Two inclination angles were adopted: $i = 90°$ (top) and $i = 45°$ (bottom). When $i = 90°$, the intrinsic flattening coincides with the observed one ($\eta = 0.08$); when $i = 45°$, the intrinsic flattening is $\eta = 0.17$.

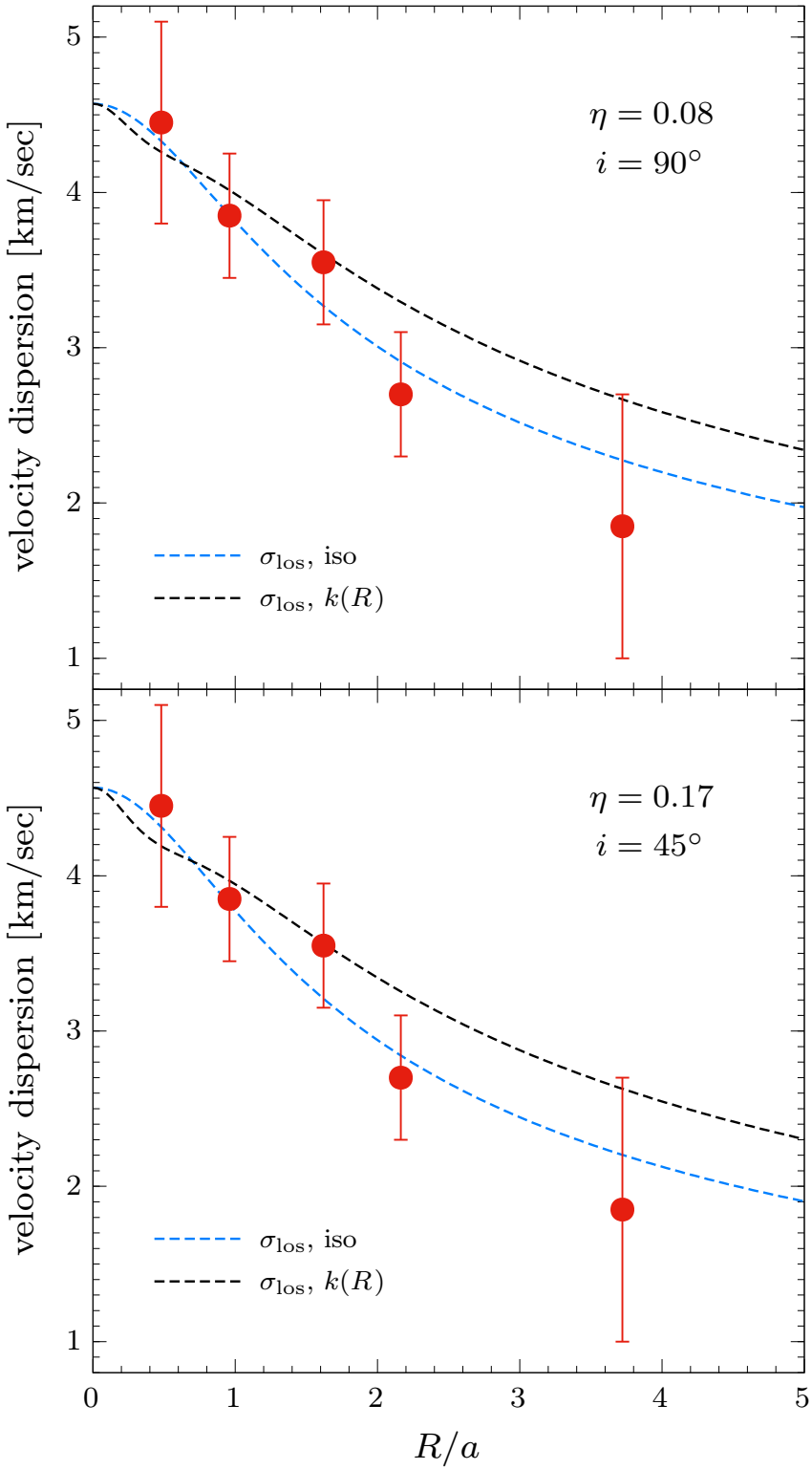

Figure 5.9. The line-of-sight velocity dispersion $\sigma_{\rm los}$ for the η-linear modelling of the Globular Cluster NGC 4372, whose observed (projected along the line-of-sight) kinematics is shown by red points (from Kacharov et al. 2014). Blue lines show the isotropic case ($k = 1$), black lines the spatially-dependent $k(R)$ in equation (5.36). As in Fig. 5.8, two inclination angles were adopted: $i = 90°$ (top), corresponding to the intrinsic flattening $\eta = 0.08$ (coincident with the observed one), and $i = 45°$ (bottom), for which $\eta = 0.17$.

obviously, we do not attach a deep physical meaning to these modifications, even though some implications can be derived. An inspection of Fig. 5.8 suggests that the required changes to $v_{\rm los}$, to be produced by a radially dependent k, are:

(i) preserve the linear rise of $v_{\rm los}$ in the central regions, but include a sharp peak at a radius of $R \simeq a/3$, that is not present in the constant k case;

(ii) be significantly lower than the isotropic rotation velocity outside $\simeq a$.

We parametrized these requests with the trial function

$$k(R) = \frac{A}{1 + (\tilde{R}/B)^n}, \tag{5.36}$$

where $\tilde{R} = R/a$, and A, B and n are three dimensionless free parameters. In Fig. 5.8 with black lines we show the intrinsic and projected streaming velocity profiles, obtained from equation (5.36), with $A = 3.5$, $B = 0.5$, and $n = 2$, and for the two inclination angles $i = 90°$ and $i = 45°$. The chosen values of A, B and n are not the result of a rigorous "best fitting" procedure; they reproduce quite reasonably the observed velocity profile, and allow us to draw three robust conclusions: the central regions must rotate faster than the isotropic rotator, as $k \simeq 3.5$ there; rotation is very concentrated; and the $\overline{v_\varphi}$ decline for $R \gtrsim a/2$ is steep, with $k \propto 1/R^2$. The lack of proper motion measurements for NGC 4372 prevented us from establishing the inclination angle, thus the intrinsic flattening. It would be interesting to extend our analysis to some other GCs with well-measured proper motions; however, as stressed above, we found a compensation between the system inclination and $v_{\rm los}$, therefore we are confident that the results obtained are quite robust.

Figure 5.9 also show that, with the $k(R)$ in equation (5.36), $\sigma_{\rm los}$ differs from that of the isotropic rotator, which is not a surprise because $v_{\rm los}$ enters the expression for $\sigma_{\rm los}$ (see equation 2.41): this is at the origin of the (small) drop of the black lines in the very central regions. In particular, the two outermost data points are better reproduced by the isotropic $\sigma_{\rm los}$ rather than the new one. We believe that a formal solution, reproducing both $v_{\rm los}$ and $\sigma_{\rm los}$, could be obtained by using a more complicated functional form of $k(R)$, for example that increases again up to unity outer of the most external observed point of $v_{\rm los}$; however, we consider this possibility quite implausible from a physical point of view. We conclude that NGC 4372 is unlikely to be an isotropic rotator, because of its lower rotation at $R \gtrsim a$, and a higher rotation in its central region. Reassuringly, some of these conclusions have been also reached with a more sophisticated approach, based on the construction of models supported by a self-consistent phase-space distribution function (e.g. Varri & Bertin 2012, Jeffreson et al. 2017).

Before concluding this analysis, it is tempting to suggest another possible interpretation for the observed kinematic features of NGC 4372: the GC could be a two-component system, with an inner rotating structure physically distinct from that of the main body of the GC, and described by its own phase-space distribution function. Our modelling so far was implicitly based on the use of a single distribution function, i.e., the GC was assumed to be a one-component system. If the total distribution function were the sum of two different distribution functions, one for the non-rotating (or slowly rotating) GC, and the other for the fast rotating substructure, the total rotational field to be modelled with Jeans's equations were the mass averaged rotational field of the GC and of the substructure (not just that of the sampled stars of the subcomponent). It would be interesting to determine observationally if the stars contributing to the projected streaming velocity in the central region show a difference in age and/or chemical composition with respect to the majority of the stars of the GC.

A different possibility would be that the rotational profile is explained by a significant change in the flattening of the system approaching the centre; in fact the ellipticity is observed to vary

in the central regions of some GC (e.g. Bianchini et al. 2013). The possibility that the inner regions can be actually interpreted as a flattened isotropic rotator is qualitatively supported by the scaling of the isotropic $\overline{v_\varphi}$ with $\sqrt{\eta}$. We note however that in NGC 4372 the fiducial value $\simeq 3$ of Satoh's k parameter in the central regions would require, if decreased to unity, an increase of the adopted η by a factor of ≈ 9, bringing the flattening well above the limiting value allowed by the homoeoidal expansion.

Part II

Bondi accretion in early-type galaxies

CHAPTER 6

Gas Accretion In Spherical Galaxies

Gas accretion onto black holes at the centre of galaxies is often modelled with the classical Bondi solution, where a spatially infinite distribution of perfect gas, subject to polytropic transformations, is steadily accreting onto an isolated central mass. In this Chapter the general considerations underlying the study of gas accretion in spherical galaxies are summarised, also taking into account the additional effect of electron scattering. After a brief overview of polytropic transformations, we recap the fundamentals of classical Bondi accretion, the starting point for all studies of gas accretion in spherically symmetrical systems. We shall then recapitulate how to introduce into the discussion the effect of radiation on the flow and of the additional potential of the galaxy. Some important thermodynamical aspects, implicitly described by the polytropic index, are then clarified.

Table 6.1: Main properties of accretion solutions in one- and two-component models with central BH.

	KCP16	CP17	CP18	This Thesis
Galaxy models	Hernquist (1990)	Hernquist (1990), Jaffe (1983)	JJ models	J3 models
Type of accretion	Polytropic	Isothermal	Isothermal	Polytropic[b]
Number of sonic points	One or two	One or two (Hernquist), One (Jaffe)	One	One or two[c]
Sonic radius	Analytic[a]	Analytic	Analytic	Analytic/numerical[d]
λ_t	Analytic[a]	Analytic	Analytic	Analytic/numerical[d]
Mach number profile	Numerical	Analytic	Analytic	Analytic/numerical[d]

[a] The general expression can be written as a function of the polytropic exponent, but only special cases were given explicitly;
[b] Together with a detailed discussion of heat exchange;
[c] Function of the polytropic exponent γ;
[d] In the isothermal ($\gamma = 1$) and monoatomic adiabatic ($\gamma = 5/3$) cases it is analytic, in the $1 < \gamma < 5/3$ case only a numerical exploration is possible.

6.1 Introduction

Theoretical and observational studies indicate that galaxies host at their centre a massive black hole that has grown its mass predominantly through gas accretion (see e.g. Kormendy & Richstone 1995). A generic accretion flow may be broadly classified as quasi-spherical or axisymmetric, and what mainly determines the deviation from spherical symmetry is the angular momentum of the flow itself. A perfect spherical flow is evidently only possible when the angular momentum is exactly zero. Spherical models are a useful starting point for a more advanced modelling, and thus gas accretion toward a central MBH in galaxies is often modelled with the classical Bondi (1952) solution. For example, in semi-analytical models and cosmological simulations of the co-evolution of galaxies and their central MBHs, the mass supply to the accretion discs is linked to the temperature and density of their environment by making use of the Bondi accretion rate (see e.g. Fabian & Rees 1995; Volonteri & Rees 2005; Booth & Schaye 2009; Wyithe & Loeb 2012; Curtis & Sijacki 2015; Inayoshi, Haiman & Ostriker 2016). In fact, in most cases, the spatial resolution of simulations cannot describe in detail the whole complexity of accretion, and so Bondi accretion represents an important approximation to more realistic treatments (see e.g. Ciotti & Ostriker 2012; Barai et al. 2012; Ramírez-Velasquez et al. 2018; Gan et al. 2019 and references therein). Recently, Bondi accretion has been generalized to include the effects on the flow of the gravitational field of the host galaxy and of electron scattering, at the same time preserving the (relative) mathematical tractability of the problem. Such a generalized Bondi problem has been applied to elliptical galaxies by Korol et al. (2016, hereafter KCP16), who discussed the case of a Hernquist (1990) galaxy model, for generic values of the polytropic index. Restricting to isothermal accretion, also taking into account the effects of radiation pressure due to electron scattering, Ciotti & Pellegrini (2017, hereafter CP17) showed that the whole accretion solution can be found analytically for the Jaffe (1983) and Hernquist galaxy models with a central MBH; quite remarkably, not only can the critical accretion parameter be explicitly obtained, but it is also possible to write the radial profile of the Mach number via the Lambert-Euler W-function (see e.g. Corless et al. 1996). Then, Ciotti & Pellegrini (2018, hereafter CP18) further extended the isothermal accretion solution to the case of Jaffe's two-component (stars plus dark matter) galaxy models (Ciotti & Ziaee Lorzad 2018, hereafter CZ18). In these JJ models, a Jaffe stellar profile is embedded in a DM halo such that the total density distribution is also a Jaffe profile, and all the relevant dynamical properties can be written with analytical expressions. CP18 derived all accretion properties analytically, linking them to the dynamical and structural properties of the host galaxies. These previous results are summarized in Table 1.

In this paper we extend the study of CP18 to a different family of two-component galaxy models with a central MBH, in the general case of a polytropic gas: the J3 models. In this family, the

stellar density follows a Jaffe profile, while the total follows a r^{-3} law at large radii, thus allowing the DM halo (resulting from the difference between the total and the stellar distributions) to reproduce the NFW profile at all radii. As we are concerned with polytropic accretion, we also clarify some thermodynamical aspect of the problem, not always stressed. In fact, it is obvious that for a polytropic index $\gamma \neq \gamma_{\rm ad}$ (the adiabatic index of the gas, with $\gamma_{\rm ad} = \mathcal{C}_p/\mathcal{C}_V$) the flow is not adiabatic, and heat exchanges with the environment are unavoidable. We investigate in detail this point, obtaining the expression of the radial profile of the heat exchange (i.e. radiative losses) of the fluid elements as they move towards the galaxy centre. Qualitatively, an implicit cooling/heating function is contained in the polytropic accretion when $\gamma \neq \gamma_{\rm ad}$.

6.2 Perfect gas and polytropic changes

From Classical Thermodynamics, the equation of state of a system consisting of a certain amount of gas occupying a volume V at temperature T and pressure p is given by the simple law

$$pV = nR_{\rm g}T, \tag{6.1}$$

(e.g. Fermi 1958; Pauli 1973), where n indicates the number of moles (i.e. the ratio between the mass and the molar mass of the gas), and $R_{\rm g} \simeq 8.31 \times 10^7\,{\rm erg\,K^{-1}mol^{-1}}$ is the well-known *gas constant*. By combining the equation of state and the First Law of Thermodynamics (e.g. Chandrasekhar 1939) it is found that

$$nR_{\rm g} = \mathscr{C}_p - \mathscr{C}_V, \tag{6.2}$$

where $\mathscr{C}_p$ and $\mathscr{C}_V$ are respectively the *heat capacity* at constant pressure and volume; historically, this important thermodynamic relation is attributed to J. von Mayer (e.g. Truesdell 1984). However, in Astrophysics it is not very useful to work in terms of the volume occupied by a gas, but it is more convenient to use the density ρ. In order to rewrite the equation by highlighting ρ, it is sufficient to divide both sides by the total mass M (say). We then obtain

$$p = \mathscr{R}\rho T, \qquad \text{where} \qquad \mathscr{R} \equiv \frac{nR_{\rm g}}{M} = \mathcal{C}_p - \mathcal{C}_V, \tag{6.3}$$

where $\mathcal{C}_p$ and $\mathcal{C}_V$ are respectively the *specific heat* (i.e. the heat capacity per unit mass) at constant pressure and volume. It is a simple exercise to prove that $\mathscr{R}$ can be rewritten in the following more practical way:

$$\mathscr{R} = \frac{k_{\rm B}}{\mu_0 m_{\rm p}} \simeq \frac{8.26}{\mu_0} \times 10^{-7}\,{\rm erg\,K^{-1}g^{-1}}, \tag{6.4}$$

where $k_{\rm B} \simeq 1.38 \times 10^{-16}\,{\rm erg\,K^{-1}}$ is Boltzmann's constant, and $m_{\rm p} \simeq 1.67 \times 10^{-24}\,{\rm g}$ indicates the mass of the proton[1]. This is the form of the (specific) gas constant usually used in the astrophysical Literature; for instance, in a neutral gas of hydrogen and helium, $\mu_0 \simeq 1.36$; in a molecular cloud mostly made up by molecular hydrogen, $\mu_0 \simeq 2.2$ (e.g., Carrol & Ostlie 2007; Stahler & Palla 2004).

[1] Let N denote the number of particles, and μ_0 the so-called *mean molecular weight* (i.e. the mass of the average mass of particles in units of the proton mass $m_{\rm p}$). Then, the mass of the gas can be found as $M = N\mu_0 m_{\rm p}$. Now, with $\mathcal{N}_{\rm A} \simeq 6.02 \times 10^{23}\,{\rm mol^{-1}}$ indicating Avogadro's number, $N = n\mathcal{N}_{\rm A}$, so that $\mathscr{R} = R_{\rm g}/(\mathcal{N}_{\rm A}\mu_0 m_{\rm p})$. Equation (6.4) is then obtained by noticing that the ratio $R_{\rm g}/\mathcal{N}_{\rm A}$ is nothing else than Boltzmann's constant $k_{\rm B}$.

A very important class of thermodynamic transformations, especially from an astrophysical point of view, is given by the polytropic transformations, in which the pressure is a function of the density only (see e.g. Mihalas & Weibel-Mihalas 1984; Acheson 1990). In particular, when

$$p = K\rho^{\gamma}, \tag{6.5}$$

with K and γ two positive constant, the transformation is called *polytropic*. The power γ is the so-called *polytropic index*[2], and in principle it can assume any positive value; to avoid any possible further confusion, we stress that γ *does not necessarily coincide with the ratio of specific heats* $\gamma_{\rm ad} \equiv \mathcal{C}_p/\mathcal{C}_V$, which we shall call *adiabatic index*. By combining equations (6.3) and (6.5) it follows that, along a polytropic,

$$p\rho^{-\gamma} = \text{constant}, \qquad T\rho^{1-\gamma} = \text{constant}, \qquad T^{\gamma}p^{1-\gamma} = \text{constant}. \tag{6.6}$$

The importance of the polytropic relation consists in the fact that it represent a broad spectrum of different possible gas configurations. In particular, we can identify five main situations.

- $\gamma \to 0$ (in practice, $\gamma \ll 1$).
  For this configuration, the pressure can be considered roughly constant during the process, while it is rigorously zero in the limiting case $\gamma \to 0$.

- $0 < \gamma < 1$.
  For this particular configuration, the temperature decreases for increasing density; in practice, more concentrated gas configurations correspond to lower values of T. For example, polytropes with γ lower than unity were first proposed to model thermally-supported interstellar clouds heated by an external flux of photons or cosmic rays (e.g., Shu et al. 1972; see also de Jong et al. 1980). More recently, it has been shown that the observed radial density profiles of filamentary clouds are well reproduced by cylindrical polytropes with γ lying between 1/3 and 2/3, indicating external heating or the presence of a dominant non-thermal contribution to the pressure (e.g., see Toci & Galli 2015).

- $\gamma = 1$.
  In this case the temperature of the gas remains constant during the entire process, i.e. the gas is isothermal.

- $\gamma > 1$.
  For this particular configuration, the temperature increases for increasing density; in practice, more concentrated gas configurations correspond to higher values of T. In the particular case $\gamma = \gamma_{\rm ad}$, no radiative losses or other forms of heat transfer take place, and the process is said to be *adiabatic*[3].

- $\gamma \to \infty$ (in practice, $\gamma \gg 1$).
  It readily follows that $p \to \infty$; however, this apparent singularity can be easily removed, showing that this case corresponds to a constant density configuration[4].

[2] Polytropic changes was first considered by Zeuner (1907, First Section, § 29), who used n instead of γ; see also Chandrasekhar (1939, Chapter II and references therein), where the polytropic index is called "polytropic exponent", and it is indicated by γ', while γ denotes the ratio of specific heats: the term "polytropic index" is reserved to n, linked to γ' by the relation $\gamma' = 1 + 1/n$. Other important references on polytropes are: Prandtl (1934, § 13), Sommerfeld (1950), Horedt (2004), Clarke & Carswell (2007, § 5.4)

[3] Notice that, from von Mayer's relation, $\gamma_{\rm ad} = 1 + \mathscr{R}/\mathcal{C}_V$, and so $\gamma_{\rm ad}$ always exceeds unity.

[4] The proof follows by setting $K = A^{\gamma-1}$, with A an appropriate constant. Under this assumption, from equation (6.5) it follows that $p^{1/(\gamma-1)} = A\rho^{\gamma/(\gamma-1)}$; therefore, for $\gamma \to \infty$, $\rho = 1/A$.

The theory of polytropes has been applied with great success to the study of stellar equilibria, and, thanks mainly to the work of important pioneers such as A. Ritter (1878) and R. Emden (1907), it has led to significant contributions to Applied Mathematics[5].

6.3 The Classical Bondi Problem

In the classical Bondi problem, a spatially infinite distribution of gas is accreting onto an isolated central point mass; it has a considerable importance in the theory of accretion in hydrodynamics because *it provides an analytical solution which is also quite simple from a mathematical point of view*. This analytical solution, however, exists at the expense of some particularly stringent hypotheses, which we summarize as follows.

1. *The hydrodynamical system is in a stationary state.*
   As a consequence, the system is in a state in which none of the quantities/variables describing it is a function of time. This hypothesis might seem contradictory for an accretion problem, since as the material falls on the central object, its mass evidently increases. To overcome this contradiction, the discussion usually focuses on a limited interval of time, during which the mass of the BH can be considered constant.

2. *The problem is spherically symmetric.*
   Consequently, all differential equations governing the problem depend on a single variable, i.e. the distance to the centre of the system, where the BH is located. This assumption allows therefore to work only with Ordinary Differential Equations. Of course, this requirement necessarily implies the absence in the discussion of angular momentum and/or magnetic fields[6].

3. *The fluid is a perfect gas following a polytropic transormation.*
   For a perfect (or "ideal") gas, the characteristic relationship linking pressure p, density ρ, and temperature T of a substance takes one of the simplest forms. In particular, this assumption allows us to exclude viscosity. With the further assumption of polytropic law allows for the consideration of different thermodynamic situations[7].

4. *The only gravitational field is that produced by the central point mass.*
   As a consequence, we completely neglect the self-gravity of the gas itself.

5. *No electromagnetic feedback is present.*
   Therefore, we completely ignore all electrodynamic phenomena; in particular, the interaction of photons with the falling material is totally neglected.

It is important to stress the fact that *Bondi's classical solution is purely hydrodynamic*, i.e. it does not take into account the effect of the radiation.

We are now in a position to set up the fundamental equations which define the classical Bondi problem. Let us consider an object (in our case, a BH), of mass $M_{\rm BH}$, at rest in an infinite cloud

[5] For an in-depth historical and bibliographical analysis of the emergence of polytropic models, and their subsequent application to various fields of Physics, see the bibliography section at the end Capter IV in Chandrasekhar (1939).

[6] In fact, as the fluid moves along radial orbits, the angular momentum vanishes. Concerning the magnetic field, in analytical and/or numerical work it is usually assumed that it is weak in such a way it does not affect the flux; not surprisingly, this approximation breaks down sufficiently close to the central mass or at sufficiently late times (see e.g. Cunningham et al. 2012).

[7] The "non-explicit" reference in Bondi (1952) to polytropic transformations is found after equation (2), which defines the relation between the pressure and the density: $p \propto \rho^{\gamma}$, with $1 \leq \gamma \leq 5/3$. As Bondi remarks, «with a suitable choice of γ, equation (2) is equivalento to the physical condition that no heat is radiated or conducted away».

of gas; at infinity the gas is itself at rest, with uniform pressure p_∞, density ρ_∞, and temperature T_∞. As the gas falls towards the centre of the cloud, i.e. on the BH, it is subjected to polytropic transformations. Consequently, by measuring p and ρ in units of the corresponding values at infinity, equation (6.5) reduces to

$$\frac{p}{p_\infty} = \left(\frac{\rho}{\rho_\infty}\right)^\gamma ; \tag{6.7}$$

in the following, both in the general discussion and in the presentation of the results, we shall *exclude* the case $0 < \gamma < 1$, and *focus only on polytropic indices greater than or equal to unity.* A very important quantity, of which we shall make extensive use in the course of this Chapter, is what we shall call *local polytropic speed of sound*, or simply speed of sound, indicated as c_s and defined by

$$c_s^2 \equiv \frac{dp}{d\rho} = \gamma \frac{p}{\rho} ; \tag{6.8}$$

physically, it represents the (local) velocity of propagation of sound waves relative to the gas[8]. For what concerns the motion of each element of fluid, we must consider only the following two time-independent equations:

$$\text{Equation of continuity:} \quad 4\pi r^2 \rho v = \dot{M}_\mathrm{B}, \tag{6.9}$$

$$\text{Bernoulli's equation:} \quad \frac{v^2}{2} + \int_{p_\infty}^{p} \frac{dp}{\rho} - \frac{GM_\mathrm{BH}}{r} = 0, \tag{6.10}$$

where $v(r)$ is the the gas radial speed, and $\dot{M}_\mathrm{B}$ indicates the time-independent accretion rate onto the BH. The integral at the left-hand side of Bernoulli's equation can be evaluated via elementary functions; in fact, by changing variable from p to ρ, and making use of equation (6.5), one readily obtains

$$\int_{p_\infty}^{p} \frac{dp}{\rho} = c_\infty^2 \int_1^{\tilde{\rho}} t^{\gamma-2} dt = \begin{cases} c_\infty^2 \ln \dfrac{\rho}{\rho_\infty}, & \gamma = 1, \\ \dfrac{c_\infty^2}{\gamma - 1}\left[\left(\dfrac{\rho}{\rho_\infty}\right)^{\gamma-1} - 1\right], & \gamma > 1, \end{cases} \tag{6.11}$$

where $c_\infty^2 \equiv \gamma p_\infty / \rho_\infty$ is the square of the speed of sound at infinty. However, it is important to remark that this quantity *coincides with the enthalpy change per unit mass only in the adiabatic case, i.e. for $\gamma = \gamma_\mathrm{ad}$, while it is just proportional to it for a generic polytropic transformation*; we shall return to this point at the end of the Chapter.

As frequently happens in Physics, it is useful to have the equations describing the problem under discussion in dimensionless form. It is convenient to define some physical dimensionless quantities which we shall use in the following. First, we introduce the so-called *Bondi radius* r_B, defined as

[8] For a general discussion of the physical concept of speed of sound, and on its hydrodynamical definition in the case of barotropic flows, see e.g. Lord Rayleigh (1945, § 246), Sommerfeld (1950, §§ 13 and 37), and Clarke & Carswell (2007, § 6.1); see also Feynman (1963, Chapter 47). For an application on the study of the stability of collisionless stellar systems, see e.g. Chapter 5 in BT87. Notice that c_s *is in general a function of the density*, and only for infinitesimal amplitude it may be considered as a constant. An interesting and detailed historical overview can be found in the essay "Historical Introduction" by R.B. Lindsay (Lord Rayleigh 1945, Foreword).

$$r_{\rm B} \equiv \frac{GM_{\rm BH}}{c_\infty^2}. \tag{6.12}$$

In practice, $r_{\rm B}$ is the natural scale length of the problem; physically, it is the radius at which the gravitational potential energy of a gas element, due to the BH, is of the order of its thermal energy at infinity. Other dimensionless quantities are:

$$x \equiv \frac{r}{r_{\rm B}}, \qquad \tilde{\rho} \equiv \frac{\rho}{\rho_\infty}, \qquad \mathcal{M} \equiv \frac{v}{c_s}, \tag{6.13}$$

where $\mathcal{M}$ denotes the *Mach number*, which plays an important role in the dynamics of gases[9]; for future use, we also define the dimensionless speed of sound:

$$\tilde{c}_s \equiv \frac{c_s}{c_\infty} = \tilde{\rho}^{\,\frac{\gamma-1}{2}}. \tag{6.14}$$

By virtue of the previous definitions, the equation of continuity can be rewritten as

$$x^2 \mathcal{M} \tilde{\rho}^{\,\frac{\gamma+1}{2}} = \lambda, \qquad \lambda \equiv \frac{\dot{M}_{\rm B}}{4\pi r_{\rm B}^2 \rho_\infty c_\infty}, \tag{6.15}$$

where λ is the so-called (dimensionless) *accretion parameter*: once known, it fixes the accretion rate for assigned $M_{\rm BH}$ and boundary conditions for the accreting gas. Regarding Bernoulli's equation, from equation (6.11) it follows that we have to distinguish two cases: $\gamma = 1$, and $\gamma > 1$.

6.3.1 The case $\gamma = 1$

In the isothermal case the speed of sound is constant along the polytriopic, and it equals its value at infinity, i.e. $c_s = c_\infty$. As a consequence, the gas velocity is simply given by $v = c_\infty \mathcal{M}$. Therefore, by measuring r in units of $r_{\rm B}$, it follows that Bernoulli's equation reduce to

$$\frac{\mathcal{M}^2}{2} + \ln \tilde{\rho} = \frac{1}{x}, \tag{6.16}$$

Now, by eliminating $\tilde{\rho}$ between the equations (6.15) and (6.16), we obtain

$$g(\mathcal{M}) = f(x) - \Lambda, \qquad \Lambda \equiv \ln \lambda, \tag{6.17}$$

where the dimensionless functions g and f are defined as

$$g(\mathcal{M}) = \frac{\mathcal{M}^2}{2} - \ln \mathcal{M}, \qquad f(x) \equiv \frac{1}{x} + 2 \ln x. \tag{6.18}$$

In practice, *solving "Bondi's problem" means, given an arbitrary value of x, finding the the corresponding value of $\mathcal{M}$ which solves equation* (6.17). Of course, Λ cannot be chosen arbitrarily. In fact, both $g(\mathcal{M})$ and $f(x)$ have a minimum, which we indicate with $g_{\rm min}$ and $f_{\rm min}$, respectively; thus, in order to satisfy equation (6.17) for all positive values of x, the requirement is that

[9] For instance, the numerical value of $\mathcal{M}$ defines the so-colled "flow régime": *subsonic* for $0 < \mathcal{M} < 1$; *transonic* for $\mathcal{M} \simeq 1$; *supersonic* for $1 < \mathcal{M} \lesssim 5$; *ipersonic* for $\mathcal{M} > 5$. When $\mathcal{M} \ll 1$, the flow may be regarded as *incompressible* (e.g. Batchelor 1967, Chapter 10; Landau & Lifshitz 1987, § 10; Chandrasekhar 1961, § 7).

$$g_{\min} \leq f_{\min} - \Lambda. \tag{6.19}$$

Since $g_{\min} = 1/2$ (corresponding to $\mathcal{M}_{\min} = 1$), and $f_{\min} = 2 - 2\ln 2$ (reached at $x_{\min} = 1/2$), the foregoing inequality reduces to

$$\Lambda \leq \Lambda_{\rm cr} \equiv f_{\min} - g_{\min} = \frac{3}{2} - 2\ln 2 \qquad \Leftrightarrow \qquad \lambda \leq \lambda_{\rm cr} \equiv \mathrm{e}^{\,f_{\min} - g_{\min}} = \frac{\mathrm{e}^{3/2}}{4}. \tag{6.20}$$

In practice, we can summarize the behaviour of the solutions in the following manner:

- for $\lambda = \lambda_{\rm cr}$ (i.e. along the *critical solutions*), $x_{\min}$ indicates the position of the so-called *sonic point*, i.e. $\mathcal{M}(x_{\min}) = 1$;
- for $\lambda < \lambda_{\rm cr}$, two regular *subcritical solutions* exist, one everywhere supersonic and another everywhere subsonic; the position $x_{\min}$ marks the minimum and maximum value of $\mathcal{M}$, respectively for these two solutions (e.g. Bondi 1952; Frank et al. 1992; Krolik 1998).

The analytical solution

In the isothermal case it is possible to obtain the solution of classical Bondi problem in fully analytical form in terms of the Lambert-Euler W-function (see CP17; Waters & Proga 2012; Herbst 2015; see also Appendix E and references therein). The problem is analogous to the one analyzed by Cranmer (2004), who first exploited the many remarkable properties of the W-function to obtain in closed form the solutions of some Solar Physics problems. For the case of isothermal accretion onto a point mass at the centre of a cloud of gas, equation (6.17) for $\lambda = \lambda_{\rm cr}$ (critical solution) takes the form (E6) with

$$a = \frac{1}{2}, \qquad b = 2, \qquad c = -1, \qquad X = \mathcal{M}, \qquad Y = \frac{1}{x} + 2\ln x - \ln \lambda_{\rm cr}, \tag{6.21}$$

i.e., by virtue of equation (E9),

$$\mathcal{M}^2 = -\begin{cases} W_0\left(-\dfrac{\mathrm{e}^{3-2/x}}{16\,x^4}\right), & x \geq x_{\min}, \\[2ex] W_{-1}\left(-\dfrac{\mathrm{e}^{3-2/x}}{16\,x^4}\right), & 0 < x \leq x_{\min}, \end{cases} \tag{6.22}$$

where $x_{\min} = 1/2$. The properties of the critical solution just obtained can be visualized with the help of Fig. E.1 in Appendix E. As x decreases from ∞ to $x_{\min}$, the argument of W_0 decreases from 0 to $-1/\mathrm{e}$ (points A and B in Fig. E.1, top panel), W_0 decreases from 0 to -1, and so $\mathcal{M}^2$ increases from 0 to 1. As x further decreases from $x_{\min}$ to 0, the argument of W_{-1} increases again from $-1/\mathrm{e}$ to 0 (points B and C), W_{-1} decreases from -1 to $-\infty$, and so $\mathcal{M}^2$ increases from 1 to ∞. In practice, the function W_{-1} function describes *supersonic* accretion, whereas the function W_0 describes *subsonic* accretion: the critical solution is then obtained by connecting the two branches; the other critical solution, with $\mathcal{M}^2$ increasing for increasing x, is obtained by switching the functions W_0 and W_{-1} in equation (6.22). Once $\mathcal{M}(x)$ is known, all the functions

involved in the accretion problem can be obtained. For example, from equation of contnuity (6.15) with $\gamma = 1$, one has

$$\tilde{\rho}(x) = \frac{\lambda_{\rm cr}}{x^2 \mathcal{M}(x)}, \tag{6.23}$$

while the gas velocity is simply given by $v(r) = c_\infty \mathcal{M}(x)$.

6.3.2 The case $\gamma > 1$

In the non-isothermal case, $v = c_s \mathcal{M} = c_\infty \tilde{\rho}^{(\gamma-1)/2} \mathcal{M}$. Then, from equation (6.11), and replacing $GM_{\rm BH}/r$ with c_∞^2/x by virtue of the definition (6.12), Bernoulli's equation reduecs to

$$\left(\frac{\mathcal{M}^2}{2} + \frac{1}{\gamma - 1}\right) \tilde{\rho}^{\,\gamma-1} = \frac{1}{x} + \frac{1}{\gamma - 1}. \tag{6.24}$$

As for the isothermal case, equations (6.15) and (6.24) can be combined to give

$$g(\mathcal{M}) = \Lambda f(x), \qquad \Lambda \equiv \lambda^{-\frac{2(\gamma-1)}{\gamma+1}}, \tag{6.25}$$

where now $g(\mathcal{M})$ and $f(x)$ read

$$g(\mathcal{M}) = \mathcal{M}^{-\frac{2(\gamma-1)}{\gamma+1}} \left(\frac{\mathcal{M}^2}{2} + \frac{1}{\gamma - 1}\right), \qquad f(x) \equiv x^{\frac{4(\gamma-1)}{\gamma+1}} \left(\frac{1}{x} + \frac{1}{\gamma - 1}\right). \tag{6.26}$$

The solution of Bondi's problem requires then obtaining the radial profile $\mathcal{M}(x)$ for given $\lambda \leq \lambda_{\rm cr}$ (e.g., Bondi 1952; Frank et al. 1992); unfortunately, equation (6.25) *does not have an explicit solution in terms of known functions for generic values of* γ*, and must be solved numerically.* Once the radial profile of the Mach number is known, both the gas density and temperature profiles can be obtained; in fact, by combining equations (6.3), (6.7), and (6.15), the following chain of relations holds:

$$\tilde{\rho} = \tilde{T}^{\frac{1}{\gamma-1}} = \left(\frac{\lambda}{x^2 \mathcal{M}}\right)^{\frac{2}{\gamma+1}}, \tag{6.27}$$

with $\tilde{T} \equiv T/T_\infty$ is the gas temperature in units of the temperature at infinity.

Anyway, as for the isothermal case, it is possible to show that both g and f have a minimum, so that the solutions of equation (6.25) exist only when

$$g_{\rm min} \leq \Lambda f_{\rm min}, \tag{6.28}$$

i.e., more precisely, for

$$\Lambda \geq \Lambda_{\rm cr} \equiv \frac{g_{\rm min}}{f_{\rm min}} \qquad \Leftrightarrow \qquad \lambda \leq \lambda_{\rm cr} \equiv \left(\frac{f_{\rm min}}{g_{\rm min}}\right)^{\frac{\gamma+1}{2(\gamma-1)}}. \tag{6.29}$$

In order to find these minima, we need to study the sign of the first derivative of the two functions. For, by differentiating g and f with respect to the arguments we obtain

$$\frac{dg}{d\mathcal{M}} = \frac{2(\mathcal{M}^2 - 1)}{\gamma + 1} \mathcal{M}^{-\frac{3\gamma-1}{\gamma+1}}, \qquad \frac{df}{dx} = \frac{4x + 3\gamma - 5}{\gamma + 1} x^{-\frac{2(3-\gamma)}{\gamma+1}}. \tag{6.30}$$

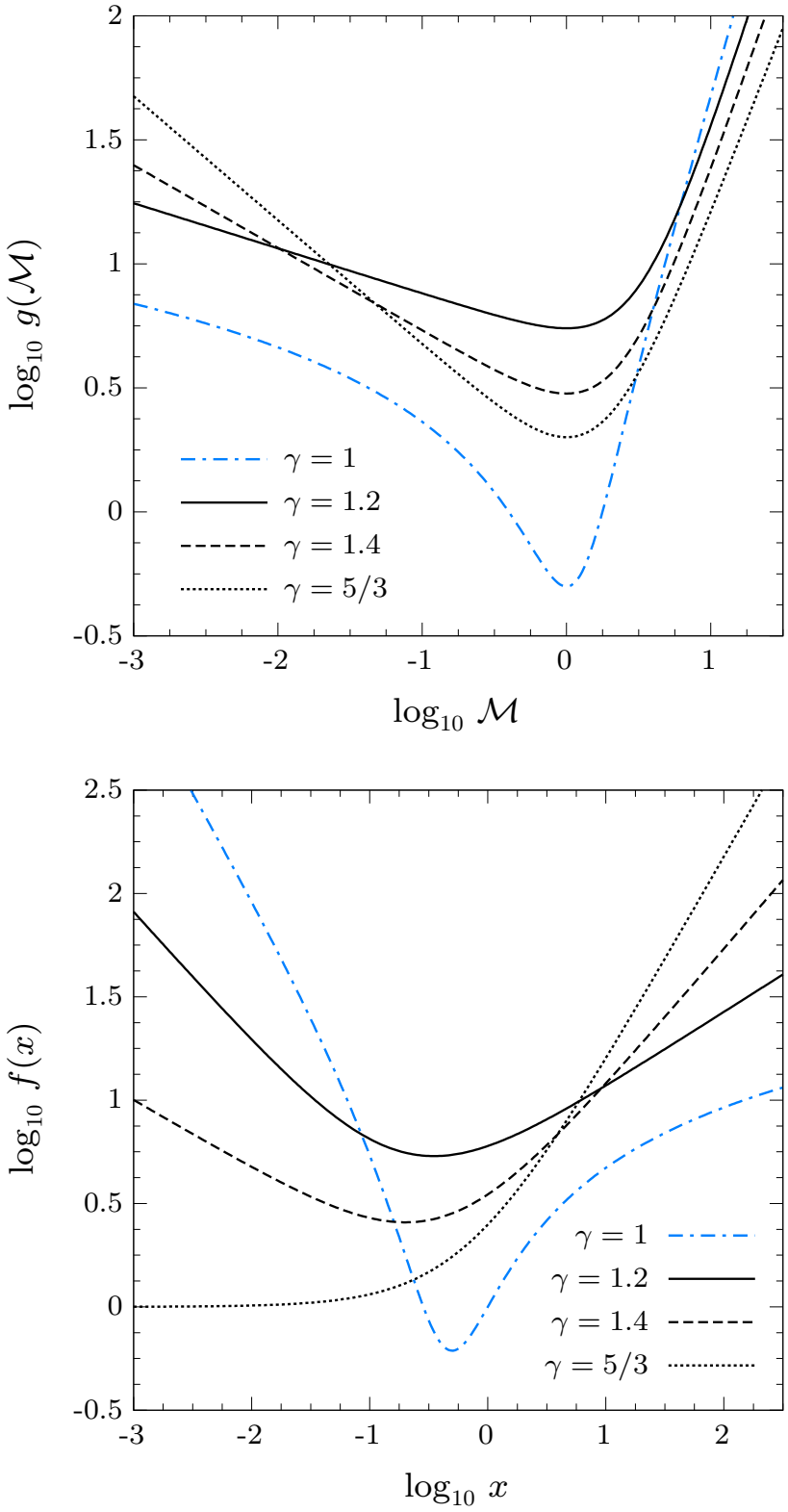

Figure 6.1. The functions $g(\mathcal{M})$ and $f(x)$ for the Classical Bondi problem. Different line styles correspond to different values of γ, from the case $\gamma = 1$ to the hydrodynamical limit $\gamma = 5/3$. Notice how, for $\gamma > 1$, the minimum of both functions decreases as the polytropic index increases, reachet at gradually lower values of $\mathcal{M}$ or x.

from which it is apparent that

$$\mathcal{M}_{\rm min} = 1, \qquad x_{\rm min} = \begin{cases} \dfrac{5-3\gamma}{4}, & 1 < \gamma < 5/3, \\ 0, & \gamma \geq 5/3. \end{cases} \tag{6.31}$$

Therefore, $g_{\rm min} = g(\mathcal{M}_{\rm min})$, and $f_{\rm min} = f(x_{\rm min})$. With some care, from equation (6.26) we find

$$g_{\rm min} = \frac{\gamma+1}{2(\gamma-1)}, \qquad f_{\rm min} = \begin{cases} \dfrac{\gamma+1}{4(\gamma-1)}\left(\dfrac{4}{5-3\gamma}\right)^{\frac{5-3\gamma}{\gamma+1}}, & 1 < \gamma < 5/3, \\ 1, & \gamma = 5/3, \\ 0, & \gamma > 5/3; \end{cases} \tag{6.32}$$

note that $g_{\rm min}$ gradually decreases as the value of the polytropic index increases, until approaching $1/2$ for very large values of γ. As a consequence, the requirement (6.28) reduces to

$$\lambda \leq \lambda_{\rm cr} = \begin{cases} \dfrac{1}{4}\left(\dfrac{2}{5-3\gamma}\right)^{\frac{5-3\gamma}{2(\gamma-1)}}, & 1 < \gamma < 5/3, \\ 1/4, & \gamma = 5/3, \\ 0, & \gamma > 5/3. \end{cases} \tag{6.33}$$

In particular, *we can exclude from the discussion the case $\gamma > 5/3$; in fact, since the critical accretion parameter is zero, no accretion can take place. For this reason, $\gamma = 5/3$ represents a hydrodynamical limit for the classical Bondi problem.*

The limiting case $\gamma = 5/3$

The hydrodynamical limit $\gamma = 5/3$, corresponding to the adiabatic monoatomic case, requires a separate discussion. On the one hand, this situation can be considered as a simple extension of the ordinary case $\gamma > 1$, thus many of the results and conclusions can be achieved simply by replacing $\gamma = 5/3$ in the appropriate non-isothermal expressions (when available); on the other hand, similar to the isothermal case, it is possible to discuss the accretion problem in fully analytical terms. In this limiting case, indeed, Bondi's problem reduces to

$$g(\mathcal{M}) = \Lambda f(x), \qquad \Lambda \equiv \lambda^{-1/2}, \tag{6.34}$$

where the functions g and f are given by

$$g(\mathcal{M}) = \frac{\mathcal{M}^2+3}{2\sqrt{\mathcal{M}}}, \qquad f(x) = 1 + \frac{3}{2}x, \tag{6.35}$$

Rearranging the terms, equation (6.34) can be rewritten as

$$\varpi^4 - \frac{2f(x)}{\sqrt{\lambda}}\varpi + 3 = 0, \qquad \varpi \equiv \sqrt{\mathcal{M}(x)}. \tag{6.36}$$

Therefore, in principle the radial Mach profile can be obtained by solving a fourth degree equation.

6.4 Bondi accretion with electron scattering in galaxy models

Since a purely spherical flow is physically well-defined, it is possible to exploit the symmetry of the problem to provide not only a hydrodynamic treatment of the accreting gas profile, but also to include some additional physical processes. In this way, while maintaining a highly idealized framework, we try to give a more realistic description of the phenomenon. For example, during the accretion process, the gravitational potential energy is expected to be converted into radiation; since radiation is able to exert a force on the accreting gas (in the opposite direction of the gravitational force), the resulting effects cannot be neglected. Under the assumption of optical thinness, it is easy to include the phenomenon of *electron scattering* (e.g. Taam et al. 1991; Fukue 2001; Lusso and Ciotti 2011; Raychaudhuri et al. 2018; Ramírez-Velasquez et al. 2019; Samadi et al. 2019). Furthermore, in order for the description of accretion to be realistic, it is necessary to consider also the *gravitational potential of a galaxy* rather than just that of a point mass (e.g. KCP16; CP17; CP18; CMP19); for, we restrict to the case of a spherically symmetric potential, which approximates quite well the potential of some early-type galaxies.

Following KCP17, we now show how to implement in a general way these two effects, i.e. the presence of radiative feedback and of an additional potential.

6.4.1 The effect of electron scattering

Bondi's solution describes a purely hydrodynamical flow, where, as we shall see in detail in § 6.5, heat exchanges are implicitly taken into account by the polytropic index. In real cases, gas is compressed while it falls toward the center, and the gas temperature increases; also, the flow is affected by the emission of radiation near the BH. The produced luminosity (i.e. energy per unit time) can be written as

$$L = \varepsilon \dot{M}_{\rm B} c^2, \tag{6.37}$$

where ε represents the *radiative efficiency*, and $\dot{M}_{\rm B}$ is the mass accretion rate (see equation 6.15), and $c \simeq 3 \times 10^{10}$ cm/sec is the speed of light in vacuum. In principle, ε could depend on L (and so on $\dot{M}_{\rm B}$), as for example in the advection dominated accretion (e.g. Yuan & Narayan 2014), when ε takes very low values. At high accretion rates, instead, $\varepsilon = 0.1$ and the accretion is likely unsteady, so that Bondi's solution cannot be applied (e.g., Ciotti & Ostriker 2012; see also Barai et al. 2012). In practice, the emitted radiation interacts with the ambient and modifies the whole accretion process: the effects of the radiation can be strong enough to shut down accretion (the so-called negative feedback) and turn off the central active galactic nucleus. Under these circumstances, the flux is evidently non-stationary (Binney & Tabor 1995; Ciotti & Ostriker 1997, 2001; Park et al. 2014). Limiting to low accretion rates, and considering only electron scattering, in the optically thin regime it is possible to include the effects of radiation pressure to generalize the classical Bondi solution (see e.g. Lusso & Ciotti 2011 and references therein). In fact, under the assumptions of spherical symmetry and optically thinness, the effective force per unit volume $\boldsymbol{f}_{\rm eff}$ experienced by a gas element can be written as

$$\boldsymbol{f}_{\rm eff}(r) = \boldsymbol{f}_{\rm grav}(r) + \boldsymbol{f}_{\rm rad}(r), \tag{6.38}$$

where $\boldsymbol{f}_{\rm grav}$ is the contribution due to the gravitational field of the BH, and $\boldsymbol{f}_{\rm rad}$ is the one due to the radiation exerted by electrons. These two contributions are given by

$$\boldsymbol{f}_{\rm grav}(r) = -\frac{G M_{\rm BH}\rho(r)}{r^2}\,\boldsymbol{e}_r, \qquad \boldsymbol{f}_{\rm rad}(r) = \frac{\alpha n_{\rm e}(r)\sigma_{\rm T} L}{4\pi c r^2}\,\boldsymbol{e}_r, \tag{6.39}$$

where $\boldsymbol{e}_r$ is the usual radial unit vector. In the foregoing equation, $n_{\rm e}(r)$ is the number density of electrons[10] within a distance r from the BH, $\sigma_{\rm T} \simeq 6.65 \times 10^{-25}\,{\rm cm}^2$ is Thomson's cross section, and α is a positive constant[11]. After some rearranging we find

$$\boldsymbol{f}_{\rm eff}(r) = -\frac{GM_{\rm BH}\rho(r)\chi}{r^2}\,\boldsymbol{e}_r, \qquad\qquad \chi \equiv 1 - \frac{L}{L_{\rm Edd}}, \tag{6.40}$$

where, for $\alpha = 1$,

$$L_{\rm Edd} \equiv \frac{4\pi c G M_{\rm BH} m_{\rm p}}{\sigma_{\rm T}} \simeq 3.28 \times 10^4 \left(\frac{M_{\rm BH}}{1\,M_\odot}\right) L_\odot \tag{6.41}$$

is the so-called *Eddington luminosity*[12]. In order for the material to fall on the central black hole, it is necessary that the gravitational force exceeds the force exerted by the radiation; given a value of L, we can then distinguish the following situations.

- $L = 0$ (i.e. $\chi = 1$).
  In this case the radiation pressure has no effect on the accretion flux, and so $\boldsymbol{f}_{\rm eff} = \boldsymbol{f}_{\rm grav}$.
- $0 < L < L_{\rm Edd}$ (i.e. $0 < \chi < 1$).
  In this situation, $\boldsymbol{f}_{\rm eff} \cdot \boldsymbol{e}_r < 0$, and so tha gas falls on the central BH.
- $L = L_{\rm Edd}$ (i.e. $\chi = 0$).
  In this case the radiation pressure cancels exactly the gravitational field of the BH everywhere, so that $\boldsymbol{f}_{\rm eff} = \boldsymbol{0}$.
- $L > L_{\rm Edd}$ (i.e. $\chi < 0$).
  In this situation, $\boldsymbol{f}_{\rm eff} \cdot \boldsymbol{e}_r > 0$, so that the gas is driven outward by the radiation pressure.

As we are dealing with an accretion problem, we shall focus on $0 \le \chi \le 1$, by considering $\chi = 0$ and $\chi = 1$ as limiting values. In any case, χ is independent of the radius, thus *the feedback radiation can be implemented in equations* (6.17) *and* (6.25) *as a simple correction which reduces the gravitational force of the BH by a factor* χ. Further, only the function $f(x)$ is affected by the contribution of χ, and so Bondi's problem reduces to the solution of equations (6.17)-(6.18), or (6.25)-(6.26), where f is now given by

$$f(x) = \begin{cases} \dfrac{\chi}{x} + 2\ln x, & \gamma = 1, \\[2ex] x^{\frac{4(\gamma-1)}{\gamma+1}}\left(\dfrac{\chi}{x} + \dfrac{1}{\gamma-1}\right), & 1 < \gamma \le \dfrac{5}{3}. \end{cases} \tag{6.42}$$

By repeating step by step the analysis performed in the previous Section it is easy to show that, in presence of electron scattering, the values of the new sonic point $x_{\rm min}^{\rm (es)}$ and of the new accretion parameter $\lambda_{\rm cr}^{\rm (es)}$ are given by

[10] In principle, one should also take protons into account. However, since in general the electromagnetic cross section is inversely proportional to the square of the particle mass, the cross section of the proton is about a million times smaller than that of the electron.

[11] More precisely, α is related to the Klein-Nishina cross section (which reduces to $\sigma_{\rm T}$ in the limit of low frequencies; see Klein & Nishina 1929) and to the shape of the so-called Spectral Energy Distribution. We recall that there might also be a (slight) effect due to metallicity (the gas indeed becomes more opaque as the number of electrons increases), but we shall ignore it in our discussion.

[12] From equation (6.37), the physical limit for the accretion rate in a stationary spherical system is given by the ratio $L_{\rm Edd}/(\varepsilon c^2)$.

$$x_{\rm min}^{\rm (es)} = \chi x_{\rm min} \qquad\qquad \lambda_{\rm cr}^{\rm (es)} = \chi^2 \lambda_{\rm cr}, \tag{6.43}$$

being $x_{\rm min}$ and $\lambda_{\rm cr}$ the sonic point and the critical parameter in the corresponding classical case (e.g. KCP16); notice that, *if χ is strictly lower than unity, both $x_{\rm min}^{\rm (es)}$ and $\lambda_{\rm cr}^{\rm (es)}$ are lower than in the classical model*. In explicit form, we have

$$x_{\rm min}^{\rm (es)} = \begin{cases} \dfrac{\chi}{2}, & \gamma = 1, \\ \dfrac{\chi(5-3\gamma)}{4}, & 1 < \gamma \le \dfrac{5}{3}, \end{cases} \qquad \lambda_{\rm cr}^{\rm (es)} = \begin{cases} \dfrac{\chi^2 {\rm e}^{3/2}}{4}, & \gamma = 1, \\ \dfrac{\chi^2}{4}\left(\dfrac{2}{5-3\gamma}\right)^{\frac{5-3\gamma}{2(\gamma-1)}}, & 1 < \gamma < 5/3, \\ \dfrac{\chi^2}{4}, & \gamma = 5/3. \end{cases} \tag{6.44}$$

Obviously, the isothermal solution continues to be fully analytical. The associated Bondi equation for the critical case can be in fact written in the form (E6) with $a = 1/2$, $b = 2$, $c = -1$, $X = \mathcal{M}$, and $Y = \chi/x + 2\ln x - \ln \lambda_{\rm cr}$; therefore, from equation (E9) its solution is given by

$$\mathcal{M}^2 = -\begin{cases} W_0\left(-\dfrac{\chi^4 {\rm e}^{3-2\chi/x}}{16 x^4}\right), & x \ge x_{\rm min}, \\ W_{-1}\left(-\dfrac{\chi^4 {\rm e}^{3-2\chi/x}}{16 x^4}\right), & 0 < x \le x_{\rm min}, \end{cases} \tag{6.45}$$

with $x_{\rm min} = \chi/2$; the associated gas velocity profile is just obtained replacing $\lambda_{\rm cr}$ by $\lambda_{\rm cr}^{\rm (es)}$ in equation (6.23).

6.4.2 The additional effect of the galaxy potential

Let us now assume that the BH occupies the centre of a galaxy. Without loss of generality for our present purposes, we write the gravitational potential $\Psi_{\rm g}$ of the (spherical) galaxy as

$$\Psi_{\rm g} = \frac{G M_{\rm g}}{r_{\rm g}} \psi\left(\frac{r}{r_{\rm g}}\right), \tag{6.46}$$

where $r_{\rm g}$ is a characteristic scale length, ψ is the dimensionless potential, and $M_{\rm g}$ is the total mass of the galaxy. It is convenient to measure $M_{\rm g}$ in units of the BH mass, and $r_{\rm g}$ in units of the Bondi radius; we then introduce the following parameters:

$$\mathcal{R} \equiv \frac{M_{\rm g}}{M_{\rm BH}}, \qquad\qquad \xi \equiv \frac{r_{\rm g}}{r_{\rm B}}. \tag{6.47}$$

Consequently, the "effective" total (BH plus galaxy) potential becomes

$$\Psi_{\rm T} = \frac{G M_{\rm BH}}{r_{\rm B}}\left[\frac{\chi}{x} + \frac{\mathcal{R}}{\xi}\psi\left(\frac{x}{\xi}\right)\right], \tag{6.48}$$

where, for the sake of generality, also the effect of the radiation pressure has been taken into

account. Of course, when $\mathcal{R} \to 0$ (or $\xi \to \infty$), the galaxy contribution to the total potential vanishes[13], and the problem reduces to classical case. In the limiting case of $\chi = 0$ (i.e. when $L = L_{\rm Edd}$), the problem describes accretion in the potential of the galaxy only, in absence of electron scattering and a BH; when $\chi = 1$ (i.e. for $L = 0$), instead, the accretion flow is not affected by the radiation. Replacing the potential of the BH in equation (6.10) by $\Psi_{\rm T}$, we obtain the new form of Bernoulli's equation, i.e.

$$\text{Bernoulli's equation:} \quad \begin{cases} \dfrac{\mathcal{M}^2}{2} + \ln\tilde{\rho} = \dfrac{\chi}{x} + \dfrac{\mathcal{R}}{\xi}\psi\left(\dfrac{x}{\xi}\right), & \gamma = 1, \\ \left(\dfrac{\mathcal{M}^2}{2} + \dfrac{1}{\gamma-1}\right)\tilde{\rho}^{\gamma-1} = \dfrac{\chi}{x} + \dfrac{\mathcal{R}}{\xi}\psi\left(\dfrac{x}{\xi}\right) + \dfrac{1}{\gamma-1}, & 1 < \gamma \leq \dfrac{5}{3}. \end{cases} \tag{6.49}$$

Now, by eliminating $\tilde{\rho}$ between the equations (6.15) and (6.49), we find that the equation describing Bondi's problem can be written

$$\text{Bondi's problem:} \quad g(\mathcal{M}) = \begin{cases} f(x) - \ln\lambda, & \gamma = 1, \\ \lambda^{-\frac{2(\gamma-1)}{\gamma+1}} f(x), & 1 < \gamma \leq \dfrac{5}{3}, \end{cases} \tag{6.50}$$

(formally coincident with equations 6.17 and 6.25), where the function g is the same as in the classical model, while all the information about the host galaxy is contained in the function f, which now reads

$$f(x) = \begin{cases} \dfrac{\chi}{x} + \dfrac{\mathcal{R}}{\xi}\psi\left(\dfrac{x}{\xi}\right) + 2\ln x, & \gamma = 1, \\ x^{\frac{4(\gamma-1)}{\gamma+1}}\left[\dfrac{\chi}{x} + \dfrac{\mathcal{R}}{\xi}\psi\left(\dfrac{x}{\xi}\right) + \dfrac{1}{\gamma-1}\right], & 1 < \gamma \leq \dfrac{5}{3}; \end{cases} \tag{6.51}$$

of course, $\Psi_{\rm g}$ affects the values of $x_{\rm min}$, $f_{\rm min}$, and of the critical λ (which now we shall call $\lambda_{\rm t}$). In any case, equation (6.50) describes the *most general problem of Bondi accretion with electron scattering in the potential of the galaxy hosting the BH at its centre*. Two considerations are in order:

1. The galaxy potential $\Psi_{\rm g}$ can produce more than one minimum for the function f (see e.g. the case of Hernquist galaxies in CP17); in this circumstance, $\lambda_{\rm t}$ is determined via equation (7.56) with $f_{\rm min}$ denoting the *absolute minimum* of f.

2. The values of $x_{\rm min}$, $f_{\rm min}$ and $\lambda_{\rm t}$ strongly depend on the form of the potential $\Psi_{\rm g}$, and for a generic galaxy model they can only be determined numerically. As recently demonstrated, two of the most common galaxy models (Jaffe and Hernquist galaxies, see CP17), and a family of two-component galaxy models (JJ models, see CP18), allow for a fully analytical expression for both the sonic point and the critical accretion parameter in the isothermal case. Another family of (two-component) galaxies models belonging to the same list is that of J3 models, as we shall prove in the next Chapter.

We now discuss separately the two limiting case $\gamma = 1$ and $\gamma = 5/3$.

[13] For galaxy models of finite total mass, or with a total density profile decreasing at large radii at least as r^{-3} (as for NFW profiles), ψ can be taken to be zero at infinity (e.g. C21, Chapter 2).

The case $\gamma = 1$

Concerning the special case $\gamma = 1$, the general solution with electron scattering and in presence of a galaxy of Bondi's problem (6.50) can be written in terms of the Lambert-Euler W function in the form (E9). As for the previous cases, from Appendix E it follows that the critical solution ($\lambda = \lambda_\mathrm{t}$) pertinent to accretion, with an increasing Mach number approaching the center, reads

$$\mathcal{M}^2 = -\begin{cases} W_0\left(-\lambda_\mathrm{t}^2 \mathrm{e}^{-2f}\right), & x \geq x_\mathrm{min}, \\ W_{-1}\left(-\lambda_\mathrm{t}^2 \mathrm{e}^{-2f}\right), & 0 < x \leq x_\mathrm{min}, \end{cases} \tag{6.52}$$

where f is given by the first expression in equation (6.51), while x_min (and then λ_t through f_min) has to be found by studying the function f itself. Of course, equation (6.52) reduces to (6.45) in absence of the host galaxy, and to (6.22) in the classical case.

The case $\gamma = 5/3$

Bondi's problem when $\gamma = 5/3$ requires a separate discussion. In this situation, equation (6.50) reduces to $g(\mathcal{M}) = f(x)/\sqrt{\lambda}$, where

$$g(\mathcal{M}) = \frac{\mathcal{M}^2 + 3}{2\sqrt{\mathcal{M}}}, \qquad f(x) = \chi + \mathcal{R}\,\frac{x}{\xi}\,\psi\!\left(\frac{x}{\xi}\right) + \frac{3}{2}\,x. \tag{6.53}$$

Accordingly, except for the more complicated form of the function f, the problem continues to be formally described by the fourth degree equation (6.36), so that *a fully analytical solution may be obtained*. Anyway, some general considerations of the monoatomic adiabatic case can be made without necessarily solving the equation explicitly. For example, it is easy to show that its minimum is *always* reached at the centre, independent of the specific form of the dimensionless potential ψ. In fact, without loss of generality we may write the galaxy density profile as

$$\rho_\mathrm{g}(r) = \frac{M_\mathrm{g}}{4\pi r_\mathrm{g}^3}\,\tilde{\rho}_\mathrm{g}\!\left(\frac{r}{r_\mathrm{g}}\right) = \frac{M_\mathrm{BH}}{4\pi r_\mathrm{B}^3}\,\frac{\mathcal{R}}{\xi^3}\,\tilde{\rho}_\mathrm{g}\!\left(\frac{x}{\xi}\right), \tag{6.54}$$

which generates a gravitational potential given by the following expression[14]:

$$\Psi_\mathrm{g}(r) = \frac{GM_\mathrm{BH}\mathcal{R}}{r_\mathrm{B}}\left[\frac{1}{x}\int_0^{x/\xi} \tilde{\rho}_\mathrm{g}(t)t^2 dt + \frac{1}{\xi}\int_{x/\xi}^{\infty} \tilde{\rho}_\mathrm{g}(t)\,t\,dt\right]. \tag{6.55}$$

On comparing this equation with equation (6.46), we find that the dimensionless potential ψ takes the form

$$\psi\!\left(\frac{x}{\xi}\right) = \frac{\xi}{x}\int_0^{x/\xi} \tilde{\rho}_\mathrm{g}(t)t^2 dt + \int_{x/\xi}^{\infty} \tilde{\rho}_\mathrm{g}(t)\,t\,dt. \tag{6.56}$$

Now, inserting this expression in equation (6.53), and differentiating with respect to x, we obtain

[14] For a generic spherically symmetrical (untruncated) density distribution $\rho(r)$, the corresponding radial profiles for the cumulative mass and for the gravitational potential (with the natural condition of vanishing at infinity) are given by

$$M(r) = 4\pi\int_0^r \rho(t)t^2 dt, \qquad \Psi(r) = \frac{GM(r)}{r} + 4\pi G\int_r^{\infty} \rho(t)\,t\,dt,$$

(e.g. BT87, § 2.1; C21, equation 2.5).

$$\frac{df}{dx} = \frac{3}{2} + \frac{\mathcal{R}}{\xi}\int_{x/\xi}^{\infty} \tilde{\rho}_{\rm g}(t)\, t\, dt, \tag{6.57}$$

which is evidently *strictly positive*; therefore, $f(x)$ *is a non-negative and monotonically increasing function for all values of* $x \geq 0$. For, the (only) minimum over the physical domain is reached at $x = 0$. In practice, for galaxy models with $r\Psi_{\rm g}(r) \to 0$ when $r \to 0$, one finds:

$$f_{\rm min} = \chi, \qquad\qquad \lambda_{\rm t} = \frac{\chi^2}{4}; \tag{6.58}$$

in particular, $\chi > 0$ in order to have accretion.

6.5 Thermodynamical aspects of the Bondi accretion

In this Section we employ the obtained polytropic solutions to elucidate some important thermodynamical aspects of the Bondi accretion, poorly stressed or discussed in the Literature. In fact, it is not uncommon to consider Bondi accretion as an "adiabatic" problem, where no radiative losses or other forms of heat transfer take place. Nevertheless, even though no heating or cooling functions *seem* to be specified, *the Bondi solution is a purely hydrodynamical flow where all the thermodynamics of heat exchange is implicitly described by the polytropic index* γ. By definition, in fact, a polytropic process is a change of state carried out in such a way that the specific heat $\mathcal{C}$ does not vary during the entire process, i.e. for which

$$\mathcal{C} \equiv \frac{\delta q}{dT} = \text{constant}, \tag{6.59}$$

where δq is the infinitesimal amount of heat (per unit mass) absorbed by the considered body (in our case, the fluid element), and dT is the infinitesimal increase in temperature produced by this heat[15]. By combining the foregoing definition with the First Law of Thermodynamics for a perfect gas, one obtains that the pressure p *must* be related to the density ρ via equation (6.7), with γ given by

$$\gamma = \frac{\mathcal{C}_p - \mathcal{C}}{\mathcal{C}_V - \mathcal{C}}, \tag{6.60}$$

(e.g. Chadrasekhar 1936, Chapter 2). By rearranging the terms in the equation above, the specific heat defining a polytope can be written in terms of the polytropic index as

$$\mathcal{C} = \mathcal{C}_V \frac{\gamma - \gamma_{\rm ad}}{\gamma - 1}. \tag{6.61}$$

The trend of $\mathcal{C}$ as a function of γ, for given $\mathcal{C}_V$ and $\mathcal{C}_p$, is shown in Fig. 6.2. In particular, restricting the values of γ greater than unity, we can identify three main situations which are particularly interesting from a thermodynamical point of view.

- $1 < \gamma < \gamma_{\rm ad}$ (e.g. the case $\gamma = 4/3$ in a monoatomic gas, where $\gamma_{\rm ad} = 5/3$).
  In this case the specific heat assumes *negative* values. As a consequence, a fluid element undergoing a polytropic transformation loses energy as it moves inward, and heats.

[15] Notice that for heat the notation δq has been used instead of dq (see e.g. Pauli 1973, Chapter 1, § 6). In fact, as is well known, the infinitesimal amount of heat *cannot* be represent as the differential of a certain finite quantity (see Planck 1945, where no differential symbol is used in front of q; in particular, see the footnote in § 79).

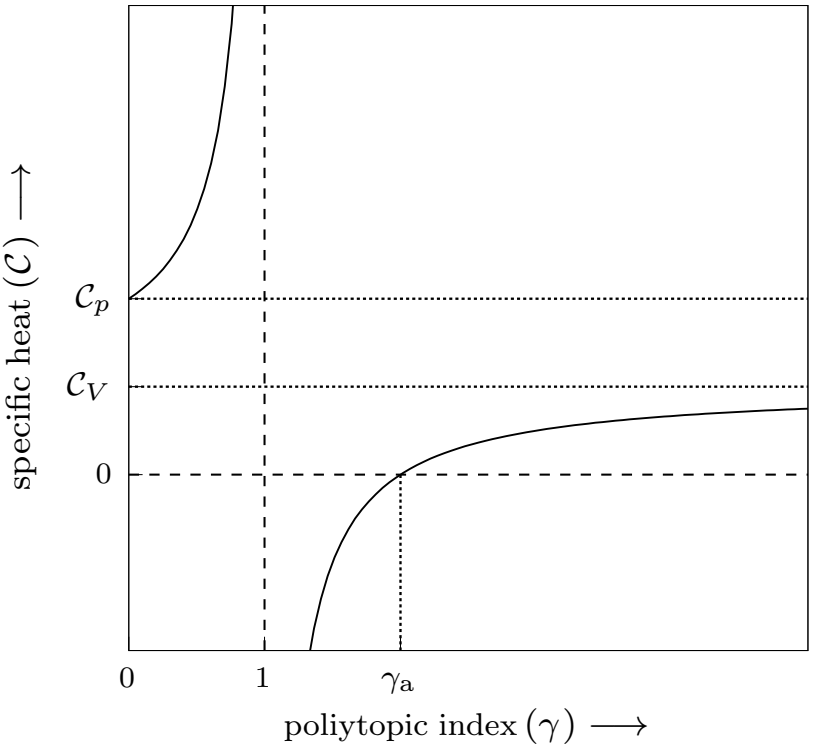

Figure 6.2. Behaviour of the $\mathcal{C}$ as a function γ; notice that range of the polytropic index is extended down to zero. The specific heat equals $\mathcal{C}_p$ for $\gamma = 0$ (isobaric process), diverges for $\gamma = 1$ (isothermal process), is negative when $1 < \gamma < \gamma_{\rm ad}$, positive for $\gamma > \gamma_{\rm ad}$, and reduces to $\mathcal{C}_V$ in the limit $\gamma = \infty$ (isochoric change).

- $\gamma = \gamma_{\rm ad}$ (e.g. the study of $\gamma = 5/3$ accretion in a monoatomic gas).
  We are dealing with an adiabatic process. The specific heat equals zero, therefore the fluid element does not exchange heat with the ambient while it falls towards the BH.

- $\gamma > \gamma_{\rm ad}$ (e.g. the case $\gamma = 5/3$ in a biatomic gas, where $\gamma_{\rm ad} = 7/5$).
  In this situation the specific heat assumes *positive* values. Therefore, as it moves towards the centre along the corresponding polytropic, the fluid element experiences a temperature increase by gaining energy.

In the polytropic Bondi accretion all the cases are possible, except for a monoatomic gas, for which $\gamma_{\rm ad} = 5/3$ and so accretion is possible *only* for $\gamma \leq \gamma_{\rm ad}$ (see Section 6.3.2). We can therefore conclude that, in general, a fluid element necessarily exchanges heat with the external environment as it falls toward the central BH. In this Section we shall show how it is possible to obtain a quantitative estimate of this amount of heat exchanged, as a function of the quantities defining Bondi's problem; to do this, we shall make use of both the definition of pecific heat itself and of the Second Law of Thermodynamics. We then introduce a new physical quantity $\mathcal{Q}$, qualitatively defined as

$$\mathcal{Q} \equiv \frac{\text{rate of heat exchange}}{\text{volume}}, \tag{6.62}$$

which is of course a function of the radius; the task is to find an *expression for* $\mathcal{Q}(r)$ *in terms of the polytropic index* γ. For, we shall briefly mention below some fundamental concepts of Hydrodynamics useful in the analysis. First, we recall that the dynamical state of a moving gas, whose thermodynamic properties are known, can be defined in terms of velocity $\boldsymbol{v}$, density ρ,

and pressure p, as a function of position $\boldsymbol{x}$ and in general of time t; these functions are in turn described by the (differential) equations of continuity, momentum and energy. In deriving the appropriate equations, and to be consistent with the assumptions of the problem, viscosity and thermal conductivity will not be considered.

6.5.1 First method to estimate the heat exchange

From the definition (6.59) it follows that the quantity $\mathcal{Q}$ can be expressed as

$$\mathcal{Q} = \rho \mathcal{C} \frac{DT}{Dt}, \qquad \frac{D}{Dt} \equiv \frac{\partial}{\partial t} + \boldsymbol{v} \cdot \boldsymbol{\nabla}, \tag{6.63}$$

where D/Dt describes the rate of change evaluated by following a moving fluid element[16]; then, by virtue of equation (6.61), in the stationary case we obtain

$$\mathcal{Q} = \mathcal{C}_V \frac{\gamma - \gamma_{\rm ad}}{\gamma - 1} \rho \boldsymbol{v} \cdot \boldsymbol{\nabla} T. \tag{6.64}$$

Now let us specialize this equation for the Bondi problem we are examining. Firstly, we have to find an expression for the (constant) $\mathcal{C}_V = \mathscr{R}/(\gamma_{\rm ad} - 1)$ in terms of the model parameters; since $\mathscr{R}$ is constant, it takes the value at infinity of the quantity $p/(\rho T)$, and so from the equation of state (6.3) the specific heat at constant volume is

$$\mathcal{C}_V = \frac{p_\infty}{(\gamma_{\rm ad} - 1)\rho_\infty T_\infty} = \frac{c_\infty^2}{\gamma(\gamma_{\rm ad} - 1) T_\infty}, \tag{6.65}$$

where the second identity follows from $c_\infty^2 = \gamma p_\infty / \rho_\infty$. Secondly, since we are working in spherical symmetry, $\boldsymbol{v} = -v(r)\boldsymbol{e}_r$, where $v(r) = c_s(r)\mathcal{M}(r)$ denotes the *modulus* of the gas velocity, and $\boldsymbol{\nabla} = \boldsymbol{e}_r d/dr$. Hence, by making use of equation (6.14), after some reductions one has

$$\mathcal{Q} = -\frac{\rho_\infty c_\infty^3}{r_{\rm B}} \frac{\gamma - \gamma_{\rm ad}}{\gamma(\gamma - 1)(\gamma_{\rm ad} - 1)} \mathcal{M} \tilde{\rho}^{\frac{\gamma+1}{2}} \frac{d\tilde{T}}{dx}. \tag{6.66}$$

Finally, by virtue of the continuity equation (6.15), along the critical solution we obtain

$$\frac{\mathcal{Q}}{\mathcal{Q}_{\rm n}} = \frac{\gamma_{\rm ad} - \gamma}{\gamma(\gamma - 1)(\gamma_{\rm ad} - 1)} \frac{\lambda_{\rm t}}{x^2} \frac{d\tilde{T}}{dx}, \qquad \mathcal{Q}_{\rm n} \equiv \frac{\rho_\infty c_\infty^3}{r_{\rm B}}. \tag{6.67}$$

Evidently, this formula does not allow us to obtain the analogous expression for the isothermal case in a direct way, i.e. by setting $\gamma = 1$. To obtain such an expression, it is convenient to find an equivalent form by writing the temperature in terms of the density as $\tilde{T} = \tilde{\rho}^{\gamma-1}$. After some minor reductions, equation (6.66) can be rewritten as

$$\frac{\mathcal{Q}}{\mathcal{Q}_{\rm n}} = \frac{\gamma_{\rm ad} - \gamma}{\gamma(\gamma_{\rm ad} - 1)} \mathcal{M} \tilde{\rho}^{\frac{3(\gamma-1)}{2}} \frac{d\tilde{\rho}}{dx} = \frac{\gamma_{\rm ad} - \gamma}{\gamma(\gamma_{\rm ad} - 1)} \frac{\lambda_{\rm t}}{x^2 \tilde{\rho}^{2-\gamma}} \frac{d\tilde{\rho}}{dx}, \tag{6.68}$$

[16] The operator D/Dt, called convective or material derivative, and representing the rate of change of a quantity associated with a given element of fluid, should not be confused with $\partial/\partial t$, i.e. the rate of change of a quantity *at a fixed point in space*. For example, DT/Dt is the rate of change of temperature of a fluid lump as it moves around, while $\partial T/\partial t$ is the rate of change of temperature at a fixed point (through which a succession of fluid particles will move). Consequently, the acceleration of a fluid element is given by $D\boldsymbol{v}/Dt$; see e.g. Chandrasekhar (1961; here the symbol d/dt is used in place of D/Dt); Batchelor (1967, Chapter 2); Shu (1991, Chapter 9; 1992, Chapter 2), Currie (1993, § 1.3), Granger (1995, § 1.7.3); see also Truesdell (1953) for an interesting historical overview of the hydrodynamical equations.

which, for $\gamma = 1$, reduce to the remarkable formula

$$\frac{\mathcal{Q}}{\mathcal{Q}_\mathrm{n}} = \mathcal{M}\frac{d\tilde{\rho}}{dx} = \frac{\lambda_\mathrm{t}}{x^2}\frac{d\ln\tilde{\rho}}{dx}. \tag{6.69}$$

where the second identity holds along the solution $\lambda = \lambda_\mathrm{t}$. If the gas density profile of an observable object such as a Galaxy Cluster is available (e.g., Eckert et al. 2012; Lyskova et al. 2023), equations (6.68) and (6.69) allow for the determination of the "heat exchange profile" in terms of the polytropic and adiabatic indices of the gas itself.

6.5.2 Second method to estimate the heat exchange

For a *reversible* thermodynamic transformation, we have the possibility to calculate the exchange (per unit mass) as $\delta q = T d\mathcal{S}$, where $\mathcal{S}$ denotes the *specific entropy*. As a consequence, in analogy with equation (6.63), $\mathcal{Q}$ can be also obtained as

$$\mathcal{Q} = \rho T\frac{D\mathcal{S}}{Dt}. \tag{6.70}$$

In general, for a gas obeying exactly the equation of state (6.3), it can be shown that

$$\mathcal{S} = \mathcal{C}_V \ln(p/\rho^{\gamma_\mathrm{ad}}) + \text{constant}, \tag{6.71}$$

(e.g. Chandrasekhar 1939, Chapter II, § 6; Landau & Lifshitz 1987, § 83). Entropy is therefore not a directly measurable quantity, since in principle it requires an estimate of both temperature and density; its precise behavior as a function of position is indeed not easily determined for astrophysical objects (with the exception of Galaxy Clusters, where it can be plotted with some precision, showing a general increase with radius; see e.g. Zhu et al. 2021, and references therein). In case of a polytropic change, $p \propto \rho^\gamma$, so that $d\mathcal{S} = \mathcal{C}_V(\gamma - \gamma_\mathrm{ad})d\ln\tilde{\rho}$; as a consequence, the change of entropy (per unit mass) of an element of the accreting flow along its radial streamline, during a polytropic transformation, is given by

$$\frac{D\mathcal{S}}{Dt} = \mathcal{C}_V(\gamma - \gamma_\mathrm{ad})\frac{D\ln\tilde{\rho}}{Dt}. \tag{6.72}$$

In practice, *for given γ (and in absence of shock waves), one can follow the entropy evolution of each fluid element along the radial streamline, and determine the reversible heat exchanges.* Of course, for $\gamma = \gamma_\mathrm{ad}$ the entropy of each mass element of the fluid remains constant along any streamline, being the process *isentropic*. By combining equations (6.70) and (6.72), and noticing that the product $\rho T\mathcal{C}_V$ equals $p/(\gamma_\mathrm{ad} - 1)$, we obtain

$$\mathcal{Q} = \frac{\gamma - \gamma_\mathrm{ad}}{\gamma(\gamma_\mathrm{ad} - 1)}\,\boldsymbol{v}\cdot\boldsymbol{\nabla}p, \tag{6.73}$$

which reduces simply to $\mathcal{Q} = -\boldsymbol{v}\cdot\boldsymbol{\nabla}p$ in the isothermal case. Clearly, when normalizing all the quantities to the scales of Bondi's problems, thus introducing the radial Mach profile, the resulting one or more expressions concide with equations (6.66), (6.67) or (6.68) for the general $\gamma > 1$ case, and with equation (6.69) for the case $\gamma = 1$.

6.5.3 The enthalphy change in Bondi accretion

We conclude this Section by showing that the heat per unit mass exchanged by a fluid element as it moves from ∞ down to the radius r admits a very simple physical interpretation.

From Classical Thermodynamics, we know that the change in internal energy of a system (i.e. the falling element of fluid in our case) during a thermodynamical process, is given by the whole energy that the system itself receives from the ambient in the form of heat and work. This is the statement of the *First Law of Thermodynamics* (e.g. Feynman 1963, Chapter 44), which, in differential form and per unit mass, takes the form $\delta q = de + pd(1/\rho)$, or

$$\delta q = dh - \frac{dp}{\rho}, \tag{6.74}$$

where, a part from an additive constant, h denotes the *specific enthalpy*. Hence, by integrating the foregoing differential form along the streamline, from ∞ down the generic radius r, we obtain

$$\int_{p_\infty}^{p} \frac{dp}{\rho} = \Delta h - \Delta q, \tag{6.75}$$

where $\Delta h \equiv h(r) - h(\infty)$ is the enthalpy change during the accretion, and Δq represents the (finite) amount of heat which the fluid element exchanges with the surroundings as it falls towards the BH. Notice that the integral at the left-hand side of the equatio above *equals* Δh *only for* $\gamma = \gamma_{\rm ad}$, while in the case $\gamma = 1$ (for which the enthalpy remains constant during the entire process) it reduces to $-T_\infty \Delta \mathcal{S}$. By substituiting equation (6.75) in (6.10), and assuming that the BH is located at the centre of a galaxy, it follows that Bernoulli's equation can be rewtitten as

$$\Delta q = \frac{v^2}{2} + \Delta h - \Psi_{\rm T}, \tag{6.76}$$

where $\Psi_{\rm T} = \Psi_{\rm g} + \Psi_{\rm BH}$ is the total potential. The right-hand side member of the previous equation corresponds to the change of $\mathcal{B} \equiv v^2/2 + h - \Psi_{\rm T}$, a quantity sometimes referred to as "Bernoulli's constant"; in practice, equation (6.76) states that *the total heat exchanged by a unit mass of fluid (moving from* ∞ *to* r*) can then be interpreted as the change of Bernoulli's constant when the enthalpy change in equation* (6.75) *is evaluated along the polytropic solution*[17]. Notice that, if the specific heat is constant (as for polytropic processes), from the definition (6.59) one has $\Delta q = \mathcal{C} \Delta T$; therefore, by virtue of the general expression $\Delta h = \mathcal{C}_p \Delta T$, equation (6.75) can be rewritten as

$$\int_{p_\infty}^{p} \frac{dp}{\rho} = \left(1 - \frac{\mathcal{C}}{\mathcal{C}_p}\right) \Delta h, \tag{6.77}$$

and so, as anticipated in § 6.3, the integral appearing in equation (6.10) is in general just *proportional* to Δh.

6.6 Hydrostatic Approximation

We conclude this Chapter by noting that the inclusion of the effects of the gravitational field of an host galaxy allows to estimate the total mass profile, $M_{\rm T}(r) = M_{\rm BH} + M_{\rm g}(r)$, *under the*

[17] $\mathcal{B}$ is a physical quantity of great importance in Fluid Dynamics. For example, It remains constant along a streamline in steady motion of a frictionless non-conducting fluid; this result is known as *Bernoulli's theorem* (e.g. Batchelor 1967, § 3.5).

assumption of hydrostatic equilibrium (see e.g. Ciotti & Pellegrini 2004; Pellegrini & Ciotti 2006). For, we assume that both the gas and the stars are in equilibrium in the same potential well; consequently, the general equation of motion reads

$$\boldsymbol{g}_{\rm est} - \frac{\boldsymbol{\nabla} p}{\rho} = \boldsymbol{0}, \tag{6.78}$$

where $\boldsymbol{g}_{\rm est}$ is the "estimated" gravitational field. This is the well-known equation of hydrostatics (e.g. Feynman 1964, Chapter 40; Batchelor 1967 § 1.4), which in spherical symmetry reduces to

$$\frac{dp}{dr} = -\rho(r)\frac{GM_{\rm est}(r)}{r^2}, \tag{6.79}$$

being $M_{\rm est}(r)$ the cumulative mass within a sphere of radius r estimated under the assumption of equilibrium. From the polytropic relation (6.7), we obtain, after some minor reductions,

$$M_{\rm est}(r) = -M_{\rm BH}\frac{x^2}{\tilde{\rho}^{2-\gamma}}\frac{d\tilde{\rho}}{dx}, \tag{6.80}$$

which is clearly an increasing function of radius if we reasonably assume a monotonically decreasing gas density profile. For practical purposes, it would be interesting to know whether the quantity $M_{\rm est}$, for a certain distance r from the centre, overestimates or underestimates the total mass $M_{\rm T}$. One way would obviously be to evaluate the ratio $M_{\rm est}/M_{\rm T}$, i.e.

$$\frac{M_{\rm est}(r)}{M_{\rm T}(r)} = -\frac{x^2\tilde{\rho}^{\gamma-2}d\tilde{\rho}/dx}{1+\mathcal{R}\tilde{M}_{\rm g}(x/\xi)}, \qquad \tilde{M}_{\rm g}\left(\frac{x}{\xi}\right) \equiv \int_0^{x/\xi}\tilde{\rho}_{\rm g}(t)t^2dt; \tag{6.81}$$

However, this approach is strongly dependent on the choice of the galaxy model. A more general approach consists of comparing equation (6.78) with the more general *equation of momentum*: assuming that the only volume force involved is the total gravitational force, and excluding all possible effects due to viscosity, it reads

$$\boldsymbol{g}_{\rm T} - \frac{\boldsymbol{\nabla} p}{\rho} = \frac{D\boldsymbol{v}}{Dt}, \tag{6.82}$$

where $\boldsymbol{g}_{\rm T}$ is the gravitational field generated from the total potential $\Psi_{\rm T}$; equation (6.82) is usually known as *Euler's equation* (e.g. Clarke & Carswell 2007, § 2.3). Combining equations (6.78) and (6.82) we obtain

$$\boldsymbol{g}_{\rm T} = \boldsymbol{g}_{\rm est} + \frac{D\boldsymbol{v}}{Dt}. \tag{6.83}$$

Therefore, for stationary spherical systems it follows that

$$M_{\rm est}(r) = M_{\rm T}(r) + \frac{r^2}{2G}\frac{dv^2}{dr}, \tag{6.84}$$

whence it is clear that *the hypothesis of hydrostatic equilibrium always leads to underestimate* $M_{\rm T}$ *in the accretion studies, where the velocity increases in magnitude towards the centre*; in the units of Bondi's problem we have

$$\frac{M_{\rm est}(r)}{M_{\rm BH}} = 1 + \mathcal{R}\tilde{M}_{\rm g}\left(\frac{x}{\xi}\right) + \frac{x^2}{2}\frac{d\tilde{v}^2}{dx}, \tag{6.85}$$

where $\tilde{v} \equiv v/c_\infty = \tilde{\rho}^{(\gamma-1)/2}\mathcal{M}$, coincident with $\mathcal{M}$ in the isothermal case.

CHAPTER 7

Polytropic Bondi Accretion in J3 Galaxies

In this Chapter we study the polytropic accretion of gas onto the BH at the centre of spherical galaxies, by applying the general considerations described in the previous Chapter to the case of the J3 galaxy models, the spherical limit of the ellipsoidal J3e models we constructed and fully analized in Chapter 4. To study the motion of gas flows we generalize the classical Bondi problem by taking into account the effects of the additional gravitational field of the host galaxy, and the radiation pressure due to electron scattering. The hydrodynamical and stellar dynamical properties are linked by imposing that the gas temperature is proportional to the virial temperature of the stellar component. In the isothermal and monoatomic adiabatic cases, we show that the radial profile of the Mach number and the value of the critical accretion parameter can be analytically calculated; thus, in these two peculiar regimes, we showed that a fully analytical solution of the accretion problem at the centre of the J3 galaxies is possible. Unsurprisingly, for generic values of the polytropic index the problem cannot be solved analytically, and so a numerical investigation of the general polytropic case is performed. Finally, we elucidate some important thermodynamical properties of accretion, and determine the underlying cooling/heating function leading to the phenomenological value of the polytropic index.

7.1 The J3 galaxy models

The J3 models are an analytically tractable family of spherical models with a central BH, with a Jaffe stellar density profile, and with a *total* density distribution such that the DM halo (obtained as the difference between the total and stellar density profiles) is described very well by the NFW profile. Such models correspond to the spherical limit of the J3e models discussed in Chapter 4; all the structural properties can then be obtained just by fixing $\eta = 0$ in the corresponding homoeoidal expressions. Of course, concerning the dynamical properties, this procedure limits the study of the orbital structure only to the isotropic case; an in-depth discussion of J3 models, in which the dynamics of the stellar component is described by the Osipkov-Merritt anisotropy, can be found in CMP19 and Mancino (2019). In this preliminary Section we shall limit ourselves to a summary of the main properties useful to set up Bondi's accretion in the potential of J3 galaxies.

7.1.1 Structure of the J3 models

The stellar and galaxy (stars plus DM) density profile of J3 models are respectively given by

$$\rho_*(r) = \frac{\rho_\mathrm{n}}{s^2(1+s)^2}, \qquad \rho_\mathrm{g}(r) = \frac{\mathcal{R}_\mathrm{g}\rho_\mathrm{n}}{s^2(\xi_\mathrm{g}+s)}, \tag{7.1}$$

where the following definitions hold:

$$\rho_\mathrm{n} \equiv \frac{M_*}{4\pi r_*^3}, \qquad s \equiv \frac{r}{r_*}, \qquad \xi_\mathrm{g} \equiv \frac{r_\mathrm{g}}{r_*}, \tag{7.2}$$

being r_* the stellar scale length, M_* the total stellar mass, and r_g the galaxy scale length. The dimensionless quantity $\mathcal{R}_\mathrm{g}$ measures the galaxy-to-stellar density[1]: for example, $\mathcal{R}_\mathrm{g}/\xi_\mathrm{g}$ gives the ratio ρ_g/ρ_* for $r \to 0$. The effective radius $R_\mathrm{e} \simeq 0.75\, r_*$ of the Jaffe profile (i.e. the radius in the projection plane encircling half of the total mass) is $R_\mathrm{e} \simeq 0.75\, r_*$.

The associated stellar and galaxy mass profiles read

$$M_*(r) = M_* \frac{s}{1+s}, \qquad M_\mathrm{g}(r) = M_* \mathcal{R}_\mathrm{g} \ln\frac{\xi_\mathrm{g}+s}{\xi_\mathrm{g}}, \tag{7.3}$$

(see footnote 14 in § 6.4.2). Notice that r_* is nothing else than the half-mass radius and, while $M_\mathrm{g}(r)$ diverges logarithmically for $r \to \infty$.

The DM halo density distribution is obtained by the difference

$$\rho_\mathrm{DM}(r) \equiv \rho_\mathrm{g}(r) - \rho_*(r) = \frac{\rho_\mathrm{n}}{s^2}\left[\frac{\mathcal{R}_\mathrm{g}}{\xi_\mathrm{g}+s} - \frac{1}{(1+s)^2}\right]. \tag{7.4}$$

By construction, the radial behaviour of ρ_DM depends in general on ξ_g and $\mathcal{R}_\mathrm{g}$; however, not all values of these two parameters are compatible with a nowhere negative DM distribution. In analogy with the case of the corresponding ellipsoidal J3e models, the condition for the positivity of the DM halo density given in (7.4) is obtained by imposing $\rho_\mathrm{DM}(r) \geq 0$ for $r \geq 0$. As shown in CMP19, such a condition reads

[1] Note that, by comparison with equation (4.2), we have slightly changed the notation for ξ and $\mathcal{R}$ by adding a subscript "g", while still mantaining the same meaning.

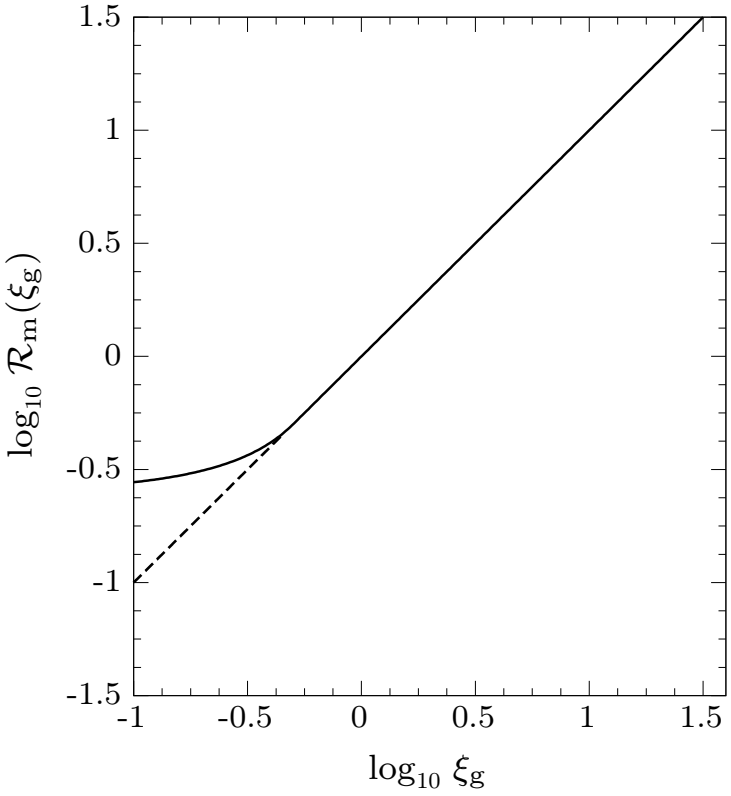

Figure 7.1. The function $\mathcal{R}(\xi_{\rm g})$, as given by equation (7.5). Only models in the region above the black solid line have a DM halo with a nowhere negative $\rho_{\rm DM}(r)$.

$$\mathcal{R}_{\rm g} \geq \mathcal{R}_{\rm m} \equiv \begin{cases} \dfrac{1}{4(1-\xi_{\rm g})}, & 0 < \xi_{\rm g} \leq \dfrac{1}{2}, \\ \xi_{\rm g}\,, & \xi_{\rm g} \geq \dfrac{1}{2}. \end{cases} \tag{7.5}$$

For given $\xi_{\rm g}$, $\mathcal{R}_{\rm m}(\xi_{\rm g})$ is the *minimum* value of $\mathcal{R}_{\rm g}$ in order to have a nowhere negative DM halo, and a DM halo of a model with $\mathcal{R}_{\rm g} = \mathcal{R}_{\rm m}(\xi_{\rm g})$ is called a *minimum halo*. Values of $(\xi_{\rm g}, \mathcal{R}_{\rm g})$ between the dashed and solid lines in Fig. 7.1 correspond to $\rho_{\rm DM}(r)$ that becomes negative off-center. Only values of $(\xi_{\rm g}, \mathcal{R}_{\rm g})$ located in the region above the black solid line are associated with a DM halo with a nowhere negative $\rho_{\rm DM}(r)$. For assigned $\xi_{\rm g}$, it is convenient to introduce the parameter α, defined as

$$\mathcal{R}_{\rm g} = \alpha \mathcal{R}_{\rm m}, \qquad \alpha \geq 1; \tag{7.6}$$

in the following we shall restrict to the "natural" situation $\xi_{\rm g} \geq 1$, so that $\mathcal{R}_{\rm g} = \alpha \xi_{\rm g}$, with $\alpha = 1$ corresponding to the minimum halo model. Therefore, from equations (7.3), the relative amount of dark-to-total mass as a function of radius is

$$\frac{M_{\rm DM}(r)}{M_{\rm g}(r)} = 1 - \frac{s}{\alpha \xi_{\rm g}(1+s)\ln(1+s/\xi_{\rm g})}, \tag{7.7}$$

where $M_{\rm DM}(r) = M_{\rm g}(r) - M_*(r)$. In Fig. 7.2 (top panel, solid lines) we plot equation (7.7) as a

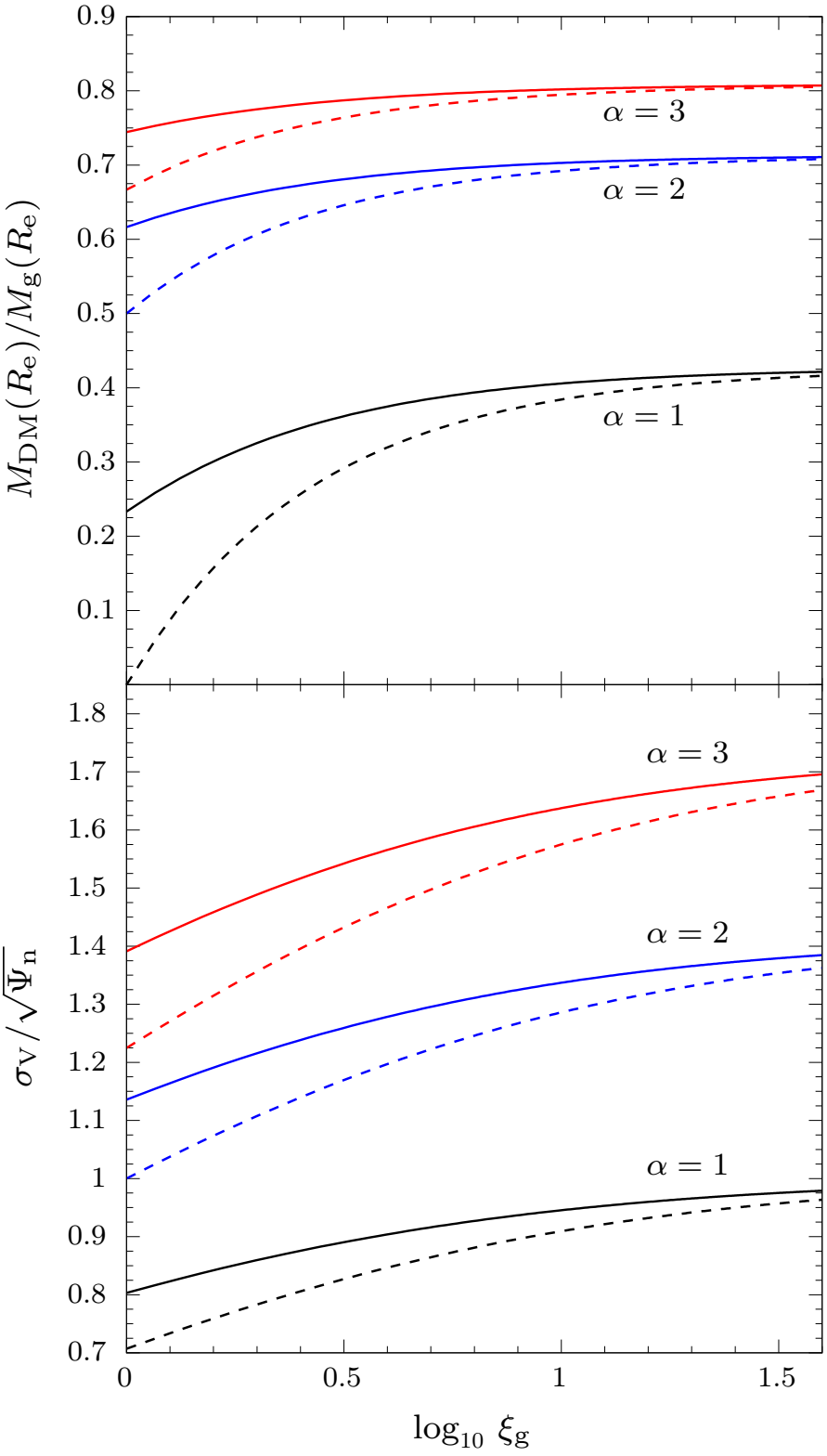

Figure 7.2. Top: dark-to-total mass ratio of the J3 models (solid lines) within a sphere of radius $r = R_{\rm e} \simeq 0.75\, r_*$ as a function of $\xi_{\rm g} = r_{\rm g}/r_*$ for the minimum halo case $\alpha = 1$ (black), $\alpha = 2$ (blue), and $\alpha = 3$ (red). For comparison, the analogous curves in the case of JJ models (dashed lines) are shown. Bottom: the galactic virial velocity dispersion $\sigma_{\rm V}$ (solid lines) as a function of $\xi_{\rm g}$, for $\alpha = 1$ (black), $\alpha = 2$ (blue), and $\alpha = 3$ (red). For comparison, the analogous curves in the case of JJ models (dashed lines) are shown.

function of $\xi_g \geq 1$ for $r = R_e$ and for three values of α: the minimum halo model ($\alpha = 1$) and two cases with $\alpha > 1$. Fractions of DM with values for the minimum halo case in agreement with those required by the dynamical modelling of early-type galaxies (see e.g. Cappellari et al. 2015) can be easily obtained. These fractions are unsurprisingly sligthly larger than those obtained in the case of JJ models for the same values of ξ_g (see dashed lines in Fig. 7.2, left panel).

Notice that by construction, $\rho_{DM} \propto r^{-3}$ at large radii, while $\rho_{DM} \propto r^{-2}$ at small radii (i.e. the DM and stellar densities are locally proportional), with the exception of the minimum halo models, in which $\rho_{DM} \propto r^{-1}$. We now compare the DM profile of J3 models with the untruncated NFW profile, that in our notation can be written as

$$\rho_{NFW}(r) = \frac{\rho_n \mathcal{R}_{NFW}}{q(c)s(\xi_{NFW} + s)^2}, \qquad q(c) \equiv \ln(1+c) - \frac{c}{1+c}, \tag{7.8}$$

(Mancino 2019, § 2.3.3), where $\xi_{NFW} \equiv r_{NFW}/r_*$ is the NFW scale length in units of r_* and, for a chosen reference radius r_t, we *define* $\mathcal{R}_{NFW} \equiv M_{NFW}(r_t)/M_*$ and $c \equiv r_t/r_{NFW}$. It is easy to show that the densities ρ_{DM} and ρ_{NFW} can be made asymptotically identical both at small *and* large radii just by fixing

$$\mathcal{R}_{NFW} = q(c)\,\xi_g, \qquad \xi_{NFW} = \frac{\xi_g}{\sqrt{2\xi_g - 1}}. \tag{7.9}$$

Hence, once a specific minimum halo galaxy model is considered, equations (7.8) and (7.9) allow to determine the NFW profile that best reproduces the DM halo density profile. Cosmological simulations suggest for galaxies $c \simeq 10$ (see e.g. Bullock & Boylan-Kolchin 2017), and $\mathcal{R}_{NFW} \simeq$ a few tens. Moreover, the value of ξ_g cannot be too large, otherwise the DM fraction inside R_e would exceed the values derived from observations (see e.g. Napolitano et al. 2010; see also Fig. 1 in CMP19). For these reasons we conclude that *the* NFW *shape and the cosmological expectations are reproduced if we consider minimum halo models with* $\xi_g \simeq 10 \div 20$. In the following, we choose as 'reference model' a minimum halo model with $\mathcal{R}_g = \xi_g = 13$, $c = 10$, $\mathcal{R}_{NFW} \simeq 20$, and $r_{NFW} = 2.6\,r_*$.

7.1.2 Dynamics of the J3 models

Now we recall a few dynamical properties of the J3 models needed in the following discussion. When a BH of mass $M_{BH} = \mu M_*$ is added at the centre of the galaxy, the total potential becomes

$$\Psi_T(r) = \Psi_{BH}(r) + \Psi_g(r). \tag{7.10}$$

Of course, even though the total mass is infinite, yet the normalization value at infinity can still be assumed equal to zero, inasmuch as the density profile at large radii is steeper than r^{-2}. With this assumption,

$$\Psi_{BH}(r) = \frac{\Psi_n \mu}{s}, \qquad \Psi_g(r) = \frac{\Psi_n \mathcal{R}_g}{\xi_g}\left(\ln\frac{\xi_g + s}{s} + \frac{\xi_g}{s}\ln\frac{\xi_g + s}{\xi_g}\right); \tag{7.11}$$

where $\Psi_n \equiv GM_*/r_*$. In particular, $\Psi_g \propto (\ln s)/s$ at large radii, while $\Psi_g \propto -\ln s$ near the centre.

By virtue of equation (7.10), the radial component of the velocity dispersion can be written as

$$\sigma_r^2(r) = \sigma_{BH}^2(r) + \sigma_g^2(r), \tag{7.12}$$

where $\sigma_{\rm BH}$ and $\sigma_{\rm g}$ indicate, respectively, the contribution of the BH and of the galaxy potential. As anticipated, Jeans's equations can be solved analytically, and the explicit expression for the associated solutions are given in § 4.1 of CMP19; in particular, in the isotropic case, we found that the asymptotic trend reads

$$\frac{\sigma_{\rm r}^2}{\Psi_{\rm n}} \sim \begin{cases} \dfrac{\mu}{3s} + \dfrac{\mathcal{R}_{\rm g}}{2\xi_{\rm g}} - \dfrac{\mu}{3}, & s \to 0, \\ \mathcal{R}_{\rm g} \dfrac{\ln s}{5s}, & s \to \infty, \end{cases} \tag{7.13}$$

where, for mathematical consistency, we retained also the constant term $-\mu/3$ in the asymptotic expansion of $\sigma_{\rm r}$ near the centre, although this contribution is fully negligible in realistic galaxy models since $\mu \approx 10^{-3}$. Notice that, when $\xi_{\rm g} \geq 1$, from equation (7.6) it follows that the constant term due to the galaxy is independent of $\xi_{\rm g}$, with $\sigma_{\rm g}^2(0) = \Psi_{\rm n}\alpha/2$. This latter expression provides the interesting possibility of adopting $\sigma_{\rm g}(0)$ as a proxy for the observed velocity dispersion of the galaxy in the central regions, outside the sphere of influence of the central MBH.

The projected velocity dispersion $\sigma_{\rm p}$ in the isotropic case is given by

$$\Sigma_*(R)\sigma_{\rm p}^2(R) = 2\int_R^\infty \frac{\rho_*(r)\sigma_{\rm r}^2(r)rdr}{\sqrt{r^2-R^2}}, \tag{7.14}$$

where R is the radius in the projection plane, and Σ_* is the projected density profile, computed by integrating the spatial density distribution along the line of sight, i.e.

$$\Sigma_*(R) = 2\int_R^\infty \frac{\rho_*(r)rdr}{\sqrt{r^2-R^2}}, \tag{7.15}$$

(e.g., BT08); unsurprisingly, the projection integral in equation (7.14) cannot be evaluated analytically for J3 models in terms of elementary functions. In analogy with equation (7.12), we can split $\sigma_{\rm p}$ into two contributions:

$$\sigma_{\rm p}^2(R) = \sigma_{\rm pBH}^2(R) + \sigma_{\rm pg}^2(R), \tag{7.16}$$

being $\sigma_{\rm pBH}$ and $\sigma_{\rm pg}$ respectively the contribution of the BH and of the galaxy potential. Particularly interesting is the trend of $\sigma_{\rm p}$ at small radii; in these regions, in fact, it is easy to show that the asymptotic behaviour for the two contributions reads.

$$\frac{\sigma_{\rm pBH}^2}{\Psi_{\rm n}} \sim \frac{2\mu}{3\pi\tilde{R}}, \qquad \frac{\sigma_{\rm pg}^2}{\Psi_{\rm n}} \sim \frac{\mathcal{R}_{\rm g}}{2\xi_{\rm g}}, \tag{7.17}$$

(see CMP19, equations 57 and 58), with $\tilde{R} \equiv R/r_*$. By comparison the foregoing equation with the first expression in (7.13) we draw the following remarkable conclusion: *in absence of the central BH, in the inner regions the projected velocity dispersion coincides with the radial component of the intrinsic velocity dispersion*[2]. Equation (7.17) allows to estimate the radius $R_{\rm inf}$ of the "sphere of influence", here defined as the *distance from the centre in the projection plane where* $\sigma_{\rm p}$ *in presence of the BH exceedes by a factor* $(1+\epsilon)$ *the galaxy projected velocity dispersion* $\sigma_{\rm pg}$ *in absence of the BH*:

[2] Actually, this particular situation occurs for any strictly positive value of the so-called "anisotropy radius", if for example the orbital structure of the stellar component follows the Osipkov-Merritt anisotropy profile.

$$\sqrt{\sigma^2_{\rm pBH}(R_{\rm inf}) + \sigma^2_{\rm pg}(R_{\rm inf})} \equiv (1+\epsilon)\sigma_{\rm pg}(R_{\rm inf}). \tag{7.18}$$

Since $R_{\rm inf} \ll r_*$, equation (7.17) yields

$$\frac{R_{\rm inf}}{r_*} \simeq \frac{4\xi_{\rm g}\mu}{3\pi\mathcal{R}_{\rm g}\epsilon(2+\epsilon)} = \frac{4\mu}{3\pi\alpha\epsilon(2+\epsilon)}, \tag{7.19}$$

where the last identity holds for minimum halo models with $\xi_{\rm g} \geq 1$. For realistic values of the model parameters, $R_{\rm inf}$ is of the order of a few pc.

A fundamental ingredient in Bondi accretion is the gas temperature at infinity T_∞. Following Pellegrini (2011), we shall use $T_{\rm V} = \mu_0 m_{\rm p}\sigma^2_{\rm V}/(3k_{\rm B})$ as the natural scale for T_∞, where $\sigma_{\rm V}$ is the (three dimensional) *virial velocity dispersion* of stars; of course, this latter quantity is obtained from the Virial Theorem, i.e.

$$M_*\sigma^2_{\rm V} \equiv 2K_* = -W_{*\rm g} - W_{*\rm BH}. \tag{7.20}$$

where K_* is the total *kinetic energy* of the stars, while $W_{*\rm g}$ and $W_{*\rm BH}$ are respectively the *interaction energy* of the stars with the gravitational field of the galaxy (stars plus DM) and of the BH, defined as

$$W_{*\rm g} = -4\pi G\int_0^\infty M_{\rm g}(r)\rho_*(r)rdr, \qquad W_{*\rm BH} = -4\pi G M_{\rm BH}\int_0^\infty \rho_*(r)rdr; \tag{7.21}$$

note that $W_{*\rm BH}$ diverges because the stellar density profile diverges near the origin as r^{-2}. Since we shall use K_* to evaluate the gas temperature over the entire galaxy (where the BH effect is negligible), we only consider $W_{*\rm g}$ in the determination of $\sigma_{\rm V}$. Hence, $\sigma^2_{\rm V} = -W_{*\rm g}/M_*$, i.e., from CMP21,

$$\sigma^2_{\rm V} = \Psi_{\rm n}\mathcal{R}_{\rm g}\tilde{W}_{*\rm g}, \qquad \tilde{W}_{*\rm g} = \mathcal{H}(\xi_{\rm g},0) - \frac{\ln\xi_{\rm g}}{\xi_{\rm g}-1}, \tag{7.22}$$

where the function $\mathcal{H}(\xi_{\rm g}, s)$ is given in Appendix C of CMP19. Fig. 7.2 (bottom panel) shows the trend of $\sigma_{\rm V}$ as a function of $\xi_{\rm g} \geq 1$, for three J3 (solid) models; for comparison, we show with dashed lines the profiles of $\sigma_{\rm V}$ for the JJ models. As expected, $\sigma_{\rm V}$ increases with $\xi_{\rm g}$, and $\sigma_{\rm V} \simeq \sqrt{\alpha\Psi_{\rm n}}$ when $r_{\rm g} \gg r_*$.

7.2 Linking Stellar Dynamics to Fluid Dynamics

We now link the stellar dynamical properties of the galaxy models with the defining parameters of Bondi accretion introduced in Section 6.4.2; in fact, the function f in equation (6.51) is written in terms of quantities referring to the central BH and to the gas temperature at infinity, while the stellar dynamical properties of the J3 models are written in terms of the observational properties of the galaxy stellar component. In practice, since the dynamical properties of the stellar component of the galaxy can be computed analytically once the total potential is assigned, the virial theorem for the stellar component can be used to compute the virial "temperature" $T_{\rm V}$ of stars, a realistic proxy for the gas temperature T_∞; the idea is then to self-consistently "close" the model by determining a fiducial value for the gas temperature as a function of the galaxy model. Following this approach, the steps to build an accretion solution are:

Table 7.1: Galaxy Structure and Accretion Flow parameters

Galaxy Structure		Accretion Flow	
Symbol	Quantity	Symbol	Quantity
M_*	Total stellar mass	T_∞	Gas temperature at infinity
r_*	Stellar density scale length	ρ_∞	Gas density at infinity
$M_{\rm g}$	Total[a] galaxy mass	c_∞	Speed of sound at infinity
$r_{\rm g}$	Total density scale length	γ	Polytropic index ($1 \leq \gamma \leq 5/3$)
$M_{\rm BH}$	Central MBH mass	$\gamma_{\rm ad}$	Adiabatic index ($=\mathcal{C}_p/\mathcal{C}_V > 1$)
μ	$M_{\rm BH}/M_*$	$\mathcal{R}$	$M_{\rm g}/M_{\rm BH}$ ($=\mathcal{R}_{\rm g}/\mu$)
$\mathcal{R}_{\rm g}$	$M_{\rm g}/M_*$ ($=\alpha\mathcal{R}_{\rm m}$)	β	$T_\infty/T_{\rm V}$
$\mathcal{R}_{\rm m}$	Minimum value of $\mathcal{R}_{\rm g}$	$r_{\rm B}$	Bondi radius
$\xi_{\rm g}$	$r_{\rm g}/r_*$	$r_{\rm min}$	Sonic radius
s	r/r_*	x	$r/r_{\rm B}$
$\sigma_{\rm V}$	Stellar virial velocity dispersion	ξ	$r_{\rm g}/r_{\rm B}$
$T_{\rm V}$	Stellar virial temperature	$\lambda_{\rm t}$	Critical accretion parameter
$W_{*{\rm g}}$	Virial energy of stars	$\mathcal{M}$	Mach number

[a] For example, from our definition $M_{\rm g} = \mathcal{R}_{\rm g} M_*$, and equation (7.1), $M_{\rm g}$ is the total mass (stellar plus DM) inside a sphere of radius $({\rm e}-1)r_{\rm g}$.

1. choose r_*, M_*, $\xi_{\rm g}$, $\mathcal{R}_{\rm g}$, and μ for a realistic galactic model;
2. obtain the gas virial temperature $T_{\rm V}$;
3. derive ξ and $\mathcal{R}$ to be used in the Bondi problem.

In the discussion below, let us assume the galaxy parameters of the first step have been chosen. The first accretion parameter (third step) we consider is $\mathcal{R}$; from its definition in equation (6.47), for assigned $\xi_{\rm g}$ and $\mathcal{R}_{\rm g}$ it is obtained as

$$\mathcal{R} = \frac{\mathcal{R}_{\rm g}}{\mu} = \frac{\alpha\xi_{\rm g}}{\mu}, \tag{7.23}$$

where the last identity derives from equation (7.6) with $\xi_{\rm g} \geq 1$, a condition we shall adopt throughout the present Section; notice that $\mathcal{R} \approx 10^4$ for $\xi_{\rm g}$ of the order of tens, α of order unity, and $\mu \approx 10^{-3}$.

The determination of the accretion parameter ξ is more articulated. This quantity depends on the Bondi radius $r_{\rm B}$, which in turn depends on the gas temperature at infinity. In principle, arbitrary values of T_∞ could be adopted, but *in real systems the natural scale for the global temperature is represented by the virial temperature* $T_{\rm V}$, defined through the virial velocity dispersion in equation (7.20). Accordingly, we introduce the (positive) parameter

$$\beta \equiv \frac{T_\infty}{T_{\rm V}}; \tag{7.24}$$

by combining this definition with the expression for $T_{\rm V}$ given before equation (7.20), we can rewrite the square of the sound speed at infinity as

$$c_\infty^2 = \gamma\,\frac{k_{\rm B}T_\infty}{\mu_0 m_{\rm p}} = \frac{\gamma\beta\sigma_{\rm V}^2}{3}. \tag{7.25}$$

From equations (6.12) and (7.22) we then obtain

$$\frac{r_{\rm B}}{r_*} = \frac{3\mu}{\alpha\beta\gamma\mathcal{F}_{\rm g}(\xi_{\rm g})}, \qquad \mathcal{F}_{\rm g} \equiv \xi_{\rm g}\tilde{W}_{*{\rm g}}(\xi_{\rm g}), \tag{7.26}$$

where the function $\mathcal{F}_{\rm g}$ monothonically increases with $\xi_{\rm g}$ from $\mathcal{F}_{\rm g}(1) = \pi^2/6 - 1$ to $\mathcal{F}_{\rm g}(\infty) = 1$. For example, for fixed values of α, β, and γ, one has

$$\frac{3\mu}{\alpha\beta\gamma} < \frac{r_{\rm B}}{r_*} \leq \frac{18\mu}{(\pi^2-6)\alpha\beta\gamma}. \tag{7.27}$$

In Fig. 7.3 (top) we show the trend of $r_{\rm B}/r_*$ as a function of $\xi_{\rm g}$ in the minimum halo case ($\alpha = 1$) with $\beta = 1$ and $\mu = 0.002$, for three values of γ; in general, $r_{\rm B}$ is of the order of a few $10^{-3} r_*$. Note that, for fixed $\xi_{\rm g}$, the isothermal profile (black line) is above that in the corresponding adiabatic case (red line); in general, for fixed α, β and $\xi_{\rm g}$, $r_{\rm B}/r_*$ always lies between the isothermal and the monoatomic adiabatic case, as shown by equation (7.27). Finally, by combining equations (6.47) and (7.26),

$$\xi = \frac{\beta\gamma\mathcal{F}_{\rm g}(\xi_{\rm g})}{3}\mathcal{R} = \frac{\alpha\beta\gamma\xi_{\rm g}\mathcal{F}_{\rm g}(\xi_{\rm g})}{3\mu}. \tag{7.28}$$

Curiously, from the general definitions in equation (6.47), and defining $\sigma^2_{\rm pg}(0) \equiv \Psi_{\rm n}\alpha/2$ by virtue of equation (7.17), it follows that

$$\frac{\mathcal{R}}{\xi} = \frac{2\sigma^2_{\rm pg}(0)}{c^2_\infty}, \tag{7.29}$$

which *links directly the parameters of Bondi accretion to the observable* $\sigma_{\rm pg}(0) = \sigma_{\rm g}(0)$. In practice, ξ *and* $\mathcal{R}$ *are linked, and increasing values of* $\mathcal{R}$ *correspond to increasing values of* ξ. The list of all parameters discussed in this work is given in Table 7.1.

For observational purposes, it is also useful to express the position of $r_{\rm B}$ in terms of the radius $R_{\rm inf}$. From equations (7.19) and (7.26) it follows that the parameter $\alpha = \mathcal{R}_{\rm g}/\mathcal{R}_{\rm m}$ cancels out, so that we obtain

$$\frac{r_{\rm B}}{R_{\rm inf}} = \frac{9\pi\epsilon(2+\epsilon)}{4\beta\gamma\mathcal{F}_{\rm g}(\xi_{\rm g})}, \tag{7.30}$$

independently of the minimum halo assumption. In Fig. 7.3 (bottom) we show the trend of $r_{\rm B}/R_{\rm inf}$ when $\epsilon = 0.5$ and $\beta = 1$, for the same three values of γ as in the upper panel: $r_{\rm B} \approx$ a few times $R_{\rm inf}$.

In concluding this Section, we recall that the effects of the galaxy do manifest themselves in the position of the *sonic radius* $r_{\rm min}$, one of the most important properties of the accretion solution. When measured in terms of the scale length r_* it can be written as

$$\frac{r_{\rm min}}{r_*} = x_{\rm min}(\chi, \mathcal{R}, \xi)\frac{r_{\rm B}}{r_*}, \tag{7.31}$$

where $x_{\rm min} \equiv r_{\rm min}/r_{\rm B}$ gives the (absolute) minimum of f, while the ratio $r_{\rm B}/r_*$ must be obtained via equation (7.26).

7.3 The case $\gamma = 1$

We begin by discussing Bondi's problem with electron scattering in J3 galaxies for the *isothermal* case, in which the entire accretion solution can be given analytically. As a consequence, it is possible to express the critical accretion parameter analytically, as well as the entire radial profile of the Mach number and of all the hydrodynamical functions.

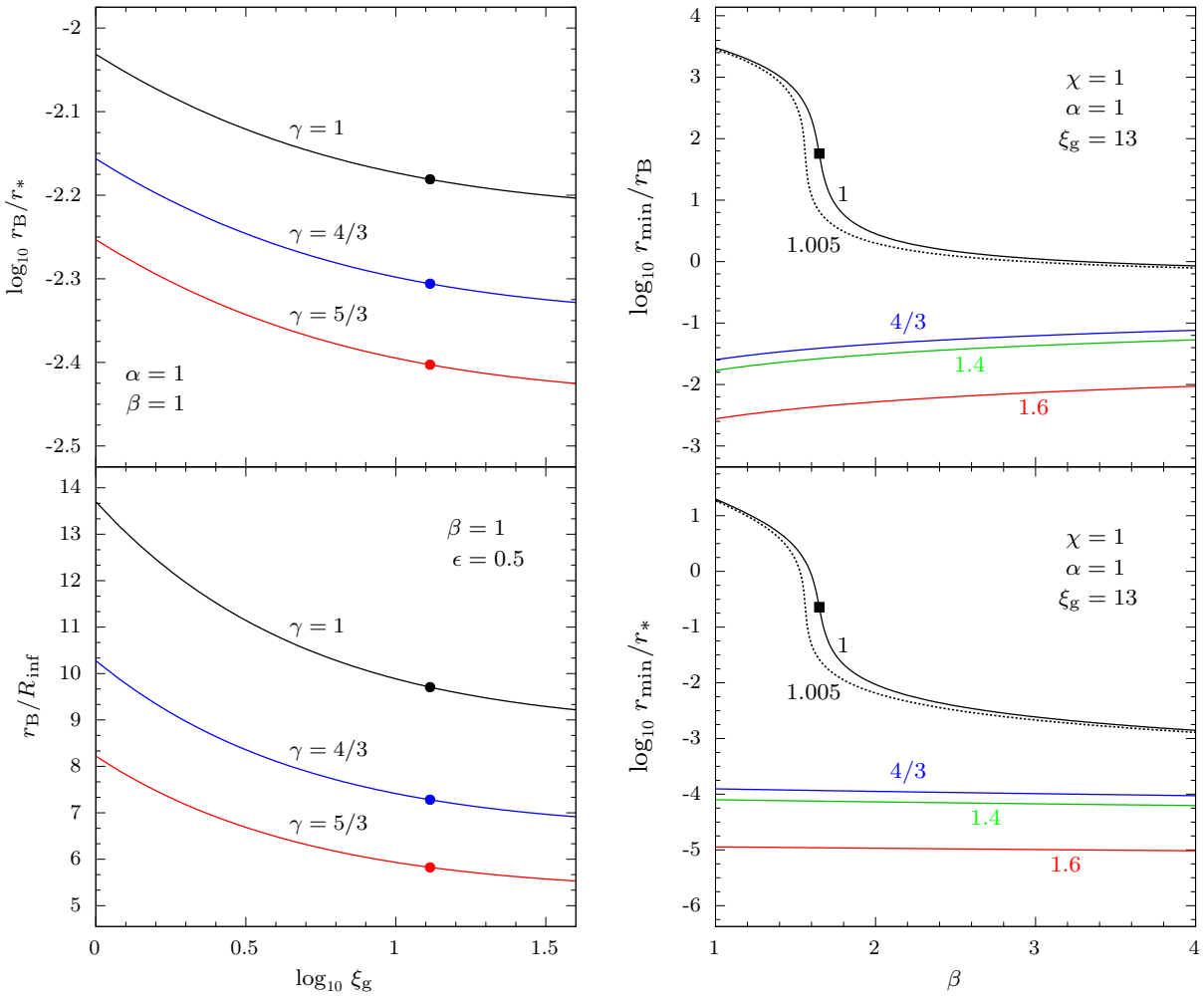

Figure 7.3. Left: Bondi radius r_B in units of r_* (top) and R_{inf} (bottom), as a function of the galaxy-to-stellar scale length ratio $\xi_g = r_g/r_*$, for three J3 galaxy models with $\beta \equiv T_V/T_\infty = 1$, $\mu = 0.002$, and $\gamma = 1$, 4/3, 5/3; the solid dots at $r_B/r_* \simeq 0.0066$, 0.0049, 0.0039 correspond to the minimum halo case with $\xi_g = 13$; solid dots at $r_B/R_{inf} \simeq 9.71$, 7.28, 5.82 correspond to the case $\xi_g = 13$ and $\epsilon = 0.5$. Right: position of $x_{min} \equiv r_{min}/r_B$ (top) and r_{min}/r_* (bottom) as a function of $\beta = T_\infty/T_V$, in the case of minimum halo models with $\xi_g = 13$, $\mu = 0.002$, and $\chi = 1$, for different values of the polytropic index given close to the curves. The black square points at $r_{min}/r_B \simeq 57.34$ and $r_{min}/r_* \simeq 0.23$ correspond to the critical case $\beta = \beta_c \simeq 1.65$.

The problem is completely described by equations (6.50)-(6.51). The dimensionless potential ψ is obtained by using the normalization scales in equation (6.48): from the identity $s/\xi_g = x/\xi$ it readily follows that

$$\psi\left(\frac{x}{\xi}\right) = \ln\left(1 + \frac{\xi}{x}\right) + \frac{\xi}{x}\ln\left(1 + \frac{x}{\xi}\right). \tag{7.32}$$

Let us begin by analyzing the radial trend of f. A simple asymptotic analysis shows that

$$f(x) = \begin{cases} \dfrac{\chi}{x} + \dfrac{2\xi - \mathcal{R}}{\xi}\ln x + \dfrac{\mathcal{R}(1 + \ln\xi)}{\xi} + \mathcal{O}(x), & x \to 0^+, \\ 2\ln x + \mathcal{O}\left(\dfrac{\ln x}{x}\right), & x \to \infty. \end{cases} \tag{7.33}$$

Notice that, while f diverges logarithmically at large radii independently of the model parameters, the behaviour of f in the central regions depends on the parameters χ, ξ, and $\mathcal{R}$; in particular,

$$\lim_{x\to 0^+} f(x) = \begin{cases} \infty, & \chi \neq 0, \\ A, & \chi = 0, \end{cases} \qquad A \equiv \begin{cases} -\infty, & \mathcal{R} < 2\xi, \\ 2(1+\ln\xi), & \mathcal{R} = 2\xi, \\ \infty, & \mathcal{R} > 2\xi. \end{cases} \tag{7.34}$$

Thanks to this simple preliminary analysis, we can schematically split the discussion of the problem into two main cases as follows.

- $\chi \neq 0$.
  Since f is a continuous function, its first derivative must vanish at one or more points $x > 0$. The sonic point $x_{\min}$ is the one corresponding to the absolute minimum of $f(x)$, i.e. such that $f(x) \geq f(x_{\min})$ for all values of x.
- $\chi = 0$.
  In this case, i.e. when radiation pressure exactly cancels the BH gravitational field, three sub-cases may occur.
  1. $\mathcal{R} < 2\xi$: formally, $f_{\min} = -\infty$ (reached at the origin), and therefore *no accretion is possible* since λ_{t} would be zero.
  2. $\mathcal{R} = 2\xi$: in this case, $x_{\min}$ must be firstly searched among the stationary points of $f(x)$, and secondly compared the corresponding local minima with the value $2(1+\ln\xi)$.
  3. $\mathcal{R} > 2\xi$: in this situation, an analysis similar to that used to discuss the case $\chi \neq 0$ must be performed.

The starting point for the whole discussion is the first derivative of the function $f(x)$, i.e.

$$\frac{df}{dx} = \frac{1}{x^2}\left(2x - \chi - \mathcal{R}\ln\frac{\xi+x}{\xi}\right). \tag{7.35}$$

Consequently, the stationary points of f are those values of x (necessarily positive) satisfying the following transcendent equation:

$$2x - \chi = \mathcal{R}\ln\frac{\xi+x}{\xi}. \tag{7.36}$$

It is easy to realize that this equation always admits two solutions: a positive and a negative one; of course, the negative one is to be discarded as physically unacceptable[3]. These solutions can be found explicitly through the Lambert-Euler W function; in fact, it is easy to see that the foregoing equation can be rewritten as

$$\frac{\xi+x}{\xi} - \frac{\mathcal{R}}{2\xi}\ln\frac{\xi+x}{\xi} = 1 + \frac{\chi}{2\xi}, \tag{7.37}$$

[3]From a graphical point of view, the solutions of equation (7.36) correspond to the abscissae of the intersection points between the functions $y = 2x - \chi$ and $y = \mathcal{R}\ln(1 + x/\xi)$ when plotted on a Cartesian plane. For arbitrary values of ξ and $\mathcal{R}$, the logarithmic function is an increasing monotone function defined for $x > -\xi$, with a vertical asymptote $x = -\xi$, and passing through the origin of the axes; the linear function, on the other hand, has an angular coefficient equal to 2, and a vertical intercept $(-\chi, 0)$. Since $\chi > 0$, the line $y = 2x - \chi$ intersects the logarithmic function at two points, one with negative abscissa, and one with positive abscissa.

which coincides with equation (E6) when setting

$$a = b = 1, \qquad c = -\frac{\mathcal{R}}{2\xi}, \qquad X = 1 + \frac{x}{\xi}, \qquad Y = 1 + \frac{\chi}{2\xi}. \tag{7.38}$$

Therefore, by virtue of equation (E9), the solution of (7.36), and so the sonic point $x_{\rm min}$, reads

$$1 + \frac{x_{\rm min}}{\xi} = cW\left(\frac{1}{c}\,\mathrm{e}^{\frac{Y}{c}}\right). \tag{7.39}$$

This equation represents the *formal solution for* $x_{\rm min}$ *in the isothermal accretion for generic values of the model parameters*. For the general validity of (7.39), two conditions are in order.

1. The first condition is that the argument of W *must* be ≤ 0. In fact, form equation (7.38) it follows that $c \leq 0$; consequently, since $x_{\rm min} \geq 0$, the right hand side of (7.39) must be ≥ 0, i.e. necessarily $W \leq 0$. From Fig. E.1 (top panel) this forces the argument to be ≤ 0. *This first condition is therefore always true for our models.*

2. The second condition, again from the top panel of Fig. E.1, is that the argument must be $\geq -1/\mathrm{e}$ for all possible choices of the model parameters. *This inequality is easily verified* by showing, with a standard minimization of a function of two variables, that the minimum of the argument over the region $Y \geq 1$ and $c \leq 0$ is indeed not smaller than $-1/\mathrm{e}$.

However, since we are dealing with *real* values of $x_{\rm min}$, the function W is defined by two branches: the "principal" branch W_0, and the branch W_{-1} (see Appendix E and references therein). Now we show that, actually, *only the* W_{-1} *function appears in the solution for* $x_{\rm min}$. This conclusion derives from the physical request that $x_{\rm min} \geq 0$, i.e. that the right hand side of equation (7.39) is grater than or equal unity. The proof is simple, and reads as follows.

Let $z \equiv 1/c$. Since $Y \geq 1$, we have $z\mathrm{e}^{Yz} \geq z\mathrm{e}^{z}$, so that by combining the fundamental properties mentioned in equations (E4) and (E5) we obtain

$$W_0(z\mathrm{e}^{Yz}) \geq W_0(z\mathrm{e}^{z}) \geq z. \tag{7.40}$$

Now, as $z \leq 0$ by definition, we conclude that $cW_0(\mathrm{e}^{Y/c}/c) \leq 1$, which necessarily implies $x_{\rm min} \leq 0$. An identical argument shows instead that $cW_{-1}(\mathrm{e}^{Y/c}/c) \geq 1$, as required. As a consequence, the *only* minimum of f is reached at

$$x_{\rm min} = -\xi - \frac{\mathcal{R}}{2}\,W_{-1}\left(-\frac{2\xi}{\mathcal{R}}\,\mathrm{e}^{-\frac{\chi+2\xi}{\mathcal{R}}}\right). \tag{7.41}$$

Once $x_{\rm min}$ is known, all the other quantities in Bondi's solution, such as the critical accretion parameter $\lambda_{\rm t} = \exp(f_{\rm min} - 1/2)$, the mass accretion rate in equation of continuity, and the Mach number profile $\mathcal{M}$, can be expressed as a function of $x_{\rm min}$. Therefore, *J3 galaxies belong to the family of models for which a fully analytical discussion of the isothermal Bondi accretion problem is possible* (see Table 7.1). In particular, the critical accretion solution (in practice, the radial Mach profile for $\lambda = \lambda_{\rm t}$) is given by equation (6.52), with W_{-1} and W_0 describing respectively supersonic and subsonic accretion, and where $\lambda_{\rm t}$ and $f(x)$ read, in explicit form,

$$\lambda_{\rm t} = \mathrm{e}^{f(x_{\rm min})-1/2}, \qquad f(x) = \frac{\chi}{x} + \frac{\mathcal{R}}{\xi}\ln\left(1+\frac{\xi}{x}\right) + \frac{\mathcal{R}}{x}\ln\left(1+\frac{x}{\xi}\right) + 2\ln x. \tag{7.42}$$

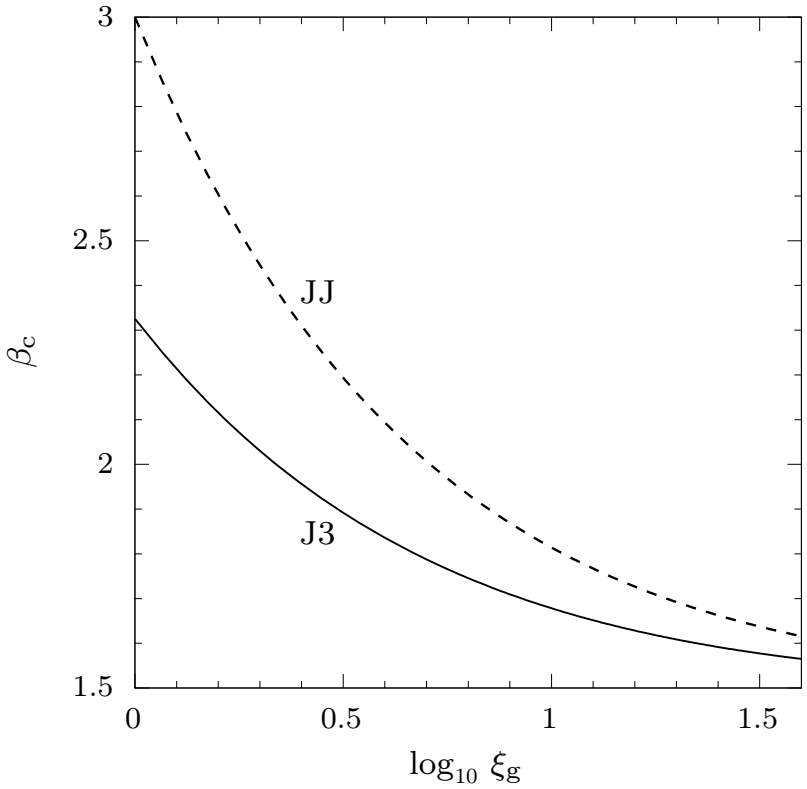

Figure 7.4. Critical temperature parameter $\beta_c \equiv 3/[2\mathcal{F}_g(\xi_g)]$ as a function of ξ_g, for J3 and JJ galaxy models. For $\beta = T_\infty/T_V > 1$, the isothermal accretion in absence of a central BH is possible provided that $\beta \leq \beta_c$. In these circumstances, once ξ_g is fixed, the upper limit of β for J3 models is lower than that for JJ ones.

Although we have an explicit expression of $\mathcal{M}$, it can be useful to have its asymptotic trend at small and large distances from the centre; this trend can be obtained in two ways: by directly expanding the equation (6.52) (with f given in 7.42), or performing an asympotic expansion of equation (6.50). In both cases, without any mathematical difficulties we obtain

$$\mathcal{M}^2 \sim \begin{cases} \dfrac{2\chi}{x} + \dfrac{2(2\xi - \mathcal{R})}{\xi} \ln \dfrac{x}{x_{\min}}, & x \to 0, \\ \lambda_t^2\, x^{-2\left(2+\frac{\mathcal{R}}{x}\right)}, & x \to \infty. \end{cases} \tag{7.43}$$

Therefore, in the central region $\mathcal{M} \propto x^{-1/2}$ for $\chi > 0$, while $\mathcal{M} \sim \sqrt{2(2 - \mathcal{R}/\xi)\ln(x/x_{\min})}$ when $\chi = 0$ (provided that $\mathcal{R} > 2\xi$).

Let us now analyze the interesting situation $\chi = 0$, formally corresponding to a galaxy without a central BH. This particular case reveals some interesting properties of the gas flow, also relevant for the understanding of the more natural situation $\chi > 0$. In discussing the problem, we follow the numbering before equation (7.35).

1. The case $\mathcal{R} < 2\xi$.
   In this situation, as shown in equation (7.34), $f(x) \to -\infty$ for $x \to 0^+$. Therefore, since f is a continuous function for all $x > 0$, the sonic point is again reached at the origin. However, as $f_{\min} = -\infty$, λ_t is formally zero, and so no accretion can take place. Of course, we can draw the same conclusion by discussing the sign of the first derivative (7.35) with a graphical approach, analogous to that described in footnote 3. In fact, if $\mathcal{R} < 2\xi$, the line $y = 2x$ has

a slope always *greater* than that of the tangent line to the function $y = \mathcal{R}\ln(1 + x/\xi)$ at the point $x = 0$, whose angular coefficient equals $\mathcal{R}/\xi$; consequently, $df/dx \geq 0$ everywhere, and f reaches its minimum at $x = 0$, corresponding to a vertical asymptote.

2. The case $\mathcal{R} = 2\xi$.
   Now the line $y = 2x$ is tangent to the function $y = \mathcal{R}\ln(1+x/\xi)$ at $x = 0$, so that the sonic point is again reached at the origin. This is confirmed by equation (7.41), which can still be used: in fact, $x_{\min} = -\xi - \xi W_{-1}(-1/\mathrm{e}) = 0$. Therefore, from equation (7.34) one has $f_{\min} = 2(1 + \ln\xi)$, whence $\lambda_{\mathrm{t}} = \xi^2\mathrm{e}^{3/2}$.

3. The case $\mathcal{R} > 2\xi$.
   The line $y = 2x$ has a slope always smaller than that of the tangent to the monotone increasing concave function $y = \mathcal{R}\ln(1+x/\xi)$ in the origin. Consequently, the two functions necessarily intersect at a certain $x > 0$, corresponding to the sonic point and obtainable by setting $\chi = 0$ in equation (7.41).

Summarising, *when* $\chi = 0$ *a solution for the accretion problem is possible only for* $\mathcal{R} \geq 2\xi$*, with* $x_{\min}$ *given by equation* (7.41); further, regarding the radial trend of $\mathcal{M}$, from the asympotic expansion of equation (6.50) it readily follows that $\mathcal{M}^2 = 1 + \mathcal{O}(x)$.

We now show how the condition $\mathcal{R} \geq 2\xi$ when $\chi = 0$, in order to have accretion, imposes an upper limit on T_∞. In fact, from equation (7.28) it follows that $\mathcal{R}/(2\xi) = 3/(2\beta\mathcal{F}_{\mathrm{g}})$ when $\gamma = 1$, so that

$$\frac{\mathcal{R}}{2\xi} \geq 1 \qquad \Leftrightarrow \qquad \beta \leq \beta_{\mathrm{c}} \equiv \frac{3}{2\mathcal{F}_{\mathrm{g}}(\xi_{\mathrm{g}})}, \tag{7.44}$$

where the critical parameter β_{c} depends only on the galaxy-to-stellar scale length ratio ξ_{g}. Figure 7.4 shows β_{c} as a function of ξ_{g} (where dashed line refers to JJ models for comparison); it is easy to prove that $3/2 < \beta_{\mathrm{c}} \leq 9/(\pi^2 - 6) \simeq 2.33$. As a natural consequence, *isothermal accretion in J3 galaxies withput a central BH is possible only for*

$$T_\infty \leq \beta_{\mathrm{c}} T_{\mathrm{V}}, \qquad \text{i.e.,} \qquad \sigma_{\mathrm{pg}}(0) = \sigma_{\mathrm{g}}(0) \geq c_\infty, \tag{7.45}$$

where the last inequality derives from equation (7.29). As anticipated, the limitation $\mathcal{R} \geq 2\xi$ when $\chi = 0$ is also relevant for the understanding of the flow behaviour when $\chi > 0$. For this purpose, it is useful to have the asymptotic trend of $x_{\min}$ for $\mathcal{R} \to \infty$; it is important to keep in mind that in the present models, in fact, $\alpha \geq 1$, $\xi_{\mathrm{g}} \geq 1$, and $\mu = 0.002$, so that the values of $\mathcal{R}$ are quite large. By defining $\tau \equiv \beta/\beta_{\mathrm{c}} = 2\xi/\mathcal{R}$, for $\mathcal{R} \to \infty$ and fixed[4] τ we obtain

$$x_{\min} \sim \begin{cases} -\dfrac{\tau + W_{-1}(-\tau\mathrm{e}^{-\tau})}{2}\mathcal{R}, & \tau < 1, \\ \sqrt{\dfrac{\chi\mathcal{R}}{2}}, & \tau = 1, \\ \dfrac{\chi\tau}{2(\tau - 1)}, & \tau > 1. \end{cases} \tag{7.46}$$

Notice that the limiting case $\mathcal{R} \to \infty$ can describe different types of models: models with increasing ξ_{g} at fixed α and μ; with increasing α at fixed μ and ξ_{g}; or finally with a vanishing BH mass at fixed α and ξ_{g}. Since $\mathcal{R} \gg 1$ reasonable values of the models parameters, the asymptotic

[4] Notice that from equation (7.41) it follows that the limit for $\mathcal{R} \to \infty$ is *not* uniform in τ.

trends in equation (7.46) provide a good approximation of the true behavior that is increasingly better for large values of α and ξ_g and small values of μ. Qualitatively, equation (7.46) shows that for $\beta < \beta_c$, x_{min} increases as $\mathcal{R}$; for $\beta > \beta_c$, instead, x_{min} is independent of $\mathcal{R}$; finally, for very large values of the gas temperature, $x_{min} \to \chi/2$, the limit value of classical Bondi accretion with electron scattering (see equation 6.44). The trend of x_{min} as a function of β is shown by the black solid line in Fig. 7.3 (right panel), for a minimum halo model with $\xi_g = 13$ and $\mu = 0.002$. For example, equation (7.46) allows to explain the drop at increasing β when τ switches from being less than unity to being larger than unity, with $x_{min} \simeq \chi/2$ independently of τ; the black square point at $r_{min} \simeq 57.34\, r_B$ correspond to $\beta = \beta_c \simeq 1.65$, well approximated by the value $57.01\, r_B$ obtained with the previous equation. Equation (7.46) allows us to find the behaviour of λ_t for large values of $\mathcal{R}$ (at fixed β). For example, in the peculiar case $\beta = \beta_c$ (i.e. $\tau = 1$), an asymptotic analysis shows that $\lambda_t \sim e^{3/2}\mathcal{R}^2/4$; for simplicity, we do not report the expression of λ_t for $\beta \neq \beta_c$, which can, however, be easily calculated. As shown in Fig. 7.5 (left panel), the presence of the galaxy makes λ_t several orders of magnitude larger than without it.

A summary of the results can be seen by inspection of Fig. 7.6 (top panels), where we show the radial profile of the Mach number for three different values of the temperature parameter ($\beta = 1$, 2, 3). Solid lines show the two critical solutions, one in which the gas flow begins supersonic and approaches the centre with zero velocity, and the other in which $\mathcal{M}$ continuously increases towards the centre. The dotted lines show two illustrative subcritical solutions with $\lambda = 0.8\, \lambda_t$. It is apparent that r_{min} decreases very rapidly with increasing temperature at the transition from $\beta = 1$ to $\beta = 2$: $r_{min} \simeq 19.89\, r_*$, $0.0093\, r_*$, and $0.0024\, r_*$, for $\beta = 1$, 2, and 3, respectively.

Finally, once the Mach number profile is known, the gas density profile is obtained via equation of continuity, i.e.

$$\tilde{\rho}(x) = \frac{\rho(x)}{\rho_\infty} = \frac{\lambda}{x^2 \mathcal{M}(x)}. \tag{7.47}$$

Along the critical solution, by virtue of equation (7.43) it follows that $\tilde{\rho} \sim \lambda_t x^{-3/2}/\sqrt{2\chi}$ at the centre when $\chi > 0$, while $\tilde{\rho} \sim x^{\mathcal{R}/x}$ at large radii. Fig. 7.7 (top panel) shows the radial trend of $\tilde{\rho}$ for the critical accretion solution in our reference model, with $\lambda_t \simeq 2.14 \times 10^8$. The bottom panel shows the gas velocity profile and, for comparision, the isotropic velocity dispersion σ_r. Notice that near the centre, $\sigma_{BH} \propto r^{-1/2}$ and $v = c_\infty \mathcal{M} \propto r^{-1/2}$ (provided that $\chi > 0$), so that their ratio is constant; it can be easily shown that $v/\sigma_{BH} \sim 6\chi$. The value of σ_{BH} near the centre (i.e. of σ_r if a central BH is present), is then a proxy for the isothermal gas inflow velocity.

An aspect deserving a brief discussion concerns the heat exchange. In Section 6.5 we have obtained some remarkable expressions for $\mathcal{Q}(r)$, written essentially in terms of the radial Mach prifile. Then, once $\mathcal{M}(x)$ is obtained via equation (6.52), with λ_t and f given in (7.42), $\mathcal{Q}(r)$ can be determined through equation (6.69). The situation is illustrated in Fig. 7.8 for three values of β. Notice that the plotted quantity is $-4\pi r^2 \mathcal{Q}(r)$, i.e. *the rate of heat per unit length exchanged by the infalling gas element. In practice, by integrating the curves between two radii r_1 and r_2, one obtain the heat per unit time exchanged with the ambient by the spherical shell of thickness* $|r_2 - r_1|$. Notice how in general the profile is almost a power law over a very large radial range, and how the heat exchange decreases for increasing T_∞. To better understand the behaviour of the function $\mathcal{Q}(r)$, especially in the central regions, important for both observational and theoretical works, it is useful as always to perform an asymptotic expansion. For $x \to 0$ and $\chi > 0$, equation (7.43) yields

$$\frac{\mathcal{Q}}{\mathcal{Q}_n} \sim -\frac{3\lambda_t}{2x^3} \sim -\frac{3\chi}{\lambda_t}\, \tilde{\rho}^2 \tilde{T}, \tag{7.48}$$

where all the information about the specific galaxy model is contained, especially for the first

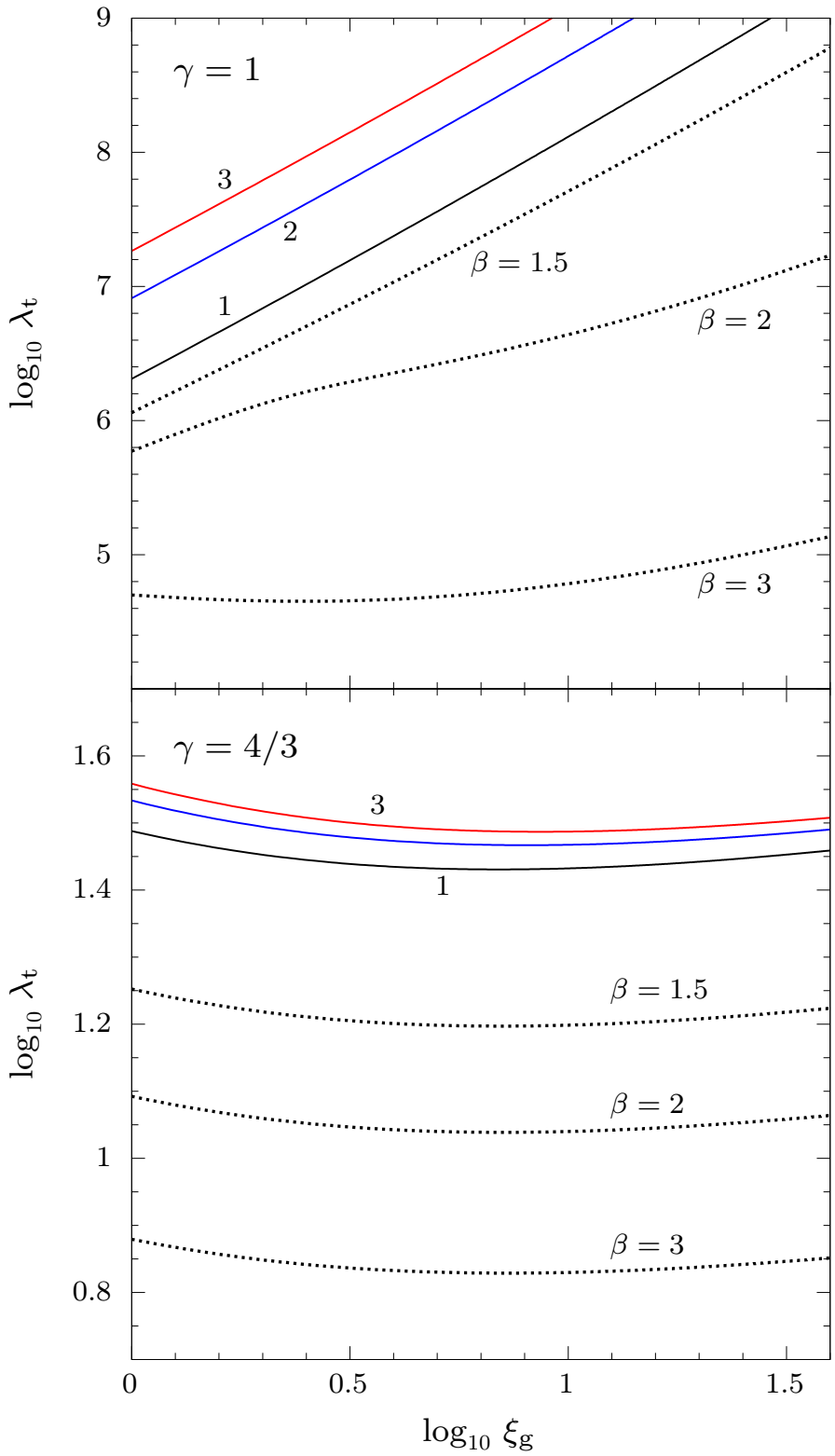

Figure 7.5. Critical accretion parameter λ_t as a function of ξ_g, for the minimum halo case $\alpha = 1$ (black), 2 (blue), and 3 (red), and $\chi = 1$ and $\beta = 1$. The dotted curves refer to $\alpha = 1$ and three different values of β. The left panel shows the case $\gamma = 1$, the right panel shows the case $\gamma = 4/3$. Notice that λ_t in the isothermal case is several order of magnitude larger than the $\gamma = 4/3$ case.

expression, in the parameter λ_t; it is then evident that the volume integrated heat exchanges are *always* dominated by the innermost region.

We conclude this Section by applying to the J3 models (for now in the isothermal case only) the general results we obtained assuming hydrostatic equilibrium. By fixing $\gamma = 1$ in equation (6.80), the contained mass inside a sphere of radius r, under this (stringent) assumption, is obtained as

$$\frac{M_{\rm est}(r)}{M_*} = -\mu x^2 \frac{d\ln\tilde{\rho}}{dx}. \tag{7.49}$$

In particular, near the BH (i.e. for $x \to 0$), where $\tilde{\rho} \sim \lambda_t x^{-3/2}/\sqrt{2\chi}$, one has

$$\frac{M_{\rm est}}{M_*} \sim \frac{3\mu}{2} x, \tag{7.50}$$

so that $M_{\rm est}$ sacale with the mass of the BH and increases linearly with radius. It is interesting to compare the estimate $M_{\rm est}(r)$ with the concept of radius influence introduced in § 7.2. For example, from the foregoing equation it is possible to evaluate the radius r containing the fraction μ of the total stellar mass (i.e. $M_{\rm BH}$), the commonly adopted estimate for the "dynamical radius" of the BH (e.g. Binney & Tremaine, Chapter 4). Combining equations (7.50) and (7.30) we obtain

$$M_{\rm est}(r) = \mu M_* \quad \Leftrightarrow \quad r = \frac{3\pi\epsilon(2+\epsilon)}{2\beta\mathcal{F}_{\rm g}(\xi_{\rm g})} R_{\rm inf}; \tag{7.51}$$

for $\xi_{\rm g} = 13$ and $\beta = 1$, $r \approx R_{\rm inf}$ when choosing $\epsilon = 0.1$.

7.4 The case $1 < \gamma < 5/3$

Let us now discuss the case $\gamma > 1$, leaving aside for the moment the limiting situation $\gamma = 5/3$, which will be the topic of the next Section. The function $f(x)$, appearing in the mathematical formulation of Bondi's problem (6.50), containing all the galaxy information of the examined models, is now given by

$$f(x) = x^{\frac{4(\gamma-1)}{\gamma+1}} \left[\frac{\chi}{x} + \frac{\mathcal{R}}{\xi} \ln\left(1 + \frac{\xi}{x}\right) + \frac{\mathcal{R}}{x} \ln\left(1 + \frac{x}{\xi}\right) + \frac{1}{\gamma - 1} \right]. \tag{7.52}$$

In analogy with the isothermal case, we start from the asymptotic behaviour at small and large radii of $f(x)$. Such a behaviour reads

$$f(x) = x^{\frac{4(\gamma-1)}{\gamma+1}} \times \begin{cases} \dfrac{\chi}{x} - \dfrac{\mathcal{R}}{\xi} \ln x + \mathcal{O}(1), & x \to 0^+, \\ \dfrac{1}{\gamma - 1} + \mathcal{R}\dfrac{\ln x}{x} + \mathcal{O}\left(\dfrac{1}{x}\right), & x \to \infty. \end{cases} \tag{7.53}$$

As a consequence, there exists at least one case in which the determination of $x_{\rm min}$ and $f_{\rm min}$ is trivial, i.e. for $\xi \to \infty$ (or $\mathcal{R} \to 0$): in this situation, indeed, the galaxy contribution vanishes, and the position of the only minimum of f reduces to $x_{\rm min} = \chi(5 - 3\gamma)/4$. Therefore, following KCP16 (Appendix A), the behaviour of the associated λ_t could be found just by carrying out a perturbative analysis; however, since in our models $\mathcal{R}$ falls in the range $10^3 \div 10^4$, we shall not further discuss this particular case. Instead, a major difference with the case discussed in the previous Section is quite evident; indeed, from the foregoing equation, it follows that

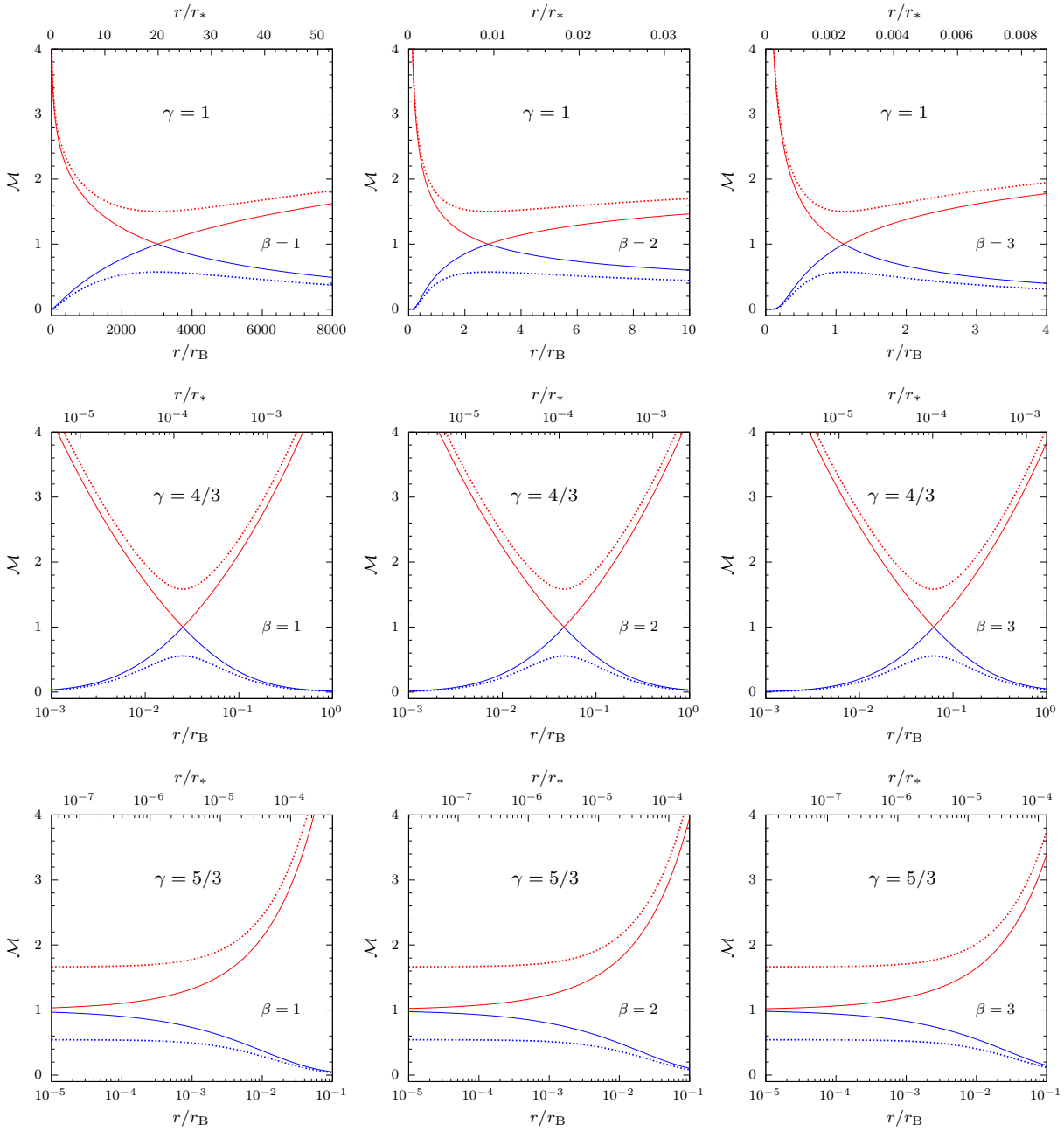

Figure 7.6. Radial profile of the Mach number for polytropic Bondi problem in a minimum halo J3 galaxy model with $\xi_g = 13$, $\chi = 1$ and $\mu = 0.002$, in case of three different values of the gas temperature ($\beta = 1$, 2, 3). Solid lines show the two critical solutions ($\lambda = \lambda_t$), while dotted lines indicate the two subcritical solutions ($\lambda = 0.8\,\lambda_t$); the distance from the centre is given in units of both r_B (bottom axis) and r_* (top axis, using equation 7.26). In blue we plot the subsonic regime and in red the supersonic one. The top panels show the isothermal case ($\gamma = 1$): notice how, in accordance with Fig. 7.3, the position of r_{min} decreases very rapidly passing from $\beta = 1$ to $\beta = 2$. Middle panels show the case $\gamma = 4/3$: in accordance with the dashed black lines in Fig. 7.3, r_{min}/r_* decreases for increasing β, while r_{min}/r_* decreases (note that a logarithmic scale for radius axes has been used). Finally, bottom panels show the adiabatic case ($\gamma = 5/3$): the position of the sonic point is reached at the centre, the accretion solutions are always subsonic (i.e. $\mathcal{M} < 1$), and the wind solutions are always supersonic (i.e. $\mathcal{M} > 1$).

$$\lim_{x\to 0^+} f(x) = \begin{cases} 0, & \chi = 0, \\ \infty, & \chi \neq 0, \end{cases} \qquad \lim_{x\to\infty} f(x) = \infty. \tag{7.54}$$

We are therefore faced with two main scenarios, summarized as follows.

- $\chi = 0$.
  In the case the sonic point is reached at the origin. Indeed, f is a f is strictly positive and continuous function of $x > 0$; hence, since it tends to zero when $x \to 0$, and runs to infinity for $x \to \infty$, necessarily $x_{\rm min} \to 0$ *for every choice of the model parameters*. Further, from equation (7.56) one has $\lambda_{\rm t} \to 0$, concluding the discussion of the problem in absence of the central BH since no accretion can take place.

- $0 < \chi \leq 1$.
  Also in this case $f(x)$ is a continuous stricly positive function; but now it diverges to infinity for both $x \to 0$ and $x \to \infty$. Therefore, *the existence of at least a minimum is guaranteed.*

In the following we shall therefore focus on *positive* values of χ. Unfortunately, the problem of the determination of $x_{\rm min}$ (and so of $\lambda_{\rm t}$) cannot be solved analytically, as apparent from the expression for the first derivative of $f(x)$, given by

$$\frac{df}{dx} = \frac{1}{x^{1-p}}\left[p\left(\frac{1}{\gamma-1} + \frac{\mathcal{R}}{\xi}\ln\frac{\xi+x}{x}\right) - \frac{1-p}{x}\left(\chi + \mathcal{R}\ln\frac{\xi+x}{\xi}\right)\right], \qquad p \equiv \frac{4(\gamma-1)}{\gamma+1}, \tag{7.55}$$

where $0 < 1-p < 1$. A detailed numerical exploration shows that it is possible to have *more than one* critical point for f as a function of β an γ. In particular, there can be a single minimum for f, or two minima and one maximum. We found that for $\xi_{\rm g} = 13$ and $\beta \approx 1 \div 2$, only one minimum is present for $\gamma \lesssim 1.01$ and $\gamma \gtrsim 1.1$; instead, for $1.01 \lesssim \gamma \lesssim 1.1$, three critical points and two minima are present. When β is small (i.e. T_∞ is low), the absolute minimum of f is reached at the outer critical point; as β increases, the value of f at the inner critical point decreases, and the flow is finally characterised by two sonic points. Increasing further T_∞, the inner critical point becomes the new sonic point, with a jump to a smaller value. Fig. 7.3 (top right panel) shows the position of $x_{\rm min}$ as a function of β for different values of γ, and confirms these trends of $x_{\rm min}$ with T_∞ and γ. Notice how the location of $x_{\rm min}$ (shown in the bottom panel) now decreases with an extremely slow decline for $\gamma > 1$. According with equation (7.31), this means that, for polytropic indeces sufficiently greater than unity, the ratio $r_{\rm B}/r_*$ decreases faster than what $x_{\rm min}$ increases.

Having determined the position $x_{\rm min}$, we can compute *numerically* the corresponding value of $\lambda_{\rm t}$, given in the polytropic case by

$$\lambda_{\rm t} = \left(\frac{f_{\rm min}}{g_{\rm min}}\right)^{\frac{\gamma+1}{2(\gamma-1)}}, \tag{7.56}$$

with $f_{\rm min} = f(x_{\rm min})$ obtained from equation (7.52), and $g_{\rm min} = (\gamma+1)/[2(\gamma-1)]$. In Fig. 7.5 (bottom panel) the critical accretion parameter is shown as a function of $\xi_{\rm g}$, for a reference model with $\gamma = 4/3$ and different values of β. We note that, at variance with the isothermal case (top panel), $\lambda_{\rm t}$ is roughly constant for fixed β independently of the extension of the DM halo; at fixed $\xi_{\rm g}$, instead, it increases for decreasing T_∞. Having also determined $\lambda_{\rm t}$, we finally solve numerically equation $g(\mathcal{M}) = \Lambda f(x)$, obtaining the Mach profile $\mathcal{M}(x)$. In Fig. 7.6 (middle panels) we show $\mathcal{M}(x)$ for three different values of the temperature parameter ($\beta = 1,\ 2,\ 3$). The logarithmic scale allows to appreciate how, according to Fig. 7.3, $x_{\rm min}$ suddenly falls down to values under

unity as γ increases with respect to the isothermal case; as an illustrative example, we show the case $\gamma = 4/3$. Although the trend is not very strong, the location of the sonic point, at variance with the $\gamma = 1$ case, moves away from the centre as the temperature increases: $r_{\rm min} \simeq 0.025\, r_{\rm B}$, $0.046\, r_{\rm B}$, and $0.062\, r_{\rm B}$, for $\beta = 1$, 2, and 3, respectively. For comparison, in the top axis we give the distance from the origin in units of r_*, from which it can be seen that, in accordance with Fig. 7.3 (bottom panel), $r_{\rm min}$ now tends to increase slightly, while still of the order of $10^{-4}\, r_*$.

Once the radial profile of the Mach number is known, both the gas density and temperature profiles can be obtained from the following relations:

$$\tilde{\rho} = \tilde{T}^{\frac{1}{\gamma-1}} = \left(\frac{\lambda}{x^2 \mathcal{M}}\right)^{\frac{2}{\gamma+1}}, \tag{7.57}$$

with $\tilde{T} = T/T_\infty$. Fig. 7.7 shows the trends of ρ (top panel) and T (middle panel), as a function of r/r_*, for the critical accretion solution in our usual reference model. The parameter β is fixed to unity, and the curves refer to different polytropic indeces.

For what concerns the Mach profile for the critical accretion solution, an asymptotic analysis of equation (6.50) shows that, at the leading order

$$\mathcal{M} \sim \begin{cases} \lambda_{\rm t}^{-\frac{\gamma-1}{2}} (2\chi)^{\frac{\gamma+1}{4}} x^{-\frac{5-3\gamma}{4}}, & x \to 0, \\ \lambda_{\rm t}\, x^{-2}, & x \to \infty. \end{cases} \tag{7.58}$$

This is a quite general asymptotic form for the radial Mach profile in galaxy models with electron scattering, where *all the information about the specific model in the two regions is contained in the parameter* $\lambda_{\rm t}$. Equation (7.58) allows us to find the asymptotic behaviour at small and large radii of the most important quantities concerning the Bondi accretion. Close to the centre, for example, $\tilde{\rho} \sim \lambda_{\rm t} x^{-3/2}/\sqrt{2\chi}$ (as for the isothermal case), independently on the value of γ, and so for the gas velocity $v = c_s \mathcal{M}$ one finds

$$\frac{v^2}{\Psi_{\rm n}} \sim \frac{2\chi\mu}{s}, \tag{7.59}$$

Now, by combining equations (4.54) and (4.81), and limiting to the spherical case (i.e. $\eta_* = 0$), one obtains that, close to the centre, $\sigma^2_{\rm BH} \sim \mu/(3s)$. For, the foregoing can be rewritten as

$$v^2(r) \sim 6\chi \sigma^2_{\rm BH}(r), \tag{7.60}$$

which proves a direct link between the (hydrodynamic) quantity v and the (stellar) quantity $\sigma_{\rm BH}$; in other words, *the central value of* $\sigma_{\rm BH}$ *represents a proxy for the gas inflow velocity also in the range* $1 < \gamma < 5/3$. Fig. 7.7 (bottom panel) shows the radial trend of v for for different values of γ: notice how, moving away from the centre, it decreases progressively faster for $\gamma > 1$ (see the green dashed line, corresponding to $\gamma = 1.1$), while deviating significantly from the isotropic stellar velocity dispersion profile.

The situation is illustrated in Fig. 7.8: the left panel refers to the isothermal case and three values of β; the right panel shows the case of a *monoatomic* gas (i.e. $\gamma_{\rm ad} = 5/3$), for a fixed β and different values of $\gamma < \gamma_{\rm ad}$. The plotted quantity is $-4\pi r^2 \mathcal{Q}(r)$, i.e. the rate of heat per unit length exchanged by the infalling gas element. In practice, by integrating the curves between two radii r_1 and r_2, one obtain the heat per unit time exchanged with the ambient by the spherical shell of thickness $|r_2 - r_1|$. For comparison, the dashed lines correspond to the same case, i.e. isothermal accretion with $T_\infty = T_{\rm V}$. Notice how in general the profile is almost a power law

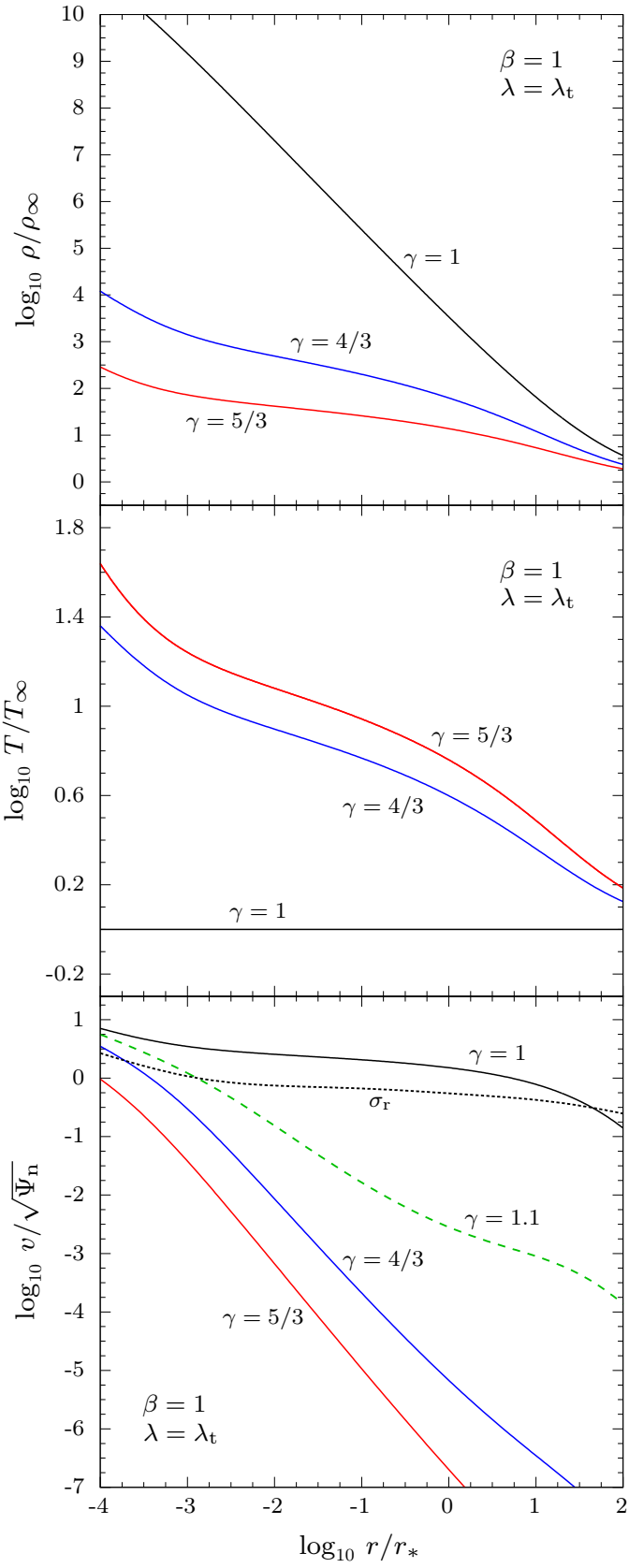

Figure 7.7. Density (top), temperature (middle), and velocity (bottom) profiles, as a function of r/r_*, for the critical (i.e. $\lambda = \lambda_t$) accretion solution of the polytropic Bondi problem in a minimum halo J3 galaxy model with $\xi_g = 13$, $\chi = 1$, and $\mu = 0.002$. The gas temperature at infinity T_∞ equals the stellar virial temperature T_V, i.e. $\beta = 1$. For comparison, the dotted line in the bottom panel shows the isotropic velocity dispersion profile σ_r.

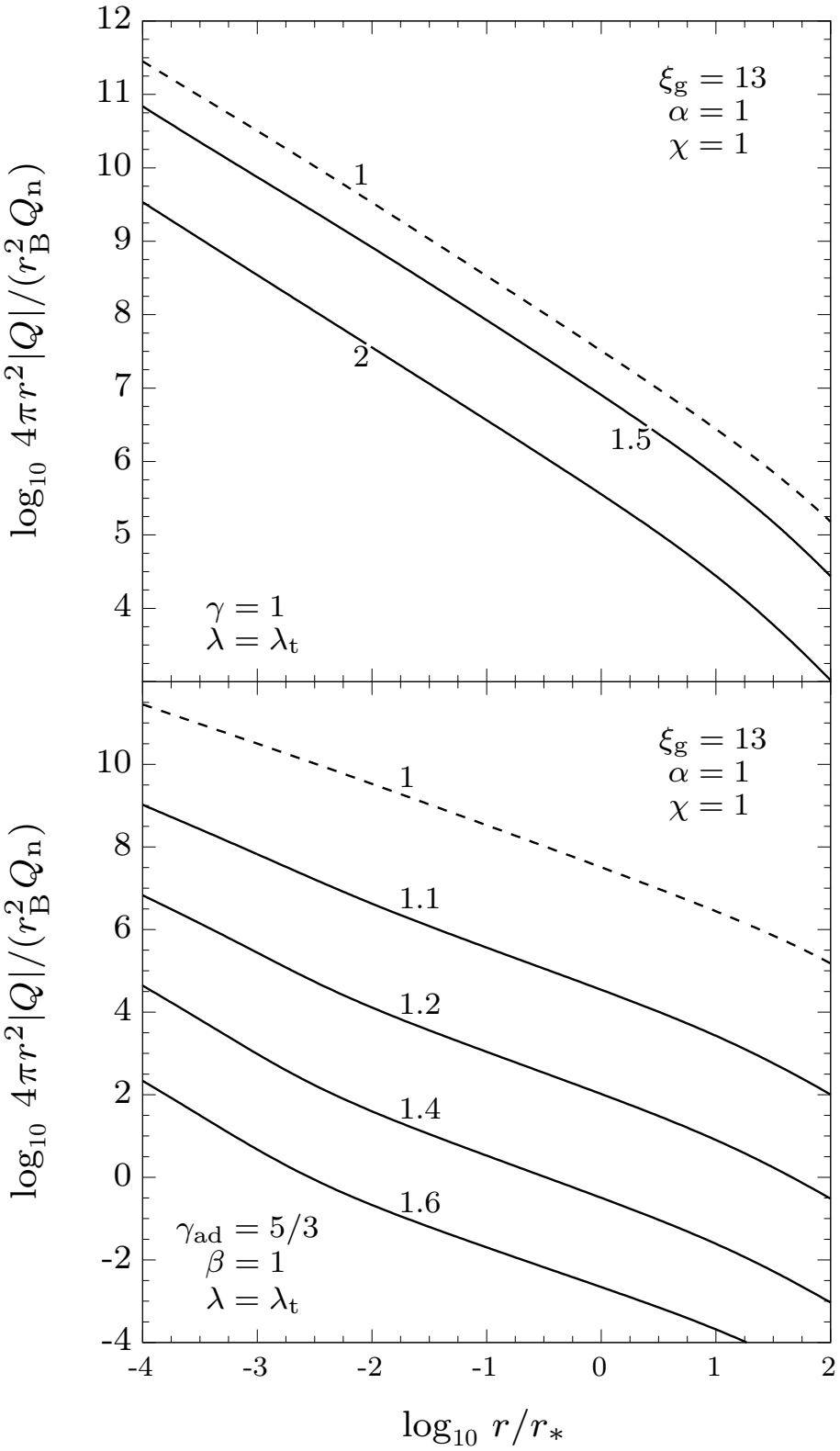

Figure 7.8. Absolute value of the rate of heat per unit length exchanged by the fluid element, $4\pi r^2|\mathcal{Q}|$, in units of $r_B^2 \mathcal{Q}_n$, as a function r/r_*, for the critical Bondi accretion of a minimum halo J3 model with $\xi_g = 13$, $\chi = 1$, and $\mu = 0.002$. Left panel: isothermal case for $\beta = 1$, 1.5, and 2. Right panel: monoatomic gas ($\gamma_{ad} = 5/3$) with $\beta = 1$, for different values of the polytropic index. In both panels, the dashed lines correspond to isothermal accretion with $T_\infty = T_V$.

over a very large radial range, and how the heat exchange decreases for increasing T_∞ and for γ approaching $\gamma_{\rm ad}$.

Concerning the amount of heat exchanged with the ambient by the element of gas as it falls onto the central BH, the function $-4\pi r^2\mathcal{Q}(r)$, already discussed for the isothermal case, is shown in Fig. 7.8 (bottom panel) for the case of monoatomic gas (i.e. $\gamma_{\rm ad}=5/3$) with fixed $\beta=1$. Even in the case $\gamma>1$ the profile is almost a power law over a very large radial range; further, notice how at fixed r the heat exchange gradually decreases for γ approaching $\gamma_{\rm ad}$. Expanding equation (6.68) by making use of (7.58), it follows that the central behaviour of $\mathcal{Q}$ with $\chi>0$ reads

$$\frac{\mathcal{Q}}{\mathcal{Q}_{\rm n}}\sim\frac{3\lambda_{\rm t}^{\gamma}(2\chi)^{-\frac{\gamma-1}{2}}(\gamma-\gamma_{\rm ad})}{2\gamma(\gamma_{\rm ad}-1)}\,x^{-\frac{3(\gamma+1)}{2}}\sim\frac{3\chi(\gamma-\gamma_{\rm ad})}{\lambda_{\rm t}\gamma(\gamma_{\rm ad}-1)}\,\tilde{\rho}^2\tilde{T}. \tag{7.61}$$

In practice, close to the centre, $\mathcal{Q}$ is a pure power law of logarithmic slope decreasing from -3 to -4 for γ increasing from 1 to 5/3; as for the case $\gamma=1$, the volume integrated heat exchanges are always dominated by the innermost region.

Concerning the quantity $M_{\rm est}(r)$, from equation (7.43), and the asymptotic trend of the density $\tilde{\rho}$, in the vicinity of the BH equation (7.51) is generalized to the case $\gamma>1$ as

$$\frac{M_{\rm est}}{M_*}\sim\frac{3\mu}{2}\left(\frac{\lambda_{\rm t}}{\sqrt{2\chi}}\right)^{\gamma-1}x^{\frac{5-3\gamma}{2}}, \tag{7.62}$$

where we have assumed $\lambda=\lambda_{\rm t}$.

7.5 The case $\gamma=5/3$

We are left with the discussion of the limiting case $\gamma=5/3$. As stressed in § 6.2, this case does *not* necessarily correspond to an adiabatic situation, since γ and $\gamma_{\rm ad}$ are in general two distinct quantities. *For $\gamma=5/3$ we are faced with an adiabatic Bondi accretion only if the gas is monoatomic*: in this case, indeed, $\gamma_{\rm ad}=5/3$, so that $\mathcal{Q}(r)$ vanishes for all $r>0$.

In this hydrodynamic limit for the Bondi accretion problem, the only minimum of the function $f(x)$ is reached at the centre *independently* of the galaxy model, provided that $r\Psi_{\rm g}(r)\to 0$ when $r\to 0$. Since the J3 models satisfy this one condition, it follows that

$$f_{\rm min}=\chi,\qquad\qquad \lambda_{\rm t}=\frac{\chi^2}{4}, \tag{7.63}$$

and so $\chi>0$ in order to have accretion. When $\lambda=\lambda_{\rm t}$, Bondi's problem reduces to

$$\mathcal{M}^2-\frac{4f(x)}{\chi}\sqrt{\mathcal{M}}+3=0, \tag{7.64}$$

with $f(x)$ given explicitly by

$$f(x)=\chi+\mathcal{R}\,\frac{x}{\xi}\ln\left(1+\frac{\xi}{x}\right)+\mathcal{R}\ln\left(1+\frac{x}{\xi}\right)+\frac{3}{2}x. \tag{7.65}$$

In the bottom panels of Fig. 7.6 we show the radial profile of the Mach number: notice that *the accretion solutions (blue lines) are subsonic everywhere.*

The asymptotic bahaviour of $\mathcal{M}(x)$ for the critical accretion solution when $x\to\infty$ is obtaned from equation (7.58) just by fixing $\lambda_{\rm t}=\chi^2/4$. When $x\to 0$, instead, the $\gamma=5/3$ case does *not*

coincide with the limit of equation (7.58) for $\gamma \to 5/3$: in fact, now $\mathcal{M} \to 1$ instead of infinity, and its asymptotic trend reads

$$\mathcal{M}(x) \sim 1 - \sqrt{-\frac{8\mathcal{R}x\ln x}{3\xi\chi}}\,, \qquad x \to 0; \tag{7.66}$$

of course, the same situation at small radii occurs in the case of any other quantity deriving from Mach's profile: for example,

$$\frac{v^2}{\Psi_{\rm n}} \sim \frac{\chi\mu}{2s}, \qquad \frac{M_{\rm est}}{M_{\rm BH}} \sim \frac{3\chi}{4}. \tag{7.67}$$

Notice that v decreases by a factor of 2 with respect to the $1 \leq \gamma < 5/3$ case, and $M_{\rm est}$ differs from what would be obtained setting $\gamma = 5/3$ and $\lambda_{\rm t} = \chi^2/4$ in equation (7.62).

CHAPTER 8

Conclusions

This Thesis is devoted to the *construction of dynamical models of stellar systems sufficiently simple to allow for the study of the main properties of galaxies.* Accurate modelling of the internal dynamics of galaxies is essential not only to understand their observed characteristics, but also as a starting point for more sophisticated models, or even to identify the initial conditions necessary to build hydrodynamic and/or N-body simulations of galaxy evolution. We focused especially on axisymmetric galaxies, defined by a density profile stratified on oblate spheroidal surfaces.

Axially symmetrical models are useful tools in stellar dynamics, and are often adopted to investigate the presence of dark matter haloes, or central black holes, or to study the orbital structure of these systems. While the solution of Jeans's equations and the recovery of the phase-space density can be performed analytically in several cases of interest under the assumption of spherical symmetry, in the axisymmetric case the problem in general cannot be solved with analytical tools, and numerical methods provide the only viable path for a solution. However, analytical models, even when simplified, are of great importance, because they can be used to:

1. understand the dynamics of the more realistic models studied numerically;

2. obtain first indications about sensible choices of parameters to be successively refined with more time-consuming numerical methods.

In order to reduce the complexity of the problem, we restricted ourselves to the case of *weakly flattened galaxies*, exploiting the *homoeoidal expansion.* In this technique, the initial ellipsoidally stratified density-potential pairs are expanded in terms of the density flattening (η), in the limit of small flattenings, retaining only the first terms of the expansion.

We first studied the structural and dynamical properties of a couple of two-component (stars plus dark matter) families of galaxy models: the JJe and J3e models. In both families, the stellar density follows an ellipsoidal Jaffe profile; then, in the JJe models, the total density is described by another ellipsoidal Jaffe law; in the J3e models, the total density is such that its difference with the stellar density (e.g. the resulting dark matter halo) can be made similar to an ellipsoidal Navarro-Frenk-White (NFW) model. We showed that *the homoeoidal expansion technique allows for a clear understanding of the flattening effects on the dynamical fields, leading to an analytical treatment of several quantities of interest in theoretical and observational works. In particular, the solution of Jeans's equations was obtained (under the assumption of a two-integral phase-space distribution function) in a fully analytical way.* The analytical formulation of all their dynamical properties (e.g. kinematical quantities and virial energies) was used to understand what is the effect of the various parameters (flattening, scale lengths, mass ratio, rotational support) in determining

these properties. The projected dynamics was instead studied by numerically deriving the profiles of the kinematic fields for a generic inclination angle, demonstrating that the projected velocity dispersion exhibits similar behaviour to the three-dimensional one.

Then, we focused on a delicate aspect concerning the homoeoidal expansion, especially relevant in modelling applications. This aspect is related to the physical interpretation of the expanded density-potential pair, which obeys exactly Poisson's equation, and which can be interpreted as the first-order expansion of the ellipsoidal parent galaxy in the limit of vanishing flattening, or as a genuinely self-consistent model (i.e. a non-spherical system of finite flattening). In practice:

- in the first interpretation ("η-linear" models), the solutions of Jeans's equations contain only linear terms in the flattening;
- in the second interpretation ("η-quadratic" models), all terms must be retained.

In order to study the difference between the two views, and thus investigate the importance of the quadratic terms, we chose to focus on simple one-component galaxy models, the ellipsoidal Plummer model and the Perfect Ellipsoid. The first result was that both models provide fully analytical η-quadratic solutions. Then, we compared these solutions with those obtained numerically for the original ellipsoidal models: we found that the maintenance of quadratic terms does not produce significant differences, and so *the η-linear models already provide an excellent approximation of the numerical solutions*. For an example of application of the use of the η-linear solution, we chose the research field of globular clusters (GCs), systems with small flattening often described by the Plummer model. We considered the GC NGC 4372, characterized by a small flattening, and with an extended rotation curve observed. Our modelling rules out the possibility that NGC 4372 is an isotropic stellar system flattened by rotation, in agreement with the conclusions obtained by using more sophisticated modelling techniques (as for example the construction of self-consistent solutions starting from the phase-space distribution function). Once more we showed that the η-linear homoeoidally expanded solutions can be a useful starting point to gain insight into the internal dynamics of weakly flattened and rotating stellar systems (as some GCs) before turning to more complex studies.

A second part of the Thesis is devoted to the accretion of gas onto the black hole (BH) at the centre of J3 galaxies (the spherical limit of the J3e models). Accretion onto central massive BHs in galaxies is often modelled with the classical Bondi solution, in which a spatially infinite distribution of perfect gas, subject to polytropic transformations, is steadily accreting onto an isolated central mass: this is the standard reference for estimates of the accretion radius and mass accretion rate. Usually, to estimate the mass accretion rate, the observed values of the gas density and temperature in the central region of galaxies are used: in this way, these values are assumed to be representative of the true boundary conditions (i.e. at infinity) for the Bondi problem. However, even the knowledge of the true boundary conditions is not sufficient for a proper discussion of mass accretion: first, because the BH is not isolated; second, because the radiation emitted by the inflowing material interacts with the material itself, breaking the steady state regime. For these reasons, *we generalized the classical Bondi problem by taking into account the effects of the additional gravitational field of the host galaxy, and of the radiation pressure due to electron scattering*. The hydrodynamical and stellar dynamical properties are linked by imposing that the gas temperature is proportional to the virial temperature of the stellar component. *The isothermal and monoatomic adiabatic cases were discussed in fully analytical way, while for generic values of the polytropic index a numerical investigation was performed*. We also considered in detail the thermodynamical properties of Bondi accretion when the polytropic index differs from the adiabatic index; under this circumstance, the entropy of fluid elements changes along their path lines, and it is possible to compute the associated heat exchanges. *We provided the mathematical expressions to compute such heat exchange as a function of radius*, once the Bondi problem is solved, toghether with its asymptotic behaviour near the central BH.

8.1 Ongoing works

Recently, De Deo et al. (2024) formalized a priori the constraints on the functional form of the relation between the velocity moments. As we showed in this Thesis, indeed, Jeans's equations do not form a closed system, so that their solutions can be found through a parametrization relating the velocity moments; for axisymmetrical models, a phenomenological choice is commonly used for the relation between the vertical and radial components of the velocity dispersion tensor. Anyway, the resulting kinematical fields can be affected by the ansatz in such a way that the analysis of these fields is usually performed only after their numerical evaluation. De Deo et. al (2024) have then presented a general procedure to study the properties of some ansatz-dependent fields, not only determining the effect of such an ansatz before solving Jeans's equations, but also by constraining the ansatz itself in order to exclude unphysical results. To better illustrate the method, the Authors discuss the cases of three well-known galaxy models: the Miyamoto & Nagai (1975) and Satoh discs, and the Binney logarithmic halo (see § 2.2 in BT87).

It is therefore interesting to understand if the homoeoidal approximation can be useful to gain some qualitative understanding of the effects produced by some chosen ansatz on the kinematical fields of weakly flattened ellipsoidal systems. For, an application of the η-linear modelling to the study of the orbital anisotropy allowed by the axisymmetric Jeans equations is currently in progress.

8.2 Future works

A problem left open by the previous studies is the recovery of the phase-space distribution function f. When considering axisymmetric stellar systems, it is quite common to choose a "natural" f depending on the two classical integrals of motion related to the assumed symmetry, i.e.

$$f(\mathcal{E}, J_z) = h(\mathcal{E}, J_z)\Theta(\mathcal{E}), \tag{8.1}$$

where $\mathcal{E}$ the energy (per unit mass), J_z indicates the component of the angular momentum (per unit mass) along the symmetry z-axis, and Θ is the Heaviside step function. In such a system:

- ordered rotation can be present only around the symmetry axis, and only the *even* part of f, defined as $f_+ \equiv [f(\mathcal{E}, J_z) + f(\mathcal{E}, -J_z)]/2$, contributes to the density $\rho = \rho(R, \Psi)$;
- the only acceptable streaming motion is along the azimuthal direction, and it is determined uniquely by the *odd* component of f, defined as $f_- \equiv [f(\mathcal{E}, J_z) - f(\mathcal{E}, -J_z)]/2$;
- the velocity dispersion ellipsoids are aligned with the local basis are rotationally symmetric around the azimuthal direction.

In this Thesis we proved that the homoeoidally expanded density-potential pairs share a common mathematical structure, so that it is tempting to explore the enticing possibility to recover their two-integral distribution function, both in its even and odd components. A preliminary analysis suggests that the mathematical structure of f might be quite similar to that of an arbitrary homoeidally expanded quantity, an interesting feature which, if confirmed, could shed some light on certain proprieties difficult to address analytically.

APPENDIX A

JEANS'S EQUATIONS

IN a general way it appears that the most convenient method of describing the state of motions in a stellar system is by specifying the mass $f_*(\boldsymbol{x},\boldsymbol{v},t)d^3\boldsymbol{x}d^3\boldsymbol{v}$ of stars having, at a certain instant of time t, position in the element of volume $d^3\boldsymbol{x}$ centred on $\boldsymbol{x}$, and velocities in the range $d^3\boldsymbol{v}$ centred on $\boldsymbol{v}$. The quantity $f_*(\boldsymbol{x},\boldsymbol{v},t)$ is called *distribution function* (DF) or *phase-space density*[1]; from its definition, it follows that

$$\int_{\Re^3} f_*(\boldsymbol{x},\boldsymbol{v},t)d^3\boldsymbol{v} = \rho_*(\boldsymbol{x},t), \tag{A1}$$

where ρ_* indicates the mass density. When the DF is known, it can be used to obtain all the required *macroscopic* (i.e., observable) informations for a given system. Let us assume that a *microscopic* function $Q(\boldsymbol{x},\boldsymbol{v},t)$ is assigned: as a consequence, the associated macroscopic counterpart $\overline{Q}(\boldsymbol{x},t)$ is given by

$$\overline{Q}(\boldsymbol{x},t) \equiv \frac{1}{\rho_*(\boldsymbol{x},t)}\int_{\Re^3} f_*(\boldsymbol{x},\boldsymbol{v},t)Q(\boldsymbol{x},\boldsymbol{v},t)d^3\boldsymbol{v}, \tag{A2}$$

i.e., by the mean value of $Q(\boldsymbol{x},\boldsymbol{v},t)$ over all the velocities of particles that at time t determine the density $\rho_*(\boldsymbol{x},t)$. For this reason, we shall refer to the function $\overline{Q}(\boldsymbol{x},t)$ as the *average value* of $Q(\boldsymbol{x},\boldsymbol{v},t)$. Obviously, from its definition it follows that this "bar-operator" is linear; indeed, if $Q_1 = Q_1(\boldsymbol{x},\boldsymbol{v},t)$, $Q_2 = Q_2(\boldsymbol{x},\boldsymbol{v},t)$, and $\alpha = \alpha(\boldsymbol{x},t)$, we have

$$\overline{Q_1+Q_2} = \overline{Q_1} + \overline{Q_2}\,, \qquad\qquad \overline{\alpha Q} = \alpha\overline{Q}\,. \tag{A3}$$

For example,

1. when $Q = 1$, then $\overline{Q} = \rho_*(\boldsymbol{x},t)$;
2. when $Q = v_i$, then $\overline{Q} = \overline{v_i}(\boldsymbol{x},t)$, the i-th component of the *streaming velocity field*;
3. when $Q = (v_i - \overline{v_i})(v_j - \overline{v_j})$, then $\overline{Q} = \sigma^2_{ij}(\boldsymbol{x},t)$, the ij-th component of the so-called *velocity dispersion tensor*.

[1] The same approach is used in Statistical Mechanics to study the laws governing the behaviour of bodies formed of a very large number of individual particles (see e.g. Chapter 1 in Pauli 1973; Landau & Lifshitz 1980). Note that hare we have inserted an asterisk in superscript to stress the fact that, in case of a multi-component stellar system, $f_*(\boldsymbol{x},\boldsymbol{v},t)$ represents the distribution function of the stellar component *only*.

In this framework, the fundamental problem of Stellar Dynamics is the determination of the temporal evolution of the DF[2]. Let the coordinates in phase-space be $(\boldsymbol{x}, \boldsymbol{v}) \equiv \boldsymbol{w} \equiv (w_1, \ldots, w_6)$. Then it can be shown that the evolutionary equation for the phase-space DF, by making use of the usual summation convention[3], is described by

$$\frac{Df_*(\boldsymbol{w},t)}{Dt} = 0, \qquad \frac{D}{Dt} \equiv \frac{\partial}{\partial t} + \dot{w}_j \frac{\partial}{\partial w_j}, \tag{A4}$$

(see e.g. Chandrasekhar 1942; Ogorodnikov 1965; Saslaw 1987; BT87; see also C21), a partial differential equation of the first order known as *Collisionless Boltzmann Equation* (hereafter, CBE). By extending the concept of the *Lagrangian derivative* to six dimensions, it follows that the quantity $Df_*(\boldsymbol{w},t)/Dt$ does represent the rate of change of the density of phase points as seen by an observer who moves through phase-space with a star at velocity $\dot{\boldsymbol{w}}$. This lead us to a simple physical meaning of equation (A4): *the flow of stellar phase points through phase space is incompressible, i.e., $f_*(\boldsymbol{w},t)$ is constant along the trajectories of stellar phase points.* For this reason, equation (A4) is often reffered to as the "equation of continuity", though this must be carefully distinguished from the ordinary macroscopic equation of continuity of hydrodynamics. In the following discussion, we shall take the CBE as the basic equation.

Let us assume that each element of volume in the phase-space moves under the action of a force field generated by the total potential $\Psi_{\rm T} = \Psi_* + \Psi_{\rm ext}$, where $\Psi_* = \Psi_*(\boldsymbol{x},t)$ is the potential associated with the density ρ_* in equation (A1), and $\Psi_{\rm ext} = \Psi_{\rm ext}(\boldsymbol{x},t)$ represents an *external potential*, generated by a different density distribution $\rho_{\rm ext}$ (for example, a distribution of gas or dark matter). Therefore, the velocity $\dot{\boldsymbol{w}}$ in the phase-space is described by

$$\dot{\boldsymbol{x}} = \boldsymbol{v}, \qquad \dot{\boldsymbol{v}} = \frac{\partial \Psi_{\rm T}}{\partial \boldsymbol{x}}. \tag{A5}$$

By virtue of this last equation, we can rewrite equation (A4), in the notation of Cartesian tensors[4], in the form

$$\frac{\partial f_*}{\partial t} + v_j \frac{\partial f_*}{\partial x_j} + \frac{\partial \Psi_{\rm T}}{\partial x_j} \frac{\partial f_*}{\partial v_j} = 0, \tag{A6}$$

where, from equation (A1),

$$\nabla^2 \Psi_*(\boldsymbol{x},t) = -4\pi G \int_{\Re^3} f_*(\boldsymbol{x},\boldsymbol{v},t) d^3\boldsymbol{v}, \tag{A7}$$

being G the constant of gravitation. The CBE, considered as an equation of f_*, is then a *quasi-linear* partial differential equation, hence its solution can be obtained by using the *method of characteristics* (see e.g. Goursat 1917; Lin & Segel 1988): in this case, the characteristic curves are given by the solutions of equation (A5). The problem is then reduced to the integration of the equations of motion for a particle in the 3-dimensional space, under the action of an arbitrary

[2] A rigorous treatment can be obtained in the collisionless regime, starting from *Liouville's equation* in the $6N$-dimensional phase-space (see e.g. Chandrasekhar 1942; see also Landau & Lifshitz 1960 for an elegant physical explanation of Liouville's theorem in Classical Mechanics). By applying the so-called *BBGKY hierarchy*, the evolutionary equation for the DF can be reduced to an equation in $\Re^6 \times \Re$ with sources (see e.g. Huang 1963). Then, by developing the source term in power series one obtains the well-known *Fokker-Planck equation*, which is a diffusive equation used to study weakly collisional systems; the limiting case of collisionless systems is derived showing that, under particular hypothesis, the source term vanishes.

[3] The suffix notation for vector components will be used here, with the usual convention of vector and tensor analysis that terms containing a repeated suffix are to be regarded as summed over all possible values of the suffix.

[4] For a detailed discussion on the notation of Cartesian tensors, see Jeffreys (1931).

force field, which is generally time-dependent and non-linear. Unfortunately, as is well known, this problem is beyond the current mathematical possibilities (see e.g. Arnold 1978). Therefore, various technique in order to extract information from the CBE have been developed. Such technique can be divide in the construction of *particular solutions for stationary systems* and in the so-called *method of moments*. In the following we shall present the second method, which lead us to obtain some general relations of great practical interest.

The idea behind this particular method is to try to construct a set of equations, the so-called *Jeans equations* (see Jeans 1915, 1919; see also Jeans 1921 and references therein), by taking the moments of the CBE. Let us consider an arbitrary microscopic function $Q = Q(\boldsymbol{x}, \boldsymbol{v}, t)$. The starting point of the method of moments is the derivation of the differential equation that describes the evolution of the associated "observable" quantity $\overline{Q}$, defined as in equation (A2). This equation is easily obtained by the identity

$$\int_{\Re^3} Q \frac{Df_*}{Dt} d^3\boldsymbol{v} = 0, \tag{A8}$$

which is a direct consequence of equation (A4). By several integration by parts, applying *Gauss's theorem*, and using the fact that f_* vanishes for large values of $|\boldsymbol{v}|$, one finds

$$\frac{\partial \rho_* \overline{Q}}{\partial t} + \frac{\partial \rho_* \overline{Q v_j}}{\partial x_j} = \rho_* \overline{\frac{\partial Q}{\partial t}} + \rho_* \overline{v_j \frac{\partial Q}{\partial x_j}} + \rho_* \frac{\partial \Psi_{\rm T}}{\partial x_j} \overline{\frac{\partial Q}{\partial v_j}}, \tag{A9}$$

where $\Psi_{\rm T} = \Psi_* + \Psi_{\rm ext}$, and

$$\Psi_*(\boldsymbol{x}, t) = G \int_{\Re^3} \frac{\rho_*(\boldsymbol{x}', t)}{|\boldsymbol{x} - \boldsymbol{x}'|} d^3\boldsymbol{x}', \qquad \Psi_{\rm ext}(\boldsymbol{x}, t) = G \int_{\Re^3} \frac{\rho_{\rm ext}(\boldsymbol{x}', t)}{|\boldsymbol{x} - \boldsymbol{x}'|} d^3\boldsymbol{x}'. \tag{A10}$$

Note that, by making use of the "bar-operator" properties described in equation (A3), equation (A9) can be alternatively written as

$$\frac{\partial \rho_* \overline{Q}}{\partial t} + \frac{\partial \rho_* \overline{Q v_j}}{\partial x_j} = \rho_* \overline{\frac{DQ}{Dt}}, \qquad \frac{D}{Dt} = \frac{\partial}{\partial t} + v_j \frac{\partial}{\partial x_j} + \frac{\partial \Psi_{\rm T}}{\partial x_j} \frac{\partial}{\partial v_j}. \tag{A11}$$

This is the general equation that describes the evolution of an arbitrary macroscopic function with respect to time. The Jeans equations[5] used in Stellar Dynamics are obtained for $Q = 1$ and $Q = v_i$ (for $i = 1, 2, 3$), i.e.,

$$\frac{\partial \rho_*}{\partial t} + \frac{\partial \rho_* \overline{v_j}}{\partial x_j} = 0, \qquad \frac{\partial \rho_* \overline{v_i}}{\partial t} + \frac{\partial \rho_* \overline{v_i v_j}}{\partial x_j} = \rho_* \frac{\partial \Psi_{\rm T}}{\partial x_i}, \tag{A12}$$

respectively. Now, since simple algebra yields

$$\sigma_{ij}^2 \equiv \overline{(v_i - \overline{v_i})(v_j - \overline{v_j})} = \overline{v_i v_j} - \overline{v_i}\,\overline{v_j}, \qquad (i, j = 1, 2, 3), \tag{A13}$$

equation (A12) can be rewritten as

[5] Actually, as pointed out in Jeans (1921), Jeans's equations were originally derived by Maxwell (1866). Indeed, they arise in Maxwell's theory of the behaviour of a gas in which molecules are supposed to be point centres of force, repelling according to the inverse fifth power of the distance. Maxwell's original theory has been considerably improved by Kirchhoff and Boltzmann, and an important generalisation has been made by Chapman (see Chapman 1916), who extended the theory to molecules repelling according to any inverse power of the distance. See Chapman & Cowling (1953) for an interesting historical summary.

$$\frac{\partial \rho_*}{\partial t} + \frac{\partial \rho_* \overline{v_j}}{\partial x_j} = 0, \qquad \frac{\partial \overline{v_i}}{\partial t} + \overline{v_j} \frac{\partial \overline{v_i}}{\partial x_j} = \frac{\partial \Psi_{\rm T}}{\partial x_i} - \frac{1}{\rho_*} \frac{\partial \rho_* \sigma_{ij}^2}{\partial x_j}. \tag{A14}$$

Note the strict analogy between Jeans's equations and the equation of Fluid Dynamics (see e.g. Batchelor 1967; Landau & Lifshitz 1987), in which the velocity dispersion tensor is replaced by the thermodynamical pressure[6]. However, at variance with the equations describing fluids in motion, no natural closure is in general possible for equation (A13): in principle, Jeans's equations are an infinite set of equations, obtained for $Q = v_i v_k$, $Q = v_i v_k v_\ell$, and so on. As a consequence, in common applications they are closed with arbitrary assumptions on the nature of the velocity dispersion tensor.

A.1 Jeans's equations for axisymmetric systems

We shall now derive Jeans's equations for an axially symmetrical system. To solve this problem, we have to start by writing down the "equation of moments" (A11) in cylindrical coordinates. In principle, we may obtain the form of equation (A11) in any system of coordinates by a simple application of the chain rule for changing partial derivatives. Fortunately, there exist a simpler procedure. Since equation (A4) is true in *any* system of coordinates (see e.g. C21), consequently it is valid in cylindrical coordinates (R, φ, z); in this case $f_* = f_*(R, \varphi, z, v_R, v_\varphi, v_z, t)$, then from equation (A4) we readily have

$$\frac{\partial f_*}{\partial t} + \dot{R} \frac{\partial f_*}{\partial R} + \dot{\varphi} \frac{\partial f_*}{\partial \varphi} + \dot{z} \frac{\partial f_*}{\partial z} + \dot{v}_R \frac{\partial f_*}{\partial v_R} + \dot{v}_\varphi \frac{\partial f_*}{\partial v_\varphi} + \dot{v}_z \frac{\partial f_*}{\partial v_z} = 0, \tag{A15}$$

where v_R, v_φ, and v_z are the components of the velocity $\boldsymbol{v}$. Notice that the derivatives of the phase-space coordinates can be expressed in terms of the coordinates themselves. Indeed, to eliminate $\dot{R}$, $\dot{\varphi}$, and $\dot{z}$ we can use the following set of relations:

$$v_R = \dot{R}, \qquad v_\varphi = R\dot{\varphi}, \qquad v_z = \dot{z}. \tag{A16}$$

To eliminate $\dot{v}_R$, $\dot{v}_\varphi$, and $\dot{v}_z$, instead, we use the *Lagrangian equations* of motion for a free particle in cylindrical coordinates, i.e.,

$$\dot{v}_R - \frac{v_\varphi^2}{R} = \frac{\partial \Psi_{\rm T}}{\partial R}, \qquad \dot{v}_\varphi + \frac{v_R v_\varphi}{R} = \frac{1}{R} \frac{\partial \Psi_{\rm T}}{\partial \varphi}, \qquad \dot{v}_z = \frac{\partial \Psi_{\rm T}}{\partial z}, \tag{A17}$$

where $\Psi_{\rm T} = \Psi_{\rm T}(R, \varphi, z, t)$ is the potential function under whose influence the stars move. Hence,

[6] Consider an ideal fluid described in terms of a mass density $\rho(\boldsymbol{x}, t)$ and an isotropic pressure $p(\boldsymbol{x}, t)$. By supposing that the only force to which the fluid motions are subject (apart from the pressure gradients that may exist), is that derived from its own gravitation. Under these assumptions, the hydrodynamic equations governing the motions, referred to an inertial frame of reference, are given by

$$\frac{\partial \rho}{\partial t} + \frac{\partial \rho v_j}{\partial x_j} = 0, \qquad \frac{\partial v_i}{\partial t} + v_j \frac{\partial v_i}{\partial x_j} = \frac{\partial \psi}{\partial x_i} - \frac{1}{\rho} \frac{\partial p}{\partial x_i},$$

where $\boldsymbol{v} = \boldsymbol{v}(\boldsymbol{x}, t)$ is the velocity field, and $\psi = \psi(\boldsymbol{x}, t)$ is the gravitational potential, related to the density through Poisson's equation $\nabla^2 \psi = -4\pi G\rho$. The similarity with Jeans's equations is not casual, since the equations of Fluid Dynamics can be derived in total analogy to those of Jeans using the *same* mathematical tool: the *transport theorem* (see e.g. C21). However, despite the formal analysis, there exist a fundamental difference between the ordinary fluids and the non-collisional "fluid" of which a galaxy is composed. Indeed, while in an ordinary fluid the temperature and pressure are scalar quantities associated with isotropic tensors, generally the "pressure" of a non-collisional system is described by an anisotropic tensor (see e.g. BT87).

by substituiting equations (A16) and (A17) in equation (A15) we obtain the CBE in cylindrical coordinates:

$$\frac{\partial f_*}{\partial t}+v_R\frac{\partial f_*}{\partial R}+\frac{v_\varphi}{R}\frac{\partial f_*}{\partial \varphi}+v_z\frac{\partial f_*}{\partial z}+\left(\frac{v_\varphi^2}{R}+\frac{\partial \Psi_{\rm T}}{\partial R}\right)\frac{\partial f_*}{\partial v_R}-\left(\frac{v_R v_\varphi}{R}-\frac{1}{R}\frac{\partial \Psi_{\rm T}}{\partial \varphi}\right)\frac{\partial f_*}{\partial v_\varphi}+\frac{\partial \Psi_{\rm T}}{\partial z}\frac{\partial f_*}{\partial v_z}=0. \tag{A18}$$

Now, by applying the method of moments to the foregoing equation we find, without any mathematical difficulties,

$$\frac{\partial \rho_* \overline{Q}}{\partial t}+\frac{1}{R}\frac{\partial R\rho_*\overline{Qv_R}}{\partial R}+\frac{1}{R}\frac{\partial \rho_*\overline{Qv_\varphi}}{\partial \varphi}+\frac{\partial \rho_*\overline{Qv_z}}{\partial z}=\rho_*\overline{\frac{\partial Q}{\partial t}}+\rho_*\left(\overline{v_R\frac{\partial Q}{\partial R}}+\overline{\frac{v_\varphi}{R}\frac{\partial Q}{\partial \varphi}}+\overline{v_z\frac{\partial Q}{\partial z}}\right)+$$

$$+\rho_*\left[\overline{\left(\frac{v_\varphi^2}{R}+\frac{\partial \Psi_{\rm T}}{\partial R}\right)\frac{\partial Q}{\partial v_R}}-\overline{\left(\frac{v_R v_\varphi}{R}-\frac{1}{R}\frac{\partial \Psi_{\rm T}}{\partial \varphi}\right)\frac{\partial Q}{\partial v_\varphi}}+\overline{\frac{\partial \Psi_{\rm T}}{\partial z}\frac{\partial Q}{\partial v_z}}\right]. \tag{A19}$$

Finally, making use of the properties of the "bar-operator", equation (A19) can be rewritten as

$$\frac{\partial \rho_* \overline{Q}}{\partial t}+\frac{1}{R}\frac{\partial R\rho_*\overline{Qv_R}}{\partial R}+\frac{1}{R}\frac{\partial \rho_*\overline{Qv_\varphi}}{\partial \varphi}+\frac{\partial \rho_*\overline{Qv_z}}{\partial z}=\rho_*\overline{\frac{DQ}{Dt}}, \tag{A20}$$

where now the operator D/Dt reads

$$\frac{D}{Dt}=\frac{\partial}{\partial t}+v_R\frac{\partial}{\partial R}+\frac{v_\varphi}{R}\frac{\partial}{\partial \varphi}+v_z\frac{\partial}{\partial z}+\left(\frac{v_\varphi^2}{R}+\frac{\partial \Psi_{\rm T}}{\partial R}\right)\frac{\partial}{\partial v_R}-\left(\frac{v_R v_\varphi}{R}-\frac{1}{R}\frac{\partial \Psi_{\rm T}}{\partial \varphi}\right)\frac{\partial}{\partial v_\varphi}+\frac{\partial \Psi_{\rm T}}{\partial z}\frac{\partial}{\partial v_z}. \tag{A21}$$

Equation (A20), in analogy with (A11), describes, in cylindrical coordinates, the moments of the CBE. Jeans's equations are now obtained simply by substituiting in equation (A20), successively, $Q=1$, $Q=v_R$, $Q=v_\varphi$, and $Q=v_z$.

For $Q=1$ the right-hand side of equation (A20) vanishes, and so we obtain

$$\frac{\partial \rho_*}{\partial t}+\frac{1}{R}\frac{\partial R\rho_*\overline{v_R}}{\partial R}+\frac{1}{R}\frac{\partial \rho_*\overline{v_\varphi}}{\partial \varphi}+\frac{\partial \rho_*\overline{v_z}}{\partial z}=0, \tag{A22}$$

where $\overline{v_R}$, $\overline{v_\varphi}$, and $\overline{v_z}$ have their usual meaning. The previous equation clearly expresses the conservation of the stellar mass, and so it can be interpreted as the "macroscopic equation of continuity". For $Q=v_R$, instead, we have

$$\frac{\partial \rho_*\overline{v_R}}{\partial t}+\frac{\partial \rho_*\overline{v_R^2}}{\partial R}+\frac{1}{R}\frac{\partial \rho_*\overline{v_R v_\varphi}}{\partial \varphi}+\frac{\partial \rho_*\overline{v_R v_z}}{\partial z}+\rho_*\frac{\overline{v_R^2}-\overline{v_\varphi^2}}{R}=\rho_*\frac{\partial \Psi_{\rm T}}{\partial R}. \tag{A23}$$

Similarly, for $Q=v_\varphi$ and $Q=v_z$ we find, respectively,

$$\frac{\partial \rho_*\overline{v_\varphi}}{\partial t}+\frac{\partial \rho_*\overline{v_\varphi v_R}}{\partial R}+\frac{1}{R}\frac{\partial \rho_*\overline{v_\varphi^2}}{\partial \varphi}+\frac{\partial \rho_*\overline{v_\varphi v_z}}{\partial z}+\rho_*\frac{2\overline{v_\varphi v_R}}{R}=\frac{\rho_*}{R}\frac{\partial \Psi_{\rm T}}{\partial \varphi}, \tag{A24}$$

and

$$\frac{\partial \rho_*\overline{v_z}}{\partial t}+\frac{\partial \rho_*\overline{v_z v_R}}{\partial R}+\frac{1}{R}\frac{\partial \rho_*\overline{v_z v_\varphi}}{\partial \varphi}+\frac{\partial \rho_*\overline{v_z^2}}{\partial z}+\rho_*\frac{\overline{v_z v_R}}{R}=\rho_*\frac{\partial \Psi_{\rm T}}{\partial z}. \tag{A25}$$

Equations (A23), (A24), and (A25), which physically represent the "macroscopic equations for mass motions", are the *Jeans equations in cylindrical coordinates*.

In an axially symmetrical system the DF and the Newtonian potential *must* be independent of φ. Consequently, also the stellar mass density and any average value depend on R, z, and t only. Moreover, by assuming that the system is in a steady state, also the dependence on time vanishes. Under these conditions, assuming further that $\overline{v_R} = \overline{v_z} = \overline{v_R v_\varphi} = \overline{v_R v_z} = \overline{v_\varphi v_z} = 0$, we obtain that equation (A24) is an identity, while equations (A23) and (A25) reduce to the following pair of equations:

$$\frac{\partial \rho_* \overline{v_R^2}}{\partial R} + \rho_* \frac{\overline{v_R^2} - \overline{v_\varphi^2}}{R} = \rho_* \frac{\partial \Psi_\mathrm{T}}{\partial R}, \qquad \frac{\partial \rho_* \overline{v_z^2}}{\partial z} = \rho_* \frac{\partial \Psi_\mathrm{T}}{\partial z}. \tag{A26}$$

Now, by virtue of the particular conditions previously assumed, and introducing the velocity dispersion tensor, equation (A26) becomes[7]

$$\frac{\partial \rho_* \sigma_R^2}{\partial R} + \rho_* \frac{\sigma_R^2 - \overline{v_\varphi^2}}{R} = \rho_* \frac{\partial \Psi_\mathrm{T}}{\partial R}, \qquad \frac{\partial \rho_* \sigma_z^2}{\partial z} = \rho_* \frac{\partial \Psi_\mathrm{T}}{\partial z}. \tag{A27}$$

By considering an axisymmetric density supported by a two-integrals phase-space distribution function $f_*(\mathcal{E}, J_z)$, where $\mathcal{E}$ and J_z are the energy and z-component of the angular momentum of each star (per unit mass), one always have $\sigma_R = \sigma_z \equiv \sigma$. Under this assumption, the foregoing equation then becomes

$$\begin{cases} \dfrac{\partial \rho_* \sigma^2}{\partial R} - \dfrac{\rho_* \Delta}{R} = \rho_* \dfrac{\partial \Psi_\mathrm{T}}{\partial R}, \\ \dfrac{\partial \rho_* \sigma^2}{\partial z} = \rho_* \dfrac{\partial \Psi_\mathrm{T}}{\partial z}, \end{cases} \qquad \Delta \equiv \overline{v_\varphi^2} - \sigma^2. \tag{A28}$$

[7] Following a standard convention, we define $\sigma_{RR}^2 \equiv \sigma_R^2$ and $\sigma_{zz}^2 \equiv \sigma_z^2$.

APPENDIX B

THE FUNCTIONS $A(s),\ldots,H(s)$

WE report here the explicit expressions of the functions entering the velocity dispersion profiles in Chapter 4.

B.1 JJe models

The five functions describing the contribution of the galaxy to the velocity dispersion in equation (4.66), an elementary integration leads to

- $$A(s) = -\frac{3\xi^2-\xi-1}{\xi^2(\xi-1)(1+s)} - \frac{(3\xi+2)s-\xi}{2\xi^2 s^2(1+s)} - \frac{1}{\xi^3(\xi-1)^2}\ln\frac{s}{\xi+s} - \frac{3\xi-4}{(\xi-1)^2}\ln\frac{s}{1+s},$$

- $$B(s) = -\frac{2(3\xi^3-6\xi^2+2\xi-1)s+9\xi^3-18\xi^2+9\xi-4}{2\xi^2(\xi-1)^2(1+s)^2} - \frac{2(\xi-1)s+\xi}{2\xi^2 s^2(1+s)^2}$$
$$+\frac{3\xi-1}{\xi^3(\xi-1)^3}\ln\frac{s}{\xi+s} - \frac{3\xi^2-9\xi+8}{(\xi-1)^3}\ln\frac{s}{1+s},$$

- $$C(s) = \frac{2(5\xi^5-8\xi^4+\xi^3+\xi^2+\xi-1)s+15\xi^5-24\xi^4+3\xi^3+3\xi^2+5\xi-4}{\xi^4(\xi-1)^2(1+s)^2}$$
$$+\frac{4(5\xi^3+2\xi^2-3)s^3-\xi(5\xi^2+2\xi-6)s^2+2\xi^2(\xi-2)s+3\xi^3}{6\xi^4 s^4(1+s)^2} - \frac{2(2\xi-1)}{\xi^5(\xi-1)^3}\ln\frac{s}{\xi+s}$$
$$+\frac{2(5\xi^2-13\xi+9)}{(\xi-1)^3}\ln\frac{s}{1+s},$$

- $$D(s) = \left[24\ln\frac{s}{1+s} + \frac{120s^5+60s^4-20s^3+10s^2-6s+4}{5s^5(1+s)}\right]\xi^2\ln\frac{\xi+s}{\xi} + \frac{5\xi^2+10\xi+9}{5\xi^3}\ln\frac{\xi+s}{s}$$

$$+\frac{\xi(24\xi^3-60\xi^2+43\xi-5)}{(\xi-1)^3}\ln\frac{\xi+s}{1+s}-\frac{1}{\xi^2(\xi-1)^2(\xi+s)}+\frac{\xi(4\xi^2-6\xi+1)}{(\xi-1)^2(1+s)}$$

$$+\frac{4(20\xi^3+5\xi^2-2)s^3-\xi(40\xi^2+10\xi+1)s^2+4\xi^2(5\xi+1)s-8\xi^3}{10\xi^2s^4}-24\xi^2\mathcal{H}(\xi,s),$$

- $$E(s)=\left[80\ln\frac{1+s}{s}-\frac{1680s^7+840s^6-280s^5+140s^4-84s^3+56s^2-40s+30}{21s^7(1+s)}\right]\xi^2\ln\frac{\xi+s}{\xi}$$

$$+\frac{2(35\xi^4+21\xi^3-14\xi-15)}{21\xi^5}\ln\frac{\xi+s}{s}-\frac{2\xi(40\xi^3-100\xi^2+75\xi-14)}{(\xi-1)^3}\ln\frac{\xi+s}{1+s}$$

$$-\frac{\xi(10\xi^2-15\xi+4)}{(\xi-1)^2(1+s)}-\frac{630\xi^5+175\xi^4+126\xi^3+63\xi^2+14\xi-9}{21\xi^4s}$$

$$+\frac{3\xi^2(252\xi^2+70\xi+27)s^2-30\xi^3(14\xi+3)s+180\xi^4}{126\xi^3s^6}+\frac{1}{\xi^4(\xi-1)^2(\xi+s)}$$

$$+\frac{3(350\xi^4+105\xi^3+63\xi^2+28\xi+6)s-\xi(630\xi^3+189\xi^2+98\xi+33)}{63\xi^3s^3}+80\xi^2\mathcal{H}(\xi,s).$$

For the BH contribution in equation (4.69), defined in (4.70), we have

- $$F(s)=\frac{12s^3+6s^2-2s+1}{3s^3(1+s)}+4\ln\frac{s}{1+s},$$

- $$G(s)=\frac{24s^4+36s^3+8s^2-2s-1}{3s^3(1+s)^2}+8\ln\frac{s}{1+s},$$

- $$H(s)=-\frac{180s^6+270s^5+60s^4-15s^3+6s^2-3s-4}{10s^5(1+s)^2}-18\ln\frac{s}{1+s}.$$

B.1.1 The case $\xi=1$

In the particular case $\xi=1$ the foregoing expressions reduce to

- $$A(s)=-\frac{(6s^2+6s-1)(2s+1)}{2s^2(1+s)^2}-6\ln\frac{s}{1+s},$$

- $$B(s)=-\frac{12s^4+30s^3+22s^2+3s+3}{6s^2(1+s)^3}-2\ln\frac{s}{1+s},$$

- $C(s) = \dfrac{60s^6 + 150s^5 + 110s^4 + 15s^3 - 3s^2 + s + 3}{6s^4(1+s)^3} + 10\ln\dfrac{s}{1+s},$

- $D(s) = \left[24\ln\dfrac{s}{1+s} + \dfrac{120s^5 + 60s^4 - 20s^3 + 10s^2 - 6s + 4}{5s^5(1+s)}\right]\ln(1+s) - \dfrac{24}{5}\ln\dfrac{s}{1+s}$

  $+ \dfrac{576s^6 + 1260s^5 + 716s^4 + 9s^3 - 9s^2 - 24}{30s^4(1+s)^3} - 24\mathcal{H}(1,s),$

- $E(s) = \left[80\ln\dfrac{1+s}{s} - \dfrac{1680s^7 + 840s^6 - 280s^5 + 140s^4 - 84s^3 + 56s^2 - 40s + 30}{21s^7(1+s)}\right]\ln(1+s)$

  $- \dfrac{10404s^8 + 23490s^7 + 14314s^6 + 711s^5 - 243s^4 + 109s^3 - 57s^2 - 30s - 180}{126s^6(1+s)^3}$

  $- \dfrac{18}{7}\ln\dfrac{s}{1+s} + 80\mathcal{H}(1,s).$

B.2 J3e models

The functions from A to E are instead given by

- $A(s) = F(s)\ln\dfrac{\xi+s}{\xi} + \dfrac{9\xi^2 + 3\xi + 1}{3\xi^3}\ln\dfrac{\xi+s}{s} + \dfrac{1}{\xi-1}\ln\dfrac{\xi+s}{1+s} - \dfrac{2(1+3\xi)s - \xi}{6\xi^2 s^2} - 4\mathcal{H}(\xi,s),$

- $B(s) = G(s)\ln\dfrac{\xi+s}{\xi} + \dfrac{9\xi^2 - 1}{3\xi^3}\ln\dfrac{\xi+s}{s} + \dfrac{5\xi - 6}{(\xi-1)^2}\ln\dfrac{\xi+s}{1+s} + \dfrac{3\xi^2 + \xi - 1}{3\xi^2(\xi-1)(1+s)}$

  $- \dfrac{(\xi-2)s + \xi}{6\xi^2 s^2(1+s)} - 8\mathcal{H}(\xi,s),$

- $C(s) = H(s)\ln\dfrac{\xi+s}{\xi} - \dfrac{100\xi^4 + 20\xi^3 - 5\xi - 4}{10\xi^5}\ln\dfrac{\xi+s}{s} - \dfrac{8\xi - 9}{(\xi-1)^2}\ln\dfrac{\xi+s}{1+s}$

  $+ \dfrac{3(40\xi^3 + 5\xi^2 - 6\xi - 8)s^3 + \xi(5\xi+4)(3-2\xi)s^2 - 4\xi^2(\xi+2)s + 6\xi^3}{60\xi^4 s^4(1+s)}$

  $+ \dfrac{10\xi^4 - 20\xi^3 - 5\xi^2 + \xi + 4}{10\xi^4(\xi-1)(1+s)} + 18\mathcal{H}(\xi,s),$

- $$D(s) = \left[12\ln\frac{1+s}{s} - \frac{60s^5+30s^4-10s^3+5s^2-3s+2}{5s^5(1+s)}\right]\xi^2\ln\frac{\xi+s}{\xi} + \frac{5\xi^2+5\xi+3}{5\xi^3}\ln\frac{\xi+s}{s}$$
$$-\frac{\xi(12\xi^2-18\xi+5)}{(\xi-1)^2}\ln\frac{\xi+s}{1+s} - \frac{30\xi^4-20\xi^3-2\xi-3}{5\xi^2(\xi-1)(1+s)}$$
$$-\frac{(20\xi^3+5\xi^2+7\xi+6)s^3-\xi(10\xi^2+3\xi+3)s^2+2\xi^2(3\xi+1)s-4\xi^3}{10\xi^2s^4(1+s)} + 12\xi^2\mathcal{H}(\xi,s),$$

- $$E(s) = \left[40\ln\frac{s}{1+s} + \frac{840s^7+420s^6-140s^5+70s^4-42s^3+28s^2-20s+15}{21s^7(1+s)}\right]\xi^2\ln\frac{\xi+s}{\xi}$$
$$+\frac{40\xi^3-60\xi^2+10\xi+9}{(\xi-1)^2}\ln\frac{\xi+s}{1+s} + \frac{420\xi^6-280\xi^5-140\xi^4+21\xi^3+7\xi^2-\xi-6}{21\xi^4(\xi-1)(1+s)}$$
$$+\frac{70\xi^4+21\xi^3-7\xi-6}{21\xi^5}\ln\frac{\xi+s}{s} + \frac{280\xi^5+70\xi^4-42\xi^3-7\xi^2+8\xi+12}{42\xi^4s(1+s)}$$
$$-\frac{(420\xi^4+126\xi^3-14\xi^2+9\xi+18)s-\xi(252\xi^3+84\xi^2+5\xi+12)}{126\xi^3s^3(1+s)}$$
$$-\frac{(56\xi^2+20\xi+3)s^2-5\xi(8\xi+3)s+30\xi^2}{42\xi s^6(1+s)} - 40\xi^2\mathcal{H}(\xi,s),$$

where $\mathcal{H}(\xi,s)$ is a function defined and fully described in Appendix D. Of course, the functions F, G and H are the same for both models.

B.2.1 The case $\xi = 1$

In the limiting case $\xi = 1$ we obtain

- $$A(s) = F(s)\ln(1+s) + \frac{13}{3}\ln\frac{1+s}{s} - \frac{2s^2+7s-1}{6s^2(1+s)} - 4\mathcal{H}(1,s),$$

- $$B(s) = G(s)\ln(1+s) + \frac{8}{3}\ln\frac{1+s}{s} + \frac{32s^3+36s^2-1}{6s^2(1+s)^2} - 8\mathcal{H}(1,s),$$

- $$C(s) = H(s)\ln(1+s) - \frac{111}{10}\ln\frac{1+s}{s} - \frac{138s^5+117s^4-34s^3+s^2+2s-2}{20s^4(1+s)^2} + 18\mathcal{H}(1,s),$$

- $$D(s) = \left[12\ln\frac{1+s}{s} - \frac{60s^5+30s^4-10s^3+5s^2-3s+2}{5s^5(1+s)}\right]\ln(1+s) + \frac{13}{5}\ln\frac{1+s}{s}$$

$$- \frac{146s^5 + 189s^4 + 22s^3 - 8s^2 + 4s - 4}{10s^4(1+s)^2} + 12\mathcal{H}(1,s),$$

- $$E(s) = \left[40 \ln \frac{s}{1+s} + \frac{840s^7 + 420s^6 - 140s^5 + 70s^4 - 42s^3 + 28s^2 - 20s + 15}{21s^7(1+s)}\right] \ln(1+s)$$

$$+ \frac{4572s^7 + 5598s^6 + 404s^5 - 206s^4 + 116s^3 - 72s^2 + 75s - 90}{126s^6(1+s)^2}$$

$$+ \frac{26}{7} \ln \frac{1+s}{s} - 40\mathcal{H}(1,s).$$

APPENDIX C

THE FUNCTIONS $H_{ij}(s)$

IN this Apppendix we report here the explicit expressions of the functions entering the velocity dispersion profiles in Chapter 5.

C.1 P11 models

The three functions describing the BH contribution in equation (4.69) and defined in (4.70) are

- $H_{00}(s) = \dfrac{1}{2(1+s^2)^3}$,

- $H_{01}(s) = \dfrac{192s^8 + 648s^6 + 760s^4 + 361s^2 + 48}{8s^2(1+s^2)^4}$

$$+ \frac{6(1+2s^2)(8s^4+8s^2-1)}{s^3(1+s^2)^{3/2}} \operatorname{arcsinh} s - 48\,L(s),$$

- $H_{10}(s) = -\dfrac{16s^2+1}{8(1+s^2)^4}$,

- $H_{02}(s) = \dfrac{768s^{10} + 2592s^8 + 3040s^6 + 1321s^4 + 24s^2 - 72}{8s^4(1+s^2)^4}$

$$+ \frac{3(128s^8 + 192s^6 + 48s^4 - 8s^2 + 3)}{s^5(1+s^2)^{3/2}} \operatorname{arcsinh} s - 192\,L(s),$$

- $H_{20}(s) = \dfrac{15}{8(1+s^2)^4}$,

- $$H_{11}(s) = \frac{384s^{10} + 1680s^8 + 2816s^6 + 2119s^4 + 641s^2 + 24}{4s^2(1+s^2)^5}$$

$$\frac{6(64s^8 + 160s^6 + 120s^4 + 20s^2 - 1)}{s^3(1+s^2)^{5/2}} \operatorname{arcsinh} s - 192\,L(s),$$

- $$H_{12}(s) = \frac{3(768s^{12} + 3360s^{10} + 5632s^8 + 4361s^6 + 1431s^4 + 92s^2 - 12)}{4s^4(1+s^2)^5}$$

$$+ \frac{9(256s^{10} + 640s^8 + 460s^6 + 80s^4 - 10s^2 + 1)}{s^5(1+s^2)^{5/2}} \operatorname{arcsinh} s - 1152\,L(s),$$

- $$H_{21}(s) = \frac{768s^{10} + 3360s^8 + 5632s^6 + 4361s^4 + 1459s^2 + 120}{4s^2(1+s^2)^5}$$

$$+ \frac{6(128s^8 + 320s^6 + 240s^4 + 40s^2 - 5)}{s^3(1+s^2)^{5/2}} \operatorname{arcsinh} s - 384\,L(s),$$

- $$H_{22}(s) = \frac{3840s^{12} + 16800s^{10} + 28160s^8 + 21805s^6 + 6983s^4 + 180s^2 - 180}{4s^4(1+s^2)^5}$$

$$+ \frac{15(2s^2+1)(128s^8 + 256s^6 + 112s^4 - 16s^2 + 3)}{s^5(1+s^2)^{5/2}} \operatorname{arcsinh} s - 1920\,L(s).$$

The three functions in equation (5.11) describing the BH contribution to the vertical velocity dispersion of the stars are

$$H_i(s) = \begin{cases} \dfrac{8s^4 + 12s^2 + 3}{s(1+s^2)^{3/2}} - 8, & (i=0), \\ \dfrac{16s^6 + 40s^4 + 30s^2 + 3}{s(1+s^2)^{5/2}} - 16, & (i=1), \\ \dfrac{3(16s^6 + 40s^4 + 30s^2 + 5)}{s(1+s^2)^{5/2}} - 48, & (i=2). \end{cases} \tag{C1}$$

C.2 ZL85 models

The three functions describing the BH contribution in equation (4.69) and defined in (4.70) are

- $$H_{00}(s) = \frac{6\arctan^2 s}{\pi^2} + \frac{4(3s^2+2)\arctan s}{\pi^2 s(1+s^2)} + \frac{2(3s^2+4)}{\pi^2(1+s^2)^2} - \frac{3}{2},$$

- $H_{01}(s) = -\dfrac{60\arctan^2 s}{\pi^2} - \dfrac{8(15s^4+10s^2-2)\arctan s}{\pi^2 s^3(1+s^2)} - \dfrac{4(45s^6+105s^4+70s^2+12)}{3\pi^2 s^2(1+s^2)^3} + 15,$

- $H_{10}(s) = \dfrac{12\arctan^2 s}{\pi^2} + \dfrac{8(3s^4+5s^2+1)\arctan s}{\pi^2 s(1+s^2)^2} + \dfrac{4(9s^4+21s^2+16)}{3\pi^2(1+s^2)^3} - 3,$

- $H_{02}(s) = -\dfrac{210\arctan^2 s}{\pi^2} - \dfrac{8(105s^6+70s^4-14s^2+6)\arctan s}{\pi^2 s^5(1+s^2)}$

  $$- \frac{2(315s^8+735s^6+476s^4+24s^2-36)}{3\pi^2 s^4(1+s^2)^3} + \frac{105}{2},$$

- $H_{20}(s) = \dfrac{30\arctan^2 s}{\pi^2} + \dfrac{4(15s^4+25s^2+8)\arctan s}{\pi^2 s(1+s^2)^2} + \dfrac{2(45s^4+105s^2+68)}{3\pi^2(1+s^2)^3} - \dfrac{15}{2},$

- $H_{11}(s) = -\dfrac{240\arctan^2 s}{\pi^2} - \dfrac{16(30s^6+50s^4+16s^2-1)\arctan s}{\pi^2 s^3(1+s^2)^2}$

  $$- \frac{8(90s^8+300s^6+343s^4+136s^2+6)}{3\pi^2 s^2(1+s^2)^4} + 60,$$

- $H_{12}(s) = -\dfrac{1260\arctan^2 s}{\pi^2} - \dfrac{24(105s^8+175s^6+56s^4-8s^2+1)\arctan s}{\pi^2 s^5(1+s^2)^2}$

  $$- \frac{4(315s^{10}+1050s^8+1211s^6+518s^4+38s^2-6)}{\pi^4(1+s^2)^4} + 315,$$

- $H_{21}(s) = -\dfrac{420\arctan^2 s}{\pi^2} - \dfrac{8(105s^6+175s^4+56s^2-8)\arctan s}{\pi^2 s^3(1+s^2)^2}$

  $$- \frac{4(315s^8+1050s^6+1211s^4+518s^2+48)}{3\pi^2 s^2(1+s^2)^4} + 105,$$

- $H_{22}(s) = -\dfrac{1890\arctan^2 s}{\pi^2} - \dfrac{12(315s^8+525s^6+168s^4-24s^2+8)\arctan s}{\pi^2 s^5(1+s^2)^2}$

  $$- \frac{2(945s^{10}+3150s^8+3633s^6+1536s^4+64s^2-48)}{\pi^2 s^4(1+s^2)^4} + \frac{945}{2}.$$

For what concerns the BH contribution we obtain

$$H_i(s) = \begin{cases} \dfrac{6\arctan s}{\pi} + \dfrac{2(3s^2+2)}{\pi s(1+s^2)} - 3, & (i=0), \\ \dfrac{12\arctan s}{\pi} + \dfrac{4(3s^4+5s^2+1)}{\pi s(1+s^2)^2} - 6, & (i=1), \\ -\dfrac{30\operatorname{arccot} s}{\pi} + \dfrac{2(15s^4+25s^2+8)}{\pi s(1+s^2)^2}, & (i=2). \end{cases} \tag{C2}$$

APPENDIX D

THE FUNCTION $\mathcal{H}$

IN Appendix D we have seen that, in solving Jeans's equations, a particular function of ξ and s has to be introduced. We define this function as

$$\mathcal{H}(\xi, s) \equiv \int_s^\infty \ln\left(1 + \frac{1}{y}\right) \frac{dy}{\xi + y}, \tag{D1}$$

where $\xi > 0$, and $s \geq 0$. Unfortunately, the integral defining $\mathcal{H}(\xi, s)$ cannot be evaluated analytically via elementary functions. Indeed, with the substitution $1 + y \equiv 1/t$, equation (D1) can be rewritten, after some minor reductions, as

$$\mathcal{H}(\xi, s) = \mathrm{Li}_2\left(\frac{1}{1+s}\right) + \mathcal{G}(\xi, s), \qquad \mathcal{G}(\xi, s) \equiv (\xi - 1)\int_0^{1/(1+s)} \frac{\ln(1-t)}{1 + (\xi - 1)t}\, dt, \tag{D2}$$

where

$$\mathrm{Li}_2(x) \equiv -\int_0^x \frac{\ln(1-t)}{t}\, dt \tag{D3}$$

is the *dilogarithm function* (see Lewin 1981; see also Gradshteyn & Ryzhik 2007). In order to find an analytical expression for $\mathcal{H}(\xi, s)$, let us focus on $\mathcal{G}(\xi, s)$.

For $\xi = 1$ the function $\mathcal{G}(\xi, s)$ vanishes, and so we have simply

$$\mathcal{H}(1, s) = \mathrm{Li}_2\left(\frac{1}{1+s}\right), \tag{D4}$$

which gives, in the special case $s = 0$, $\mathcal{H}(1, 0) = \mathrm{Li}_2(1) = \pi^2/6$.

For $\xi \neq 1$, instead, we have to distiguish the case $\xi < 1$ from the case $\xi > 1$. In the first case, the substitution $1 + (\xi - 1)t \equiv \xi/z$ yield

$$\mathcal{G}(\xi, s) = \frac{1}{2} \ln \frac{1+s}{\xi+s} \ln \frac{(1-\xi)^2(1+s)}{\xi+s} - \int_\xi^d \frac{\ln(1-z)}{z}\, dz, \qquad d \equiv \frac{\xi(1+s)}{\xi+s}, \tag{D5}$$

whence, by applying equation (D3), we find

$$\mathcal{G}(\xi,s)=\frac{1}{2}\ln\frac{1+s}{\xi+s}\ln\frac{(1-\xi)^2(1+s)}{\xi+s}+\mathrm{Li}_2\left[\frac{\xi(1+s)}{\xi+s}\right]-\mathrm{Li}_2(\xi). \tag{D6}$$

In the second case, i.e. for $\xi>1$, it is convenient to use the change of variable $1+(\xi-1)t\equiv\xi u$. By this substitution we obtain

$$\mathcal{G}(\xi,s)=\ln\frac{\xi}{\xi-1}\ln\frac{\xi+s}{1+s}+\int_{1/\xi}^{b}\frac{\ln(1-u)}{u}\,du,\qquad b\equiv\frac{\xi+s}{\xi(1+s)}, \tag{D7}$$

whence, from equation (D3),

$$\mathcal{G}(\xi,s)=\ln\frac{\xi}{\xi-1}\ln\frac{\xi+s}{1+s}-\mathrm{Li}_2\left[\frac{\xi+s}{\xi(1+s)}\right]+\mathrm{Li}_2\left(\frac{1}{\xi}\right). \tag{D8}$$

Summarising, the explicit expression for the function $\mathcal{H}(\xi,s)$ reads

$$\mathcal{H}(\xi,s)=\mathrm{Li}_2\left(\frac{1}{1+s}\right)+\begin{cases}\dfrac{1}{2}\ln\dfrac{1+s}{\xi+s}\ln\dfrac{(1-\xi)^2(1+s)}{\xi+s}+\mathrm{Li}_2\left[\dfrac{\xi(1+s)}{\xi+s}\right]-\mathrm{Li}_2(\xi), & 0<\xi<1,\\ 0, & \xi=1,\\ \ln\dfrac{\xi}{\xi-1}\ln\dfrac{\xi+s}{1+s}-\mathrm{Li}_2\left[\dfrac{\xi+s}{\xi(1+s)}\right]+\mathrm{Li}_2\left(\dfrac{1}{\xi}\right), & \xi>1.\end{cases} \tag{D9}$$

At the centre, remember the identity $\mathrm{Li}_2(1)=\pi^2/6$, we have

$$\mathcal{H}(\xi,0)=\begin{cases}\dfrac{\pi^2}{3}+\dfrac{\ln^2\xi}{2}-\ln\xi\ln(1-\xi)-\mathrm{Li}_2(\xi), & 0<\xi<1,\\ \dfrac{\pi^2}{6}, & \xi=1,\\ \ln^2\xi-\ln\xi\ln(\xi-1)+\mathrm{Li}_2\left(\dfrac{1}{\xi}\right), & \xi>1.\end{cases} \tag{D10}$$

We shall now prove that it is possible to obtain a series representation of this particular function. For, we shall focus directly on equation (D1). First, we rewrite $\mathcal{H}(\xi,s)$ as

$$\mathcal{H}(\xi,s)=\mathcal{H}(\xi,0)-\int_0^s\ln\left(1+\frac{1}{y}\right)\frac{dy}{\xi+y}, \tag{D11}$$

or, alternatively,

$$\mathcal{H}(\xi,s)=\mathcal{H}(\xi,0)-\frac{\mathcal{D}_1(\xi,s)-\mathcal{D}_2(\xi,s)}{\xi}, \tag{D12}$$

where the following definitions apply:

$$\mathcal{D}_1(\xi,s)\equiv\int_0^s\frac{\ln(1+y)}{1+y/\xi}\,dy,\qquad\qquad \mathcal{D}_2(\xi,s)\equiv\int_0^s\frac{\ln y}{1+y/\xi}\,dy. \tag{D13}$$

Now, since for $|x| \leq 1$ we have, in general,

$$\ln(1+x) = \sum_{n=0}^{\infty} (-1)^n \, \frac{x^{n+1}}{n+1}, \qquad\qquad \frac{1}{1+x} = \sum_{n=0}^{\infty} (-1)^n \, x^n, \tag{D14}$$

the functions $\mathcal{D}_1(\xi, s)$ and $\mathcal{D}_2(\xi, s)$ becomes[1], for $s < \xi$,

$$\mathcal{D}_1(\xi, s) \equiv -\int_0^s \sum_{n=1}^{\infty} \sum_{k=1}^{n} (-1)^n \, \frac{y^n}{k\,\xi^{n-k}} \, dy, \qquad\qquad \mathcal{D}_2(\xi, s) \equiv -\int_0^s \sum_{n=1}^{\infty} (-1)^n \, \frac{y^{n-1}}{\xi^{n-1}} \, \ln y \, dy. \tag{D15}$$

Then, performing the integration, we have

$$\mathcal{D}_1(\xi, s) = \sum_{n=1}^{\infty} a_n(\xi) s^{n+1}, \qquad\qquad a_n(\xi) \equiv -\frac{(-1)^n}{n+1} \sum_{k=1}^{n} \frac{1}{k\,\xi^{n-k}}, \tag{D16}$$

$$\mathcal{D}_2(\xi, s) = \sum_{n=1}^{\infty} (1 - n \ln s) b_n(\xi) s^n, \qquad\qquad b_n(\xi) \equiv \frac{(-1)^n}{n^2 \xi^{n-1}}.$$

Finally, by inserting equation (D16) in (D12), and defining $a_0(\xi) \equiv 0$, we obtain the following series representation:

$$\mathcal{H}(\xi, s) = \mathcal{H}(\xi, 0) + \frac{1}{\xi} \sum_{n=1}^{\infty} [(1 - n \ln s) b_n(\xi) - \, a_{n-1}(\xi)] s^n, \qquad (s < \xi). \tag{D17}$$

Now, in order to find the series representation of $\mathcal{H}(\xi, s)$ for $s > \xi$, we use the change of variable $t \equiv 1/y$ in equation (D1). This substitution readily yield

$$\mathcal{H}(\xi, s) = \int_0^{1/s} \frac{\ln(1+t)}{t(1+\xi t)} \, dt. \tag{D18}$$

[1] Let

$$S_a \equiv a_0 + a_1 + a_2 + \cdots + a_n + \cdots \qquad \text{and} \qquad S_b \equiv b_0 + b_1 + b_2 + \cdots + b_n + \cdots$$

be any two series whatever. By multiplying terms of the first series by terms of the second in all possible ways, we obtain a new series:

$$S \equiv S_a \times S_b = a_0 b_0 + (a_0 b_1 + a_1 b_0) + (a_0 b_2 + a_1 b_1 + a_2 b_0) + \cdots + (a_0 b_n + a_1 b_{n-1} + \cdots + a_n b_0) + \cdots,$$

or, alternatively,

$$\left(\sum_{n=0}^{\infty} a_n \right) \times \left(\sum_{n=0}^{\infty} b_n \right) = \sum_{n=0}^{\infty} c_n, \qquad\qquad c_n \equiv \sum_{k=0}^{n} a_k \, b_{n-k}.$$

If each of the series S_a and S_b is absolutely convergent, the series S converges, and its sum is the product of the sums of the two given series. This theorem, which is due to Augustin-Louis Cauchy, was generalized by Franz Mertens (1874), who showed that it still holds if only one of the series S_a and S_b is absolutely convergent and the other is merely convergent (see e.g. Goursat 1904).

Following the discussion after equation (D11), by using (D14) we find that (D18) can be rewritten, for $s > \xi$, as

$$\mathcal{H}(\xi, s) = \int_0^{1/s} \sum_{n=1}^{\infty} \sum_{k=1}^{n} (-1)^{n-1} \frac{\xi^{n-k}}{k} t^{n-1} dt, \tag{D19}$$

whence, performing the integration,

$$\mathcal{H}(\xi, s) = \sum_{n=1}^{\infty} \frac{h_n(\xi)}{s^n}, \qquad h_n(\xi) \equiv -\frac{(-1)^n}{n} \sum_{k=1}^{n} \frac{\xi^{n-k}}{k}, \qquad (s > \xi). \tag{D20}$$

Therefore, the asymptotic expansion of the function $\mathcal{H}(\xi, s)$ for "small" and "large" values of s, useful to examine the behaviour of the velocity dispersion profile, can be written more explicitly, by retaining the first three terms of the expansion, as

$$\mathcal{H}(\xi, s) = \begin{cases} \mathcal{H}(\xi, 0) + \dfrac{s \ln s}{\xi} - \dfrac{s}{\xi} + \mathcal{O}\left(s^2 \ln s\right), & s < \xi, \\ \dfrac{1}{s} - \dfrac{2\xi + 1}{4s^2} + \dfrac{6\xi^2 + 3\xi + 2}{18 s^3} + \mathcal{O}\left(\dfrac{1}{s^4}\right), & s > \xi. \end{cases} \tag{D21}$$

For what concerns the asymptotic behaviour of the function of one variable $\mathcal{H}(\xi, 0)$, useful to study the relevant quantities entering the *Virial Theorem* (see CMPZ21; see also Chapter 5 in Mancino 2019), it can be obtained directly by expanding equation (D10): such expansion gives, at the leading order,

$$\mathcal{H}(\xi, 0) \sim \begin{cases} \dfrac{\ln^2 \xi}{2}, & \xi \to 0, \\ \dfrac{\ln \xi}{\xi}, & \xi \to \infty. \end{cases} \tag{D22}$$

APPENDIX E

The Lambert-Euler Function

The Lambert-Euler function is a multivalued function defined implicitly by

$$W(z)\,\mathrm{e}^{W(z)} = z\,, \tag{E1}$$

being z a complex variable in general; the two real-valued branches of the W are denoted as W_{-1} and W_0 (see Fig. E.1, top panel). The asymptotic expansion of W_0 reads

$$W_0(z) = \begin{cases} z + \mathcal{O}(z^2)\,, & z \to 0\,, \\ \ln z + \mathcal{O}(\ln \ln z)\,, & z \to \infty\,, \end{cases} \tag{E2}$$

(see e.g. de Bruijn 1981), while for $z \to 0$ it can be shown that $W_{-1}(z) \sim \ln(-z)$. Moreover, it can be proved that

$$\begin{cases} W_{-1}\left(z\,\mathrm{e}^{z}\right) = z\,, & W_0\left(z\,\mathrm{e}^{z}\right) \geq z\,, \quad \text{for} \quad z \leq -1, \\ W_{-1}\left(z\,\mathrm{e}^{z}\right) \leq z\,, & W_0\left(z\,\mathrm{e}^{z}\right) = z\,, \quad \text{for} \quad z \geq -1; \end{cases} \tag{E3}$$

(see Fig. E.1, bottom panel). Therefore, for all values of z it follows that

$$W_{-1}\left(z\,\mathrm{e}^{z}\right) \leq z, \qquad W_0\left(z\,\mathrm{e}^{z}\right) \geq z. \tag{E4}$$

Finally, we recall the following monotonicity properties, valid for $z_1 \geq z_2$:

$$W_0(z_1) \geq W_0(z_2), \qquad W_{-1}(z_1) \leq W_{-1}(z_2). \tag{E5}$$

For a general discussion of the properties of W, see e.g. Corless et al. (1996).

In physics the W-function has been used to solve problems ranging from Quantum Mechanics (see e.g. Valluri et al. 2009; Wang & Moniz 2019) to General Relativity (see e.g. Mező & Keady 2016; see also Barry et al. 2000 for a summary of recent applications), including Stellar Dynamics (CZ18). Indeed, several trascendental equations accuring in applications can be solved in terms of W; for example, let us consider the following equation:

$$aX^b + c\ln X = Y, \tag{E6}$$

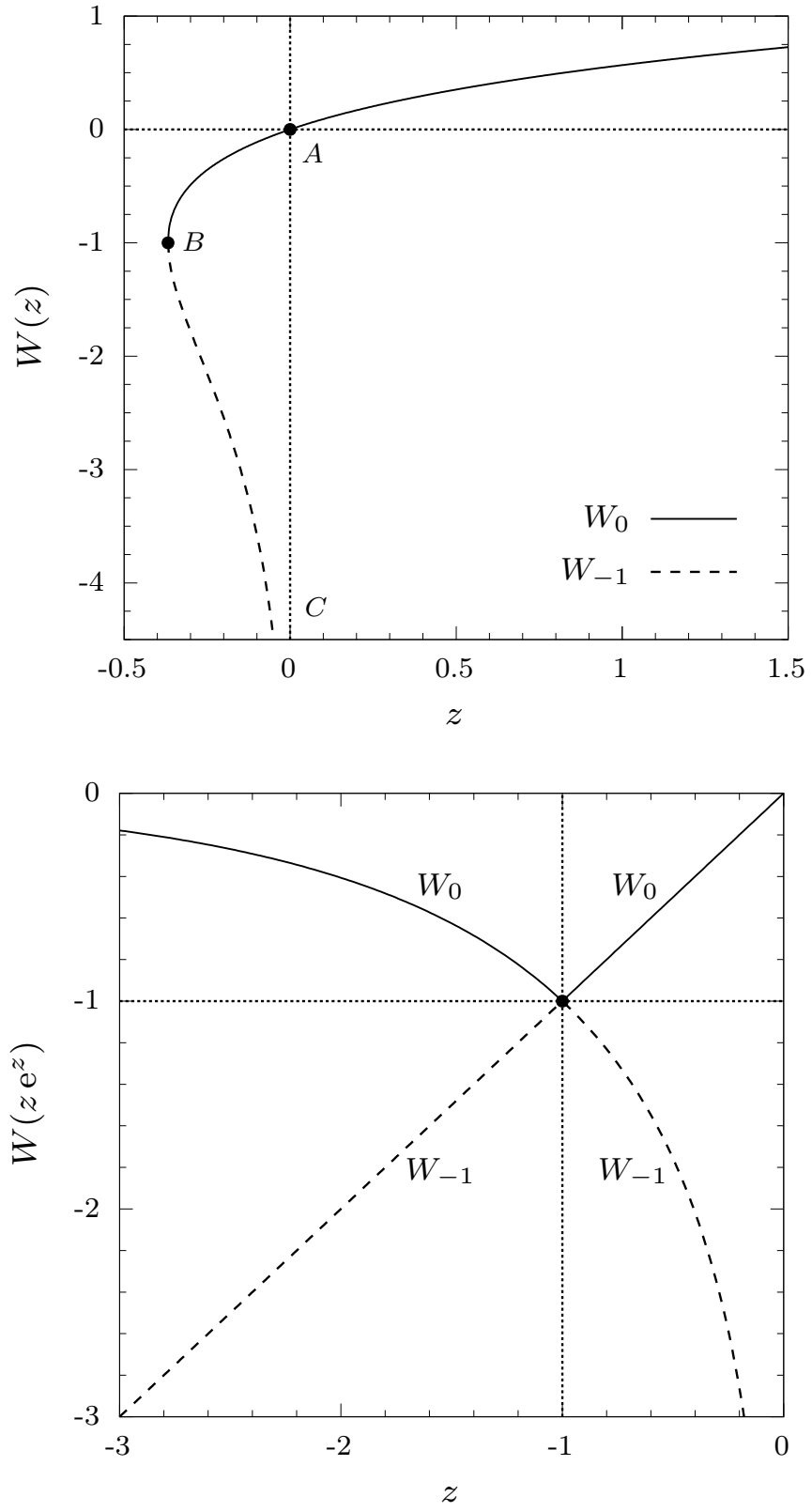

Figure E.1. Top: the two real branches W_0 (solid line) and W_{-1} (dashed line), where $A = (0, 0)$ and $B = (-1/\mathrm{e}, -1)$, while C indicates the asymptotic point $(0, -\infty)$. Bottom: the two real branches of the function $W(z\mathrm{e}^z)$.

where a, b, c, and Y are quantities independent of $X > 0$. Multiplying both sides of the foregoing equation by b/c we obtain

$$\frac{ab}{c} X^b + \ln X^b = \frac{bY}{c}, \tag{E7}$$

i.e., by exponentiating,

$$X^b \exp\left(\frac{ab}{c} X^b\right) = \exp\left(\frac{bY}{c}\right). \tag{E8}$$

Finally, multiplying both sides by ab/c, and comparing the resulting expression with the definition (E1), we conclude that

$$X^b = \frac{c}{ab} W\left(\frac{ab}{c} \mathrm{e}^{bY/c}\right). \tag{E9}$$

As a simple application, consider a disc galaxy represented quite well in its face-on view by the following surface density profile (Freeman 1970; C21, exercise 2.30):

$$\Sigma(R) = \Sigma_0 \, \mathrm{e}^{-R/R_\mathrm{d}}, \tag{E10}$$

where Σ_0 is the central surface density, and R_d denotes a scale lenght. Let us calculate the corresponding half-mass radius R_h. Firstly of all, since the density profile has cylindrical symmetry, the mass contained within a radius R is given by

$$M(R) = 2\pi \int_0^R \Sigma(R') R' dR'. \tag{E11}$$

Now, by inserting the expression for Σ, after an integration by parts we obtain

$$M(R) = 2\pi R_\mathrm{d}^2 \Sigma_0 \left(1 - \frac{R + R_\mathrm{d}}{R_\mathrm{d}} \, \mathrm{e}^{-R/R_\mathrm{d}}\right). \tag{E12}$$

Notice that $\Sigma \propto R^2$ for $R \to 0$ (in practice, for $R \ll R_\mathrm{d}$), and it reduces to $M_\mathrm{d} = 2\pi R_\mathrm{d}^2 \Sigma_0$ when $R \to \infty$ (in practice, for $R \gg R_\mathrm{d}$). The radius R_h obeys equation $M(R_\mathrm{h}) = M_\mathrm{d}/2$, i.e.

$$(1 + x)\mathrm{e}^{-x} = \frac{1}{2}, \qquad\qquad x \equiv \frac{R_\mathrm{h}}{R_\mathrm{d}}. \tag{E13}$$

and, after multiplication by $-1/\mathrm{e}$, it redues to

$$-(1 + x)\mathrm{e}^{-(1+x)} = -\frac{1}{2e}. \tag{E14}$$

As a consequence, by definition of W function in equation (E6) we obtain

$$-(1 + x) = W\left(-\frac{1}{2\mathrm{e}}\right) \qquad \Rightarrow \qquad x = -1 - W\left(-\frac{1}{2\mathrm{e}}\right).$$

Further, it is immediate to show that the branch W_0 leads to negative values for R_h. In fact, by

virtue of the monotonicity property for W_0 in equation (E5), from the inequality $-(1/2)\mathrm{e}^{-1} > -(1/2)\mathrm{e}^{-1/2}$ it follows that

$$W_0\left(-\frac{1}{2\mathrm{e}}\right) > W_0\left(-\frac{1}{2}\mathrm{e}^{-\frac{1}{2}}\right) = -\frac{1}{2}, \tag{E15}$$

The branch returning a physically acceptable solution (i.e. positive) is therefore the negative one, so that

$$x = -1 - W_{-1}\left(-\frac{1}{2\mathrm{e}}\right), \tag{E16}$$

i.e., $R_\mathrm{h} \simeq 1.68\, R_\mathrm{d}$.

References

[1] Arnold V.I., 1978, *Mathematical Methods of Classical Mechanics*, New York: Springer

[2] Artin M., 1991, *Algebra*, Prentice Hall

[3] Barai P., Proga D. & Nagamine K., 2012, MNRAS, 424, 728

[4] Barnabè M. et al., 2006, A&A, 446, 61

[5] Batchelor G.K., 1967, *An Introduction to Fluid Dynamics*, Cambridge University Press

[6] Bertin G. et al., 1994, A&A, 292, 381

[7] Bertin G., 2014, *Dynamics of Galaxies*, 2nd ed. Cambridge University Press

[8] Bertin G. & Lin C.C., 1996, *Spiral Structure in Galaxies: A Density Wave Theory*, MIT Press, Cambridge, MA

[9] Bertin G. & Stiavelli M., 1993, Rep. Prog. Phys., 56, 493

[10] Bianchini P. et al., 2013, ApJ , 772, 67

[11] Bianchini P. et al., 2018, MNRAS , 481, 2125

[12] Binney J., 1981, MNRAS, 196, 455

[13] Binney J. & Tabor G., 1995, MNRAS, 276, 663

[14] Binney J., & Tremaine S., 1987, *Galactic Dynamics*, 3rd printing Princeton University Press

[15] Binney J., & Tremaine S., 2008, *Galactic Dynamics*, 2nd Ed. University Press

[16] Bondi H., 1952, MNRAS, 112, 195

[17] Booth C.M. & Schaye J., 2009, MNRAS, 398, 53

[18] Bullock J.S. & Boylan-Kolchin M., 2017, Annu. Rev. Astron. Astrophys., 55, 343

[19] Byrd P.F. & Friedman M., 1971, *Handbook of Elliptic Integrals for Engineers and Physicists*, 2nd ed. Springer-Verlag

[20] Cappellari M. et al., 2007, MNRAS, 379, 418

[21] Cappellari M. et al., 2015, ApJL, 804, L21

[22] Cappellari M., 2016, ARA&A, 54, 597

[23] Caravita C., Ciotti L. & Pellegrini S., 2021, MNRAS, 506, 1480

[24] Carlson B.C., 1977, *Special Functions of Applied Mathematics*, Academic Press

[25] Carlson B.C., 1979, Numer. Math., 33, 1

[26] Carrol B.W. & Ostlie D.A., 2007, *An Introduction to Modern Astrophysics*, Addison Wesley

[27] Chandrasekhar S., 1939, *An introduction to the study of Stellar Structure*, Dover Publications

[28] Chandrasekhar S., 1942, *Principles of Stellar Dynamics*, Chicago University Press

[29] Chandrasekhar S., 1961, *Hydrodynamic and Hydromagnetic Stability*, Oxford University Press

[30] Chandrasekhar S., 1969, *Ellipsoidal Figures of Equilibrium*, Yale University Press

[31] Chapman S., 1916, in Proceedings of the Royal Society of London. Series A, Containing Papers of a Mathematical and Physical Character, Vol. 93, No. 646, pp. 1-20

[32] Chapman S. & Cowling T.G., 1953, *The Mathematical Theory of Non-uniform Gases*, Cambridge Mathematical Library

[33] Ciotti L., 1991, A&A, 249, 99

[34] Ciotti, L. 1996, ApJ, 471, 68

[35] Ciotti L., 1999, ApJ, 520, 574

[36] Ciotti L., 2000, *Lecture Notes on Stellar Dynamics*, Scuola Normale Superiore Ed.

[37] Ciotti L., Bertin G., 2005, A&A, 437, 419

[38] Ciotti L., Lanzoni B. & Renzini A., 1996, MNRAS, 282, 1

[39] Ciotti L., Mancino A., Pellegrini S., 2019, MNRAS, 490, 2656

[40] Ciotti L. et al., 2021, MNRAS, 500, 1054

[41] Ciotti L., Morganti L. & de Zeeuw P.T., MNRAS, 2009, 393, 491

[42] Ciotti L. & Ostriker J.P., 1997, APJ, 487, L105

[43] Ciotti L. & Ostriker J.P., 2012, in Kim D.-W., Pellegrini S., eds., Astrophysics and Space Science Library, Vol. 378, *Hot Interstellar Matter in Elliptical Galaxies*, Springer-Verlag, Berlin, p. 83

[44] Ciotti L. & Pellegrini S., 1996, MNRAS, 279, 240

[45] Ciotti L. & Pellegrini S., 2004, MNRAS, 350, 609

[46] Ciotti L. & Pellegrini S., 2017, ApJ, 848, 29

[47] Ciotti L. & Pellegrini S., 2018, ApJ, 868, 91,

[48] Ciotti L. & Ziaee Lorzad A., 2018, MNRAS, 473, 5476

[49] Ciotti L., 2021, *Introduction to Stellar Dynamics*, Cambridge University Press, Cambridge

[50] Clarke C. & Carswell B., 2007, *Principles of Astrophysical Fluid Dynamics*, Cambridge University Press

[51] Corless R.M. et al., 1996, Adv Comput Math, 5, 329

[52] Cranmer S.R., 2004, Am. J. Phys., 72, 1397

[53] Cunningham A.J., 2012, ApJ, 744, 185

[54] Currie I.G., 1993, *Fundamental Mechanics of Fluids*, 3rd Ed. Marcel Dekker

[55] Curtis M. & Sijacki D., 2015, MNRAS, 454, 3445

[56] Czoske O. et al., 2008, ApJ, 384, 987

[57] De Deo L., Ciotti L. & Pellegrini S., 2024, MNRAS (accepted)

[58] Dehnen W., 1993, MNRAS, 265, 250

[59] de Jong T., Boland W. & Dalgarno A., 1980, A&A, 91, 68

[60] Delgado Serrano R., *The Evolution of the Hubble Sequence: morpho-kinematics of distant galaxies*, PhD thesis, Observatoire de Paris-Meudon

[61] de Vaucouleurs G., 1948, Ann.Astr., 11, 247

[62] de Vaucouleurs G., 1959, in *Handbuch der Physik* 53, ed. S. Flügge (Berlin: Springer), 275

[63] de Zeeuw P.T., 1984, *Dynamics of Triaxial Stellar Systems*, PhD Thesis, Leiden University

[64] de Zeeuw P.T., 1985a, MNRAS, 216, 273

[65] de Zeeuw P.T., 1985b, MNRAS, 216, 599

[66] de Zeeuw P.T., Hunter C. & Schwarzschild M., 1987, ApJ, 317, 607

[67] de Zeeuw P.T. & Lynden-Bell D., 1985, MNRAS, 215, 713

[68] de Zeeuw P.T. & Pfenniger D., 1988, MNRAS, 235, 949

[69] Dye S. et al., 2008, MNRAS, 388, 384

[70] Eckert D., 2012, A&A, 541, 15

[71] Emden R., 1907, *Gaskigeln*, Leipzig

[72] Emsellem E. et al., 2007, MNRAS , 379, 401

[73] Evans N.W. & de Zeeuw P.T., 1992, MNRAS, 257, 152

[74] Evans N.W., 1994, MNRAS, 267, 333

[75] Evans N.W. & de Zeeuw P.T., 1994, MNRAS, 271, 202

[76] Fabian A.C. & Rees M.J., 1995, MNRAS, 277, L55

[77] Feynman R.P., Leighton R.B. & Sands M., 1963, *The Feynman Lectures on Physics*, Volume I, Addison-Wesley, Reading, MA

[78] Feynman R.P., Leighton R.B. & Sands M., 1964, *The Feynman Lectures on Physics*, Volume II, Addison-Wesley, Reading, MA

[79] Fermi E., *Termodinamica*, 1958, Boringhieri, Torino

[80] Ferraro F.R. et al., 2018, ApJ, 860, 36

[81] Ferrers N.M., 1877, Quart. J. Pure Appl. Math., 14, 1

[82] Fiestas J., Spurzem R. & Kim E., 2006, MNRAS, 373, 677

[83] Frank J., King A. & Raine D., 1992, *Accretion Power in Astrophysics*, Cambridge University Press, Cambridge

[84] Fukue J., 2001, PASJ, 53, 687

[85] Gan Z. et al., 2019, ApJ, 872, 167

[86] Gantmacher F., 1975, *Lectures in Analytical Mechanics*, 2nd ed. Mir Publishers

[87] Gavazzi R. et al., 2007, ApJ, 667, 176

[88] Gerhard O. et al., 2001, AJ, 121, 1936

[89] Giersz M. et al., 2013, MNRAS, 431, 2184

[90] Goursat E., 1917, *A Course in Mathematical Analysis. Volume II, Part Two*, New York: Ginn & Co.

[91] Gradshteyn I. S., Ryzhik I. M., 2007, in Jeffrey A., Zwillinger D. E., eds, Table of Integrals, Series, and Products, 7th edn. Elsevier, Amsterdam

[92] Granger R.A., 1991, *Fluid Mechanics*, Dover Publucations, New York

[93] Herbst R.S., 2015, PhD thesis, Univ. Witwatersrand

[94] Hernquist L., 1990, ApJ, 356, 359

[95] Horedt G.P., *Polytropes. Applications in Astrophysics and Related Fields*, Kluwer Academic Publishers

[96] Hubble E., 1926, ApJ, 64, 321

[97] Hubble E., 1936, *The Realm of the Nebulae*, Dover, 1936

[98] Hunter C., 1977, AJ, 82, 271

[99] Hurley J.R. & Shara M.M., 2021, MNRAS, 425, 2872

[100] Inayoshi K., Haiman Z. & Ostriker J.P., 2016, MNRAS, 459, 3738

[101] Jacobi C.G.J., 1839, J. Für Math., 19, 309

[102] Jaffe W., 1983, MNRAS, 202, 995

[103] Jeans J., 1915, MNRAS, 76, 70

[104] Jeans J., 1919, *Problems of Cosmology and Stellar Dynamics*, Cambridge University Press, 1919

[105] Jeans J., 1921, *The Dynamical Theory of Gases*, 3rd ed. Cambridge University Press

[106] Jeffreson S.M.R. et al., 2017, MNRAS, 469, 4740

[107] Jeffreys H., 1931, *Cartesian Tensors*, Cambridge, England

[108] Jeffreys H. & Jeffreys B.S., 1956, *Methods of Mathematical Physics*, Cambridge, England

[109] Jeong H. et al., 2009, MNRAS , 398, 2028

[110] Kacharov N. et al., 2014, A&A , 567, A69

[111] Kamann S. et al., 2018, MNRAS, 480, 1689

[112] Kamlah A.W.H. et al., 2022, MNRAS, 516, 3266

[113] Kellogg O.D., 1967, *Foundation of Potential Theory*, Springer-Verlag, New York

[114] Klein O. & Nishina Y., 1929, Z. Phys., 52, 853

[115] Kochanek C.S., 1994, ApJ, 436, 56

[116] Koopmans L.V.E. et al., 2006, ApJ, 649, 599

[117] Kormendy J. & Bender R., 1996, ApJL, 464, L119

[118] Kormendy J. & Ho L.C., 2013, ARA&A, 51, 511

[119] Kormendy J. & Kennicutt R.C., 2004, ARA&A, 42, 603

[120] Kormendy J. & Richstone D., 1995, ARA&A , 33, 581

[121] Kormendy et al., 2009, ApJS, 182, 216

[122] Korol V., Ciotti L. & Pellegrini S., 2016, MNRAS, 460, 1188

[123] Krajnović D. et al., 2008, MNRAS , 390, 93

[124] Krolik J.H., 1998, *Active Galactic Nuclei: From the Central Black Hole to the Galactic Environment*, Princeton University Press, Princeton, NJ

[125] Kuzmin G.G., 1956., AZh, 33, 27

[126] Lacchin E. et al. 2022, MNRAS, 517, 1171

[127] Lamé G., 1837, J. de Math., 2, 147

[128] Landau L. & Lifshitz E., 1960, *Course of theoretical physics. Vol. 1: Mechanics*, Pergamon Press

[129] Landau L. & Lifshitz E., 1980, *Course of theoretical physics. Vol. 5: Statistical Physics, Part 1*, Third Revised and Enlarged Edition, Pergamon Press

[130] Landau L. & Lifshitz E., 1987, *Course of theoretical physics. Vol. 6: Fluid Mechanics*, Second Edition, Pergamon Press

[131] Lanzoni B. & Ciotti L., 2003, A&A, 404, 819

[132] Leanza S. et al., 2022, ApJ, 929, 186

[133] Lewin L., 1981, *Polylogarithms and Associated Functions*, New York: North-Holland

[134] Lin C.C., Segel L.A., 1988, *Mathematics Applied to Deterministic Problems in the Natural Sciences*, SIAM Classics Ed., Philadelphia

[135] Lin C.C. & Shu F.H., 1964, ApJ, 140, 646

[136] Livernois A.R. et al., 2022, MNRAS, 512, 2584

[137] Lord Rayleigh (J.W. Strutt, Sc.D. F.R.S.), 1945, *The Theory of Sound*, Two Volumes, New York, Dover Publications

[138] Lusso E. & Ciotti L., 2011, A&A, 525, 115

[139] Lyskova N. et al., 2023, MNRAS, 525, 898

[140] Lyttleton R.A., 1953, *The Stability of Rotating Liquid Masses*, Cambridge University Press

[141] Magorrian J. et al., 1998, AJ, 115, 2285

[142] Mancino A., 2019, *On the structural and dynamical properties of a new class of galaxy models with a central BH*, Master Thesis, University of Bologna

[143] Mancino A., Ciotti L. & Pellegrini S., 2022, MNRAS, 512, 2474

[144] Mancino A. et al., 2024, MNRAS, 527, 9904

[145] Maxwell J.C., 1866, Phil. Trans. R. Soc., 156, 249

[146] Merritt D., 1985, AJ, 90, 1027

[147] Mertens F., 1874, Journal für die Reine und Angewandte Mathematik, 79, 182

[148] Mihalas D. & Weibel-Mihalas B., 1984, *Foundations of Radiation Hydrodynamics* Oxford University Press

[149] Misner C.W., Thorne K.S., Wheeler J.A., 1973, *Gravitation*, Freeman & Co.

[150] Miyamoto M. & Nagai R., 1975, PASJ, 27, 533

[151] Muccione V. & Ciotti L., 2004, A&A, 421, 583

[152] Naab T., Ostriker J.P., 2007, MNRAS, 366, 899

[153] Nagai R. & Miyamoto M., 1976, PASJ, 28, 1

[154] Napolitano N.R., Romanowsky A. & Tortora C., 2010, MNRAS, 405, 2351

[155] Navarro J.F., Frenk C.S., White S.D.M., 1997, ApJ, 490, 493

[156] Negri A., Posacki S., Pellegrini S., Ciotti L., 2014, MNRAS, 445, 1351

[157] Nipoti C., Treu T. & Bolton A.S., 2008, MNRAS, 390, 349

[158] Ogorodnikov K.F., 1965, *Dynamics of Stellar Systems*, Pergamon Press LTD

[159] Osipkov L.P., 1979, Astron. Lett., 5, 77

[160] Park K. et al., 2014, MNRAS, 445, 2325

[161] Pauli W., 1973, *Pauli Lectures on Physics. Vol 4. Statistical Mechanics*, MIT Press, Cambridge

[162] Pellegrini S., 2011, ApJ, 738, 57

[163] Pellegrini S. & Ciotti L., 2006, MNRAS, 370, 1797

[164] Planck M., 1945, *Treatise on Thermodynamics*, Dover Publications

[165] Plummer H.C., 1911, MNRAS, 71, 460

[166] Posacki S., Pellegrini S., Ciotti L., 2013, MNRAS, 433, 2259

[167] Prandtl L., 1934, *Fundamentals of Hydro- and Aeromechanics*, Dover Publications

[168] Ramírez-Velasquez J.M. et al., 2018, MNRAS, 477, 4308

[169] Ramírez-Velasquez J.M. et al., 2019, A&A , 631, A13

[170] Raychaudhuri S., Ghosh S. & Joarder P.S., 2018, MNRAS, 479, 3011

[171] Ritter A., 1878, Wiedemann Annalen, 6, 135

[172] Rix H.W. et al., 1997, ApJ, 488, 702

[173] Roberts P.H., 1962, ApJ, 136, 1108

[174] Rosseland S., 1926, ApJ, 63, 342

[175] Rusin D., Kochanek C.S., Keeton C.R., 2003, ApJ, 595, 29

[176] Rusin D., Kochanek C.S., 2005, ApJ, 623, 666

[177] Samadi M., Zanganeh S. & Abbassi S., 2019, MNRAS, 489, 3870

[178] Saslaw W.C., 1987, *Gravitational Physics of Stellar and Galactic Systems*, Cambridge University Press

[179] Satoh C., 1980, Publ. Astron. Soc. Japan 32, 41

[180] Sérsic J.L., 1963, Boletín de la Asociación Argentina de Astronomía, 6, 41

[181] Shankar F. et al., 2017, ApJ, 840, 34

[182] Shu F.H. et al., 1972, ApJ, 173, 557

[183] Shu F.H., 1991, *The Physics of Astrophysics. Volume I. Radiation*, University Science Books

[184] Shu F.H., 1991, *The Physics of Astrophysics. Volume II. Gas Dynamics*, University Science Books

[185] Smet C.O., Posacki S. & Ciotti L., 2015, MNRAS, 448, 2921

[186] Sommerfeld A., 1950, *Mechanics of Deformable Bodies*, New York Academic Press

[187] Spurzem R. & Kamlah A., 2023, Living Rev. Comput. Astrophys., 9, 3

[188] Stahler S.W. & Palla F., 2004, *The Formation of Stars*, Wiley-VCH, Weinheim

[189] Taam R.E., Fu A. & Fryxell B.A., 1991, ApJ , 371, 696

[190] Tassoul J.-L., 1978, *Theory of Rotating Stars*, Princeton University Press

[191] Tiongco M.A., Vesperini E. & Varri A.L., 2017, MNRAS , 469, 683

[192] Toci D. & Galli D., 2015, MNRAS, 446, 2110

[193] Toomre A., 1963, ApJ, 138, 385

[194] Tremaine S. et al., 1994, AJ, 107, 634

[195] Treu T. & Koopmans L.V.E., 2002, ApJ, 575, 87

[196] Treu T. & Koopmans L.V.E., 2004, ApJ, 611, 739

[197] Truesdell C.A., 1953, The American Mathematical Monthly, 445

[198] Truesdell C.A., 1984, *Rational Thermodynamics*, Springer-Verlag

[199] van den Bergh S., 1976, ApJ, 206, 883

[200] van den Bosch R.C.E. et al., 2008, MNRAS, 385, 647

[201] van Gorkom J.H, 2004, in *Clusters of Galaxies: Probes of Cosmological Structure and Galaxy Evolution*, ed. J.S. Mulchaey, A. Dressler & A. Oemler, Cambridge University Press, 305

[202] Varri A.L., Bertin G., 2012, A&A , 540, A94

[203] Volonteri M. & Rees M.J., 2005, ApJ, 633, 624

[204] Waters T.R. & Proga D., 2012, MNRAS, 426, 2239

[205] Waxman A.M., 1978, ApJ, 222, 61

[206] Whittaker E.T. & Watson G.N., 1902, *A Course of Modern Analysis*, Cambridge University Press

[207] Whittaker E.T., 1917, *A Treatise on the Analytical Dynamics of Particles and Rigid Bodies*, 2nd ed. Cambridge University Press

[208] Wyithe J.S.B. & Loeb A., 2012, MNRAS, 425, 2892

[209] Yuan F. & Narayan R., 2014, ARA&A, 52, 529

[210] Zeuner G., 1907, *Technical Thermodynamics*, Volume I, New York, D. Van Nostrand Company

[211] Zhu Z. et al., 2021, ApJ, 908, 17